



University of Sheffield

Large-scale ^{129}Xe -Rb Spin-Exchange Optical Pumping

James Ball

Supervised by
Dr. Graham Norquay
Professor Jim Wild

A thesis submitted in partial fulfilment of the requirements for the
degree of Doctor of Philosophy

POLARIS group
Division of Clinical Medicine
School of Medicine & Population Health
Faculty of Health
University of Sheffield

September 2023

Large-scale ^{129}Xe -Rb Spin-Exchange Optical Pumping © 2023 by James Ball is licensed under Attribution-NonCommercial-NoDerivatives 4.0 International. To view a copy of this license, visit <http://creativecommons.org/licenses/by-nc-nd/4.0/>.
Third-party content is included in this licence except where otherwise indicated.

Abstract

Spin-exchange optical pumping (SEOP) is a process by which the nuclear polarisation of xenon-129 (^{129}Xe) can be enhanced by a factor 10^5 of its thermal equilibrium value, enabling clinical hyperpolarised (HP) gas magnetic resonance imaging (MRI). This thesis is concerned with accurately modelling SEOP and implementing informed polariser design upgrades in order to improve the production of HP- ^{129}Xe for clinical hyperpolarised gas MRI. This was pursued through the following projects:

1. Modelling SEOP using 1D and 3D simulations in order to understand the effect of realistic gas flow dynamics, temperatures, and Rubidium (Rb) source distribution on Rb vapour density, $[\text{Rb}]$, and ^{129}Xe polarisation, P_{Xe} . It was found that implementing a sufficiently long presaturator leads to near-saturation homogeneous $[\text{Rb}]$ across the optical cell, and high P_{Xe} .
2. Optimisation of atomic absorption spectroscopy (AAS) for direct $[\text{Rb}]$ measurements across the optical cell. Determination of accuracy limits stemming from the breakdown of the Beer-Lambert law and line shape fitting at low spectral signal-to-noise ratios (SNR) was conducted over infrared and violet Rb valence electron transitions. It was observed that increasing Rb sources within the main cell body led to the most homogeneous $[\text{Rb}]$ distribution across the cell, however Rb runaway and cell temperature heterogeneity were observed to limit $[\text{Rb}]$ homogeneity. $[\text{Rb}]$ was measured to be consistently lower than saturation $[\text{Rb}]$, even at high laser absorption. In addition, the Rb- ^{129}Xe spin-exchange cross section, γ' , was calculated from the measured $[\text{Rb}]$ values and was determined to be $\gamma' = (1.1 \pm 0.1) \times 10^{-21} \text{ m}^3\text{s}^{-1}$.
3. Evaluating the use of a multi-compartment oven and optimal Rb source distribution to optimise thermal management. These upgrades led to reduced Rb runaway susceptibility and improved cell temperature homogeneity and laser absorption. Characterisation and optimisation of the upgraded polariser for HP- ^{129}Xe production was performed. Optimal running conditions for 1L volume HP-Xe dose were $P_{\text{Xe}} = 23.7\%$, and 29.6% at dose equivalence rates of $\Delta\text{DE} = 725\text{ml/hr}$ and $\Delta\text{DE} = 398\text{ml/hr}$ respectively. In addition, analytical and numerical models of SEOP were shown to differ at high laser absorption and/or low gas flow rates. The discrepancy between theoretical and measured P_{Xe} values persisted after the incorporation of measured spin-exchange values from $[\text{Rb}]$ measurements, suggesting the origin of this discrepancy extends to unexplored optical pumping and Rb spin-destruction considerations.

Acknowledgements

Firstly, I would like to thank my primary supervisor Graham Norquay. His encouragement and passion for research has been motivating. I am thankful for our many discussions over the last 4 years. Through his support I have learnt about being a successful researcher and he has inspired me to continue down this path. I would like to thank my secondary supervisor Jim Wild for the opportunity to undertake my PhD within the POLARIS group in Sheffield. The research output of POLARIS is a reflection of the outstanding research environment he has set up and led and I'm grateful to be a part of it. I'm thankful to both my supervisors for funding conference attendances to participate in and engage with the NMR and MRI communities.

I would like to thank Olly Rodgers and Ryan Munro for their practical abilities which have been of much help throughout my PhD, particularly in constructing the SEOP polariser. In addition, through our stimulating scientific conversations I have learnt about many aspects of mechanical engineering. I'd also like to thank Ryan for running our 5-a-side football team, which has been a great outlet. I would like to thank the mechanical workshop, in particular Simon Wiles, for building the bespoke components for the polariser, and Daniel Jackson, for glassblowing the intricate optical cells and miscellaneous parts that I tested, and broke, throughout my PhD.

I would like to thank everyone in the POLARIS team past and present for making the many days spent at my computer or in the lab a joy. In no particular order, Neil Stewart, Guilhem Collier, Helen Marshall, Laurie Smith, Ho-Fung Chan, Alberto Biancardi, Martin Brook, Jen Rodgers, Leanne Armstrong, Madhwesha Rao, Laura Saunders, Paul Hughes, Josh Astley, Bilal Tahir, Claudio Puddu, Kanishka Sharma, Joao Dos Santos Periquito, Eve Lennie, Jemima Pilgrim-Morris, Amy Simmons, Lynne Schofield, Demi-Jade Jakymelen, David Capener, Anna Zalewska, Shagufta Fazal, Jody Bray and Linda Clarke.

Finally, I would like to thank my friends and family. Thank you to Cathy for going to football matches with me and being very fun to be around. Thank you to my parents Clare and Chris and my brother and sister Rob and Mads for their support over the years. Thank you to my partner Sarah, I couldn't have done this without you.

Contents

1	Thesis overview	1
2	Introduction	2
3	Theory	4
3.1	Introduction	4
3.2	NMR principles	4
3.2.1	Zeeman effect	5
3.2.2	RF interaction	6
3.2.3	Semi-classical approach	7
3.2.4	Bloch equations and relaxation	10
3.2.5	Relaxation mechanisms	11
3.2.6	Fourier Transform NMR	16
3.3	Spin-exchange optical pumping	21
3.3.1	Optical pumping	21
3.3.2	Spin-exchange	29
3.3.3	^{129}Xe nuclear spin-destruction	35
3.4	Atomic absorption spectroscopy	38
3.4.1	Deviation from the Beer-Lambert law	41
4	1D and 3D modelling of the SEOP polariser	43
4.1	Introduction	43
4.2	Methods	45
4.2.1	1D simulations	45
4.2.2	3D simulations	46
4.2.3	Rb presaturator modelling	58
4.3	Results and Discussion	59
4.3.1	1D simulations	59
4.3.2	Varying Rb pool size	62
4.3.3	Varying flow rate in a Rb presaturator	66

4.3.4	Incorporating the Rb presaturator into the cell design	69
4.4	Conclusions	74
5	Using atomic absorption spectroscopy to measure in-cell Rb vapour density	75
5.1	Introduction	75
5.2	Methods	77
5.2.1	Polariser components	77
5.2.2	^{129}Xe polarimetry and laser absorption	85
5.2.3	Atomic absorption spectroscopy	92
5.2.4	Acquisition procedure	96
5.2.5	Accuracy of AAS fitting at low SNR	97
5.2.6	Spin-exchange cross section	98
5.3	Results and Discussion	99
5.3.1	^{129}Xe polarimetry	99
5.3.2	Accuracy of AAS fitting	102
5.3.3	Closed cell Rb density for different oven temperatures	103
5.3.4	AAS during continuous-flow SEOP	105
5.3.5	γ' and Γ' measurements	111
5.4	Conclusions	113
6	Optimisation of the large-scale Rb-^{129}Xe hyperpolariser	114
6.1	Introduction	114
6.2	Methods	116
6.2.1	Oven modification	116
6.2.2	Laser absorption for different Rb source distributions	118
6.2.3	1D simulations of Rb density heterogeneity and laser absorption	120
6.2.4	HP- ^{129}Xe production optimisation	124
6.3	Results and Discussion	130
6.3.1	Oven characterisation	130
6.3.2	Laser absorption for different Rb source distributions	134
6.3.3	1D simulations of Rb density heterogeneity and laser absorption	140
6.3.4	HP- ^{129}Xe production optimisation	147
6.4	Conclusions	161
7	Summary and future work	162
7.1	Summary	162
7.2	Future work	163
A	List of publications	167

A.1 List of publications from this thesis	167
A.2 Other co-authored publications	168
List of Figures	172
List of Tables	184
Bibliography	186

This page is intentionally blank

Chapter 1

Thesis overview

The overall aim of this work was to develop techniques for investigating the discrepancy between theoretical and measured high-throughput, continuous flow ^{129}Xe -Rb spin-exchange optical pumping hyperpolariser performance, and test polariser design improvements to optimise hyperpolarised ^{129}Xe production.

Chapter 2 and 3 are background and theoretical chapters relevant to all original research chapters. **Chapter 2** gives an overview of ^{129}Xe -Rb spin-exchange optical pumping hyperpolarisers and their importance for hyperpolarised gas MRI.

Chapter 3 provides the theoretical background of nuclear magnetic resonance, spin-exchange optical pumping and atomic absorption spectroscopy needed to understand how the polariser operates, as well as the diagnostic techniques used in its optimisation.

Chapter 4, 5 and 6 are original research chapters. **Chapter 4** reports on finite-element modelling of the polariser. Simulations of the existing polariser setup were performed. The simulated optimal Rb presaturator length is reported.

Chapter 5 looks to validate Rb density and temperature distributions produced by simulations with direct measurements. To do this, atomic absorption spectroscopy was developed for use on our system, as well as low- B_0 field Xe polarimetry.

Chapter 6 looks to implement the Rb source changes to the polariser setup, as well as incorporating spin-exchange parameters determined from direct Rb vapour density measurements into modelling, in order to optimise HP- ^{129}Xe production. In addition, different ^{129}Xe polarisation build up theoretical models are compared and their suitability assessed.

Chapter 7 summarises the original work, its impact on polariser design and future work objectives are discussed.

Chapter 2

Introduction

Nuclear magnetic resonance (NMR) was discovered by Rabi [1], where nuclei absorb radio-frequency energy of a particular frequency, specific to the isotope, when placed in a magnetic field. The first experiments of NMR in condensed matter were then carried out in 1945 [2,3]. NMR spectroscopy was made possible by the discovery of the chemical shift effect [4,5] and magnetic resonance imaging (MRI) was subsequently developed by Lauterbur [6] and Mansfield [7], allowing 3D images of matter, and importantly alive humans, to be performed.

Elsewhere in physics, optical pumping (OP) was proposed and observed [8,9]. In optical pumping, the populations of valence electrons across hyperfine energy levels in alkali metals can be polarised with photons in a beam of circularly polarised light. The non-thermal electronic populations (hyperpolarised (HP)) in alkali metals can transfer their angular momenta to noble gas nuclei through collisional spin-exchange interactions, first demonstrated by Bouchiat, Carver and Varnum [10]. The phenomenon of optical pumping followed by spin exchange is known as spin-exchange optical pumping (SEOP).

Throughout the 1960s to 1990s, numerous experiments along with theoretical models were developed to improve our understanding and optimisation of SEOP within rubidium-xenon (Rb-Xe) spin systems, such as measurements and modelling of Rb- ^{129}Xe spin-exchange cross sections [11–15], Rb relaxation rates [16–19] and ^{129}Xe relaxation rates [20–24]. This enhancement of nuclear spin polarisation proved beneficial for NMR and MRI applications of HP ^{129}Xe , significantly amplifying signal strength. Key to the development of HP ^{129}Xe gas MRI was demonstration of the first high-volume throughput Rb- ^{129}Xe SEOP polariser in 1996 [25].

In 1994, the first study of HP- ^{129}Xe MRI in vivo was published [26]. Subsequently, HP- ^{129}Xe MRI in a human was performed [27] (HP- ^3He MRI [28] in 1996). Although

HP- ^{129}Xe MRI had been established, HP- ^3He MRI was more widely adopted due to the higher achievable polarisations, production rates and magnitude gyromagnetic ratio ($\gamma_{^3\text{He}} = -32.44\text{MHz/T}$, compared to $\gamma_{^{129}\text{Xe}} = -11.78\text{MHz/T}$), leading to overall greater signal to noise ratio (SNR) of MRI of the lung air spaces. However, world shortages of ^3He , with limited availability and high costs per litre [29], resulted in MR research moving away from ^3He to the readily available and less expensive ^{129}Xe nucleus.

This roughly coincided with the development of narrower line width and higher power 795nm diode lasers used in Rb- ^{129}Xe SEOP. Major developments in ^{129}Xe -Rb polarisers followed, with large-scale production, $> 1\text{L/hr}$ of HP- ^{129}Xe , polarised to $\sim 42\%$ from Ruset and colleagues [30,31], giving on-demand up to 1L doses for HP- ^{129}Xe gas MRI. Another important development was that near-unity (theoretical maximum) polarisation was achieved in the open-source batch mode polariser developed by Peter Nikolaou and colleagues [32].

This has enabled clinical trials involving HP- ^{129}Xe MRI for pulmonary research as well as clinical diagnostic imaging, providing insight into obstructive lung conditions including chronic obstructive pulmonary disease [33–35], asthma [36,37], and cystic fibrosis [38–40]; as well as interstitial lung disease [41–46], and COVID-19 [47,48]. In addition, the high solubility of Xe in blood and tissues enables MR imaging of Xe in well perfused organs such as the brain [49], kidneys [50] and heart [51], offering a unique diagnostic tool to quantify physiological parameters associated with pathologies in organs beyond the lungs.

Since 2007, ^{129}Xe -Rb SEOP polarisers have been developed at the University of Sheffield, and the latest polariser generation has a production rate of $\sim 3.5\text{L/hour}$ of HP- ^{129}Xe [52], which has enabled clinical-scale research studies as well as clinical diagnostic referrals with a regulatory license for manufacturing HP- ^{129}Xe gas. However, the achievable production rates and polarisations are still too low for wider adoption of natural abundance Xe (26.4% ^{129}Xe), as opposed to the currently used enriched Xe (86% ^{129}Xe), which would decrease the cost per dose by \sim factor-10, especially due to the emergence of dissolved-phase ^{129}Xe MRI as a useful diagnostic tool, which requires high magnetisation (\propto polarisation and ^{129}Xe concentration). There are discrepancies between achievable polarisations given by existing theoretical models and experimentally measured values [52–55], suggesting that greater understanding of SEOP physics is required to further optimise ^{129}Xe -Rb SEOP. This is the motivation for this work in understanding and further optimising the ^{129}Xe -Rb SEOP polariser for clinical-scale HP- ^{129}Xe production.

Chapter 3

Theory

3.1 Introduction

This chapter describes the theory of nuclear magnetic resonance (NMR), spin-exchange optical pumping (SEOP) and atomic absorption spectroscopy (AAS) which are relevant to the experiments conducted in this thesis.

Firstly, practical aspects of NMR signal detection are outlined. Theoretical considerations of SEOP are then described in the context of how it is used to enhance the polarisation of noble gas nuclei. Finally, AAS of alkali electronic transitions, and its use to measure Rb vapour densities is explained.

3.2 NMR principles

Nuclear magnetic resonance arises from the intrinsic property of particles known as nuclear spin angular momentum, \mathbf{I} . Nuclei with non-zero spin have an associated dipolar magnetic moment

$$\boldsymbol{\mu} = \gamma\hbar\mathbf{I}, \quad (3.1)$$

where \hbar is the reduced Planck's constant, γ is the gyromagnetic ratio of the particle and $I = |\mathbf{I}|$ is the spin quantum number (integer or half-integer). A spin system can be described by its wavefunction, $|\psi(t)\rangle$, and obeys the time-dependent Schrödinger equation

$$i\hbar\frac{\partial}{\partial t}|\psi(t)\rangle = \hat{H}|\psi(t)\rangle, \quad (3.2)$$

where \hat{H} is the Hamiltonian operator for the system. For NMR, the Born-Oppenheimer approximation allows separation of the nuclear spin terms in the wavefunction and Hamiltonian. The effects of electrons are then included as additional terms in the

nuclear spin Hamiltonian. The nuclear spin Hamiltonian is defined as

$$\hat{H}_N = \underbrace{\hat{H}_Z + \hat{H}_{RF}}_{\text{external}} + \underbrace{\hat{H}_D + \hat{H}_{CS} + \hat{H}_J + \hat{H}_Q}_{\text{internal}}, \quad (3.3)$$

where \hat{H}_Z describes the Zeeman effect (see Section 3.2.1), \hat{H}_{RF} describes the interaction with radio frequency (RF) (see Section 3.2.2), \hat{H}_D is the result of dipole-dipole effects, \hat{H}_{CS} describes chemical-shift, which is affected by the interaction of surrounding electron orbitals with the applied magnetic field, \hat{H}_J is the indirect spin-spin interaction between nuclei mediated by the involved electrons and \hat{H}_Q is the quadrupolar effects of nuclei with $I > 1/2$. \hat{H}_D is not discussed, however a semi classical approach to dipole-dipole interactions is discussed in section 3.2.5. \hat{H}_{CS} , \hat{H}_J and \hat{H}_Q do not need to be discussed further in the context of the experiments performed in this work, due to uncoupled $I = 1/2$ ^{129}Xe nuclei involved in this work.

3.2.1 Zeeman effect

The Zeeman effect is the lifting of the degeneracy between magnetic energy states in the presence of an external magnetic field. The interaction between $\boldsymbol{\mu}$ and an applied static magnetic field, \mathbf{B}_0 , and can be described by the Hamiltonian

$$\hat{H}_Z = -\boldsymbol{\mu} \cdot \mathbf{B}_0 = -\gamma\hbar\mathbf{I} \cdot \mathbf{B}_0. \quad (3.4)$$

If the magnetic field is applied in the z-direction ($\mathbf{B}_0 = B_0\hat{\mathbf{z}}$) then

$$\hat{H}_Z = -\mu_z B_0 = -\gamma\hbar I_z B_0, \quad (3.5)$$

where μ_z is the z component of the nuclear magnetic moment. The eigenvalues of \hat{H}_Z give rise to discrete magnetic energy levels,

$$E_m = -m\gamma\hbar B_0, \quad (3.6)$$

where m is the magnetic quantum number and can be $-I, -(I-1), \dots, (I-1), I$. An energy level diagram of Zeeman splitting for different half-integer nuclei can be seen in Fig. 3.1.

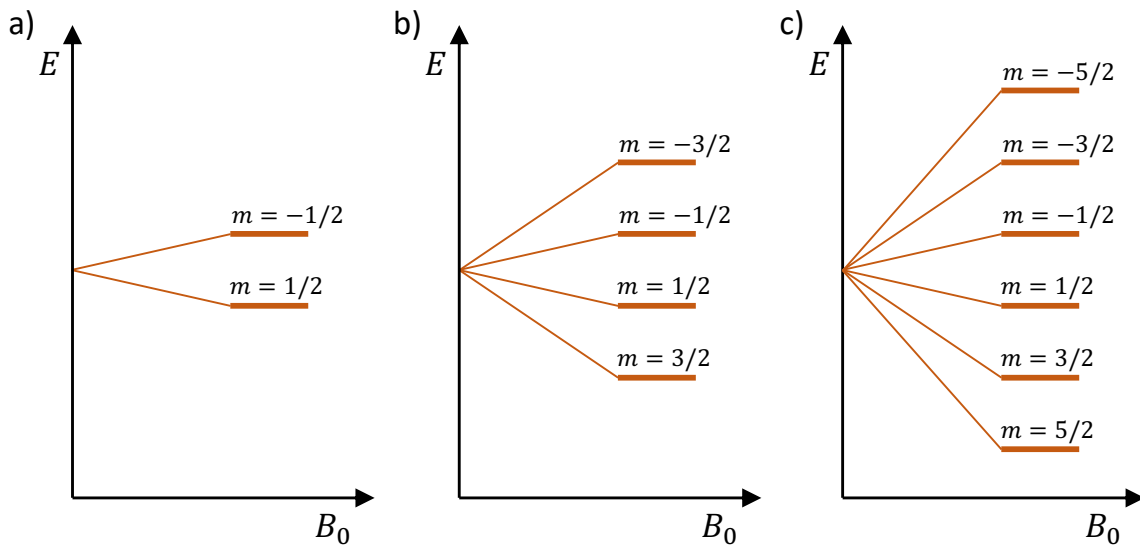


Figure 3.1: Zeeman splitting for spin half-integer systems. (a) $I = 1/2$, (b) $I = 3/2$, (c) $I = 5/2$.

For ^{129}Xe , $I = 1/2$, resulting in two energy levels ($E_{m=1/2} = -\gamma\hbar B_0/2$, $E_{m=-1/2} = \gamma\hbar B_0/2$). The difference in these energy levels, or the energy associated with transitions between nuclear energy levels, is

$$\Delta E = E_{m=-1/2} - E_{m=1/2} = \frac{1}{2}\gamma\hbar B_0 - \left(-\frac{1}{2}\gamma\hbar B_0\right) = \gamma\hbar B_0 = \hbar\omega_0, \quad (3.7)$$

where ω_0 is the Larmor frequency.

3.2.2 RF interaction

The application of an RF interaction is fundamental for NMR experiments. A radio frequency field consists of a linear oscillating magnetic field, $\mathbf{B}_1(t)$, given by

$$\mathbf{B}_1(t) = 2B_1 \cos(\omega t)\mathbf{i}. \quad (3.8)$$

It is convenient to split \mathbf{B}_1 into 2 counter-rotating circular fields, oscillating at frequency ω ,

$$\mathbf{B}_1 = \mathbf{B}_{1,-} + \mathbf{B}_{1,+} = B_1 [\cos(\omega t)\mathbf{i} - \sin(\omega t)\mathbf{j}] + B_1 [\cos(\omega t)\mathbf{i} + \sin(\omega t)\mathbf{j}]. \quad (3.9)$$

In a rotating frame oscillating at ω , $\mathbf{B}_{1,+}$ is stationary whilst $\mathbf{B}_{1,-}$ oscillates -2ω . This off-resonance oscillation means $\mathbf{B}_{1,-}$ can be neglected. The RF interaction Hamiltonian can then be described as

$$\hat{H}_{RF} = -\boldsymbol{\mu} \cdot \mathbf{B}_1 = -\gamma\hbar\mathbf{I} \cdot \mathbf{B}_1 = -\gamma\hbar I B_1 [I_x \cos(\omega t) + I_y \sin(\omega t)], \quad (3.10)$$

which is used for NMR detection, discussed in Section 3.2.6.

3.2.3 Semi-classical approach

So far, NMR has been explored with a quantum mechanical approach, concerned with systems containing a low number of spins. For systems containing a large numbers of spins, such as in this work, a semi-classical approach is less cumbersome.

Polarisation

For a system containing a large number of homonuclear (same spin I) spins, the energy level population sizes can be defined by a Boltzmann distribution. The probability of spins occupying an energy level E within the system is

$$\rho(E) = \frac{e^{\frac{-E}{k_B T}}}{Z} = \frac{e^{\frac{-E}{k_B T}}}{\sum_{m=-I}^I e^{\frac{-E_m}{k_B T}}}, \quad (3.11)$$

where Z is the partition function, k_B is the Boltzmann constant and T is the temperature in Kelvin. For a two-spin system such as ^{129}Xe or ^1H , the excess number of spins in the $m = 1/2$ (N_+) state compared to the $m = -1/2$ (N_-) state may be defined as $\Delta N \equiv N_+ - N_- = N(\rho_+ - \rho_-)$, where N is the total number of spins populating the two levels, and from Eq. 3.11 and 3.7

$$\rho_{\pm} = \frac{e^{\pm a/2}}{e^{a/2} + e^{-a/2}}, \quad (3.12)$$

where $a = \gamma\hbar B_0/k_B T$. The ratio of population excess ΔN to the total number of spins across all energy levels N is known as the nuclear spin polarisation. For ^{129}Xe nuclei, the polarisation is therefore given by

$$P = \frac{\Delta N}{N} = \frac{N(\rho_+ - \rho_-)}{N} = \left(\frac{e^{\frac{\gamma\hbar B_0}{2k_B T}} - e^{-\frac{\gamma\hbar B_0}{2k_B T}}}{e^{\frac{\gamma\hbar B_0}{2k_B T}} + e^{-\frac{\gamma\hbar B_0}{2k_B T}}} \right) = \tanh \frac{\gamma\hbar B_0}{2k_B T}. \quad (3.13)$$

For high temperatures ($k_B T \gg \gamma\hbar B_0$), ^{129}Xe polarisation can be approximated as

$$P = \frac{\gamma\hbar B_0}{2k_B T}. \quad (3.14)$$

The sum of the magnetic moments of nuclei within a Boltzmann distribution within the sample results in a net magnetisation, M_0 , given by

$$M_0 = N\mu_z P = N \frac{(\gamma\hbar)^2 B_0}{4k_B T}. \quad (3.15)$$

Greater NMR signal strength (proportional to M_0) is beneficial for MRI, however thermal magnetisation, as given by Eq. 3.15, is low at high temperatures and low magnetic fields, B_0 . Engineering limitations restrict current achievable magnetic field strengths, low temperatures cannot be used on living samples and increasing sample size, N , may not always be practical, especially if measuring signals from near-atmospheric pressure gases. Hyperpolarisation techniques allow temporary non-thermal polarisation to be reached, leading to high M_0 for increased NMR signal strength.

Equations of motion

A semi-classical approach is used to describe the motion of spins in a static magnetic field, \mathbf{H} . For a macroscopic spin ensemble, magnetic susceptibility must be considered and so \mathbf{H} is replaced with the magnetic induction, \mathbf{B} ,

$$\mathbf{B} = \mu_0 (1 + \chi) \mathbf{H}, \quad (3.16)$$

where μ_0 is the permeability of free space and χ is the magnetic susceptibility of the sample. Classical theory of electromagnetism states that a magnetic moment, $\boldsymbol{\mu}$, will undergo a torque $\boldsymbol{\tau}$, in the presence of an applied magnetic field \mathbf{B} , which is equal to the rate of change of its angular momentum.

$$\boldsymbol{\tau} = \frac{d\mathbf{I}}{dt} = \boldsymbol{\mu} \times \mathbf{B}. \quad (3.17)$$

Similarly, a spin ensemble with net magnetisation per unit volume is

$$\mathbf{M} = \frac{1}{V} \sum_i^N \boldsymbol{\mu}_i. \quad (3.18)$$

By combining Eq. 3.17 and 3.18, the motion of \mathbf{M} is described by

$$\frac{d\mathbf{M}}{dt} = \gamma \mathbf{M} \times \mathbf{B}. \quad (3.19)$$

In order to solve this, it is helpful to transform from the conventional laboratory frame, $S(x, y, z)$, to a rotating coordinate system, ‘the rotating frame’, $S'(x', y', z)$. S' is rotating with respect to S with angular velocity described by vector $\boldsymbol{\Omega}$ [56], as shown in Fig. 3.2. According to the general law of relative motion, the time derivative of any time-dependent vector computed in laboratory frame, $\frac{d\mathbf{A}}{dt}$, and its derivative in the rotating frame, $\frac{\partial \mathbf{A}}{\partial t}$, are related through

$$\frac{d\mathbf{A}}{dt} = \frac{\partial \mathbf{A}}{\partial t} + \boldsymbol{\Omega} \times \mathbf{A}. \quad (3.20)$$

Combining Eq. 3.19 and 3.20 gives

$$\frac{\partial \mathbf{M}}{\partial t} = \gamma \mathbf{M} \times \left(\mathbf{B} + \frac{\boldsymbol{\Omega}}{\gamma} \right). \quad (3.21)$$

Eq. 3.19 and 3.21 have the same form provided \mathbf{B} is replaced by an effective field, $\mathbf{B}_e = \mathbf{B} + \frac{\boldsymbol{\Omega}}{\gamma}$ consisting of the laboratory field, \mathbf{B} , and a fictitious field, $\frac{\boldsymbol{\Omega}}{\gamma}$. Setting the rotating frame as $\boldsymbol{\Omega} = -\gamma \mathbf{B}$ leads to $\mathbf{B}_e = 0$ and subsequently $\frac{\partial \mathbf{M}}{\partial t} = 0$, i.e. the magnetisation is a fixed vector in the rotating frame.

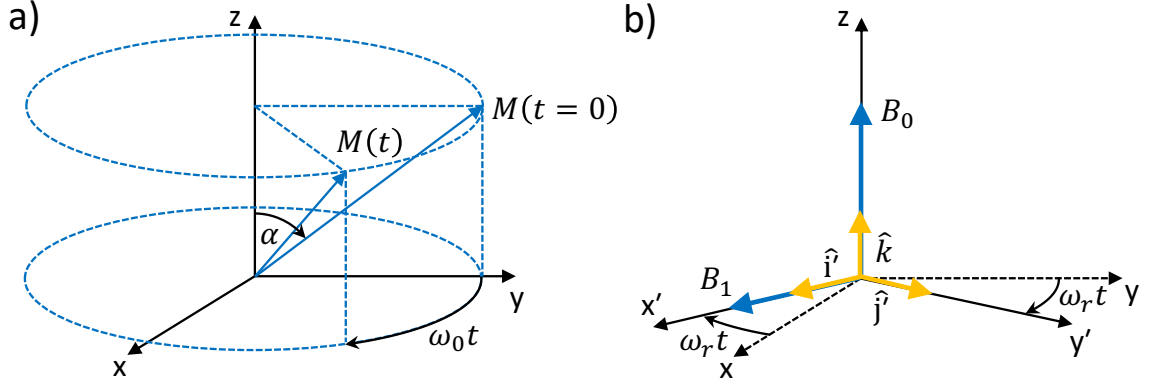


Figure 3.2: (a) Laboratory frame and (b) Rotating frame. Figure adapted with permission of John Wiley & Sons, from Ref. [57] 2023; permission conveyed through Copyright Clearance Center, Inc.

RF excitation

When an excitation pulse, i.e. a perpendicular transient magnetic field, $\mathbf{B}_1 = B_1 \hat{\mathbf{i}}$, is applied on resonance (i.e. $\frac{\Omega}{\gamma} = -B_0 \hat{\mathbf{k}}$), in addition to the static magnetic field, $\mathbf{B} = \mathbf{B}_0 = B_0 \hat{\mathbf{k}}$, in the z -direction, then $\mathbf{B}_e = \mathbf{B} + \frac{\Omega}{\gamma} = B_1 \hat{\mathbf{i}}$, and the equation of motion in the rotating frame (Eq. 3.21) becomes

$$\frac{\partial \mathbf{M}}{\partial t} = \gamma B_1 \mathbf{M} \times \hat{\mathbf{i}}. \quad (3.22)$$

This describes the precession of the magnetisation about the x -axis with angular velocity γB_1 . After time τ has past, the magnetisation will rotate through an angle $\alpha = \gamma B_1 \tau$, known as the flip angle. However, if the excitation pulse is off-resonance (i.e. $\frac{\Omega}{\gamma} \neq B_0 \hat{\mathbf{k}}$) then

$$\mathbf{B}_e = \mathbf{B} + \frac{\Omega}{\gamma} = \left(B_0 - \frac{\omega_r}{\gamma} \right) \hat{\mathbf{k}} + B_1 \hat{\mathbf{i}} = \Delta B \hat{\mathbf{k}} + B_1 \hat{\mathbf{i}}, \quad (3.23)$$

where ω_r is the frequency of the rotating frame or B_1 field about the z -axis and $\Delta B = B_0 - \frac{\omega_r}{\gamma}$ is the field offset between B_0 and the fictitious field ω_r/γ . Substituting Eq. 3.23 into Eq. 3.21 gives

$$\frac{\partial \mathbf{M}}{\partial t} = \gamma \mathbf{M} \times \left(\Delta B \hat{\mathbf{k}} + B_1 \hat{\mathbf{i}} \right). \quad (3.24)$$

The effective field, of magnitude $\sqrt{\Delta B^2 + B_1^2}$, makes an angle $\theta = \arctan\left(\frac{B_1}{\Delta B}\right)$. If $\Delta B \ll B_1$, $\theta \sim \pi/2$ and the magnetisation will be tipped into the y -axis, however if $\Delta B \gg B_1$, $\theta \sim 0$ and the magnetisation will evolve unaffected by the RF pulse.

3.2.4 Bloch equations and relaxation

Perturbation from equilibrium, as the result of an applied transient oscillating field, \mathbf{B}_1 , results in precession of the magnetisation \mathbf{M} about the effective field, \mathbf{B}_e . \mathbf{M} will not precess indefinitely, and instead will return to its equilibrium position due to damping mechanisms. This is known as spin-lattice or longitudinal relaxation and is described as

$$\frac{dM_z}{dt} = -\frac{M_z - M_0}{T_1}, \quad (3.25)$$

where T_1 is the longitudinal relaxation time constant. The solution of this is

$$M_z(t) = M_z(t=0) \exp\left(-\frac{t}{T_1}\right) + M_0 \left(1 - \exp\left(-\frac{t}{T_1}\right)\right). \quad (3.26)$$

In addition, an applied transient oscillating field leads to transverse magnetisation, M_x and M_y . The dampening process of this is known as spin-spin or transverse relaxation, and is described by

$$\frac{dM_{xy}}{dt} = -\frac{M_{xy}}{T_2}, \quad (3.27)$$

where T_2 is the transverse relaxation time constant. The solution of this is

$$M_{xy}(t) = M_{xy}(0) \exp\left(-\frac{t}{T_2}\right). \quad (3.28)$$

Combining Eqs. 3.25, 3.27 and 3.21 gives the equation of motion in the rotating frame

$$\frac{\partial \mathbf{M}}{\partial t} = \gamma \mathbf{M} \times \mathbf{B}_e - \frac{M_x \hat{\mathbf{i}} + M_y \hat{\mathbf{j}}}{T_2} - \frac{M_z - M_0}{T_1} \hat{\mathbf{k}}. \quad (3.29)$$

If $\mathbf{B}_e = \Delta B \hat{\mathbf{k}} + B_1 \hat{\mathbf{i}}$, then Eq. 3.29 can be re-written as the following equations, known as the Bloch equations in the rotating frame,

$$\frac{\partial M_x}{\partial t} = \gamma \Delta B M_y - \frac{M_x}{T_2}, \quad (3.30)$$

$$\frac{\partial M_y}{\partial t} = \gamma B_1 M_z - \gamma \Delta B M_x - \frac{M_y}{T_2}, \quad (3.31)$$

$$\frac{\partial M_z}{\partial t} = -\gamma B_1 M_y - \frac{M_z - M_0}{T_1}. \quad (3.32)$$

These equations are fundamental for many NMR experiments. After an excitation pulse that causes the magnetisation to be perturbed by 90° from the z-direction and lie entirely in the y-direction, the initial conditions are $M_z = M_x = 0$ and $M_y = M_0$ and the magnetisation will evolve in time according to

$$M_x(t) = M_0 \exp\left(-\frac{t}{T_2}\right) \sin(\omega' t), \quad (3.33)$$

$$M_y(t) = M_0 \exp\left(\frac{-t}{T_2}\right) \cos(\omega't), \quad (3.34)$$

$$M_z(t) = M_0 \left[1 - \exp\left(\frac{-t}{T_1}\right)\right], \quad (3.35)$$

where $\omega' = \omega_0 - \omega_r$ is the difference between the Larmor frequency ω_0 and the receive/mixing frequency ω_r of the spectrometer. This example of magnetisation evolution is used throughout this thesis.

3.2.5 Relaxation mechanisms

Relaxation is the process by which spins return to their equilibrium state after perturbation [58]. After RF perturbation, coherent spin precession is temporarily established. Spins precess at slightly different phases, which leads to decoherence, and the return of the net transverse magnetisation to zero over time. This is known as transverse (T_2) relaxation, and is described by Eq. 3.27.

In addition, after RF perturbation, the net longitudinal magnetisation changes due to non-Boltzmann spin populations. Over time, energy losses result in the spin population returning to Boltzmann levels. This is known as longitudinal (T_1) relaxation, and is described by Eq. 3.25.

Molecular motion causes translations and rotations of molecules, which rapidly alters the direction and position of the magnetic moment of each nuclei. These rapid fluctuations in local magnetic fields are experienced by neighbouring nuclei and will contribute efficiently to relaxation at fields close to the Larmor frequency via e.g. dipole-dipole coupling.

Induced electric currents give rise to small induced magnetic fields. Molecular motion will cause these induced magnetic fields to fluctuate. Relaxation due to local magnetic field fluctuations is known as chemical shift anisotropy. The sum of these fluctuating local magnetic fields causes the large static magnetic field to modulate slightly, and this results in spin-rotation relaxation.

$I > 1/2$ nuclei experience an additional relaxation mechanism due to electric quadrupole couplings, which will not be considered further as it is not relevant for the NMR spin systems in this work.

Correlation times

Molecular motion can be characterised by the molecular correlation time, τ_c , which is the time taken for a molecule to rotate through one radian. τ_c depends on the molecular

species, as well as the state of matter, temperature and pressure. The correlation time is an important parameter when considering the fluctuations of time-varying magnetic fields. A randomly varying magnetic field, $F(t)$, will average to zero, $\langle F(t) \rangle = 0$, however the mean square will be non-zero, $\langle F(t)^2 \rangle \neq 0$, defined by the magnitude of $\langle F(t) \rangle$. To define the rate of fluctuations of $F(t)$, the autocorrelation function, $\mathbb{G}(\tau)$ is used and is defined as

$$\mathbb{G}(\tau) = \langle F(t)F(t+\tau) \rangle \neq 0, \quad (3.36)$$

where τ is a time interval. At $\tau = 0$, $\mathbb{G}(\tau) = \langle F^2(t) \rangle$ and $\tau = \infty$, $\mathbb{G}(\tau) = 0$. For a slow fluctuating field, $F(t)$ and $F(t+\tau)$ values will be similar, meaning that $\langle F(t)F(t+\tau) \rangle$ will be high. However for fast fluctuating field, $F(t)$ and $F(t+\tau)$ values will differ and $\langle F(t)F(t+\tau) \rangle$ will be close to zero. In general the autocorrelation function is assumed to be a simple exponential

$$\mathbb{G}(\tau) = \langle F^2 \rangle \exp\left(\frac{-|\tau|}{\tau_c}\right). \quad (3.37)$$

Spectral density

The spectral density, $\mathbb{J}(\omega)$, is the Fourier transform of the autocorrelation function (integrating over time from $-\infty$ to $+\infty$, otherwise multiplied by 2 when integrating from 0 to $+\infty$), i.e. the frequency composition of this function,

$$\mathbb{J}(\omega) = 2 \int_0^{\infty} \mathbb{G}(\tau) \exp(-i\omega\tau) d\tau. \quad (3.38)$$

This defines the amount of motion within a system. The more motion there is (higher $\mathbb{J}(\omega)$) the faster the field fluctuations, increasing relaxation. Substituting Eq. 3.37 into Eq. 3.38 gives rise to

$$\mathbb{J}(\omega) = 2 \langle F^2 \rangle \frac{\tau_c}{1 + \omega^2 \tau_c^2} = 2 \langle F^2 \rangle \mathcal{J}(\omega), \quad (3.39)$$

where $\mathcal{J}(\omega) = \frac{\tau_c}{1 + \omega^2 \tau_c^2}$ is the normalised spectral density. Short τ_c broadens $\mathbb{J}(\omega)$ whilst long τ_c narrows $\mathbb{J}(\omega)$. While $\int_{-\infty}^{+\infty} \mathbb{J}(\omega)$ is independent of τ_c , there is a steep decrease in $\mathcal{J}(\omega)$ for $\omega > (\omega_0 \tau_c)^{-1}$, as shown in Fig. 3.3. In addition, at $\omega = \omega_0$, \mathcal{J} is maximum when $\omega_0 \tau_c = 1$, and relaxation will be at its most efficient.

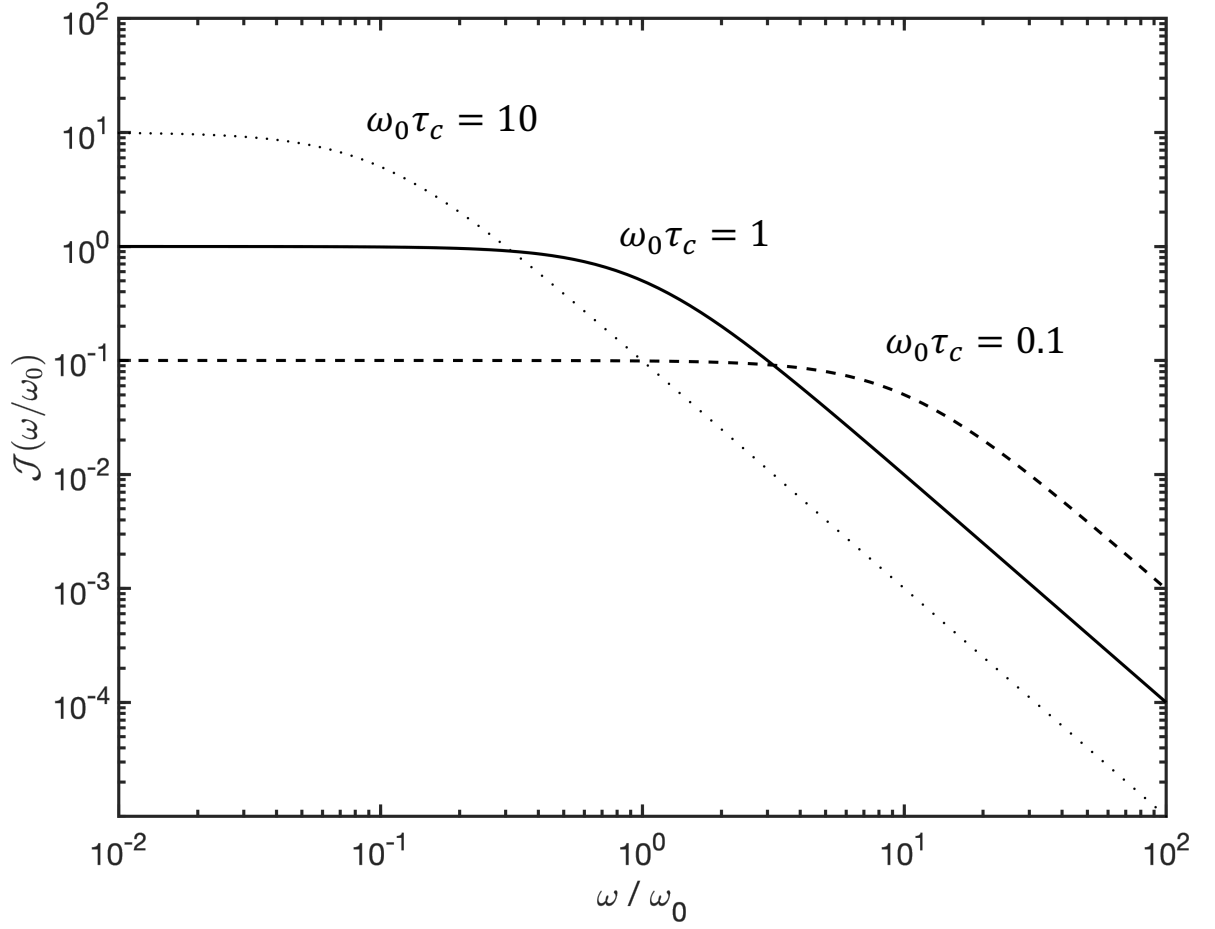


Figure 3.3: Spectral density vs frequency. $\omega_0 = 1$ was used. $\omega_0\tau_c = 0.1, 1$ and 10 are the dashed, solid and dotted lines respectively.

Transition probabilities

The fluctuating field induces transitions between spin energy levels. For a spin-1/2 system, there are n_α and n_β spins in the $|\alpha\rangle$ and the $|\beta\rangle$ energy states, respectively. The transition probability rate is W_- and W_+ for $|\alpha\rangle \rightarrow |\beta\rangle$ and $|\beta\rangle \rightarrow |\alpha\rangle$, respectively. The rate of population change for each state are

$$\frac{dn_\alpha}{dt} = W_+n_\beta - W_-n_\alpha, \quad (3.40)$$

$$\frac{dn_\beta}{dt} = W_-n_\alpha - W_+n_\beta. \quad (3.41)$$

The population difference is $n = n_\alpha - n_\beta$ and the total number of spins in the system is $N = n_\alpha + n_\beta$, therefore the change in population difference is

$$\begin{aligned} \frac{dn}{dt} &= \frac{d(n_\alpha - n_\beta)}{dt} = \frac{dn_\alpha}{dt} - \frac{dn_\beta}{dt} \\ &= 2(W_+n_\beta - W_-n_\alpha) \\ &= (W_+n_\beta - W_-n_\alpha)N - (W_+n_\beta + W_-n_\alpha)n. \end{aligned} \quad (3.42)$$

At equilibrium $\frac{dn}{dt} = 0$ which means $n = n_0 = \frac{(W_+n_\beta - W_-n_\alpha)}{(W_+n_\beta + W_-n_\alpha)}N$ and $n_0 \ll N$ so $W_+ \approx W_-$. Eq. 3.42 therefore becomes

$$\frac{dn}{dt} = 2W_-(n_0 - n). \quad (3.43)$$

Relating Eq. 3.43 to Eq. 3.25, and using $M_z = \frac{\gamma\hbar}{2}n$ and $M_0 = \frac{\gamma\hbar}{2}n_0$ derived from Eq. 3.15 and $n = NP$, gives

$$T_1 = \frac{1}{2W_-}. \quad (3.44)$$

By considering time-dependent perturbation theory, W_- is determined to be

$$W_- = \frac{1}{2}\gamma^2 \langle F^2 \rangle \mathcal{J}(\omega_0). \quad (3.45)$$

Substituting this into Eq. 3.44 gives the T_1 relaxation rate

$$\frac{1}{T_1} = \gamma^2 \langle F^2 \rangle \mathcal{J}(\omega_0) = \gamma^2 \langle F^2 \rangle \frac{\tau_c}{1 + \omega_0^2 \tau_c^2}. \quad (3.46)$$

The minimum of T_1 is where $\omega_0 \tau_c \approx 1$. Similarly, the fluctuating field effects on T_2 relaxation are [59]

$$\frac{1}{T_2} = \frac{\gamma^2 \langle F_{x,y}^2 \rangle}{2} \mathcal{J}(\omega_0) + \frac{\gamma^2 \langle F_z^2 \rangle}{2} \mathcal{J}(0) = \frac{1}{2T_1} + \frac{\gamma^2 \langle F_z^2 \rangle \tau_c}{2}, \quad (3.47)$$

where $\langle F_{x,y}^2 \rangle = \langle F^2 \rangle$, as only the transverse field fluctuations have been considered so far as they induce transitions. $\langle F_z^2 \rangle$ is the longitudinal field fluctuations, and its term in Eq. 3.47 only includes $\mathcal{J}(0)$, as $\langle F_z^2 \rangle$ does not induce transitions [59]. In the extreme narrowing limit ($\tau_c \rightarrow 0$), where field fluctuations in all directions are of similar magnitude, $T_2 \sim T_1$. As τ_c increases (in the case of solids or very viscous liquids), $\mathcal{J}(0)$ becomes increasingly significant and $T_2 < T_1$, similar to dipole-dipole relaxation presented in Fig. 3.5.

Dipole-dipole relaxation

Dipole-dipole relaxation can be explained by transitions between two coupled spins in an ensemble of weakly coupled homonuclear AX spin systems, as shown in Fig. 3.4.

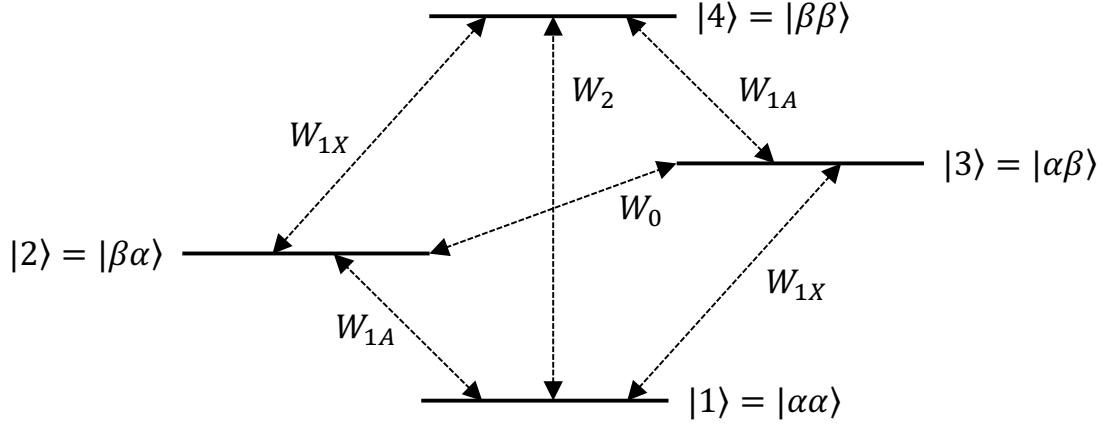


Figure 3.4: Transition probabilities in a homonuclear AX system.

The Solomon equations [60] define the time evolution of each of the two spins, which leads to the following relaxation rates: R_{auto} is the auto-relaxation rate, given by

$$R_{\text{auto}} = W_0 + 2W_1 + W_2, \quad (3.48)$$

where $W_1 = W_{1A} = W_{1X}$ for homonuclear AX systems; and R_{cross} is the cross-relaxation rate, given by

$$R_{\text{cross}} = W_0 - W_2. \quad (3.49)$$

The total longitudinal relaxation rate is given by

$$\frac{1}{T_1} = R_{\text{auto}} - R_{\text{cross}} = 2(W_1 + W_2). \quad (3.50)$$

Eq. 3.48, 3.49 and 3.50 have identical forms for the transverse relaxation rate ($= 1/T_2$). Applying the perturbing Hamiltonian for the dipole-dipole interaction gives

$$\frac{1}{T_1} = \frac{3}{10}b^2 [\mathcal{J}(\omega_0) + 4\mathcal{J}(2\omega_0)], \quad (3.51)$$

$$\frac{1}{T_2} = \frac{3}{20}b^2 [3\mathcal{J}(0) + 5\mathcal{J}(\omega_0) + 2\mathcal{J}(2\omega_0)], \quad (3.52)$$

where b is the dipole-dipole coupling constant. Eq. 3.51 and 3.52, shown in Fig. 3.5, are similarly shaped to relaxation due to fluctuation fields, Eq. 3.46 and Eq. 3.47.

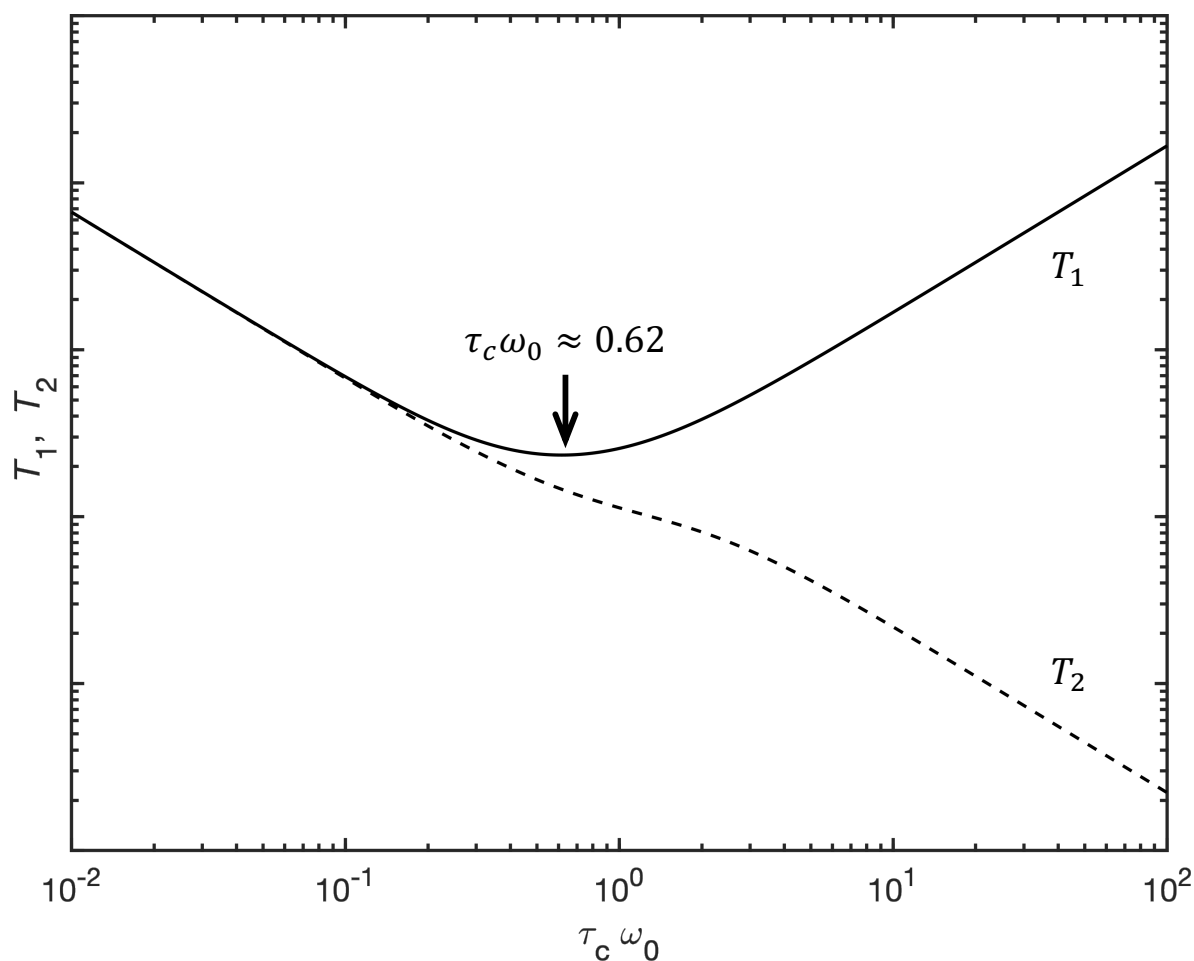


Figure 3.5: T_1 (solid line) and T_2 (dashed line) relaxation times due to dipole-dipole relaxation vs correlation time, τ_c . $\omega_0 = 1$ was used.

3.2.6 Fourier Transform NMR

Whilst NMR was historically performed using the continuous-wave method [3], Fourier transform NMR is the more convenient and intuitive technique for most applications. In summary, this involves a pulsed RF excitation followed by reception at a fixed magnetic field. This causes the temporary coherent precession of spins described previously. After excitation, the spins will continue to precess, slowly losing coherence over time. The precession induces a proportional signal in an RF coil (tuned LC circuit), with decay rate ($=1/T_2^*$) due to spin decoherence. If the sample is homogeneous, then the time-domain (signal vs time) is sufficient for determining information about the species. However, if the sample is heterogeneous, then performing a Fourier transform and analysing the data in the frequency domain over multiple resonances can be used to more efficiently extract information about its heterogeneous environment.

Free induction decay

The NMR circuit can be split into two parts, transmit and receive. These may consist of separate coils, but often one coil or an array of coils is used to perform both functions. For transmission, an oscillating current, $I_B = I_0 \cos(\omega t)$, is applied to the coil. Ampere's law means that this will produce an oscillating magnetic field, \mathbf{B}_1 , given by Eq. 3.8. The B_1 field tips the magnetisation into the transverse plane, as discussed in Section 3.2.3. For reception of the NMR signal, the coherent precession of spins after excitation is an oscillating magnetic field, $\mathbf{M}(\mathbf{r}, t)$. If placed near a coil, Faraday's law of induction means that an electromotive force, emf, in the coil will be induced, given by

$$\text{emf}(t) = -\frac{\partial}{\partial t} \int_{\text{sample}} \mathbf{M}(\mathbf{r}, t) \cdot \mathbf{B}(\mathbf{r}) d^3r, \quad (3.53)$$

where \mathbf{r} is the spatial position vector, \mathbf{M} is the time-varying magnetisation at \mathbf{r} and \mathbf{B} is the magnetic field when a unit current is passing through the coil at \mathbf{r} . If T_1^{-1} and T_2^{-1} are shorter than ω_0 , then using Eq. 3.34 and incorporating all time-independent parameters into the initial induced signal amplitude, $V_{s,0}$, the read signal, V_s , has the form

$$V_s(t) = V_{s,0} \cos(\omega_0 t) \exp\left(-\frac{t}{T_2^*}\right). \quad (3.54)$$

$1/T_2^* = 1/T_2 + 1/T_2'$, where $1/T_2'$ is due to B_0 heterogeneity and $1/T_2$ is due to spin-spin coupling (see Section 3.2.5). Phase sensitive detection (PSD) is then used in order to reduce the frequency of $V_s(t)$, reducing sampling rate requirements of data acquisition components. A reference signal, $V_{\text{ref}} = V_{\text{ref},0} \cos(\omega_{\text{ref}} t)$, is multiplied by the read signal (Eq. 3.54), which gives

$$\begin{aligned} S(t) &= V_{s,0} \cos(\omega_0 t) \exp\left(-\frac{t}{T_2^*}\right) \cdot V_{\text{ref},0} \cos(\omega_{\text{ref}} t) \\ &= \frac{1}{2} V_{s,0} V_{\text{ref},0} [\cos((\omega_0 - \omega_{\text{ref}}) t) + \cos((\omega_0 + \omega_{\text{ref}}) t)] \exp\left(-\frac{t}{T_2^*}\right). \end{aligned} \quad (3.55)$$

A low-pass filter is used to remove the high frequency $(\omega_0 + \omega_{\text{ref}})$ component, leaving a cosine which oscillates at frequency $\Delta\omega = \omega_0 - \omega_{\text{ref}}$, and initial amplitude $S_0 = \frac{1}{2} V_{s,0} V_{\text{ref},0}$,

$$S_{\text{Re}}(t) = S_0 \cos(\Delta\omega t) \exp\left(-\frac{t}{T_2^*}\right). \quad (3.56)$$

An additional PSD with 90° phase shift from the first PSD is used to distinguish between positive and negative frequency differences, known as quadrature detection. The resulting signal is

$$S_{\text{Im}}(t) = S_0 \sin(\Delta\omega t) \exp\left(-\frac{t}{T_2^*}\right). \quad (3.57)$$

Re and Im labels in Eq. 3.56 and 3.57 denote the real and imaginary components of the complex signal, S . This signal is known as free induction decay (FID), given by

$$S(t) = S_0 \exp(i\Delta\omega t) \exp\left(-\frac{t}{T_2^*}\right). \quad (3.58)$$

The Fourier transform of S leads to a complex Lorentzian function

$$\begin{aligned} \mathcal{F}[S(t)] &= \int_0^\infty S(t) \exp(-i\omega t) dt \\ &= \int_0^\infty S_0 \exp(i(\Delta\omega - \omega)t) \exp\left(-\frac{t}{T_2^*}\right) dt \\ &= S_0 \left(\frac{T_2^*}{1 + [(\omega - \Delta\omega) T_2^*]^2} - i \frac{(\omega - \Delta\omega) T_2^{*2}}{1 + [(\omega - \Delta\omega) T_2^*]^2} \right). \end{aligned} \quad (3.59)$$

The real part is the absorption Lorentzian and the imaginary part is the dispersion Lorentzian. The full width at half maximum (FWHM) of the absorption Lorentzian is $\frac{1}{\pi T_2^*}$, as shown in Fig. 3.6.

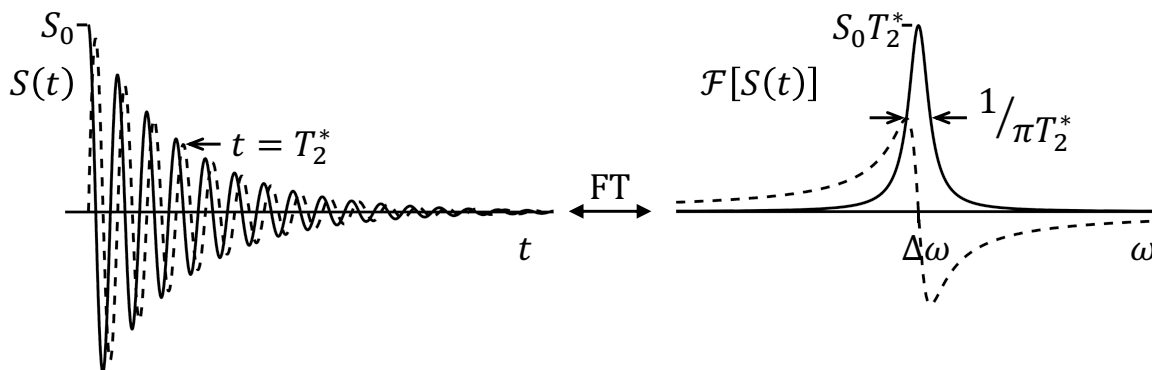


Figure 3.6: FID, $S(t)$, and NMR spectrum after Fourier transform, $\mathcal{F}[S(t)]$. The solid and dashed lines represent the real (absorption) and imaginary (dispersion) parts respectively.

NMR sensitivity

RF coils are LC circuits, tuned to resonate at the Larmor frequency, ω_0 , for greatest sensitivity. The sensitivity of a coil is given by its Quality (Q)-factor. This defines the self-dampening of the coil, and is given by

$$Q = \frac{L\omega_0}{R}, \quad (3.60)$$

where R is the resistance and $(L\omega_0)$ is the admittance at ω_0 . For detection, high Q is often desirable, at the expense of bandwidth. Coil bandwidth is defined as $\Delta f = f_c/Q$, where f_c is the resonance frequency of the coil. Radiation damping effects may limit

the Q desired for a NMR circuit. Random electronic noise (Johnson Noise) is given by

$$V_{rms} = \sqrt{4k_B T R \Delta f}, \quad (3.61)$$

where T is the temperature of the probe and Δf is the receiver circuit bandwidth. Environmental noise can be systematic (constant or periodic) or random, and can be dealt with by shielding or relocating apparatus away from noise sources. The signal to noise ratio is $SNR = S/\sigma_n$. σ_n is often equal to V_{rms} but not always. Therefore, typically low R is good for both high Q as well as low V_{rms} . Finally, the filling factor, η is important for efficient excitation of the sample and high signal, which is the ratio of sample volume to internal volume of the coil or the volume of high B_1 .

The coil design must be such that the produced B_1 excites the sample and that the subsequent time evolution of magnetisation induces a signal with high SNR. B_1 field produced by a coil can be predicted using the Biot-Savart approximation and superposition, which is

$$\mathbf{B}(\mathbf{r}) = \frac{\mu_0}{4\pi} \int_C \frac{I \mathbf{ds} \times \mathbf{r}}{|\mathbf{r}^3|}, \quad (3.62)$$

where C is path of the wire in which current, I , flows. \mathbf{ds} is a small section of the wire.

Heterogeneous resonator

An example of a heterogeneous resonator is a surface coil, as shown in Fig. 3.7a. This is a loop of wire, consisting of a number of turns, N . The magnetic field along the coil axis is [61]

$$B_y = \frac{\mu_0 N I}{2} \frac{a^2}{(a^2 + y^2)^{3/2}} = 2B_1, \quad (3.63)$$

where a is the radius of the coil, I is the current in the coil, assuming infinitely thin wires and tight windings. The magnetic field produced decreases rapidly away from the perpendicular axis. The steep drop off means B_1 is a highly localised field, and as such a high filling factor is readily obtainable, resulting in high sensitivity. However, the heterogeneous field is undesirable for many pulse sequences, which require homogeneous B_1 across the sample.

Homogeneous resonator

Design considerations for homogeneous B_1 fields also apply to homogeneous B_0 fields, important for both NMR and SEOP (discussed in Section 3.3). A Helmholtz coil design, as shown in Fig. 3.7b, is used where access to the sample is important. A Helmholtz configuration is defined such that the longitudinal separation of the coils is equal to the

coil radii, a . The magnetic field at the centre of the coils is given by [61]

$$B_x = \left(\frac{4}{5}\right)^{3/2} \frac{\mu_0 I}{a} = 2B_1. \quad (3.64)$$

A Helmholtz coil-pair consists of 2 coils, however a larger number of coils can be used to improve homogeneity (see Chapter 8 of ref. [61]).

Another example of a homogeneous resonator is a solenoid coil, as shown in Fig. 3.7c. The field along the coil axis is [61]

$$B_x = \frac{\mu_0 N I}{2l} \left(\frac{x + l/2}{\sqrt{a^2 + (x + l/2)^2}} - \frac{x - l/2}{\sqrt{a^2 + (x - l/2)^2}} \right), \quad (3.65)$$

where a and l are the radius and length of the solenoid. The magnetic field at the centre is given by

$$B_x = \frac{\mu_0 N I}{l_D} = 2B_1, \quad (3.66)$$

where l_D is the length of the solenoid diagonal. When a is small compared to l , the magnetic field is homogeneous near the centre of the solenoid.

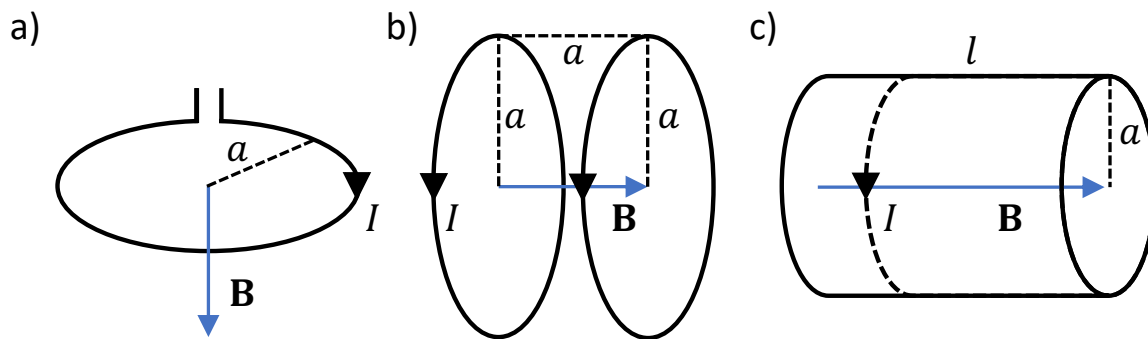


Figure 3.7: Coil designs showing the direction of the current, I , through the wire for (a) a surface coil, (b) a Helmholtz coil-pair and (c) a solenoid. The direction of \mathbf{B} , in blue, is given by the right-hand rule.

The coil designs shown in Fig. 3.7 are used in this work, however many other designs exist, such as saddle or birdcage [61]. In MRI, the spatial localisation and often large samples (i.e. part or whole body) make multi-array coils preferential.

While impedance matching is an important NMR circuit design criteria for high frequency systems ($\omega > \text{MHz}$), they are less relevant for the low frequency systems (order 10kHz) applicable to this work.

3.3 Spin-exchange optical pumping

The two-stage process of SEOP involves (i) optical pumping of Rb valence electrons, leading to high Rb electronic polarisation and (ii) spin-exchange between Rb valence electrons and ^{129}Xe nuclei. The Rb vapour density, $[\text{Rb}]$, governs the spin dynamics during both stages of SEOP and is therefore studied in detail throughout this work.

3.3.1 Optical pumping

The Rb valence electron undergoes several interactions and can occupy many energy levels, as shown in Fig. 3.8. The orbital structure, which defines the initial energy levels that the electron may occupy, is characterised by the electron orbital angular momentum quantum number, L (for $5S$, $L = 0$ and for $5P$, $L = 1$). The interaction of the orbit, \mathbf{L} and electron spin, \mathbf{S} , gives rise to the fine structure, characterised by the total angular momentum quantum number, J . The Rb nuclear spin, \mathbf{I} , and total angular momentum, \mathbf{J} , interact to form the hyperfine structure. This results in non-excited Rb valence electrons occupying $m_j = \pm 1/2$. The population differences between states is described by Boltzmann statistics (Eq. 3.13).

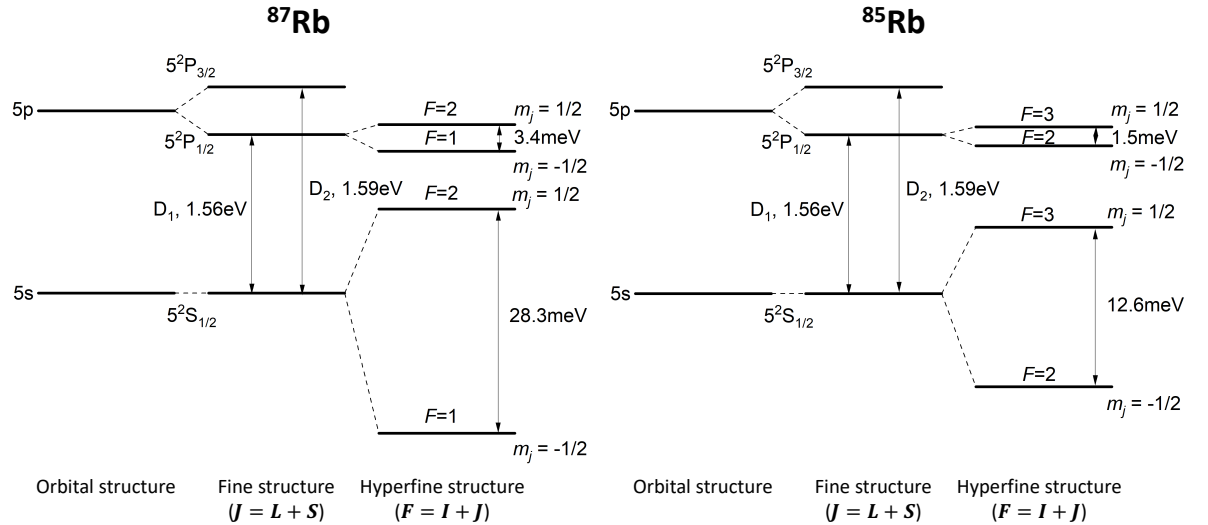


Figure 3.8: Rb energy level diagram of the orbital, fine and hyperfine structure. Diagram not to scale. Hyperfine transition energies are given by Steck [62, 63]. The hyperfine structure of $5^2P_{3/2}$ is not shown.

Left circularly polarised (photon spin $s_z = +1$) parallel to a static B_z field (helicity σ_+) and resonant on the D_1 line can only induce transitions from $5S_{1/2}$, $m_j = -1/2$ state, to the $5P_{1/2}$, $m_j = +1/2$ state due to the quantum selection rule of $\Delta m_j = +1$ imposed on the spin system. Spontaneous decay from the $5P_{1/2}$, $m_j = +1/2$ state

then follows. In the absence of buffer gases, decay to $5S_{1/2}$, $m_j = -1/2$ and $5S_{1/2}$, $m_j = +1/2$ occur with relative probabilities of $2/3$ and $1/3$ respectively [64]. However, in the presence of buffer gases (typically He and/or N_2), collisional mixing between $5P$ states leads to relative probabilities of $1/2$ for both decay channels. This decay can be non-radiative, provided a sufficient quantity of diatomic N_2 is present to absorb the energy into its translational, rotational and vibrational degrees of freedom [64]. Without N_2 quenching gas, relaxation of Rb electrons from the $5P_{1/2}$ to $5S_{1/2}$ state would result in emission of unpolarised photons which can then be reabsorbed by Rb electrons, leading to optical pumping of electrons in the $5S_{1/2}$, $m_j = +1/2$ state to the $5P_{1/2}$, $m_j = -1/2$ state, thereby reducing the build-up of ground-state Rb polarisation. This is known as radiation trapping. The branching ratio, which is a measure of the probability of radiation trapping occurring, is [64–66]

$$w_\gamma = \frac{3}{3 + 835[\text{amg}^{-1}][N_2]}, \quad (3.67)$$

where $[N_2]$ is in amagat¹. w_γ is $< 5\%$ for $[N_2] > 0.07$ amg.

Build up in the population of the $5S_{1/2}$, $m_j = +1/2$ state is described by the time-evolution of the probability of finding the Rb atom in the $m_j = +1/2$ state, $\rho_{+1/2}$, [64]

$$\frac{d}{dt}\rho_{+1/2} = \left(\frac{\Gamma_{\text{SD}}}{2} + R\right)\rho_{-1/2} - \frac{\Gamma_{\text{SD}}}{2}\rho_{+1/2}, \quad (3.68)$$

where $\rho_{-1/2}$ is the probability of finding the Rb atom in the $m_j = -1/2$ state, R is the optical pumping rate and Γ_{SD} is the Rb electronic spin-destruction rate. This process is summarised in Fig. 3.9.

¹1 amagat (amg) is the number of ideal gas molecules at standard temperature ($T_0 = 0^\circ\text{C}$) and pressure ($p_0 = 1$ atm). This is equivalent to 2.687×10^{25} atoms m^{-3} , which is known as the Loschmidt constant.

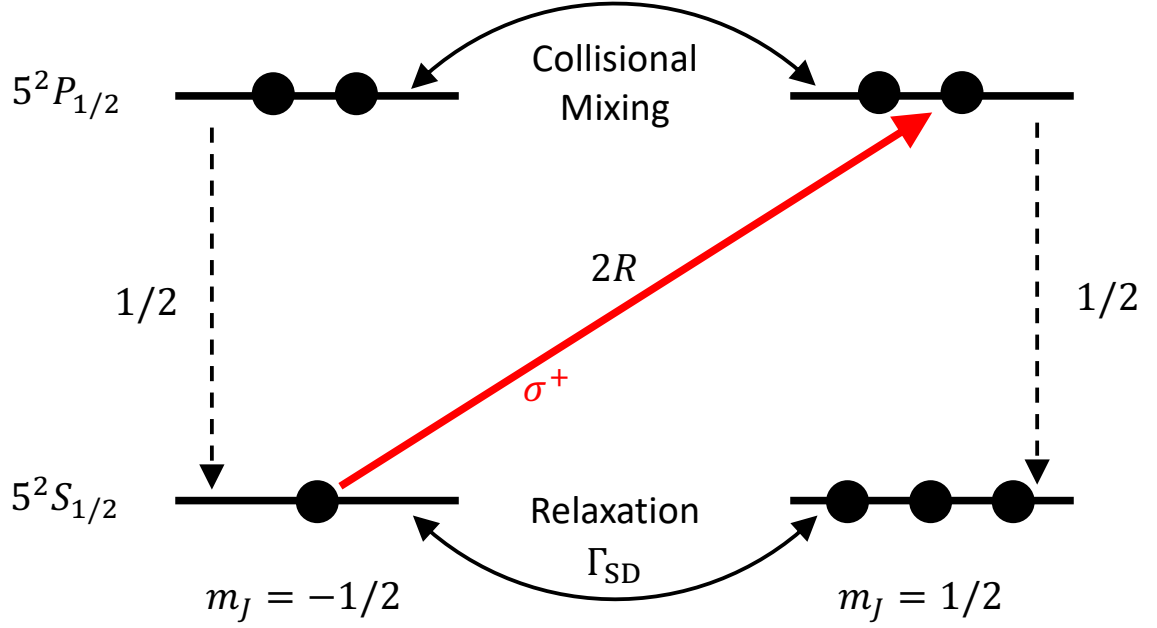


Figure 3.9: Optical pumping of the Rb D₁ line with left-circularly polarised light parallel to a static field B_z (σ^+).

Rb polarisation is defined as

$$P_{\text{Rb}} = \rho_{+1/2} - \rho_{-1/2}. \quad (3.69)$$

Given initial Rb polarisation, $P_{\text{Rb}}(t=0) = 0$, the time-dependent solution of Eq. 3.68 is

$$P_{\text{Rb}}(t) = \frac{R}{R + \Gamma_{\text{SD}}} [1 - \exp(-(R + \Gamma_{\text{SD}})t)]. \quad (3.70)$$

$R + \Gamma_{\text{SD}}$ is typically very fast and P_{Rb} quickly reaches equilibrium

$$P_{\text{Rb}} = \frac{R}{R + \Gamma_{\text{SD}}}. \quad (3.71)$$

R is related to the photon flux, Φ , and the absorption cross section for scattering of unpolarised light, σ_s by [64]

$$R(z) = \int \Phi(\nu, z) \sigma_s(\nu) d\nu. \quad (3.72)$$

σ_s typically has a Lorentzian spectral profile [64] and Φ has an initial Gaussian spectral profile before attenuation is considered.

The atomic centre frequency, ν_a , and linewidth, $\Delta\nu_a$, are defined for any gas composition as

$$\nu_a = \nu_{D_1} + \sum [G]_i (\nu_a)_i, \quad (3.73)$$

where ν_{D_1} is the non-shifted Rb D_1 absorption line centre frequency. $(\nu_a)_i$ and $[G]_i$ are the lineshift density coefficient and number density for each gas species i respectively.

$$\Delta\nu_a = \sum [G]_i (\Delta\nu_a)_i, \quad (3.74)$$

where $(\Delta\nu_a)_i$ is the linewidth broadening density coefficient for each gas species i . $(\nu_a)_i$ and $(\Delta\nu_a)_i$ values are given in Table 3.1.

Photon attenuation

So far we have only considered a thin ($\delta z \rightarrow 0$) slab of uniformly illuminated Rb vapour, however, in practice, the photon flux incident on a sample will be attenuated by absorption and lead to decreasing flux penetrating into the Rb vapour sample within the optical cell, as shown in Fig. 3.10.

Attenuation of the circularly polarised resonant photon flux, Φ , along the cell length, z , is described by [64]

$$\frac{d\Phi(\nu, z)}{dz} = -\lambda_{\sigma_+}^{-1} \Phi(\nu, z). \quad (3.75)$$

The mean absorption length per photon is given by

$$\lambda_{\sigma_+}^{-1} = 2[\text{Rb}] \sigma_s(\nu) \rho_{-1/2}. \quad (3.76)$$

Combining $\rho_{+1/2} + \rho_{-1/2} = 1$ with Eq. 3.69 gives an expression for $\rho_{-1/2}$,

$$\rho_{-1/2} = \left(\frac{1 - P_{\text{Rb}}}{2} \right). \quad (3.77)$$

Using Eq. 3.76 and 3.77, Eq. 3.75 can then be rewritten as

$$\frac{d\Phi(\nu, z)}{dz} = -[\text{Rb}] \sigma_s(\nu) (1 - P_{\text{Rb}}(z)) \Phi(\nu, z). \quad (3.78)$$

Laser (or photon) absorption, which is the proportion of photon flux absorbed across the full optical cell length, L_{cell} , is

$$L_{\text{abs}} = \frac{\Phi(z=0) - \Phi(z=L_{\text{cell}})}{\Phi(z=0)} \times 100\%. \quad (3.79)$$

Optical pumping rate attenuation

Alternatively, attenuation of the optical pumping rate can be described by rewriting Eq. 3.78 as

$$\frac{d\Phi(z)}{dz} = -[\text{Rb}] (1 - P_{\text{Rb}}(z)) R(z). \quad (3.80)$$

Eq. 3.72 can be evaluated for the photon flux at the SEOP cell incidence which gives [67]

$$R(0) = \alpha\Phi(0) = \alpha \frac{P_l n_p}{A}, \quad (3.81)$$

where P_l is the laser power, A is the beam area and n_p is the number of photons per Joule at the pump laser centre wavelength, λ_l . α is the coefficient relating Φ to R , which for a Gaussian laser profile has previously been shown to be [67,68]

$$\alpha = \frac{2\sqrt{\pi \ln 2} r_e f_{D_1} \lambda_l^3 w'(r, s)}{hc \Delta \lambda_l n_p}, \quad (3.82)$$

where $\Delta \lambda_l$ is the pump laser linewidth. $w'(r, s)$ is the real part of the complex overlap function, w , given by $w = w' + iw'' = e^{[\ln 2(r+is)^2]} \text{erfc}(\sqrt{\ln 2}[r + is])$. Here $s = 2(\nu_l - \nu_a)/\Delta \nu_l$ is the relative detuning and $r = \Delta \nu_a/\Delta \nu_l$ is the relative atomic linewidth of the atomic absorption line to the laser spectral output. erfc is the complimentary error function. If we assume that Φ remains Gaussian along z with attenuation ($R(z) = \alpha\Phi(z)$), which is valid when the line shape of the absorption cross section and laser profile are similar, then attenuation of R along the SEOP cell length, z , can be described by [69]

$$\frac{dR(z)}{dz} = -[\text{Rb}] \alpha (1 - P_{\text{Rb}}(z)) R(z). \quad (3.83)$$

Laser absorption can be estimated by substituting $\Phi(z) = R(z)/\alpha$ into Eq. 3.79 to give

$$L_{\text{abs}} = \frac{R(0) - R(L_{\text{cell}})}{R(0)} \times 100\%. \quad (3.84)$$

The validity of Eq. 3.83 and 3.84 diminishes as the absorption line and laser line shape overlap decreases.

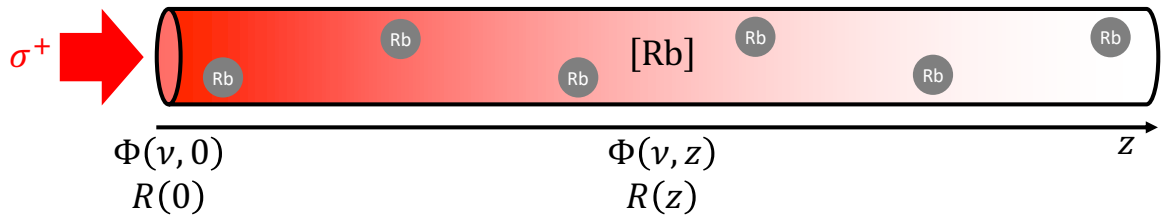


Figure 3.10: Schematic of photon or optical pumping attenuation along the optical cell. As circularly-polarised photons are absorbed by Rb in the optical cell, the photon flux, Φ , and optical pumping rate, R , decrease with cell position, z , represented by the red shading.

Rb spin-destruction rate

Rb electronic spin-destruction occurs due to both S-damping, which is not affected by Rb nuclear polarisation due to the short interaction times, and F-damping which is affected by Rb nuclear polarisation due to the relatively long interaction times. Rb electronic spin-destruction rate, Γ_{SD} is [68]

$$\Gamma_{SD} = \sum_i \eta_i \left[\frac{1}{T_{S,i}} + \frac{\nu_i(P)}{T_{F,i}} \right], \quad (3.85)$$

for $i \in \{^{85}\text{Rb}, ^{87}\text{Rb}\}$, where η_i is the abundance of the Rb isotope i , $\frac{1}{T_S}$ and $\frac{1}{T_F}$ are the S and F damping rates respectively. $\nu(P)$ is the coefficient that accounts for relaxation in long lived van der Waals (vdW) molecules given by

$$\nu(P_{\text{Rb}}) = \frac{q(I, P)}{[I]^2}, \quad (3.86)$$

where $[I] = 2I + 1$ is the statistical weight of the Rb nuclear spin quantum number I and $q(I, P) = 1 + \epsilon(I, P_{\text{Rb}})$ is the paramagnetic coefficient for P_{Rb} within a spin-temperature distribution. The q values for ^{87}Rb ($I = 3/2$) and ^{85}Rb ($I = 5/2$) isotopes are given by [68]

$$1 + \epsilon\left(\frac{3}{2}, P_{\text{Rb}}\right) = 1 + \frac{5 + P_{\text{Rb}}^2}{1 + P_{\text{Rb}}^2}, \quad (3.87)$$

$$1 + \epsilon\left(\frac{5}{2}, P_{\text{Rb}}\right) = 1 + \frac{35 + 42P_{\text{Rb}}^2 + 3P_{\text{Rb}}^4}{3 + 10P_{\text{Rb}}^2 + 3P_{\text{Rb}}^4}. \quad (3.88)$$

Rb electronic spin-destruction due to S-damping has contributions from both binary and vdW interactions ($\frac{1}{T_S} = \frac{1}{T_S^{bc}} + \frac{1}{T_S^{\text{vdW}}}$). The binary S-damping Rb spin destruction rate is

$$\frac{1}{T_S^{bc}} = \underbrace{[\text{Xe}] \langle \nu \sigma_{NS} \rangle}_{\text{depolarising Rb-Xe binary collisions}} + \underbrace{\eta_K \langle \nu \sigma_{KS} \rangle}_{\text{Rb - }^{129}\text{Xe binary SE collisions}} + \underbrace{[\text{Rb}] \langle \nu \sigma_{SS} \rangle}_{\text{depolarising Rb-Rb binary collisions}} + \underbrace{\sum_i [\text{Y}]_i \langle \nu \sigma_{NS} \rangle_i}_{\text{depolarising Rb-buffer gas binary collisions}}, \quad (3.89)$$

where $[\text{Xe}]$ is the Xe density, $[\text{Y}]_i$ is i buffer gas density (He or N_2), $\langle \nu \sigma_{NS} \rangle_i$ is rate coefficient for binary Rb and i gas collisions, $\langle \nu \sigma_{KS} \rangle$ is the rate coefficient for Rb- ^{129}Xe spin-exchange interactions during binary collisions, $\langle \nu \sigma_{SS} \rangle$ is the rate coefficient of Rb-Rb binary collisions and η_K is the ^{129}Xe abundance. Gas composition dependent expressions for $\langle \nu \sigma_{NS} \rangle_i$, $\langle \nu \sigma_{KS} \rangle$ and $\langle \nu \sigma_{SS} \rangle$ are given in Table 3.1.

The vdW S-damping Rb spin destruction rate is

$$\frac{1}{T_{S,i}^{\text{vdW}}} = \underbrace{\frac{C_{\alpha\gamma}}{T_{vW,A}}}_{\text{short-lived vdW molecules}} f_{S,i}, \quad (3.90)$$

where the three-body formation rate per Rb atom, $\frac{1}{T_{vW,A}}$, is defined as

$$\frac{1}{T_{vW,A}} = \frac{k[\text{Xe}]}{\tau}, \quad (3.91)$$

where k , is the molecular chemical equilibrium constant [14]. τ is the molecular lifetime, defined for any gas density composition $[G]_i$ by [13, 52]

$$\frac{1}{\tau} = \frac{\omega}{\phi_\gamma} = \sum_i \frac{\gamma N}{\hbar} \frac{[G]_i}{[G]_{0,i}}, \quad (3.92)$$

for $i \in \{\text{Xe}, \text{N}_2, \text{He}\}$, where $[G]_{0,i}$ is defined as the characteristic third-body density for which the molecular break-up rate τ^{-1} is equal to the spin-rotation frequency, $\omega = \gamma N/\hbar$, of the Rb electron spin vector \mathbf{S} about the rotational angular momentum vector \mathbf{N} of the RbXe molecule. ϕ_γ is the phase angle subtended by \mathbf{S} within a molecular lifetime τ , γ is the coupling constant that determines the strength of the spin-rotation interaction $\gamma \mathbf{N} \cdot \mathbf{S}$ [13].

$$C_{\alpha\gamma} = \frac{\eta_K \phi_\alpha^2}{2} + \frac{2\phi_\gamma^2}{3} \quad (3.93)$$

is a coefficient defined by the phase evolution angles for the vdW molecules ϕ_γ and $\phi_\alpha = \phi_\gamma/x$, where x is the Breit-Rabi field parameter, which determines the fractions of Rb electronic S momentum that is transferred to rotational angular momentum N and to the ^{129}Xe nuclear spin $K = 1/2$. The fraction of very-short regime vdW interactions is

$$f_{S,i} = \frac{1}{1 + (\omega_{hf,i}\tau)^2}, \quad (3.94)$$

where $\omega_{hf,i}$ is the Rb isotope i hyperfine frequency [70]. The vdW F-damping Rb spin destruction rate is

$$\frac{1}{T_{F,i}} = \underbrace{\frac{C_{\alpha\gamma}}{T_{vW,A}}}_{\text{long-lived vdW molecules}} f_{F,i}, \quad (3.95)$$

where $f_{F,i} = 1 - f_{S,i}$ is the fraction of short regime interactions. Combining Eq. 3.90 and 3.95, we get a full expression for Rb spin-destruction due to vdW molecules,

$$\Gamma_{\text{SD}}^{\text{vdW}} = \sum_i \eta_i \left[\frac{1}{T_{S,i}^{\text{vdW}}} + \frac{\nu_i(P)}{T_{F,i}} \right] = \frac{C_{\alpha\gamma}}{T_{vW,A}} \sum_i \eta_i [f_{S,i} + \nu_i(P)f_{F,i}]. \quad (3.96)$$

For low $[\text{N}_2]$, radiation trapping also contributes to Γ_{SD} . The frequency of radiation trapping is [71]

$$\Gamma_{\text{trap}} = \Gamma_{\text{trap}}([\text{N}_2] = 0) \cdot w_\gamma, \quad (3.97)$$

where w_γ is given by Eq. 3.67 and $\Gamma_{\text{trap}}([\text{N}_2] = 0)$ has been measured as $3.3 \times 10^4 \text{s}^{-1}$ [72] or $4 \times 10^4 \text{s}^{-1}$ [71]². Throughout this work, Γ_{trap} is ignored due to the high fraction

²Expression for Γ_{trap} in Eq. 3.97 does not include [Rb] dependence, which is expected as noted by Wagshul and Chupp [64].

(= 10%) of N_2 in the gas mixture used. Wall relaxation, interactions between Rb and impurities in the cell wall surface, also contribute to Γ_{SD} but are ignored due to slow Rb diffusion, high optical pumping rates and low surface to volume ratios of the optical cells used [73].

Limiting factors of optical pumping efficiency

In practice, optical pumping efficiency and Rb polarisation build up are affected by imperfect circularly polarised light [68], skewed light effects [74] and circular dichroism [75,76]. Lost photons due to scattering at the optical cell windows also occurs.

Imperfect circularly polarised light, $|s_z| < 1$, results in lower P_{Rb} by a factor $|s_z|$ [68] and increases laser absorption, due to the highly attenuating absorption of right circularly polarised light. However, attenuation of right circularly light is greater than left circularly polarised light for $s_z > 0$, and s_z approaches +1 along the light propagation axis for high [Rb] and cell lengths.

Skewed light effects are due to misalignment between the laser propagation and B_0 field directions, by an angle θ . This leads to an elevated fraction of absorbed photons that do not contribute to optical pumping. This lowers P_{Rb} by a factor $\cos\theta$ and increases laser absorption by a factor $1 + \frac{R \sin^2\theta}{\Gamma_{SD}}$. Unlike imperfect light polarisation, this effect persists through the optical cell [74].

Circular dichroism is where the differential absorption of light of opposite helicities causes a reduction in P_{Rb} by a factor $P_\infty = C/P_{Rb}$, which is the ratio of the normalised circular dichroism to Rb polarisation, and higher laser absorption by a factor $1 + 2R/\Gamma_{SD}(1 - P_\infty)$. At the centre of the D_1 absorption line, $P_\infty \approx 1$ and P_∞ decreases with detuning. Thus optical pumping with broad spectral width lasers is more susceptible to this effect than narrow spectral width lasers [76]. This has been characterised for ^3He -Rb SEOP [75,76] but is yet to be systematically studied in ^{129}Xe -Rb SEOP.

3.3.2 Spin-exchange

Spin-exchange occurs during interactions between Rb and ^{129}Xe atoms, described by the Hamiltonian [13]

$$\mathcal{H} = A\mathbf{I} \cdot \mathbf{S} + \gamma\mathbf{N} \cdot \mathbf{S} + \alpha\mathbf{K} \cdot \mathbf{S}, \quad (3.98)$$

where $A\mathbf{I} \cdot \mathbf{S}$ is the magnetic dipole interaction between the Rb electronic spin, \mathbf{S} , and the Rb nuclear spin, \mathbf{I} . $\gamma\mathbf{N} \cdot \mathbf{S}$ is the spin-rotation interaction between \mathbf{S} and the rotational angular momentum of the Rb-Xe van der Waals molecule or colliding pair, \mathbf{N} , and $\alpha\mathbf{K} \cdot \mathbf{S}$ is the magnetic dipole interaction between \mathbf{S} and ^{129}Xe nuclear spin, \mathbf{K} . The angular momentum vectors are shown in Fig. 3.11.

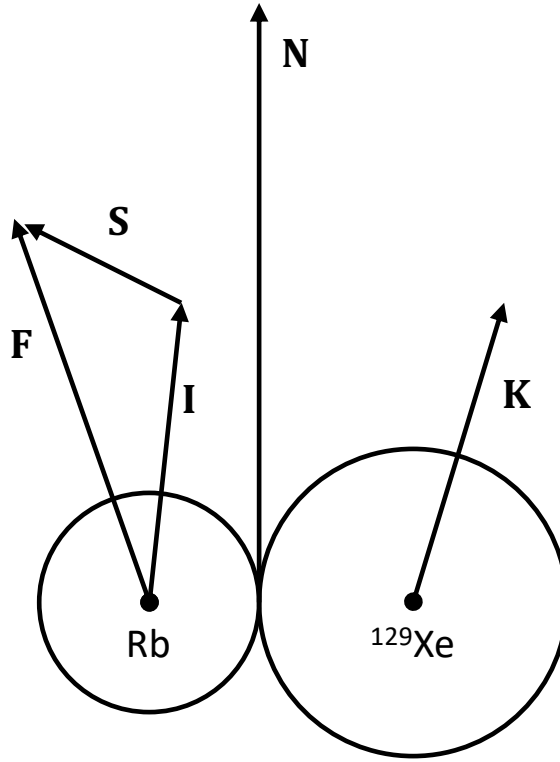


Figure 3.11: Angular momentum vectors associated with the Rb- ^{129}Xe van der Waals molecule or colliding pair.

The time-evolution of the alkali metal spin during spin-exchange is [68]

$$\frac{d\langle F_z \rangle}{dt} = -(R + \Gamma_{\text{SD}}) \langle S_z \rangle + \frac{R s_z}{2} + (\gamma_{\text{SE, Rb}}) \langle K_z \rangle, \quad (3.99)$$

where s_z is the photon spin of the circularly polarised pumping laser and $\gamma_{\text{SE, Rb}}$ is the ^{129}Xe to Rb spin-exchange rate given by

$$\gamma_{\text{SE, Rb}} = \gamma_{\text{SE}} \frac{\eta_K [\text{Xe}]}{[\text{Rb}]}, \quad (3.100)$$

where γ_{SE} is Rb to ^{129}Xe spin-exchange rate and $\eta_K[\text{Xe}]$ is the ^{129}Xe density. The steady-state solution of Eq. 3.99 is

$$P_{\text{Rb}} = 2 \langle S_z \rangle = \frac{s_z R + 2 \langle K_z \rangle \gamma_{\text{SE, Rb}}}{R + \Gamma_{\text{SD}}}, \quad (3.101)$$

where $2 \langle K_z \rangle$ is equal to the ^{129}Xe polarisation, P_{Xe} . Typically under optical pumping conditions, $s_z = 1$ and $s_z R \gg 2 \langle K_z \rangle \gamma_{\text{SE, Rb}}$, and Eq. 3.101 reduces to Eq. 3.71.

The time evolution of the noble gas nuclear spin during spin-exchange is

$$\frac{d \langle K_z \rangle}{dt} = \gamma_{\text{SE}} \langle S_z \rangle - (\gamma_{\text{SE}} + \Gamma') \langle K_z \rangle, \quad (3.102)$$

where Γ' is the ^{129}Xe relaxation rate in the absence of Rb. The steady-state solution of Eq. 3.102 is

$$P_{\text{Xe}} = \langle P_{\text{Rb}} \rangle \frac{\gamma_{\text{SE}}}{\gamma_{\text{SE}} + \Gamma'} [1 - \exp(-(\gamma_{\text{SE}} + \Gamma')t)], \quad (3.103)$$

where $\langle P_{\text{Rb}} \rangle$ is the average P_{Rb} over the Rb vapour sample. In practice, gas flow, thermodynamics and photon attenuation leads to spatial variability of parameters, for which P_{Xe} build up must be described by the time-independent convection-diffusion partial differential equation

$$\nabla \cdot (-\mathbf{D}_{\text{Xe}} \cdot \nabla \mathbf{P}_{\text{Xe}}) + \mathbf{v} \cdot \nabla \mathbf{P}_{\text{Xe}} = \gamma_{\text{SE}} \cdot \mathbf{P}_{\text{Rb}} - (\gamma_{\text{SE}} + \Gamma') \cdot \mathbf{P}_{\text{Xe}}, \quad (3.104)$$

where \mathbf{D}_{Xe} is the Xe diffusion coefficient and \mathbf{v} is the gas velocity.

Spin-exchange rate equation

Similarly to the Rb spin-destruction rate, the Rb to ^{129}Xe spin-exchange rate,

$$\gamma_{\text{SE}} = \gamma_{\text{SE}}^{\text{bc}} + \gamma_{\text{SE}}^{\text{vdW}}, \quad (3.105)$$

has contributions from S-damping binary collisions and the formation and break-up of RbXe vdW molecules, with S-damping and F-damping contributions, as shown in Fig. 3.12.

$$\gamma_{\text{SE}}^{\text{bc}} = \langle \sigma \nu \rangle_{\text{SE}} [\text{Rb}], \quad (3.106)$$

where $\langle \sigma \nu \rangle_{\text{SE}}$ is the binary ^{129}Xe -Rb spin-exchange cross section. The contribution to spin exchange from vdW interactions can be described by [68, 77]

$$\gamma_{\text{SE}}^{\text{vdW}} = \frac{\phi_\alpha^2}{2T_{vW,X}} \sum_i \eta_i [f_{S,i} + \nu_i(P) f_{F,i}] = \gamma'_{\text{vdW}} [\text{Rb}] \quad (3.107)$$

where $1/T_{vW,X} = [\text{Rb}]k/\tau$ is the Rb ^{129}Xe molecular formation rate per ^{129}Xe atom.

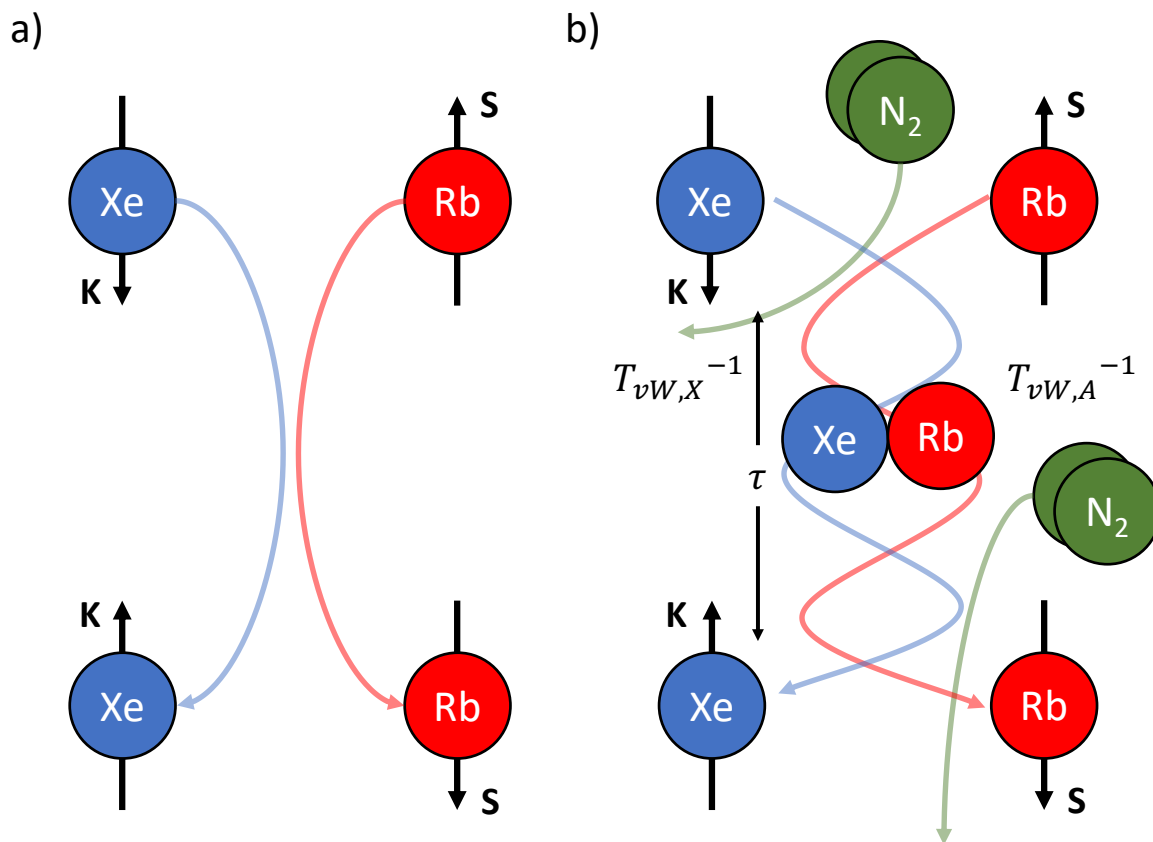


Figure 3.12: Spin-exchange between Rb and ^{129}Xe during (a) binary collisions and (b) the presence of the third body mediates spin exchange in van der Waals molecules.

η_K is important during Rb spin-destruction, but not spin-exchange due to the concentration of the second body involved, as seen in Fig. 3.13.

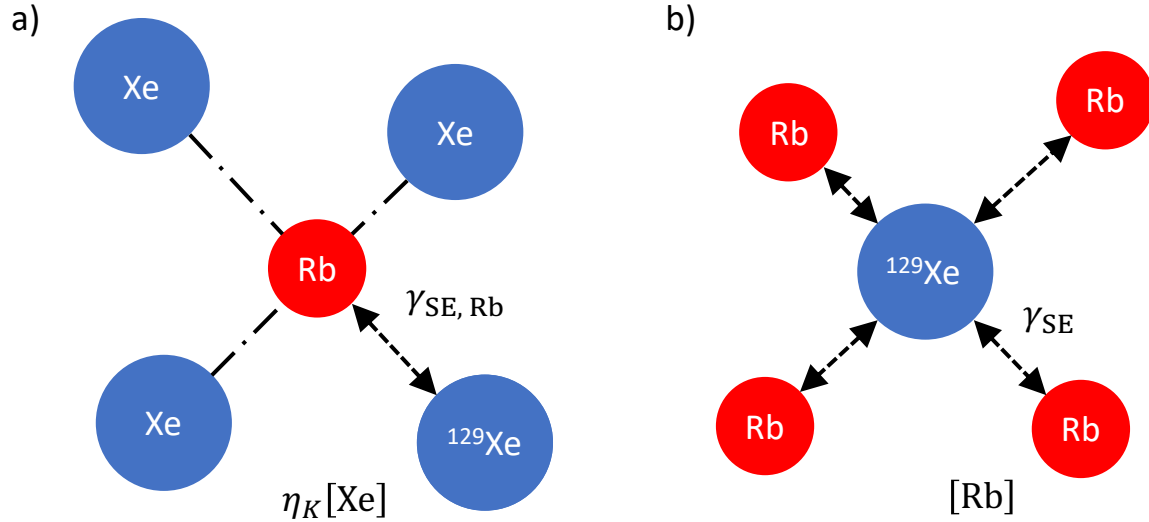


Figure 3.13: (a) Rb spin-destruction due to spin-exchange and (b) Xe polarisation build up due to spin-exchange. The arrows indicate polarisation transfer (spin-exchange interaction between S and K) whilst dashed lines without arrows indicates interactions without a transfer of polarisation.

We can define the total Rb- ^{129}Xe spin-exchange cross section as

$$\gamma' = \langle \sigma\nu \rangle_{\text{SE}} + \gamma'_{\text{vdW}}. \quad (3.108)$$

Spin-exchange parameter values are given in Table 3.1.

Table 3.1: SEOP Parameters. A range of values is given where multiple, differing, applicable values are present in the literature.

Parameter	Description	Equation/Value	Reference
$\frac{\omega}{2\pi}$	Spin-rotation frequency of S about N	$\gamma N/h = 109 - 135\text{MHz}$ (specific values: (109, 120, 121, 135) MHz)	[78], [20], [14, 79], [78, 79] respectively
x	The Breit-Rabi field parameter	3.2, 4.1	[22], [12] respectively
k	Molecular chemical equilibrium constant	$244 \text{ \AA}^3 (T/373)^{-3/2}$	[14]

Table continued over the page.

Continuation of Table 3.1.

Parameter	Description	Equation/Value	Reference
$[G]_{0,\text{Xe}}$	Xe characteristic gas density	$\left(\frac{28.3\text{Torr}}{760\text{Torr}}\right) \cdot \left(\frac{273.15\text{K}}{349\text{K}}\right) \cdot \left(\frac{349\text{K}}{T}\right)^{1/2} \text{amg}$	[15, 18, 22]
$[G]_{0,\text{N}_2}$	N ₂ characteristic gas density	$\left(\frac{103\text{Torr}}{760\text{Torr}}\right) \cdot \left(\frac{273.15\text{K}}{349\text{K}}\right) \cdot \left(\frac{349\text{K}}{T}\right)^{1/2} \text{amg}$	[22], with T dependence from [15]
$[G]_{0,\text{He}}$	He characteristic gas density	$\left(\frac{175\text{Torr}}{760\text{Torr}}\right) \cdot \left(\frac{273.15\text{K}}{358.45\text{K}}\right) \cdot \left(\frac{358.45\text{K}}{T}\right)^{1/2} \text{amg}$	[80], with T dependence from [15]
$[\text{Rb}]_{\text{sat}}$	Saturation Rb vapour density	$\frac{10^{10.55 - \frac{4132\text{K}}{T}}}{k_B T} \times 10^{-1} \text{m}^{-3}$	[81]
η_{85}	Relative abundance of ⁸⁵ Rb	0.7215	-
η_{87}	Relative abundance of ⁸⁷ Rb	0.2785	-
$\omega_{hf,85}$	⁸⁵ Rb hyperfine frequency	$2\pi \times 3.0357 \text{ GHz}$	[70]
$\omega_{hf,87}$	⁸⁷ Rb hyperfine frequency	$2\pi \times 6.8347 \text{ GHz}$	[70]
P_l	Laser power with cell window transmission losses	160W	this work
$\lambda_l = c/\nu_l$	Laser centre wavelength	794.77 nm	this work
$\Delta\lambda = \Delta\nu_l \frac{\lambda_l^2}{c}$	Laser full width at half maximum	0.25, 0.3 nm	this work, [52] respectively
A	Laser and optical cell cross sectional area	$4.4 \times 10^{-3} \text{ m}^3$	this work
L_{cell}	Internal cell length	78.7cm	this work
$\lambda_{D_1} = c/\nu_{D_1}$	Non-shifted Rb D ₁ centre wavelength	794.77 nm	[52]
$(\nu_a)_{4\text{He}}$	Rb D ₁ line shift due to ⁴ He	4.3 GHz/amg	[82]

Table continued over the page.

Continuation of Table 3.1.

Parameter	Description	Equation/Value	Reference
$(\nu_a)_{N_2}$	Rb D ₁ line shift due to N ₂	-8.25 GHz/amg	[82]
$(\nu_a)_{Xe}$	Rb D ₁ line shift due to Xe	-5.05 GHz/amg	[82]
$(\Delta\nu_a)_{^4He}$	Rb D ₁ linewidth broadening due to ⁴ He	18 GHz/amg	[82]
$(\Delta\nu_a)_{N_2}$	Rb D ₁ linewidth broadening due to N ₂	17.8 GHz/amg	[82]
$(\Delta\nu_a)_{Xe}$	Rb D ₁ linewidth broadening due to Xe	18.9 GHz/amg	[82]
$\langle\nu\sigma_{SS}\rangle$	Rb-Rb binary spin-destruction rate	$4.2 \times 10^{-19} \text{ m}^3\text{s}^{-1}$	[83]
$\langle\nu\sigma_{NS}\rangle_{^4He}$	Rb-He binary spin-destruction rate	$1 \times 10^{-35} T^{4.26} \text{ m}^3\text{s}^{-1}$	[83]
$\langle\nu\sigma_{NS}\rangle_{N_2}$	Rb-N ₂ binary spin-destruction rate	$1.3 \times 10^{-31} T^3 \text{ m}^3\text{s}^{-1}$	[84]
$\langle\nu\sigma_{NS}\rangle + \eta_K \langle\nu\sigma_{KS}\rangle$	Rb-Xe binary spin-destruction rate	$7.44 \times 10^{-21} (T/353\text{K})^{1.17} \text{ m}^3\text{s}^{-1}$	[78]
$\langle\sigma\nu\rangle_{SE}$	Binary ¹²⁹ Xe-Rb spin-exchange cross section	$(1.26 - 10) \times 10^{-22} \text{ m}^3\text{s}^{-1}$ (specific values: $(1.26, 4.02, 4.1, 10) \times 10^{-22} \text{ m}^3\text{s}^{-1}$)	[85], [86], [17, 22], [87] respectively
End of Table.			

3.3.3 ^{129}Xe nuclear spin-destruction

Short T_1 ($= 1/\Gamma'$ from Eq. 3.103) relaxation times are detrimental to the hyperpolarisation process, as well as limiting the lifetime of hyperpolarised ^{129}Xe . T_1 relaxation from a hyperpolarised state can be described by Eq. 3.26, where the initial magnetisation, $M_z(t=0)$ is the initial hyperpolarised magnetisation, M_{HP} , and the equilibrium (thermal) state is given by Eq. 3.15. Hyperpolarised ^{129}Xe relaxes through the mechanisms described in Section 3.2.5. In practice, hyperpolarised ^{129}Xe relaxation in the optical cell at $B_0 < 100\text{G}$ is determined by intrinsic and extrinsic processes, given by

$$\Gamma' = \Gamma_{\text{in}} + \Gamma_{\text{ex}} = (\Gamma_{\text{t}} + \Gamma_{\text{p}}) + (\Gamma_{\text{g}} + \Gamma_{\text{o}} + \Gamma_{\text{w}}). \quad (3.109)$$

Intrinsic contributions consist of transient (binary collisions) and persistent dimers (vdW molecular formation), Γ_{t} and Γ_{p} respectively. Extrinsic contributions consist of diffusion through gradients in the magnetic field, Γ_{g} , paramagnetic oxygen, Γ_{o} and wall relaxation, Γ_{w} .

Intrinsic contributions

Relaxation due to Xe-Xe binary collisions (transient dimers) is given by [88]

$$\Gamma_{\text{t}} = (5.0 \pm 0.5) \times 10^{-6} [\text{Xe}] \text{s}^{-1}, \quad (3.110)$$

where $[\text{Xe}]$ is in amagat. Relaxation due to the formation of vdW molecules (persistent dimers) is given by

$$\Gamma_{\text{p}} = \Gamma_{\text{vdW}}^{\text{Xe}} \left(1 + r \frac{[\text{B}]}{[\text{Xe}]} \right), \quad (3.111)$$

where $\Gamma_{\text{vdW}}^{\text{Xe}} = (6.7 \pm 0.1) \times 10^{-5} \text{s}^{-1}$ is the vdW relaxation term for pure Xe, $[\text{B}]$ is the buffer gas density and $r = k_{\text{B}}/k_{\text{Xe}}$ where k_{B} and k_{Xe} are the the breakup rate coefficients of the buffer gas and Xe respectively [89].

Extrinsic contributions

Relaxation due to paramagnetic oxygen at high field ($B_0 = 4.7\text{T}$) is given by [24, 90]

$$\Gamma_{\text{o}} = 0.388[\text{s}^{-1}] \frac{p_{\text{O}_2}[\text{Bar}]}{1.013[\text{Bar}]} \frac{273[\text{K}]}{T[\text{K}]} \left(\frac{300[\text{K}]}{T[\text{K}]} \right)^{0.03}, \quad (3.112)$$

where p_{O_2} is the oxygen partial pressure. Γ_{o} is decreased by careful gas loading of the optical cell. Given vacuum $< 3\text{mbar}$ is achievable, assuming air (21% O_2) contamination, $\Gamma_{\text{o}} < 2.2 \times 10^{-4} \text{s}^{-1}$ at $T = 20^\circ\text{C}$. For Xe in air at $p = 1\text{atm}$, $\Gamma_{\text{o}} = 7.6 \times 10^{-2} \text{s}^{-1}$.

The relaxation rate due to diffusion through transverse magnetic field gradients, $\frac{|\nabla B_{\perp}|}{B_0}$, is given by [23]

$$\Gamma_{\text{g}} = D_{\text{Xe}} \left(\frac{|\nabla B_{\perp}|}{B_0} \right)^2, \quad (3.113)$$

where D_{Xe} is the Xe diffusion coefficient. A homogeneous magnetic field is easily attainable for most SEOP setups, so this contribution is usually negligible within the main SEOP field. However, care must be taken that the polarised ^{129}Xe does not cross significant field gradients during its journey from the SEOP cell exit to the sample collection space.

Wall relaxation

Wall relaxation is driven by interactions between Xe and the surface of the optical cell wall, which contains paramagnetic impurities. If wall relaxation is sufficiently slow, and ^{129}Xe polarisation is homogeneous across the cell, then wall relaxation can be modelled as follows. If we consider the flux of spin into the cell wall [91],

$$j_I = \frac{[\text{Xe}]\bar{w}\langle I_z \rangle}{4}, \quad (3.114)$$

where $\bar{w} = \sqrt{8k_B T / \pi M_{\text{Xe}}}$ is the Xe thermal speed [92], then the rate at which spin polarisation is lost at the cell walls is given by

$$[\text{Xe}]V_{\text{cell}}\Gamma_w \langle I_z \rangle = \alpha j_I S_{\text{cell}}, \quad (3.115)$$

where S_{cell} is the internal surface area of the cell, V_{cell} is the volume of the cell and α is the probability of spin destruction per a single wall encounter [91], or $\alpha = 1/N_b$ where N_b is the number of coherent bounces [92]. The wall relaxation rate, Γ_w , is then determined by rearranging Eq. 3.115 and substituting j_I defined in Eq. 3.114 to give

$$\Gamma_w = \eta_w \frac{S_{\text{cell}}}{V_{\text{cell}}}, \quad (3.116)$$

where $\eta_w = \frac{\alpha\bar{w}}{4}$ is the relaxivity of the cell walls. η_w of Pyrex, the typical material of optical cells, has been determined to be $1.14 \times 10^{-3} \text{cm s}^{-1}$ [93, 94]. However, it has been observed that Γ_w is B_0 field dependent, through the magnetisation of impurities in the glass [88]. Γ_w may also be temperature and/or [Rb] dependent as reported in studies of both ^3He -Rb [95] and ^{129}Xe -Rb [96] SEOP. Increased Xe wall contact time under flow due to convection rolls, and hence increased Γ_w has been simulated [71], further complicating Γ_w . Additionally, Γ_w has been shown to increase over time, for which cleaning is necessary to restore lower values of Γ_w [97].

Finally, surface coatings, which provide distance between impurities in the glass and/or reduce the contact time during Xe wall collisions, have been used to decrease Γ_w compared to uncoated Pyrex [32, 73, 93, 98, 99], as shown in Table 3.2.

Table 3.2: In-cell ^{129}Xe relaxation times in the absence of Rubidium, $T_1 = 1/\Gamma'$, measured in different SEOP cells. BM = batch-mode and CF = continuous-flow.

SEOP application	Coating	$T_1 = 1/\Gamma'$ (min)	B_0 field (G)	Reference
CF clinical-polariser	Uncoated Pyrex	44	30	[52]
CF clinical-polariser	-	3.7	≈ 20	[100]
CF clinical-polariser	-	≈ 1.28	30	[53]
BM clinical-polariser	SurfaSil	114 ± 36	52.6	[32]
BM clinical-polariser	SurfaSil	≈ 150	35	[99]
BM clinical-polariser	Uncoated Pyrex	0.83	≈ 450	[73]
BM clinical-polariser	OTS	5 (up to 10 and 17 also quoted)	≈ 450	[73]
Flame-sealed cells	Uncoated Pyrex	22 to 48	47000	[93]
Flame-sealed cells	SurfaSil	160 to 180	47000	[93]

3.4 Atomic absorption spectroscopy

Atomic absorption spectroscopy (AAS) is the absorption of radiant energy by atoms. This absorption is through the valence electronic energy transitions, in a similar manner to optical pumping, however rather than hyperfine transitions that result in non-thermal population differences in the $m_j = -1/2$ and $m_j = +1/2$ states, AAS uses unpolarised light to induce fine structure transitions from the ground state ($5^2S_{1/2}$) at low photon fluxes. The structure of Rb electronic transitions is given in Fig. 3.14, with corresponding parameters in Table 3.3, showing the different possible ground state energy transitions.

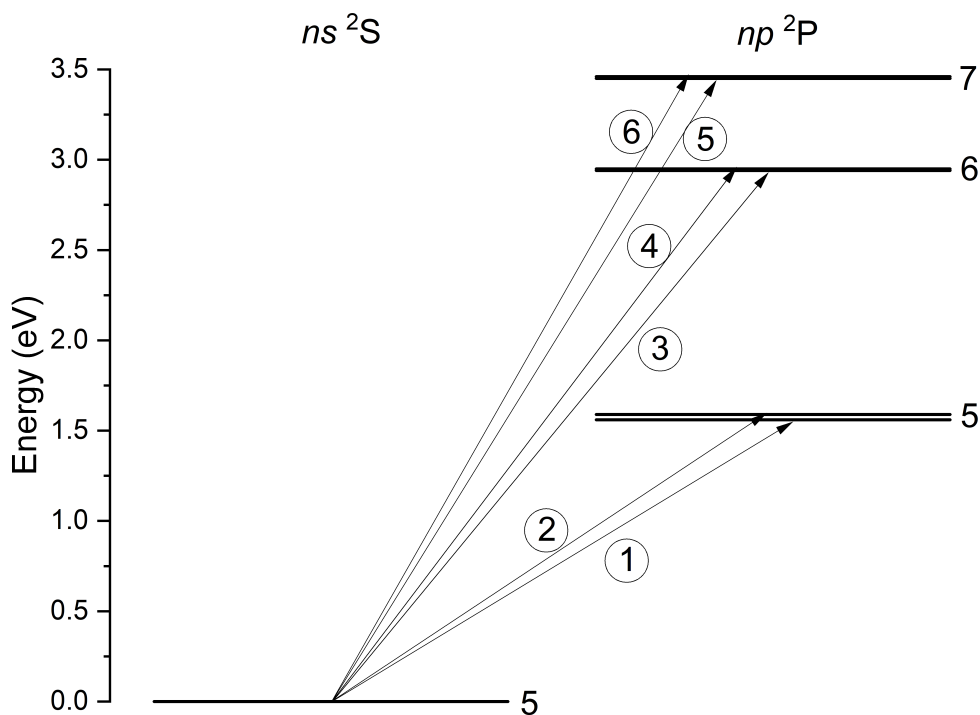


Figure 3.14: Grotrian Rubidium energy level diagram. Transition parameters are given in Table 3.3.

Table 3.3: Rubidium electronic transition parameters.

Fig. 3.14 transition number	Transition	Energy (eV)	Wavelength (nm)	Absorption oscillator strength, f	Reference
①	$5S_{1/2} \rightarrow$ $5P_{1/2}$ (D ₁)	1.56	795	0.3422	[62, 63, 101]
②	$5S_{1/2} \rightarrow$ $5P_{3/2}$ (D ₂)	1.59	780	0.6957	[62, 63, 101]
③	$5S_{1/2} \rightarrow$ $6P_{1/2}$	2.94	422	3.87×10^{-3}	[101, 102]
④	$5S_{1/2} \rightarrow$ $6P_{3/2}$	2.95	420	9.46×10^{-3}	[101, 102]
⑤	$5S_{1/2} \rightarrow$ $7P_{1/2}$	3.45	359.3	5.24×10^{-4}	[101, 102]
⑥	$5S_{1/2} \rightarrow$ $7P_{3/2}$	3.46	358.8	1.51×10^{-3}	[101, 102]

AAS relies on the Beer-Lambert law, which describes the attenuation of light through a medium, as shown in Fig. 3.15, and is described by

$$I(\nu) = I_0(\nu) e^{-[\text{Rb}]l\sigma(\nu)}, \quad (3.117)$$

where I_0 is the spectral profile of the light source in the absence of Rb vapour and I is the spectral profile of the light after passing through the sample of path length l . σ is the absorption cross section specific to a given electronic Rb transition, which can be integrated over frequency to get the expression

$$\int \sigma(\nu) d\nu = \pi r_0 c f, \quad (3.118)$$

where r_0 is the classical electron radius, c is the speed of light and f is the absorption oscillator strength specific to each Rb transition, as given in Table 3.3. f is the probability of absorption (or emission) of energy in a transition between energy levels, which can be theoretically calculated [103] or experimentally measured [104].

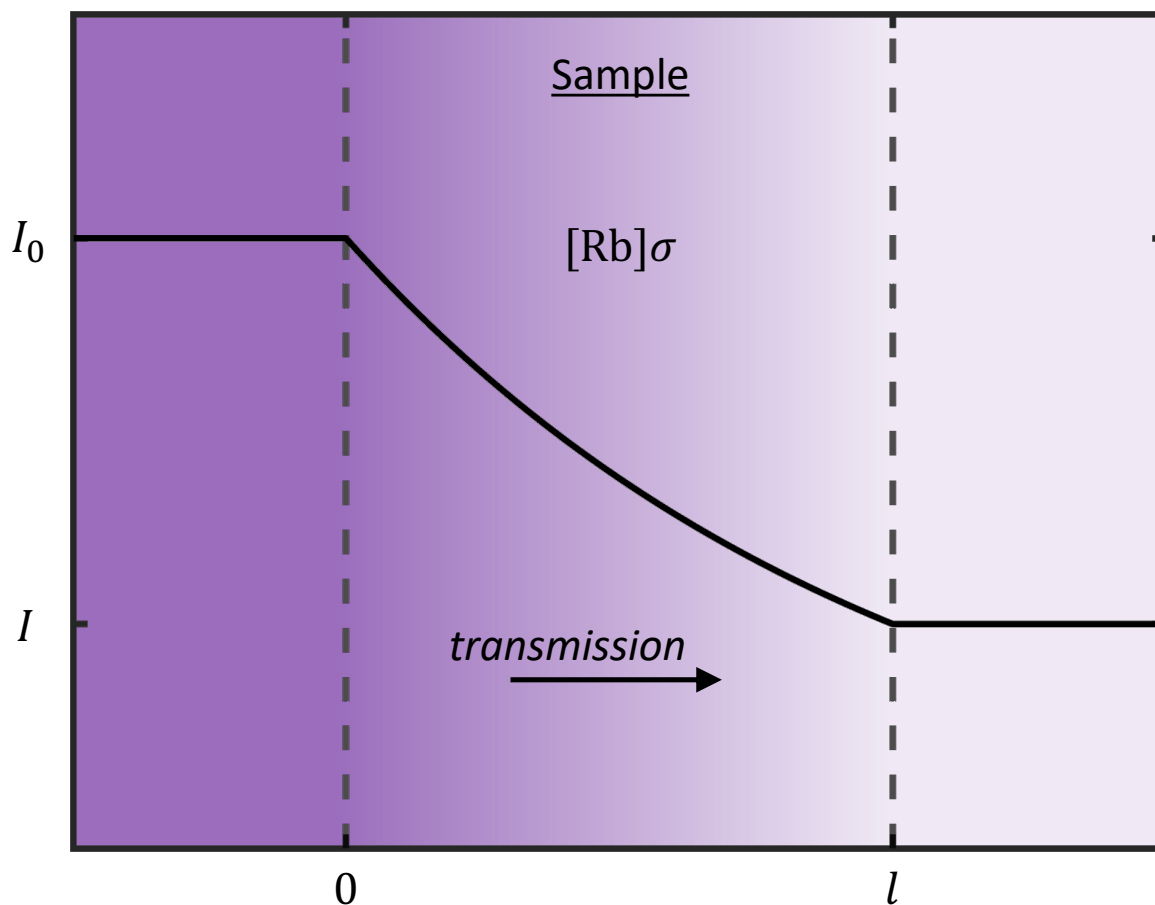


Figure 3.15: Transmission of incident light, I_0 , through the sample of Rb vapour, of path length l , during AAS, based on Eq. 3.117. The arrow indicates the direction of transmission and the violet shading represents the attenuation of I_0 through the sample.

The absorbance of light by the medium is given by

$$A = \int_{-\infty}^{\infty} \ln \left(\frac{I_0(\nu)}{I(\nu)} \right) d\nu. \quad (3.119)$$

The absorption line shape arises due to the following phenomena [105, 106];

- The natural line width, which is due to the finite lifetime of the excited state, also known as radiation damping. This produces a Lorentzian line shape, and is small so can be neglected.
- Doppler broadening due to the motion of the atoms relative to the observer, which produces a Gaussian line shape.
- Collisional broadening, which is due to collisions between atoms and produces a Lorentzian line shape. If the atoms are similar it is known as resonance broadening, which is often small given the small concentrations needed for accurate AAS. If the atoms are different then it is known as pressure broadening.

- Stark broadening, which is caused by external electron fields or charged particles. We do not expect these to be present in typical ^{129}Xe -Rb SEOP setups.

Doppler broadening and collisional broadening are therefore the most significant phenomena that contribute to the observed linewidth in AAS. In the past, line light sources combined with photodetectors were used for AAS measurements as spectrometers with high resolutions were not available. The absorption linewidth had to be larger than the probe source linewidth, otherwise unabsorbed light would be introduced, causing Beer-Lambert law deviation. Nowadays, a broader spectral light source combined with a high-resolution spectrometer can be used to perform AAS.

3.4.1 Deviation from the Beer-Lambert law

The accuracy of AAS varies with absorbance. At very low absorbance, the lower detection limit of the setup limits accuracy. As absorbance increases, accuracy improves, reaching a maximum at a specific absorbance. As absorbance increases further, deviation of Beer-Lambert law occurs, i.e. Eq. 3.117 no longer holds. This is due to the spectral properties of the lines measured and instrumental defects [105], with the latter typically being most significant.

Spectral properties that cause Beer-Lambert law deviation include changes in the absorption coefficient due to the significance of hyperfine structure at high optical depth [105]. In addition, factors that affect the number of atoms in the ground state will cause Beer-Lambert law deviation, such as ionisation (Rb ionization potential = 4.16eV) [105], or incomplete dissociation [105, 107] (dissociation energy of Rb-Rb bond = 0.47eV [108]). However, most of these issues should not occur at the relatively low temperature conditions used on a SEOP polariser.

Instrumental defects that contribute to Beer-Lambert law deviation result from unabsorbed light due to optical mis-alignment with the sample, differing path lengths, heterogeneous concentrations across path length and emission of the absorbing medium [105]. Unabsorbed light is different to constant background light, which can be accounted for by subtracting background spectra from both the initial intensity, I_0 and measured intensity, I spectra. Deviations from the Beer-Lambert law due to unabsorbed light can be modelled by considering the fraction of unabsorbed (stray) light, f_{stray} [107]. Eq. 3.117 then becomes

$$I(\nu) = I_0(\nu) [(1 - f_{\text{stray}}) e^{-[\text{Rb}]l\sigma(\nu)} + f_{\text{stray}}]. \quad (3.120)$$

In the limit of low [Rb], and if $f_{\text{stray}} \ll 1$, Eq. 3.120 is close to Eq. 3.117. However, at high [Rb], $e^{-[\text{Rb}]l\sigma(\nu)} \rightarrow 0$ and $A \rightarrow -\ln(f_{\text{stray}})$, as shown in Fig. 3.16. Beer-Lambert law deviation in Rb AAS measurements is investigated in Chapter 5 of this thesis.

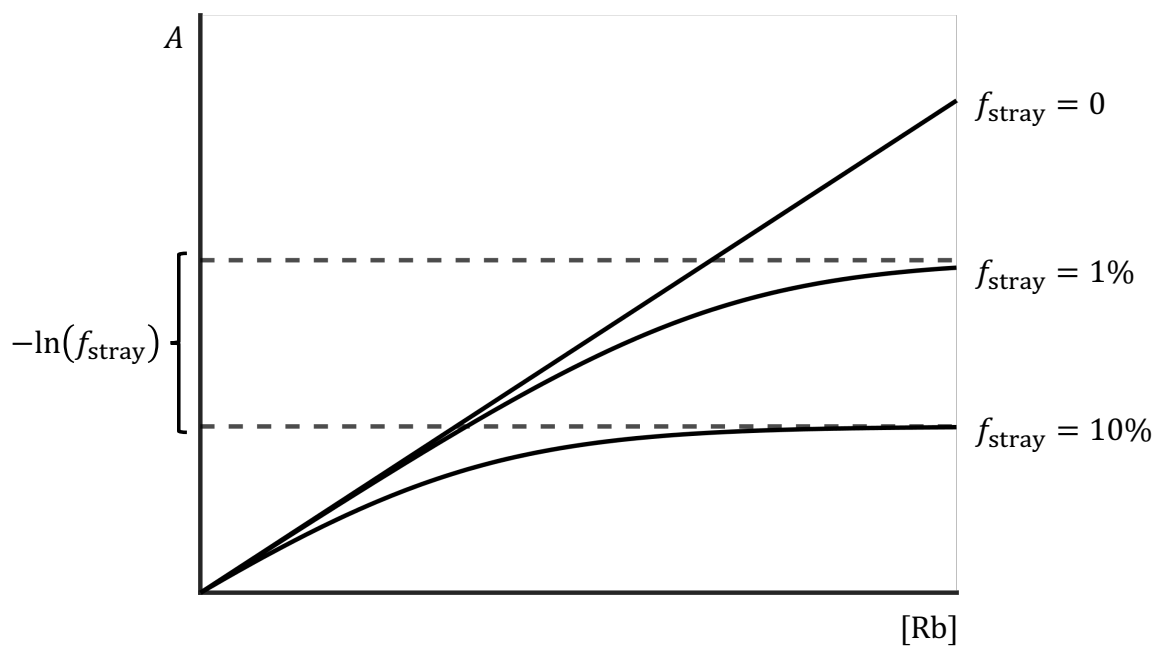


Figure 3.16: Beer-Lambert law deviation in absorbance, A , vs Rb vapour density, $[Rb]$, defined by the amount of unabsorbed (stray) light, f_{stray} . Asymptotes occur at $A = -\ln(f_{\text{stray}})$.

Chapter 4

1D and 3D modelling of the SEOP polariser

4.1 Introduction

Computational modelling enables prediction of the behaviour of systems without the need for physical setup and testing, which is costly and time consuming. Such models can be easily modified, facilitating systematic exploration of a diverse range of conditions, thereby contributing to the advancement of system optimisation endeavours. Owing to the extensive theoretical framework established by researchers in SEOP's early development, SEOP has been modelled for a wide range of different experimental setups and conditions. This includes modelling of Rb optical pumping and photon attenuation [64,69,109], batch-mode SEOP polarisers [71,73,110,111] and continuous-flow (CF) SEOP polarisers [30,52–55,112–115]. Modelling exhibits a spectrum of complexity and computational demands, spanning from 1D modelling, which encompasses the utilisation of closed-form equations to describe SEOP quantities, to intricate 3D fully-coupled modelling involving the interplay of gas flow and thermal dynamics coupled to SEOP phenomena.

While near-unity ^{129}Xe polarisation, P_{Xe} , has been achieved in a batch-mode SEOP system [32], continuous-flow systems suffer from under performance based on current theoretical frameworks [52–55,112]. A frequently proposed source of discrepancy is the Rb vapour density, $[\text{Rb}]$, which is a key parameter that governs spin dynamics in SEOP. Kelley and Branca [100] addressed discrepancies with reported ^{129}Xe -Rb spin-exchange rates, arriving at a closed-form expression similar to that of Walker and Larsen [77], and suggested that variations in calculated $[\text{Rb}]$ when measuring binary and vdW spin-exchange cross sections in previous studies contributed significantly to the widely reported discrepancies between theoretical and experimental polariser per-

formance. Indeed, Kelley and Branca [100] measured $[Rb]$ much lower than saturation in a small-cell continuous-flow SEOP setup which, unless accounted for, would lead to significant underestimations in measured ^{129}Xe -Rb spin-exchange cross sections. In large SEOP cell setups, indirect observation of lower than expected $[Rb]$ has been made by Plummer et al. [94]. Thus it is clear that accurate knowledge of $[Rb]$ in the optical cell is essential for correctly modelling and optimising CF-SEOP. To our knowledge, $[Rb]$ and its distribution within the SEOP cell has not yet been measured directly within large SEOP cell polarisers that implement high power ($\geq 100W$), spectral-narrowed ($\leq 0.3nm$) laser diodes, similar to the Sheffield polariser.

Typically for our setup, the required $[Rb]$ in the SEOP cell is created by placing a droplet of Rb within the heated and illuminated main body of the cell. Over time, evaporation of Rb from the Rb droplet leads to a saturated Rb vapour density, $[Rb]_{sat}$. Unlike batch mode production, where the gas is sealed within the SEOP cell during P_{Xe} build up, in continuous-flow setups, gas flow may disturb $[Rb]$ in the SEOP cell. If Rb vapour is displaced by the gas flow faster than it can be replaced by Rb evaporation from the Rb sources, then $[Rb]$ will be lower than $[Rb]_{sat}$. Lower-than-expected $[Rb]$ in SEOP cells have been observed where the surface area of the Rb coating is low [21]. The surface area of Rb in the main body of the cell could be increased, however this may increase susceptibility to undesirable Rb runaway effects [116]. During Rb runaway, continuous coupling of laser heating and Rb evaporation is established, resulting in a highly opaque region within the SEOP cell, which can lead to dark Rb (i.e. low Rb polarisation due to low photon absorption and optical pumping rates) regions of the cell. In continuous-flow SEOP with large SEOP cells, this is particularly challenging compared to configurations involving small SEOP cells. This challenge arises as thermal management demands are higher, attributable to the larger SEOP cell volume, coupled with higher degrees of laser heating, owing to the high laser powers used and the higher proportion of laser absorption. To improve $[Rb]$ distribution, and mitigate Rb runaway effects, Rb presaturation regions have been implemented on other polariser systems [53,94,115,117]. This involves an upstream section of the SEOP cell where the Rb sources are placed and heated outwith the pumping laser beam. The Rb presaturation region is not illuminated by the pumping laser, thus decoupling laser heating from Rb evaporation. However, lower-than-saturation Rb densities have still been observed in these setups [94, 115]. Therefore, we hypothesise that the Rb source distribution, gas-flow and thermal dynamics lead to non-saturation and/or heterogeneous $[Rb]$ and lower P_{Xe} build up in the optical cell of the Sheffield polariser.

In order to model these effects in SEOP, the finite element method (FEM) can be used. This is a widely used mathematical modelling technique which can be used to simulate a diverse set of physical systems. Its application extends across various engineering

applications including biomedical engineering. FEM showing the effect of Rb source distribution on resulting [Rb] in SEOP has been previously performed on small cell CF-SEOP polarisers [112–115]. To our knowledge, SEOP modelling involving different Rb sources that considers gas-flow dynamics and heat transfer has not been performed within a configuration featuring a large optical cell ($V_{\text{cell}} > 1\text{L}$), spectral-narrowed ($\leq 0.3\text{nm}$) laser diode and high production rate ($Q = 2\text{SLM}$) setup similar to the polariser developed at the University of Sheffield [52].

In this chapter, the existing polariser setup [52] was simulated using 1D and 3D methods in order to gain insight into the discrepancy between theoretical and measured P_{Xe} . Updated spin-exchange parameters, measured with direct [Rb] measurements, were used. Simulations of various Rb source distributions were performed. Introducing a presaturator was also simulated. The flow rate dependence of the length of presaturator required for near-saturation [Rb] of the gas flowing into the cell main body was determined. P_{Xe} temperature dependence has been investigated previously on the Sheffield SEOP polariser [52], however, due to updates to the SEOP theoretical framework, we repeat this for direct comparison with 3D simulations, as well as explore the effect of different laser powers, P_l and ^{129}Xe longitudinal relaxation rates in the absence of Rb, Γ' .

4.2 Methods

4.2.1 1D simulations

1D simulations were performed in MATLAB (MathWorks). Eq. 3.71 and Eq. 3.85 show that P_{Rb} and Γ_{SD} form a circular variable dependency. This is difficult to simulate and so we assume a fixed high P_{Rb} regime ($P_{\text{Rb}} = 0.8$) for Γ_{SD} only, as the most significant spin-exchange will occur in high P_{Rb} areas. P_{Rb} was then calculated using Eq. 3.71.

Optical pumping rate attenuation was calculated using an explicit solution of Eq. 3.83, which is derived by substitution of Eq. 3.71 into Eq. 3.83, followed by separation of variables to give the implicit solution,

$$R + \Gamma_{\text{SD}} \ln(R) + \Gamma_{\text{SD}} (\alpha[\text{Rb}]z - k) = 0, \quad (4.1)$$

where $k = \ln(R_0) + R_0/\Gamma_{\text{SD}}$ [69]. The explicit solution of this is

$$R(z) = \Gamma_{\text{SD}} W(e^{(k - \alpha[\text{Rb}]z)}/\Gamma_{\text{SD}}), \quad (4.2)$$

where W is the Lambert W function ($f(x) = xe^x$, $W(f(x)) = x$) [52].

P_{Xe} build up due to spin-exchange, given by Eq. 3.104, neglecting Xe diffusion, D_{Xe} , was evaluated using Euler's method. Euler's method is an approach for solving differential equations where an initial value, y_1 , is given, and the first order differential equation is evaluated. The point which is a step, h , beyond this initial point is calculated as the sum of the initial point and the evaluated first order differential multiplied by the step size, h , hence

$$y_{n+1} = y_n + hy'(h, t_n). \quad (4.3)$$

This is repeated for all points up to the limit of the independent variable range. In the limit of $h \rightarrow 0$, the numerical solution approaches the exact solution.

The z-gas velocity, v_z , where z is the direction of the laser propagation, for plug flow is

$$v_z = -\frac{Q_V}{A_{\text{cell}}} = -\frac{Q \text{ [SLM]}}{A_{\text{cell}}\eta} \quad (4.4)$$

where the $(-)$ sign is due to the direction of the gas flow opposing the laser propagation direction. Q_V is the volumetric gas flow rate, $\eta = \frac{T_0 p}{T p_0}$ is the gas number density in amagat, A_{cell} is the cell cross-sectional area and Q is the mass flow rate in standard litres per minute (SLM). Initial $P_{Xe}(z = L_{\text{cell}}) = 0$ and a total number of points, $n = 2000$, across the cell length, L_{cell} , corresponding to a step size of $h = L_{\text{cell}}/(n - 1) = 394\mu\text{m}$ was used.

1D simulations were ran at nominal running conditions ($p = 1.25$ bar, $Q = 2$ SLM¹) for a range of temperatures in order to determine optimal conditions for maximum P_{Xe} output, and compared for different P_l and Γ' . The laser FWHM, $\Delta\nu_l$, was set to 0.3nm throughout. The effect of [Rb] on output P_{Xe} was determined and compared for different P_l and Γ' . At near-optimal temperature, [Rb] and Γ' were varied for different P_l . This was to simulate both the effects of laser (lowering laser power) and cell (increasing Γ') degradation over time.

4.2.2 3D simulations

3D simulations involve five physics models: gas-flow dynamics, heat transfer, Rb transport, optical pumping rate attenuation and P_{Xe} build up. This was performed using FEM in COMSOL Multiphysics 5.6. The microfluidics module was required for simulating gravity and enforcing mass flow boundary conditions, and livelink to MATLAB, in order to perform the complimentary error function, erfc, in Eq. 3.82. Simulations are produced in successive iterations until the solution error estimate is sufficiently small.

¹After completion of this work, it was found that the mass flow regulator was calibrated for normal litre per minute, NLPm ($p = 1$ atm, $T = 20^\circ\text{C}$) instead of SLM ($p = 1$ atm, $T = 0^\circ\text{C}$). Flow rates in subsequent chapters of this thesis are in units of NLPm.

Simulation domain, optical cell geometries and material properties

FEM is able to numerically solve coupled partial differential equations (PDE) by dividing the object or space in which the physical system takes place into a lattice consisting of vertices, faces and edges, defined as the mesh. In this work, the simulation space or object is the optical cell. This includes the main cell body, inlet and outlet stems and the enclosed gas that flows from inlet to outlet. The optical cell geometries used are shown in Fig. 4.1. CAD drawings of a cylindrical Pyrex optical cell were produced using COMSOL Multiphysics. The optical cell has an internal diameter of $w_{\text{cell}} = 7.5\text{cm}$ and external length of $L_{\text{cell}}^{\text{ex}} = 80\text{cm}$. The cell walls are $t_{\text{wall}} = 5\text{mm}$ thick. The optical flat windows have a thickness of $t_{\text{OF}} = 6.5\text{mm}$. The cylindrical stems have an internal diameter of $w_{\text{stem}} = 6\text{mm}$ and length of $L_{\text{stem}} = 10\text{cm}$. The stem walls are $t_{\text{stem}} = 1.5\text{mm}$ thick. Optical pumping only occurs in the main cell body, which is illuminated by the optical pumping laser.

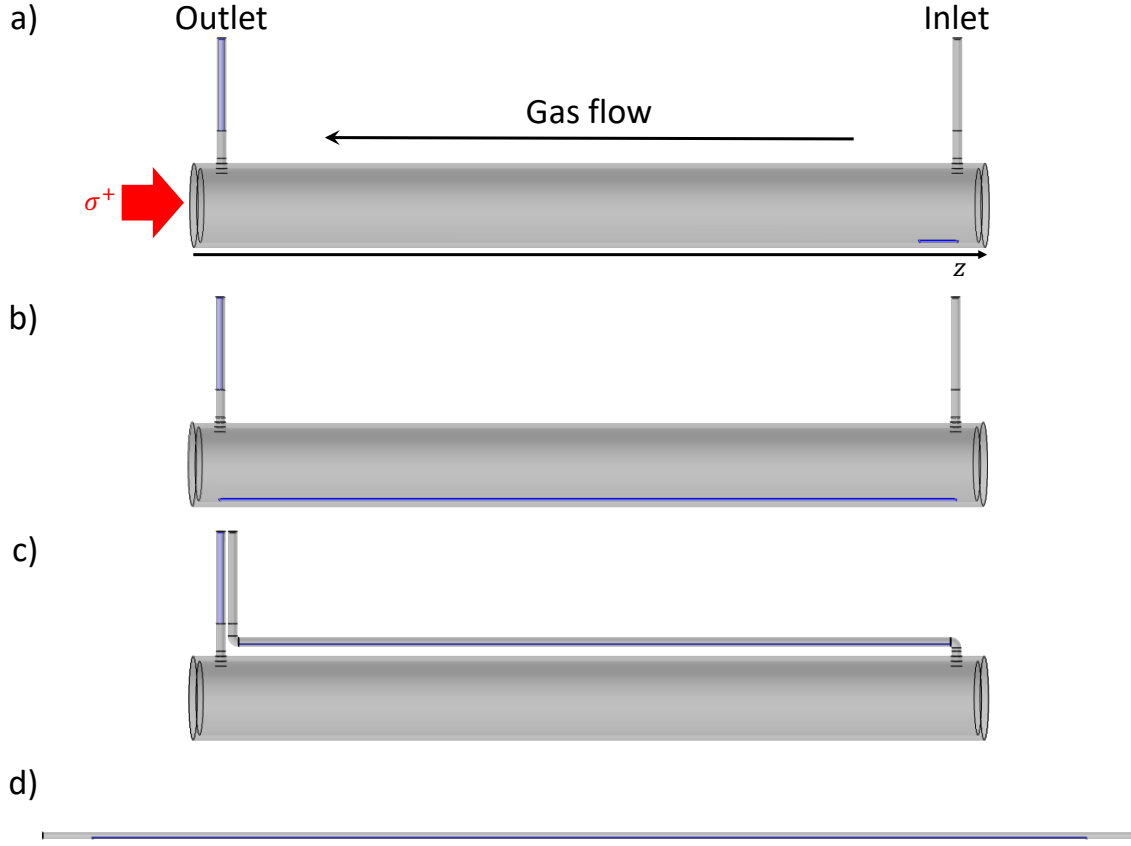


Figure 4.1: CAD models of four optical cell geometries, where the Rb source is highlighted in violet. (a) The small (10cm^2) Rb source placed within the cell main body, (b) the large (194cm^2) Rb source placed within the cell main body, (c) Rb placed only within the 72cm presaturator and (d) Rb within a 1m presaturator only (not to scale). The Rb source boundary condition is applied to all internal cell outlet walls outside of the oven, where Rb deposition is typically observed. The optical pumping laser propagates along z , from the front to the back of the main cell body, and the gas flows counter to this from the inlet to the outlet.

The cell walls are made of borosilicate glass (also known as Pyrex). Its properties are only used in the thermal transfer model and are the density = 2230Kg m^{-3} [118–120], thermal conductivity = $1.143\text{W m}^{-1}\text{ K}^{-1}$ [119, 120] and heat capacity, $C_p = 750\text{J Kg}^{-1}\text{ K}^{-1}$ [120, 121].

The Xe gas mixture properties are used within the gas-flow dynamics and thermal transfer models. The gas mixture consists of 3% enriched Xe (86% ^{129}Xe), 10% N_2 and 87% He. The gas mixture density, ρ_{mix} , is given by

$$\rho_{mix} = \sum_{\alpha=1} x_{\alpha}\rho_{\alpha} = \frac{p}{RT} \sum_{\alpha=1} x_{\alpha}M_{\alpha} = 1.228 \times 10^{-3}[\text{Kg m}^{-3}\text{K Pa}^{-1}] \times \frac{p[\text{Pa}]}{T[\text{K}]}, \quad (4.5)$$

where ρ_α is the density, x_α is the mole fraction and M_α is the molecular weight of gas species α , p is the gas pressure, T is the gas temperature and R is the molar gas constant.

The gas mixture viscosity, μ_{mix} was calculated as

$$\mu_{mix} = \sum_{\alpha=1} \frac{x_\alpha \mu_\alpha}{\sum_{\beta} x_\beta \Phi_{\alpha\beta}}, \quad (4.6)$$

where α and β correspond to each gas species within the mixture, μ_α is the viscosity, x_α is the mole fraction of species α and $\Phi_{\alpha\beta}$ is a dimensionless quantity defined as

$$\Phi_{\alpha\beta} = \frac{1}{\sqrt{8}} \left(1 + \frac{M_\alpha}{M_\beta}\right)^{-1/2} \left[1 + \left(\frac{\mu_\alpha}{\mu_\beta}\right)^{1/2} \left(\frac{M_\beta}{M_\alpha}\right)^{1/4}\right]^2, \quad (4.7)$$

where M_α is the molecular weight of species α [122]. μ_α is calculated using Sutherland's formula as

$$\mu = \mu_0 \left(\frac{T_0 + C}{T + C}\right) \left(\frac{T}{T_0}\right)^{3/2}, \quad (4.8)$$

where T_0 is the reference temperature, μ_0 is the viscosity at T_0 and C is Sutherland's constant, specific for each gas species [123]. $C_{\text{He}} = 72.9\text{K}$, $C_{\text{N}_2} = 104.7\text{K}$ and $C_{\text{Xe}} = 252\text{K}$. $\mu_{0,\text{He}} = 0.0196\text{cP}$, $\mu_{0,\text{N}_2} = 0.0189\text{cP}$ and $\mu_{0,\text{Xe}} = 0.0228\text{cP}$. $T_0 = 293.15\text{K}$ for all gas species [123].

The thermal conductivity of the gas mixture, k_{mix} , is calculated as

$$k_{mix} = \sum_{\alpha=1} \frac{x_\alpha k_\alpha}{\sum_{\beta} x_\beta \Phi_{\alpha\beta}}, \quad (4.9)$$

where k_α is the thermal conductivity of species α [122]. For a monatomic gas (He, Xe), k is given by

$$k = \frac{15}{4} \frac{R}{M} \mu. \quad (4.10)$$

For a diatomic gas (N_2), k is

$$k = \left(\hat{C}_p + \frac{5}{4} \frac{R}{M}\right) \mu, \quad (4.11)$$

where \hat{C}_p is the molar heat capacity at constant pressure, which is calculated as [124]

$$C_p[\text{J mol}^{-1}\text{K}^{-1}] = A + BT_* + CT_*^2 + DT_*^3 + ET_*^{-2}, \quad (4.12)$$

where A , B , C , D and E are coefficients specific to each gas species stated in Table 4.1. $T_* = T[\text{K}]/1000[\text{K}]$ and the heat capacity at constant pressure of the gas mixture is given by $C_{p,\text{mix}} = \sum_{\alpha=1} x_\alpha C_{p,\alpha}$. Likewise, the ratio of specific heats, $\gamma_{mix} = \sum_{\alpha=1} x_\alpha \gamma_\alpha$, where $\gamma = 5/3$ for a monatomic gas, and $\gamma = 7/5$ for a diatomic gas.

Table 4.1: Table of gas molar heat capacity coefficients given by ref. [124].

Coefficient	Coefficient value (J mol ⁻¹ K ⁻¹)		
	Xe	N ₂	He
<i>A</i>	20.786	28.98641	20.78603
<i>B</i>	7.449320×10^{-7}	1.853978	4.850638×10^{-10}
<i>C</i>	-2.049401×10^{-7}	-9.647459	$-1.582916 \times 10^{-10}$
<i>D</i>	1.066661×10^{-8}	16.63537	1.525102×10^{-11}
<i>E</i>	2.500261×10^{-8}	0.000117	3.196347×10^{-11}

Xe diffusion

Xe diffusion, D_{Xe} , is included in the gas dynamics model. The mutual diffusion coefficient of Xe and gas species β is calculated as [125]

$$D_{\text{Xe}\beta} = \frac{3}{8} \sqrt{\frac{(k_B T)^3}{\pi}} \sqrt{\frac{M_{\text{Xe}} + M_\beta}{2M_{\text{Xe}}M_\beta}} \frac{f_D}{p\sigma_{\text{Xe}\beta}^2 \Omega_{\text{Xe}\beta}}, \quad (4.13)$$

where M_{Xe} and M_β are the molecular masses of Xe and species β , f_D is a correction factor that accounts for the gas mixture, which can be approximated as $f_D \sim 1$ for most gas mixtures [125], $\sigma_{\text{Xe}\beta} = 1/2(\sigma_{\text{Xe}} + \sigma_\beta)$ is the characteristic length of the Lennard-Jones potential. $\Omega_{\text{Xe}\beta}$ is the collision integral, which is given by [125–127]

$$\Omega_{\text{Xe}\beta} = \frac{1.06036}{(T^*)^{0.15610}} + \frac{0.19300}{\exp(0.47635(T^*))} + \frac{1.03587}{\exp(1.52996(T^*))} + \frac{1.76474}{\exp(3.89411(T^*))}, \quad (4.14)$$

where $T^* = kT/\epsilon_{\text{Xe}\beta}$ and $\epsilon_{\text{Xe}\beta} = \sqrt{\epsilon_{\text{Xe}}\epsilon_\beta}$. ϵ_{Xe} and ϵ_β are the energy parameters of Xe and species β . Diffusion parameter values are given in Table 4.2.

The observable Xe diffusion coefficient is

$$D_{\text{Xe}} = \left(\sum_i \frac{x_i}{D_{\text{Xe}i}} \right)^{-1}, \quad (4.15)$$

where i ($= \text{Xe}, \beta$) is each gas species in the mixture.

Table 4.2: Xe diffusion coefficient parameters, given by ref. [125].

Gas species	σ (Å)	ϵ/k (K)	M (g/mol)
Xe	4.047	231.0	129.44*
N ₂	3.798	71.4	28.013
He	2.551	10.22	4.003

*Enriched Xe (86% ¹²⁹Xe).

Gas-flow dynamics

The gas-flow was modelled using the laminar flow model within COMSOL Multiphysics, which is based on the Navier-Stokes equations. The Reynolds number, Re , can be calculated as

$$Re = \frac{\rho L}{\mu} u = \frac{\rho L}{\mu} \frac{Q_V}{A_{\text{stem}}}, \quad (4.16)$$

where $u = Q_V/A$ is the mean gas velocity. For $Q = 2$ SLM and $T = 120^\circ\text{C}$, $\mu = 2.74 \times 10^{-5} \text{Pa}\cdot\text{s}$, $\rho = 0.389 \text{Kg m}^{-3}$. $Q_V = 38.9 \text{cm}^3 \text{s}^{-1}$ is the volumetric gas flow rate and A is the cross-sectional area of region and L is the characteristic length, equal to the pipe diameter. Within the $T = 120^\circ\text{C}$ region of the cell inlet and outlet ($A_{\text{stem}} = 0.283 \text{cm}^2$, $L = 6 \text{mm}$), $Re = 117$. Within the main cell body ($A_{\text{cell}} = 44.2 \text{cm}^2$, $L = 7.5 \text{cm}$), $Re = 9.4$. Both Re values are below the transition from laminar flow to turbulent flow regimes ($2300 < Re < 2900$). Therefore, the gas flow was modelled as laminar flow of a compressible gas. It is worth noting that initial simulations used a gas velocity condition to constrain the flow rate, as mass flow was not available on the base COMSOL Multiphysics software. The microfluidics module was added to access mass flow, as well as gravity. The gas velocity condition was found to lead to issues with mass conservation within the simulations, which was mesh dependent as finer meshes resulted in greater mass conservation.

The inlet is defined as a surface within the inlet stem and a mass-flow boundary condition is applied to enforce a specified mass flow rate, $Q = 2$ SLM. All internal surfaces have a “no slip” boundary condition applied, assuming gas velocity equals zero at the internal cell walls. The outlet was defined similarly as a surface within the outlet stem with a pressure boundary condition, $p_0 = 1.25 \text{bar}$. Static ($\mathbf{u} = 0$) initial conditions and initial pressure, $p = 1.25 \text{bar}$ were applied. The gas is modelled as a compressible gas, allowing for changes in gas density with temperature variation in the cell. This differs from a 1D simulation, where plug flow is used and thermal considerations are not considered.

Rb vapour dynamics

Rb vapour transport consists of the Rb source distribution, which is the surfaces where the Rb vaporisation flux condition is applied, and Rb diffusion within the gas mixture.

The Rb vapour distribution was modelled using a convection-diffusion model. The Rb source-sink boundary condition is the inward flux of Rb vapour, $N_{0,c}$, which is given by

$$N_{0,c} = \alpha_{\text{Rb}} ([\text{Rb}]_{\text{sat}} - [\text{Rb}]) \sqrt{\frac{k_B T}{2\pi M_{\text{Rb}}}}, \quad (4.17)$$

where α_{Rb} is the evaporation coefficient of Rb, $[\text{Rb}]$ is the Rb vapour density at the Rb source surface, $[\text{Rb}]_{\text{sat}}$ is the saturation Rb vapour density, given in Table 3.1 and M_{Rb} is the molecular mass of Rb [112]. α_{Rb} has not been measured, but is expected to be close to 1 [112]. α_{Rb} is set to 1 in this work, consistent with Rb vapour transport in SEOP simulations in the literature [112, 113, 115]. The Rb source distribution assumes a thin layer applied to the cell wall, i.e. the Rb layer is assumed to have zero thickness.

The Rb diffusion coefficient in the gas mixture, $D_{\text{Rb-mix}}$, was calculated as

$$D_{\text{Rb-mix}} = \left(\sum_{\alpha} \frac{x_{\alpha}}{D_{\text{Rb-}\alpha}} \right)^{-1} \cdot \left(\frac{T}{305\text{K}} \right)^{\frac{3}{2}} \cdot \frac{1\text{atm}}{p}, \quad (4.18)$$

where x_{α} are the molar fractions of each gas within the mixture, $D_{\text{Rb-}\alpha}$ is the diffusion coefficient of Rb within each gas, evaluated at $T = 305\text{K}$ and $p = 1\text{atm}$. $D_{\text{Rb-He}} = 0.42\text{cm}^2\text{s}^{-1}$ [19], $D_{\text{Rb-N}_2} = 0.16\text{cm}^2\text{s}^{-1}$ [19], $D_{\text{Rb-Xe}} = 0.067\text{cm}^2\text{s}^{-1}$ [128]. For our gas mixture, Eq 4.18 therefore simplifies to

$$D_{\text{Rb-mix}} = 0.32\text{cm}^2\text{s}^{-1} \cdot \left(\frac{T}{305\text{K}} \right)^{\frac{3}{2}} \cdot \frac{1\text{atm}}{p}. \quad (4.19)$$

N.B. unlike previous work involving 1% Xe gas mixtures that considered Rb diffusion in helium only [112, 115], considering all gases in the mixture here (3% enriched-Xe ($86\%^{129}\text{Xe}$), 10% N_2 , 87%He) contributes to a $(1 - D_{\text{Rb-mix}}/D_{\text{Rb-He}}) = 24\%$ lower $D_{\text{Rb-mix}}$.

Simulations were ran for different size Rb pool source distributions. The size of the Rb pool was increased by extending the Rb pool length with respect to an edge aligned with the centre of the inlet, as shown in Fig. 4.2. The smallest and largest Rb pools tested are shown in Fig. 4.1a and Fig. 4.1b respectively.

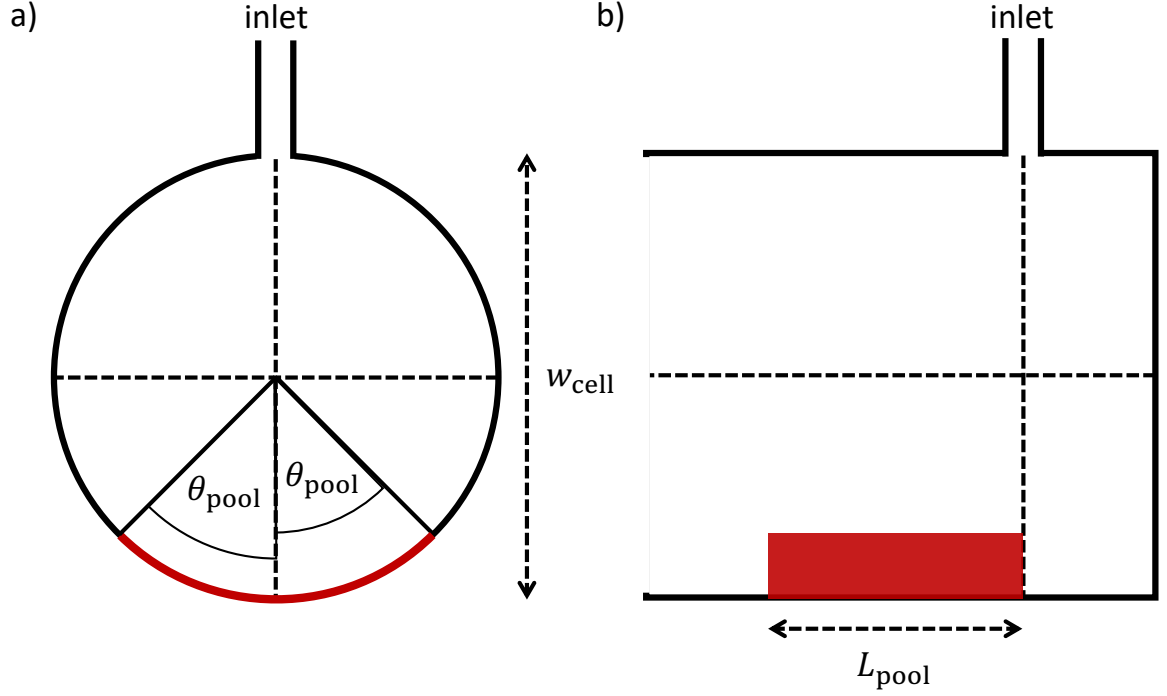


Figure 4.2: Rb flux boundary condition geometry in the main cell body viewed from (a) the rear optical cell window and (b) the side. The Rb pool edge is aligned with the centre of the cell inlet and extends a length L_{pool} towards the front of the cell. θ_{pool} is the angle of the boundary condition.

Thermal transfer

The thermal transfer model is based on the differential form of Fourier's law and involves two sources of heat. Firstly, the oven is simulated by applying a constant temperature condition to the external cell walls. The cell main body and stems up to 3cm from the outer wall of the cell are held at the oven temperature $T_{\text{oven}} = 120^\circ\text{C}$. The remaining portions of the stems are held at room temperature $T = 20^\circ\text{C}$.

The other source of heat is due to laser heating. The dissipation of the 10s of Watts of laser light absorbed during optical pumping through spin-relaxation contributes to the total thermal energy within the optical cell. This can be modelled as an addition source term, Q_{LH} within the thermal transfer model [71],

$$Q_{LH} = 2R\rho_{-1/2}h\nu_L[\text{Rb}] = R\frac{\Gamma_{SD}}{R + \Gamma_{SD}}h\nu_L[\text{Rb}], \quad (4.20)$$

where $2R$ is the photon absorption rate per electron in the $5S_{1/2}$, $m_j = -1/2$ state, $\rho_{-1/2}$ is the relative $5S_{1/2}$, $m_j = -1/2$ state population size given by Eq. 3.77 and $h\nu_L$ is the non-radiative energy dissipated with complete N_2 quenching per Rb electron relaxation from the $5P_{1/2}$ to $5S_{1/2}$ state, where h is Planck constant and ν_L is the laser

frequency [71]. Equation 4.20 shows that laser heating will occur in areas of high [Rb]. In addition, Equation 3.83 shows that high [Rb] will lead to greater gradients in the z-direction of R , and as a result, greater laser heating gradients across the cell.

Optical pumping attenuation

The optical pumping attenuation, $R(z)$, is modelled by solving Eq. 3.83, in the form

$$-\frac{\partial R}{\partial z} - \alpha[\text{Rb}] \left(1 - \frac{R}{R + \Gamma_{SD}} \right) R = 0. \quad (4.21)$$

The boundary flux condition for R imposed at $z = 0$ is given by Eq. 3.81. $R(z)$ is used for both laser heating, described by Eq. 4.20, and P_{Xe} build up, given by Eq. 3.104.

Xe polarisation build up

After the other coupled models have been solved, spatial Xe polarisation maps were produced by using Eq. 3.104. At the initial inlet surface, $P_{\text{Xe}} = 0$, is imposed. Physically, this can be interpreted as complete Xe depolarisation at this boundary if any Xe backflow occurs.

Simulation approach

Owing to the intricate coupling between numerous physics models, a fully-coupled model was difficult to solve. Consequently, simulations were executed iteratively using a subset of coupled physics models, akin to the approach employed by Kelley et al. [115]. Each step uses the solution from the previous step, and the simulation workflow is as follows:

1. Gas flow and heat transfer models coupled.
2. Rb vapour transport only.
3. Optical pumping rate only.
4. Gas flow, heat transfer, laser heating and Rb vapour transport models coupled.
5. Optical pumping rate only.
6. Steps 4 to 5 repeated until $< 0.1\%$ change in parameter solutions.
7. Final step: Xe polarisation computation.

Once the simulation was complete, laser absorption values were calculated using Eq. 3.79.

Mesh analysis is performed first in order to determine the mesh size dependence of solutions. Ideally, very fine meshes would be used to simulate physical phenomena correctly at short length scales improving solution accuracy. However, run time increases

with increasing number of elements within the mesh. Therefore, the optimal mesh size balances run time with solution accuracy. Several of the meshes utilised in the mesh analysis are shown in Fig. 4.3.

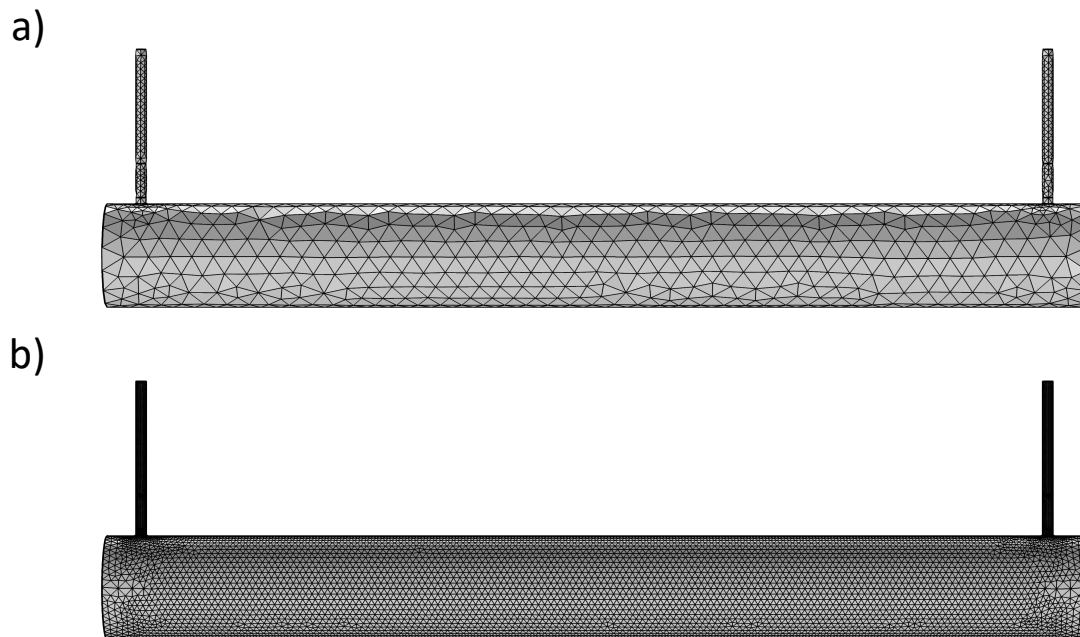


Figure 4.3: Meshes of the 10cm^2 Rb pool optical cell geometry shown in Fig. 4.1a. (a) ‘Coarser’ mesh and (b) ‘Finer’ mesh. Only the external surface mesh shown, however the mesh extends in 3D space within the object.

A summary of the 1D and 3D simulation methods and boundary conditions are given in Tables 4.3 and 4.4 respectively.

Table 4.3: 1D vs 3D simulation methods.

Model	1D		3D	
	Method	Equation	Method	Equation
Optical Pumping attenuation	Implicit solution	4.2	FEM	3.81, 3.83
Spin-exchange, P_{Xe} build up	Euler's method	3.104	FEM	3.104
Gas-flow	Plug flow	4.4	Laminar flow and Xe diffusion	4.13
Rb vapour transport	$[Rb] = [Rb]_{sat}$, homogeneous everywhere	see Table 3.1	Vaporisation flux condition, Rb diffusion coupled to gas-flow	4.17, 4.19
Thermal transfer	$T = T_{oven}$, homogeneous everywhere	-	$T = T_{oven}$ at the external cell walls, $T = 20^\circ\text{C}$ on the stems outside the oven, laser heating	4.20
Geometry	Main cell body only	-	Main cell body, inlet and outlet stems	-

Table 4.4: 3D simulation boundary conditions.

Model	Boundary condition	Location
Initial optical pumping rate	Eq. 3.81	Front cell window
Spin-exchange, P_{Xe} build up	$P_{Xe} = 0$	Cell inlet
Gas-flow: mass-flow constraint	$Q = 2$ SLM	Cell inlet
Gas-flow: pressure constraint	$p = 1.25$ bar	Cell outlet
Rb vaporisation flux condition	Eq. 4.17	Rb source surfaces on internal cell walls or presaturator
External cell wall temperature constraint within the oven	$T = T_{oven}$	External cell walls and 3cm section of external inlet and outlet walls
External cell wall temperature constraint outside of the oven	$T = 20^\circ\text{C}$	Remaining sections of external inlet and outlet walls

Limitations of modelling and phenomena not modelled

The following phenomena were not modelled: Rb cluster formation [55] as this has not been directly measured yet in optical cells, Rb latent heat of vaporisation and condensation [115] as the change in temperature at the Rb source is expected to be small, the effects of optical cell orientation [112] as our cells are positioned horizontally and radiation trapping [71] due to the high N_2 partial pressure used in this work.

Rb and ^{129}Xe surface relaxation at the cell walls were not modelled as surface boundary conditions. ^{129}Xe surface relaxation was considered within the bulk term Γ' in Eq. 3.104, whilst Rb depolarisation was not considered, given the short distance to the cell wall over which complete Rb depolarisation at the cell wall is significant, which is of the order $\sqrt{D_{\text{Rb}}/R} \leq 10^{-3}\text{cm}$ for our setup and running conditions ($D_{\text{Rb}} = 0.38\text{cm}^2\text{s}^{-1}$ and $R \geq 10^5\text{s}^{-1}$) [73]. Rb depolarisation at the cell walls would lower P_{Rb} near the cell walls and increase optical pumping rate attenuation in these areas.

Photon flux attenuation, which accounts for changes in the absorption profile and line shape with photon attenuation along the cell length, was not modelled. Photon flux attenuation cannot be performed using FEM due to the integral present in Eq. 3.72, when the spatial distribution of R is evaluated [113].

Setup limitations that were not included in the model are skewed light effects [74], imperfect photon polarisation [68], which lead to lower photon efficiency as described in Section 3.3.1, and imperfect oven performance leading to external cell wall temperature heterogeneity. The effects of circular dichroism [75, 76] were not considered.

Lowering of Rb vaporisation due to reaction with impurities [129] was not modelled. Adsorption of Rb to the cell walls, which has been suggested as a mechanism for lower alkali metal vapour densities [130], was not modelled. Over time, Rb forms a thin layer and may act as an increase in the Rb source distribution or change the Rb deposition characteristics at the cell wall. Kelley et al. [115] measured significantly lower [Rb] in brand new cells than cells which had formed a Rb layer on the cell walls (“broken-in cells”).

4.2.3 Rb presaturator modelling

After producing the simulations for different Rb pool sizes, it was evident that a Rb presaturator could constitute a valuable design modification aimed at improving [Rb] homogeneity.

The length of presaturator required for near-saturation [Rb] of the in-flowing gas has previously been measured to be 20 to 30cm [112], however this was performed at $p = 10\text{bar}$, which is a much higher pressure than is typically used in CF ^{129}Xe -Rb SEOP (up to 4bar) where the volumetric gas flow rates are faster. Also, the length of presaturator required as a function of gas flow rate had not been evaluated.

We therefore simulated [Rb] build-up along a 1m presaturator only (Fig. 4.1d) for different flow rates, Q , under previously optimal conditions determined in ref. [52] to be $Q = 2\text{SLM}$, $p = 1.25\text{bar}$, $T = 125^\circ\text{C}$. 25% Rb presaturator wall coverage (i.e. $\theta_{\text{pool}} = 45^\circ$) was used. These simulations involved the gas transfer and Rb vapour transport models only, which were coupled throughout, rather than the iterative step approach used for the full SEOP simulations. An optimal presaturator length, constrained to realistic design lengths, was then incorporated into the existing optical cell design and simulated using the full SEOP modelling.

4.3 Results and Discussion

4.3.1 1D simulations

The results of simulating the temperature dependence of P_{Xe} for different P_l and Γ' are shown in Fig 4.4.

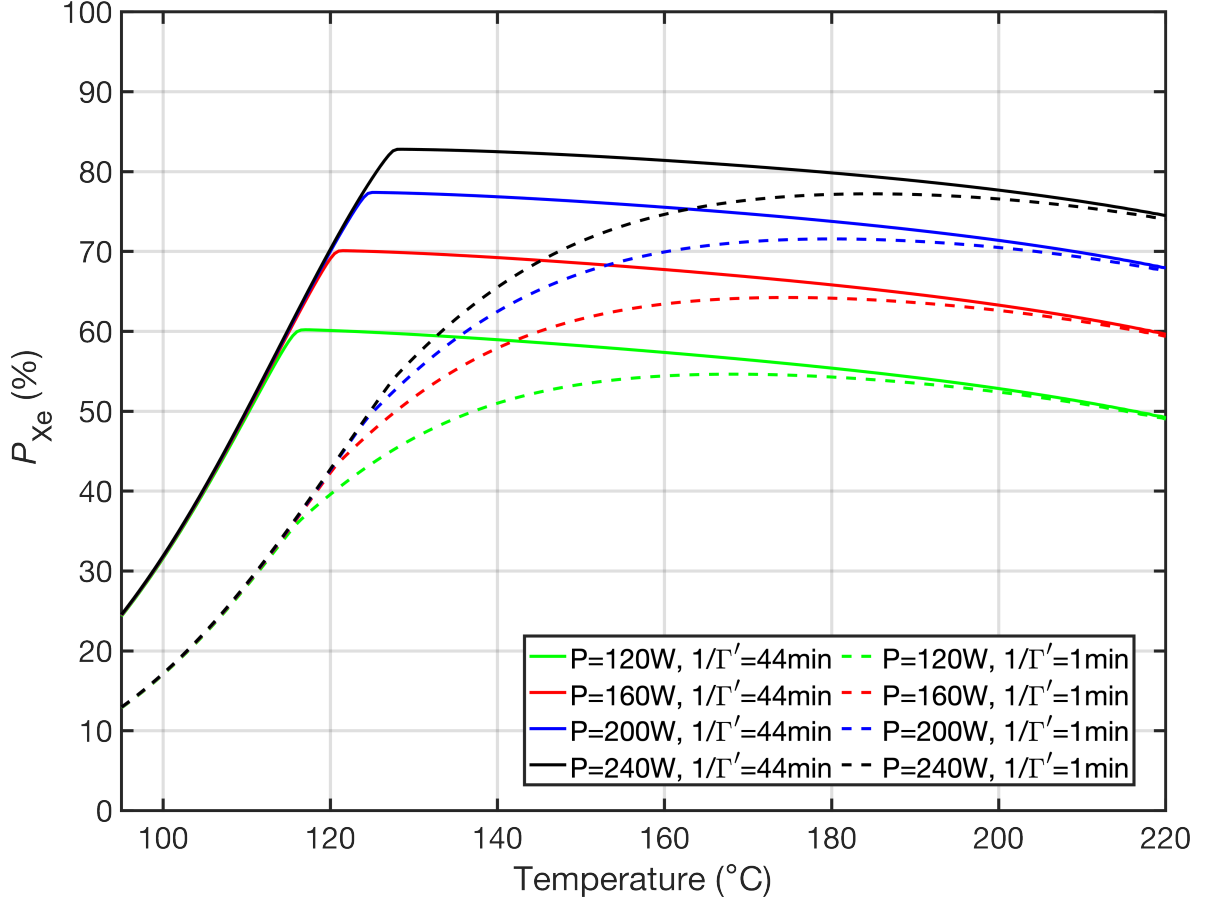


Figure 4.4: Xe polarisation, P_{Xe} vs temperature for different values of laser absorption, P_l , and Xe relaxation rate in the absence of Rb, Γ' . $p = 1.25\text{bar}$, $Q = 2\text{SLM}$ and $[\text{Rb}] = [\text{Rb}]_{\text{sat}}$ were used.

Fig. 4.4 shows that the optimal temperature at which maximum P_{Xe} occurs increases with laser power. Optimal temperature also increases with decreasing Γ' . The change in optimal temperature is greater with change in Γ' than laser power, suggesting monitoring Γ' is essential for determining if operating temperature needs to be adjusted to achieve maximum P_{Xe} . For the expected laser power of our setup $P_l = 160\text{W}$ (180W output from laser with $\sim 90\%$ transmission through the front cell window), and $\Gamma' = 44\text{min}$, the optimal temperature is $121.5 \pm 0.5^\circ\text{C}$. In initial 3D/FEM simulations at $T = 125^\circ\text{C}$, the previously measured optimal temperature of our setup defined in ref. [52], non-convergent simulations were observed for Rb distributions which re-

sulted in approximately zero optical pumping rate at the back of the cell. We therefore used 120°C, which is slightly lower than optimal temperature to avoid near-zero optical pumping rate, for subsequent simulations, with the exception of the presaturator only simulations which were performed at $T = 125^\circ\text{C}$. The optimal temperature and maximum P_{Xe} determined here are lower than determined by Norquay et al. [52], likely due to the faster Rb spin-destruction rate due to vdW molecules and Rb- ^{129}Xe spin-exchange rate used in this work.

Fig. 4.4 shows that higher than optimal T (and corresponding [Rb]) results in a slow decline in P_{Xe} . This is because, under these conditions, even though low $\langle P_{\text{Rb}} \rangle$ is present, as observed in Fig. 4.5a, P_{Rb} is heterogeneous across the cell length, with high P_{Rb} at the front of the cell and near-zero P_{Rb} at the back of the cell. Since meaningful spin-exchange will only occur in the high P_{Rb} region at the front of the cell, the Xe residency time is lower. However, the increase in $[\text{Rb}]_{\text{sat}}$ with temperature results in a higher spin-exchange rate, thus compensating somewhat for the reduction in Xe residency time, and resulting in a more gradual decrease in P_{Xe} with T (and corresponding [Rb]) compared to modelling using cell averaged spin-exchange times and polarisations as performed in ref. [52]. Thus higher than optimal [Rb] is less detrimental to output P_{Xe} than lower than optimal [Rb]. This is explored in more detail in Chapter 6.

In the limit of very high [Rb], $\gamma_{\text{SE}} \gg \Gamma'$, and so P_{Xe} for $\Gamma' = 1\text{min}$ and 44min are approximately equal, as shown in Fig. 4.4. This would correspond to a thin slab of high P_{Rb} at the front of the cell and so modelled P_{Xe} build up may be unrealistic when realistic gas flow and diffusion are considered.

Simulations were performed for $T = 120^\circ\text{C}$ where [Rb] and Γ' were varied for different P_l , with results plotted in Fig. 4.5.

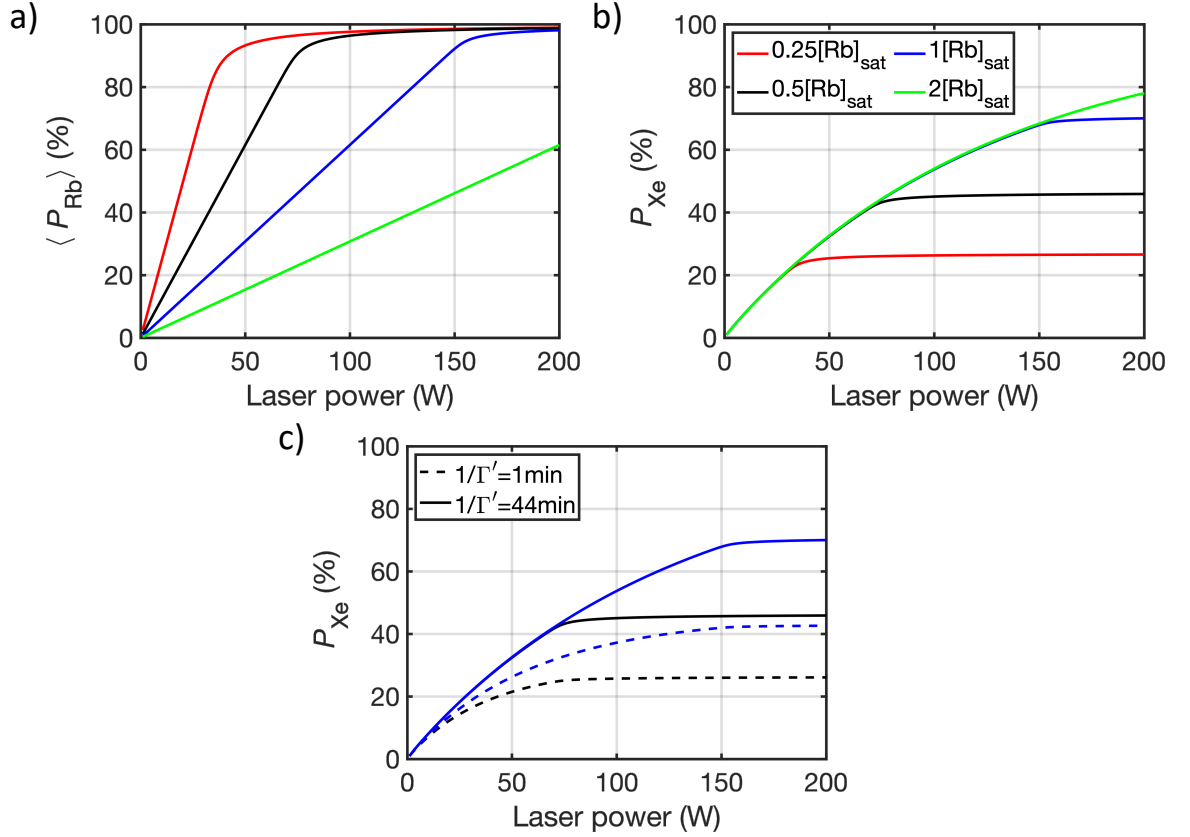


Figure 4.5: (a) Rb polarisation, P_{Rb} , and (b, c) P_{Xe} vs laser power for different (b) Rb vapour densities, $[\text{Rb}]$, and (c) Γ' . $T = 120^\circ\text{C}$, $p = 1.25\text{bar}$ and $Q = 2\text{SLM}$ were used.

Fig. 4.5a shows that at a specific laser power for each $[\text{Rb}]$, $\langle P_{\text{Rb}} \rangle$ begins to level off. This coincides with a levelling off in P_{Xe} , as shown in Fig. 4.5b. Showing that operating $[\text{Rb}]$ must be increased to harness higher P_{Xe} at higher laser powers.

Fig. 4.5c shows that for our optimal conditions, lower Γ' leads to lower P_{Xe} . The strong P_{Xe} dependence on Γ' shows that for accurate modelling, accurate measurement of Γ' is essential.

These simulations illustrate the significance of attaining optimal $[\text{Rb}]$ and high Γ' to optimise P_{Xe} . Furthermore, they illustrate the impact of laser power and delineate the regimes where P_{Xe} is influenced by P_l and those where it is not. Subsequent 3D simulations focus on what $[\text{Rb}]$ are achieved when realistic thermal and gas flow considerations are accounted for.

4.3.2 Varying Rb pool size

Mesh analysis

The mesh size dependence was determined by evaluating the key solutions for each physics model, namely v_z , T , $[Rb]$, R and P_{Xe} for different mesh sizes. This was performed for $Q = 2SLM$ and $P_l = 160W$ with the $10cm^2$ Rb pool, $\theta_{pool} = 20^\circ$. The number of mesh elements for each mesh size are given in Table 4.5. Results are shown in Table 4.6.

From Table 4.6, absolute percentage change from “finer” mesh solutions to other mesh size solutions is less than 10% for all meshes finer or equal to the “normal” mesh for all parameters investigated. The greatest variation was from the mean and standard deviation of $[Rb]$. “Fine” mesh size was chosen as a balance between the simulation run time and the accuracy of the solution.

The longitudinal cell position in z distribution of each parameter for each mesh size was also checked for expected solution convergence with increasingly finer mesh size and was seen to be as expected.

Table 4.5: Mesh elements corresponding to Table 4.6.

Physics-controlled mesh size	Domain elements	Boundary elements	Edge elements
Coarser	37190	7200	248
Coarse	90057	14540	350
Normal	201371	28234	534
Fine	513198	50634	756
Finer	1528240	106520	1110

Table 4.6: Mesh dependent parameters for the 10cm² Rb pool cell, pressure $p = 1.25$ bar, flow rate $Q = 2$ SLM, $T_{\text{oven}} = 120^\circ\text{C}$. Highlighted values are where maximum absolute percentage change compared to ‘finer’ mesh solution occurs.

Parameter	Mesh size*				
	Coarser	Coarse	Normal	Fine	Finer
Run time (s)	165	289	594	1320	(3656 + 355 [†] = 4011)
Mean optical pumping rate (10^5 s^{-1})	6.47	6.32	6.27	6.17	6.14
SD [‡] optical pumping rate (10^5 s^{-1})	0.682	0.770	0.797	0.854	0.869
Mean T ($^\circ\text{C}$)	134.3	135.9	136.3	137.3	137.5
SD T ($^\circ\text{C}$)	8.06	8.81	9.01	9.46	9.52
Mean [Rb] (10^{18} m^{-3})	6.14	6.98	7.22	7.77	7.94
SD [Rb] (10^{18} m^{-3})	1.04	1.04	1.10	1.09	1.01
Mean P_{Xe} (%)	18.3	20.1	20.0	20.4	20.5
SD P_{Xe} (%)	8.05	8.93	9.34	10.00	10.13
P_{Xe} at the cell outlet (%)	31.6	34.7	35.2	36.6	36.8
Mean z-gas velocity (-mm/s)	8.64	8.67	8.70	8.73	8.75
SD z-gas velocity (mm/s)	17.3	18.9	18.6	17.9	18.9
Maximum absolute percentage change to ‘Finer’ mesh solution (%)	22.7	12.1	9.19	8.44	n/a

*Physics-controlled mesh size feature on COMSOL. The number of mesh elements are stated in Table 4.5. [†]Fine initial solution run time. [‡]SD = standard deviation.

Results

The results of varying Rb pool size on simulated parameters are shown in Fig. 4.6.

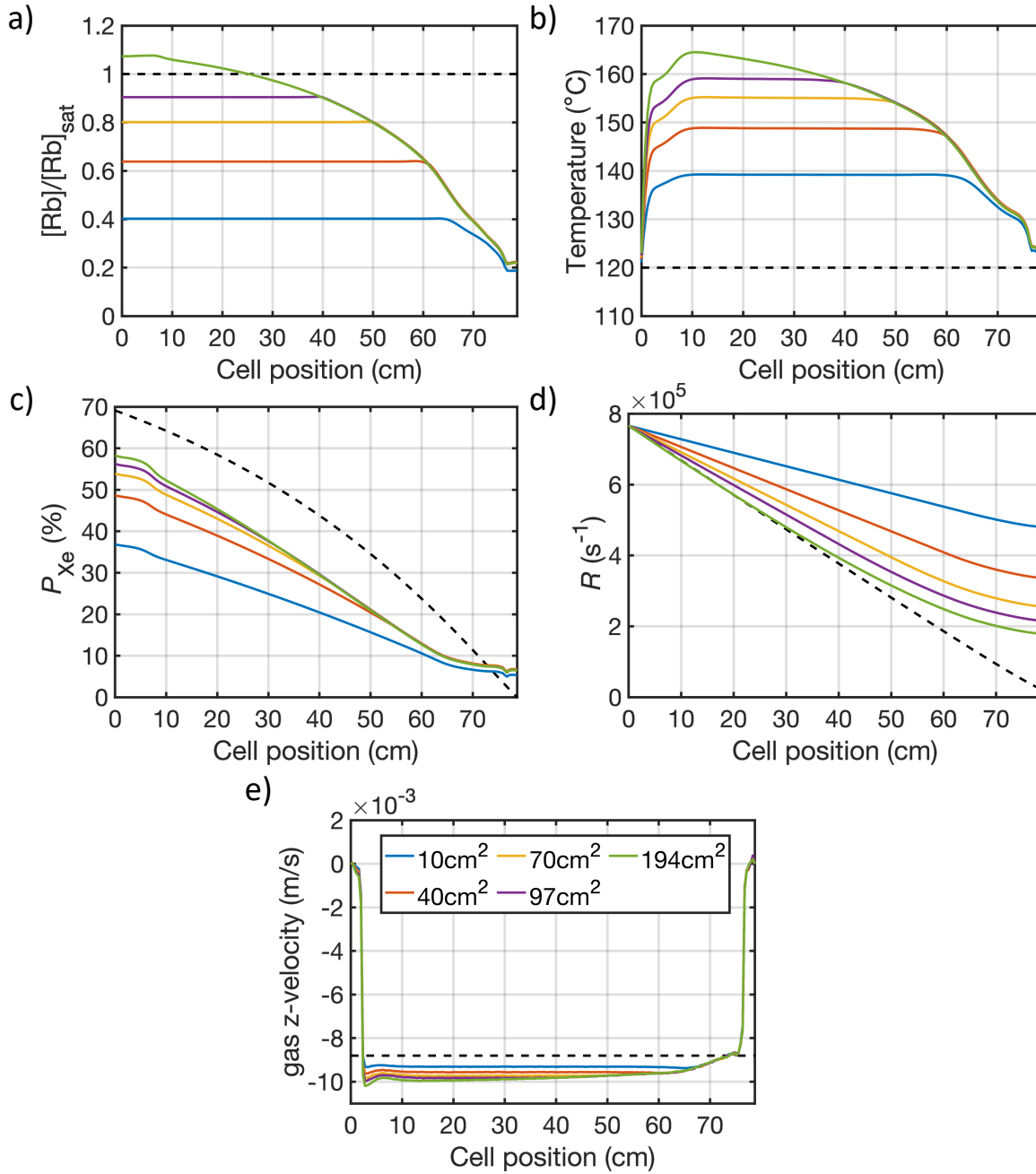


Figure 4.6: Simulations for different Rb pool sizes for $Q = 2\text{SLM}$, $p = 1.25\text{bar}$ and Rb pool angle $\theta_{\text{pool}} = 20^\circ$. The dashed line indicates the results of the 1D simulation, showing parameter cell position dependence for (a) normalised Rb density, $[Rb]/[Rb]_{\text{sat}}$, (b) cell internal gas temperature, (c) Xe polarisation, P_{Xe} , (d) optical pumping rate, R , (e) z gas velocities.

Fig. 4.6a shows lower than $[Rb]_{\text{sat}}$ across the cell for all but the highest surface area

Rb pool. $[\text{Rb}]$ is lowest towards the back of the cell (front of cell corresponds to $z = 0$ cm) and does not increase with Rb pool size. This corresponds to low initial P_{Xe} build up at the back of the cell as shown in Fig. 4.6c. $[\text{Rb}]$ towards the front of the cell does increase with Rb pool size, which leads to greater P_{Xe} build up with increasing Rb pool size.

Fig. 4.6b shows high temperature variation across the cell, with temperature heterogeneity becoming more pronounced as the size of the Rb pool increases. The internal gas temperatures within the cell increase towards the front of the cell, aligning with the spatial distribution of $[\text{Rb}]$. While the decrease in optical pumping rate towards the back of the cell, shown in Fig. 4.6d, also contributes to temperature heterogeneity, its impact is comparatively less pronounced than that of $[\text{Rb}]$.

The 10cm^2 Rb pool is comparable to the Rb source distribution prepared for cells used in ref. [52]. Noting slight differences in laser power (150W, not considering laser transmission losses at the front cell window, in ref. [52] and 160W in this work) and oven temperature (125°C in ref. [52] and 120°C in this work), we compare P_{Xe} , $[\text{Rb}]$ and laser absorption, L_{abs} values from ref. [52] and our 10cm^2 Rb pool simulations. Ref. [52] measured P_{Xe} at $Q = 2\text{SLM}$ to be $31.0 \pm 1.7\%$, which is similar to the simulated value of $P_{\text{Xe}} = 36.8\%$ at the cell outlet in Table 4.9. $[\text{Rb}]$ can be determined from ref. [52], using their measured values of the spin up time, $\tau_{\text{up}} = 71\text{s}$, $\gamma' = 1.63 \times 10^{-21}\text{m}^3\text{s}^{-1}$ and $1/\Gamma' = 44\text{min}$. $[\text{Rb}] = (\tau_{\text{up}} - \Gamma')/\gamma' = 8.4 \times 10^{18}\text{m}^{-3} = 0.31[\text{Rb}]_{\text{sat}}(T = 125^\circ\text{C})$ which is similar to the mean simulated value of $[\text{Rb}] = 7.8 \times 10^{18}\text{m}^{-3} = 0.38[\text{Rb}]_{\text{sat}}(T = 120^\circ\text{C})$ in Fig. 4.6. This means that $[\text{Rb}]$ was likely significantly lower than $[\text{Rb}]_{\text{sat}}$ in ref. [52] and this accounts for lower than expected P_{Xe} . We note however that higher laser absorption, $L_{\text{abs}} = 88\%$, was observed in ref. [52] compared to 37% in this work. The significant difference in L_{abs} is not due to the differences in incident laser power and suggests discrepancy in the optical pumping model.

For the largest Rb pool size (194cm^2), high temperatures lead to $[\text{Rb}]$ exceeding $[\text{Rb}]_{\text{sat}}$, suggesting that Rb sources towards the front of the cell may lead to higher than desired $[\text{Rb}]$. The elevated temperatures coupled to the Rb sources indicates potential susceptibility to Rb runaway effects. These simulations emulate perfect oven performance in maintaining the external temperature of the cell. In practice, this may not be the case and the high temperature heterogeneity could potentially impact the regulation of temperatures throughout the optical cell. Subsequent chapters of this thesis delve into the investigation of external cell temperature variations and their effect on optimal oven performance.

Fig. 4.6e shows increasing v_z with temperature. Elevated temperatures combined with a constant gas pressure, leads to lower gas density. In order to conserve mass flow rate,

the volumetric gas flow rate, and consequently v_z , must increase. This will reduce Xe residency time in the optical cell leading to lower P_{Xe} build up.

Based on the findings presented in Fig. 4.6 it is indicated that implementing a presaturator could prove beneficial in decoupling cell gas temperatures from [Rb], while simultaneously improving the levels and homogeneity of [Rb] for P_{Xe} build up, particularly towards the back of the optical cell.

4.3.3 Varying flow rate in a Rb presaturator

Mesh analysis

Mesh analysis for presaturator-only simulations was performed for $Q = 2\text{SLM}$, evaluating v_z and [Rb] for different mesh sizes. The results of mesh analysis are shown in Table 4.7.

Table 4.7: Mesh parameters for presaturator-only simulations, $p = 1.25\text{bar}$, $Q = 2\text{SLM}$, $T = 125^\circ\text{C}$. Highlighted values are where maximum absolute percentage change compared to ‘finer’ mesh solution occurs.

Parameter	Mesh size *				
	Coarser	Coarse	Normal	Fine	Finer
Run time (s)	41	105	160	362	779 + 362 [†] = 1141
mean [Rb] (10^{18} m^{-3})	19.7	19.8	19.4	18.6	18.0
SD [‡] [Rb] (10^{18} m^{-3})	7.91	7.85	7.87	7.91	7.96
mean z- gas velocity (m/s)	1.41	1.39	1.39	1.39	1.39
SD z- gas velocity (m/s)	0.753	0.745	0.762	0.786	0.797
Maximum absolute percentage change to ‘finer’ mesh solutions (%)	9.57	9.85	7.80	3.40	n/a

*Physics-controlled mesh size feature on COMSOL. The number of mesh elements are stated in Table 4.8. [†]Fine initial solution run time. [‡]SD = standard deviation.

Table 4.8: Mesh elements corresponding to Table 4.7.

Physics- controlled mesh size	Domain elements	Boundary elements	Edge elements
Coarser	87110	16948	1134
Coarse	256880	39970	1694
Normal	436258	55326	2134
Fine	1188147	111784	3056
Finer	4023945	284964	4912

Since optical pumping and laser heating simulations were not conducted, run times were considerably shorter than for the SEOP simulations above. Consequently, physics-controlled fine mesh size was used to improve accuracy of simulated parameters. Table 4.7 shows the most significant deviation was observed in the mean $[Rb]$, which was found to decrease as the mesh size increased.

Results

The simulated build up in $[Rb]$ along the presaturator for different Q is shown in Fig. 4.7a. This was then converted into $[Rb]$ at the end of the presaturator vs Q for different presaturator lengths, as shown in Fig. 4.7b. The presaturator length or position required to reach a level of Rb saturation was then determined for different Q , shown in Fig. 4.7c.

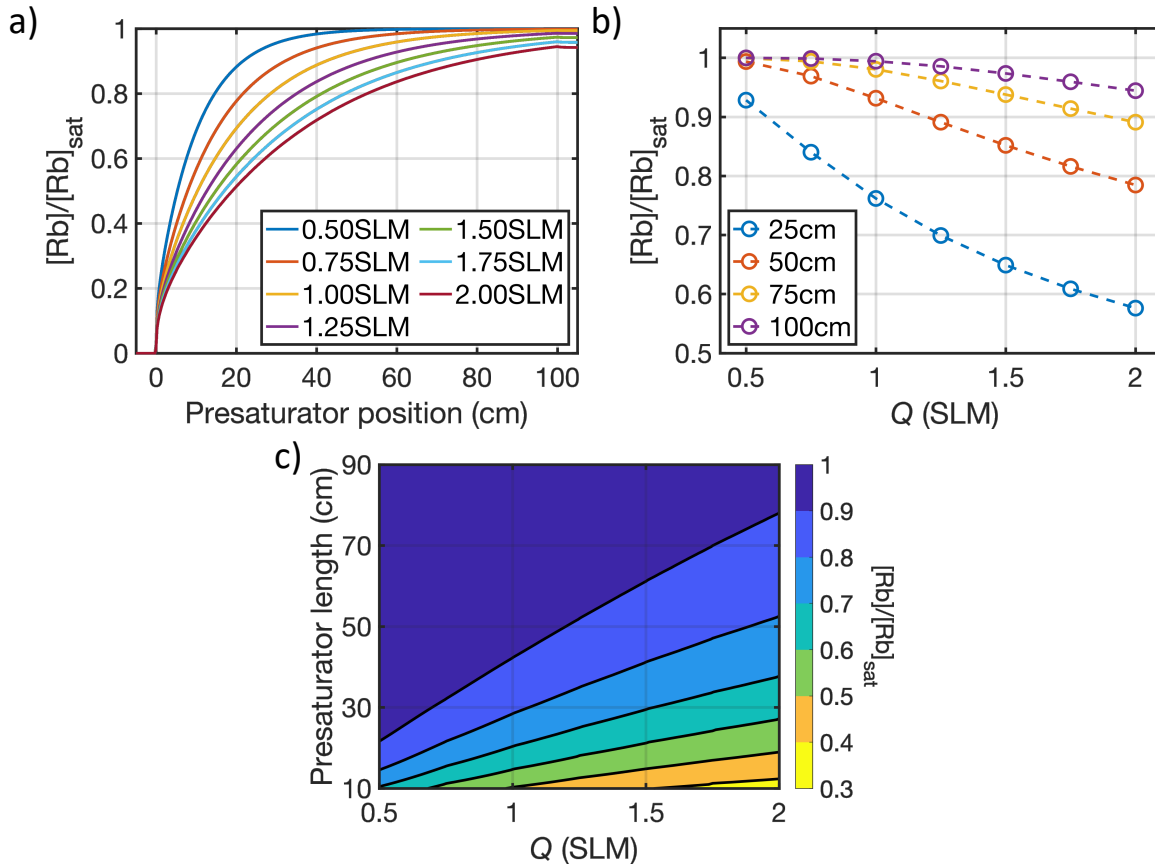


Figure 4.7: 1m Rb presaturator only simulations for $p = 1.25\text{bar}$ and $T = 125^\circ\text{C}$. (a) $[Rb]/[Rb]_{sat}$ vs presaturator position for different Q . (b) $[Rb]/[Rb]_{sat}$ at the end of the presaturator vs Q for different presaturator lengths. (c) $[Rb]/[Rb]_{sat}$ contour plot for presaturator length vs Q .

Fig. 4.7b shows that $[Rb]$ decreases significantly with Q for a 25cm presaturator, the length previously deemed sufficient in ref. [112], where for $Q = 2\text{SLM}$, $[Rb]/[Rb]_{sat} = 58\%$. In contrast, with a 1m presaturator operating under the same flow rate $Q = 2\text{SLM}$, $[Rb]/[Rb]_{sat}$ increases to 94%. This illustrates that using a presaturator of sufficient length mitigates the dependency of $[Rb]$ on Q , given a fixed presaturator length.

Fig. 4.7c shows the presaturator length required to reach a level of $[Rb]$ for a given

Q . As expected, the required presaturator length increases with the desired level of $[\text{Rb}]$ saturation. Required presaturator length increases approximately linearly with operating Q for a specified level of $[\text{Rb}]$ saturation. In addition, the separation of the contour lines increases with increasing Q . This suggests that for near-unity $[\text{Rb}]/[\text{Rb}]_{\text{sat}}$, the required presaturator length at $Q > 2\text{SLM}$ rapidly increases beyond practical presaturator lengths. Therefore, a realistic and practical aim of $[\text{Rb}]/[\text{Rb}]_{\text{sat}}$ is ~ 70 to 90% , at the expense of some Q dependence of $[\text{Rb}]$. Uncertainty in the external optical cell wall temperature maintained by the oven in practice will also limit achievable $[\text{Rb}]/[\text{Rb}]_{\text{sat}}$.

In ref. [131], in which a small ($V_{\text{cell}} = 491\text{cm}^3$) optical cell and no Rb presaturator was used, photon absorption was observed to decrease with increasing Q , indicating $[\text{Rb}]$ decreasing with increasing Q . This would cause γ_{SE} and τ_{up} to decrease with Q , lowering P_{Xe} at higher flow rates. Freeman [55] also observed a decrease in τ_{up} when switching from a cell involving both Rb in a presaturator and the cell main body to a cell where Rb is only placed with a presaturator, attributed to the short presaturator used². The results here show in both cases extending the presaturator would reduce the Q dependence of $[\text{Rb}]$, which is expected to increase γ_{SE} .

4.3.4 Incorporating the Rb presaturator into the cell design

Finally, the inlet of the current optical cell design was extended to produce a 72cm presaturator, expected to produce $[\text{Rb}]/[\text{Rb}]_{\text{sat}} = 88\%$. Rb boundary conditions (Eq. 4.17) were applied to 25% of the presaturator, as in the presaturator-only simulations. Rb boundary conditions were not applied within the main body of the cell. Simulations were then performed for the same running conditions as used for the varying Rb pool size simulations. Results are shown in Fig. 4.8 and Table 4.9. $[\text{Rb}]$ and T distributions were also incorporated into 1D simulations separately. P_{Xe} and L_{abs} values were then determined and compared to the FEM values for the full simulation to investigate the relative contribution of the $[\text{Rb}]$ and T distributions to the resulting P_{Xe} and L_{abs} values, and are shown in Table 4.9. In addition, 3D $[\text{Rb}]/[\text{Rb}]_{\text{sat}}$ distribution maps for the most notable Rb source distributions – the smallest and largest Rb pools, the Rb presaturator cell and the Rb presaturator only simulations – are shown in Fig. 4.9.

²Freeman [55] measured the critical flow rate, described later in Chapter 6, which is related to τ_{up} .

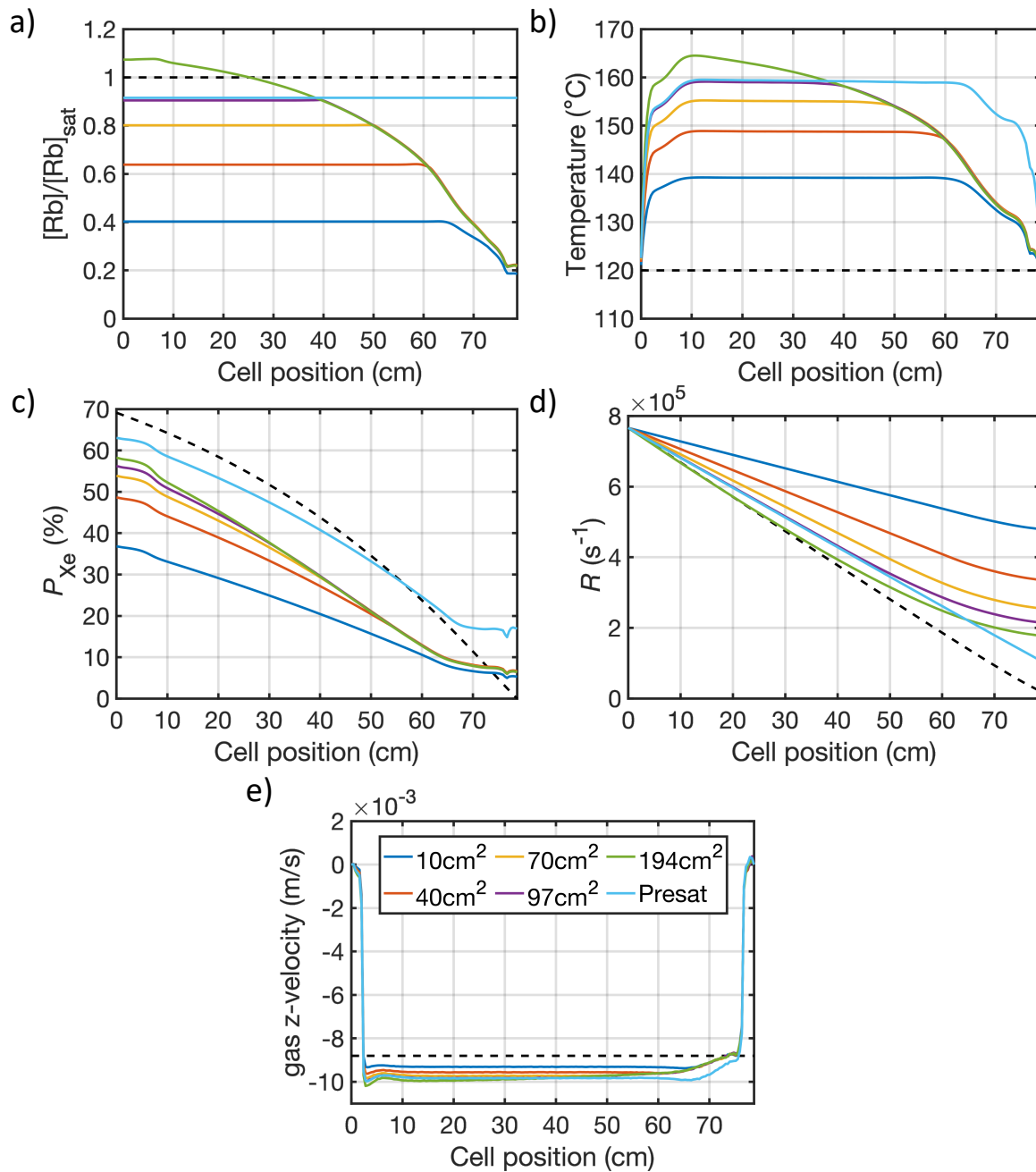


Figure 4.8: Simulations for different Rb pool sizes ($\theta_{pool} = 20^\circ$) and the Rb presaturator for $Q = 2\text{SLM}$ and $p = 1.25\text{bar}$. The dashed line indicates the results of the 1D simulation, showing parameter cell position dependence for (a) $[Rb]/[Rb]_{sat}$, (b) cell internal gas temperature, (c) P_{Xe} , (d) R , (e) z gas velocities.

Table 4.9: Output P_{Xe} for different modelled Rb distributions, $p = 1.25\text{bar}$, $Q = 2\text{SLM}$.

Rb distribution	FEM	1D: [Rb] and T	1D: T only	1D: [Rb] only	1D: [Rb] = [Rb] _{sat} everywhere
P_{Xe} at the outlet exit (%)					
Rb pool - 10cm ²	36.8	35.8	67.1	37.6	69.1
Rb pool - 40cm ²	48.4	47.9	66.2	51.1	69.1
Rb pool - 70cm ²	53.6	53.4	65.8	57.3	69.1
Rb pool - 97cm ²	56.0	55.9	65.5	60.1	69.1
Rb pool - 194cm ²	58.0	58.1	65.3	62.6	69.1
72cm pre-saturator	62.8	61.9	64.9	66.4	69.1
Total laser absorption across the cell, L_{abs} (%)					
Rb pool - 10cm ²	37.4	37.4	95.2	38.4	97.2
Rb pool - 40cm ²	56.3	56.1	94.3	58.3	97.2
Rb pool - 70cm ²	66.9	66.6	93.9	69.7	97.2
Rb pool - 97cm ²	72.0	71.9	93.7	75.4	97.2
Rb pool - 194cm ²	76.8	76.7	93.5	80.7	97.2
72cm pre-saturator	85.9	85.8	93.1	90.1	97.2

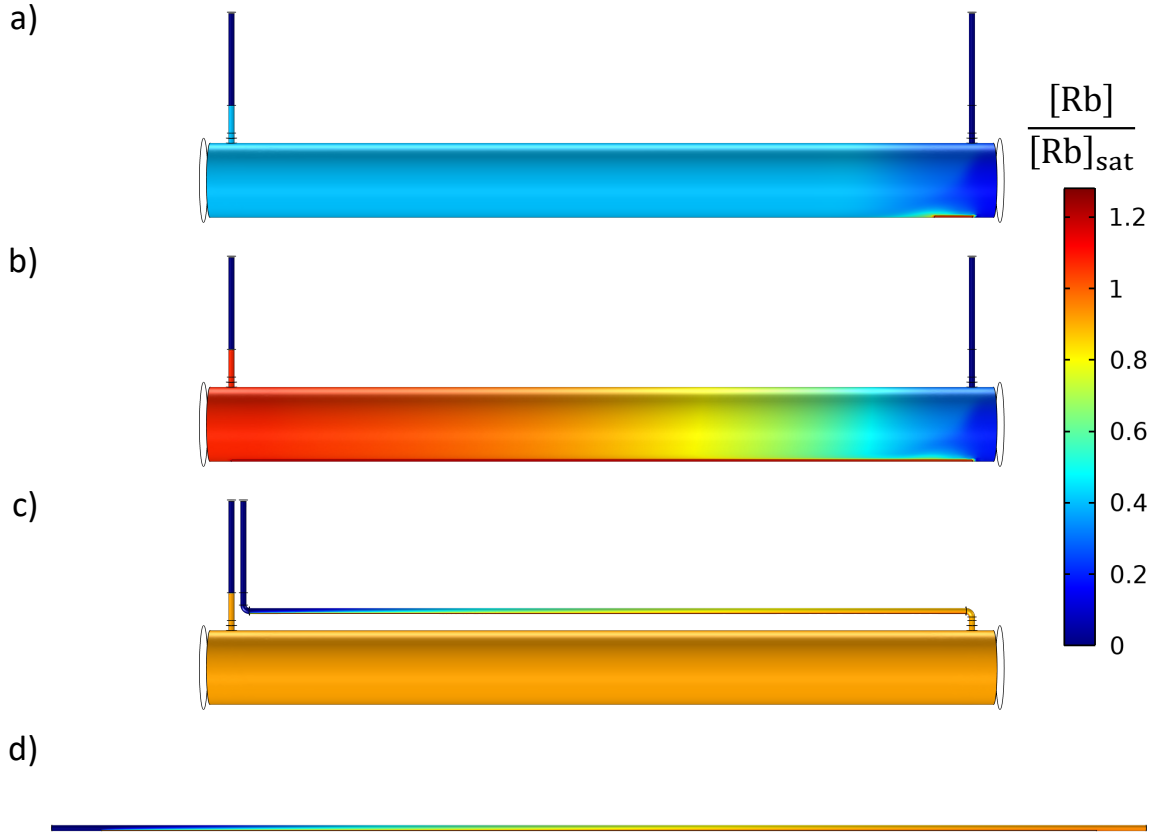


Figure 4.9: $[\text{Rb}]/[\text{Rb}]_{\text{sat}}$ distributions for $P_l = 160\text{W}$, $Q = 2\text{SLM}$ and $p = 1.25\text{bar}$ for the optical cells given in Fig. 4.1. (a) Small (10cm²) Rb source placed within the cell main body. (b) Large (194cm²) Rb source placed within the cell main body. (c) Rb placed only within the 72cm presaturator. (d) Rb within a 1m presaturator only (not to scale).

Fig. 4.8a shows that for Rb sources located only within the presaturator, there is homogeneous, near saturation $[\text{Rb}]$ ($[\text{Rb}]/[\text{Rb}]_{\text{sat}} = 92\%$) across the optical cell. This corresponds to a more homogeneous temperature profile across the cell compared to simulations with Rb pools only within the cell body. The temperature decreases rapidly near the front and back cell windows (Fig. 4.8b), likely due to heat dissipation through the cell windows and the gas velocity changes indicating turbulence due to the inlet and outlet. In practice, we would expect incident pumping laser light on these windows to cause heating due to incomplete transmission.

Simulations from Rb located only within the presaturator exhibits greater optical pumping attenuation, L_{abs} and P_{Xe} build up than all other tested Rb source distributions. This is due to the increased $[\text{Rb}]$ at the back of the cell providing more rapid γ_{SE} and initial P_{Xe} build-up. Our results support the conclusion of Kelley et al. [115] that large

presaturators are needed to reach near $[\text{Rb}]_{\text{sat}}$ for optimal P_{Xe} build up.

In all Rb distributions tested, the gradient of P_{Xe} build up is initially low to zero at the back of the cell, and $P_{\text{Xe}} > 0$, which differs from the results of the 1D simulations. Fig. 4.8e shows that z -velocities go to zero at the front and back of the cell. This suggests that gas is turbulent and residing in this area for longer than expected from plug flow. Consequently, conservation of momentum means that gas velocities must be higher in other regions of the cell, reducing residency time in these areas. From Table 4.9, this does not appear to detrimentally affect out-flowing P_{Xe} when compared to 1D simulations in which plug flow is assumed. If this effect was more dramatic, and the regions of turbulence and higher Xe residency time had detrimental SEOP attributes, such as low $[\text{Rb}]$ or P_{Rb} , then we may observe a lowering of out-flowing P_{Xe} . In addition, smaller cells where turbulence at the cell inlet is likely to affect a larger proportion of gas flow within the optical cell, this phenomenon may be more significant. Indeed, FEM performed on a small cell continuous-flow polariser has shown shorter Xe residency times compared to that assumed by plug flow due to convection rolls [115]. The small diameter of the inlet and outlet stems limits the internal gas volume for un-illuminated Rb and un-polarised ^{129}Xe , as well as due to the stopcocks requiring a small diameter to ensure a tight seal and prevent cell contamination. However, other polarisers have looked to implemented conical inlet, outlet openings which may reduce gas turbulence and homogenise Xe residency across the cell [115].

Table 4.9 illustrates that 1D simulations incorporating solely the T distribution from the FEM simulations depicted in Fig. 4.8 indicate that as temperature rises along with a greater distribution of Rb source, there is an increase in P_{Xe} buildup and a decrease in L_{abs} . This is likely due to the lower total gas number density within the cell, leading to lower Xe residency time within the cell, shown by the higher gas z -velocities in Fig. 4.8.

For Rb pool sources, where $[\text{Rb}] < [\text{Rb}]_{\text{sat}}$ distributions were produced, the $[\text{Rb}]$ distribution difference contributes more to the difference in P_{Xe} and L_{abs} between the FEM and 1D models than differences in T distributions, as shown in Table 4.9. Only for the presaturator Rb source distribution, where near saturation $[\text{Rb}]$ was produced, are P_{Xe} and L_{abs} values most similar between the FEM and 1D simulations and the T distribution contributes more significantly than the $[\text{Rb}]$ distribution to the discrepancy. Therefore, in general $[\text{Rb}]$ distribution is more significant than T in contributing to lower than expected P_{Xe} and L_{abs} .

We note that the discrepancy in L_{abs} between these simulations and previous measured in ref. [52] may suggest that higher $[\text{Rb}]$ may not lead to higher P_{Xe} due to complete photon attenuation. Instead, if near- $[\text{Rb}]_{\text{sat}}$ can be reached, operating temperatures

may be able to be decreased to achieve the same desired $[\text{Rb}]$, which may improve P_{Xe} by increasing the Xe residency time. Freeman [132] noted an increase in P_{Xe} for the same photon absorption by lowering operating temperatures due to the use of a Rb presaturator.

4.4 Conclusions

In this work, P_{Xe} temperature dependence was simulated for different P_l and Γ' . The optimal temperature was determined to be $T = 121.5^\circ\text{C}$, assuming $[\text{Rb}] = [\text{Rb}]_{\text{sat}}$. At near-optimal temperature, non-saturation $[\text{Rb}]$ and higher Γ' was shown to reduce P_{Xe} . In addition, laser degradation (lower P_l) was shown to lower P_{Xe} and alter optimal conditions. In practice, accurate knowledge of $[\text{Rb}]$ and Γ' are essential for accurate modelling and prediction of P_{Xe} for system optimisation.

3D finite-element modelling of a large ($V_{\text{cell}} > 1\text{L}$) optical cell at high gas flow rate ($Q = 2\text{SLM}$) and utilising high power ($> 100\text{W}$) spectral-narrowed ($\leq 0.3\text{nm}$) was demonstrated, to our knowledge, for the first time. 3D simulations showed the effect of realistic Rb source distributions, gas flow and thermal dynamics on modelled SEOP parameters. $[\text{Rb}]$ was shown to be heterogeneous and lower than saturation levels for all Rb pool sizes in the main cell body. This resulted in lower P_{Xe} build up across the cell, as well as temperature heterogeneity. Comparison with previous work investigating the Sheffield polariser in ref. [52] showed improved agreement between modelled and measured P_{Xe} and $[\text{Rb}]$ values. However, we note a clear discrepancy in simulated and measured laser absorption values suggesting an incomplete optical pumping model. $[\text{Rb}]$ exiting the presaturator was shown to be approximately linearly dependent on the length of presaturator for a given $[\text{Rb}]$ saturation percentage. A sufficiently extended presaturator resulted in achieving near-saturation $[\text{Rb}]$ levels and diminished the flow rate dependency of $[\text{Rb}]$. By placing Rb sources only within the presaturator volume, $[\text{Rb}]$ and temperature homogeneity were improved, leading to greater P_{Xe} build-up across the cell.

In subsequent chapters, accurate $[\text{Rb}]$ and Γ' measurements were performed in order to validate these simulations. Incorporating a presaturator cell design into the Sheffield SEOP polariser was also explored.

Chapter 5

Using atomic absorption spectroscopy to measure in-cell Rb vapour density

5.1 Introduction

In Chapter 4, the simulated Rb vapour density, $[Rb]$, in an optical cell with Rb sources placed only in the cell main body, was shown to be heterogeneous and lower than saturation levels. By introducing a Rb presaturator upstream of the cell main body, $[Rb]$ homogeneity was improved, leading to greater predicted ^{129}Xe polarisation build up.

The aim of the work in this chapter¹ was to experimentally validate the simulation work by directly measuring $[Rb]$ in the optical cell of the Sheffield polariser. Direct measurements of $[Rb]$ in SEOP polarisers can be performed by two general methods: Faraday rotation or atomic absorption spectroscopy (AAS), described in Section 3.4.

Faraday rotation methods can be performed on Rb spin systems as alkali metal vapours become birefringent within an applied magnetic field. This means they have two different indices of refraction for right and left circularly polarised light. The plane of polarisation of a probe light source passing through the Rb vapour will rotate by an amount proportional to $[Rb]$ and P_{Rb} [133, 134]. The advantage of this method is that measurements can be performed far from atomic resonance, without knowledge of the line shape, to avoid high optical thickness that would lead to reduced measurement

¹This Chapter is based on the publication Ball, *et al.* Investigating Rubidium Density and Temperature Distributions in a High-Throughput ^{129}Xe -Rb Spin-Exchange Optical Pumping Polarizer. *Molecules* 2023, 28, 11. DOI: 10.3390/molecules28010011

accuracy. In contrast, AAS requires knowledge of the atomic resonance line shape if performed far from resonance [135]. A downside of Faraday rotation is that knowledge of P_{Rb} to determine $[\text{Rb}]$ is required under optical pumping conditions. Alternatively, $[\text{Rb}]$ can be determined through Faraday rotation in the absence of optical pumping. However, under these conditions, low Faraday rotation angles at the typical field strengths used in SEOP polarisers (order 10G) means that a high number of scan averages must be performed if sufficient signal-to-noise ratio (SNR) is to be obtained. Also, Faraday rotation cannot be applied orthogonal to B_0 , which means spatially localised measurements along the optical cell, where a small longitudinal component exists, come at the expense of SNR, and $[\text{Rb}]$ heterogeneity along the longitudinal cell length is more difficult to investigate.

AAS using broadband light sources is therefore a simpler method to implement for transverse measurements of $[\text{Rb}]$ along the length of an optical cell. AAS has been used to directly measure Rb and other alkali metal vapour densities in SEOP cells [134–136]. Consideration of the optical thickness of the atomic transition probed is important to avoid deviation from the Beer-Lambert law and reduced accuracy of determined $[\text{Rb}]$. However, reduced optical thickness typically also comes at the expense of lower SNR, making large ranges of $[\text{Rb}]$ difficult to measure using only one absorption line. Therefore, simultaneously probing multiple transitions can extend the range of measurable $[\text{Rb}]$ for a setup. Comparison of $[\text{Rb}]$ measured for each transition enables characterisation of reduced measurement accuracy due to breakdown in the Beer-Lambert law at high absorbance levels. In addition, the use of broadband light sources eliminates the need to use narrow probe lasers that are scanned across each absorption line shape in other AAS configurations [134, 135], a practice which significantly increases acquisition times.

In this chapter, in-cell $[\text{Rb}]$ heterogeneity using near-infrared (NIR) and violet AAS on cells with differing spatial distributions of Rb sources was investigated. Cell temperature distributions were also measured to assess thermal management and its role in $[\text{Rb}]$ distributions. The validity of the Beer-Lambert law was systematically characterised for each absorption line over a range of $[\text{Rb}]$ levels. Measurements of $[\text{Rb}]$ from AAS were used to measure the ^{129}Xe -Rb spin-exchange cross section, γ' , and this was compared to values derived from the literature.

5.2 Methods

5.2.1 Polariser components

The continuous-flow Sheffield SEOP polariser consists of a number of components shown in Fig. 5.1 and 5.2. The key components, which are discussed below, are the optical pumping laser, B_0 field and the optical cell. N.B. in this Chapter the cryogenic accumulation setup, known as the cryotrap, was only used for flip-angle calibration measurements.

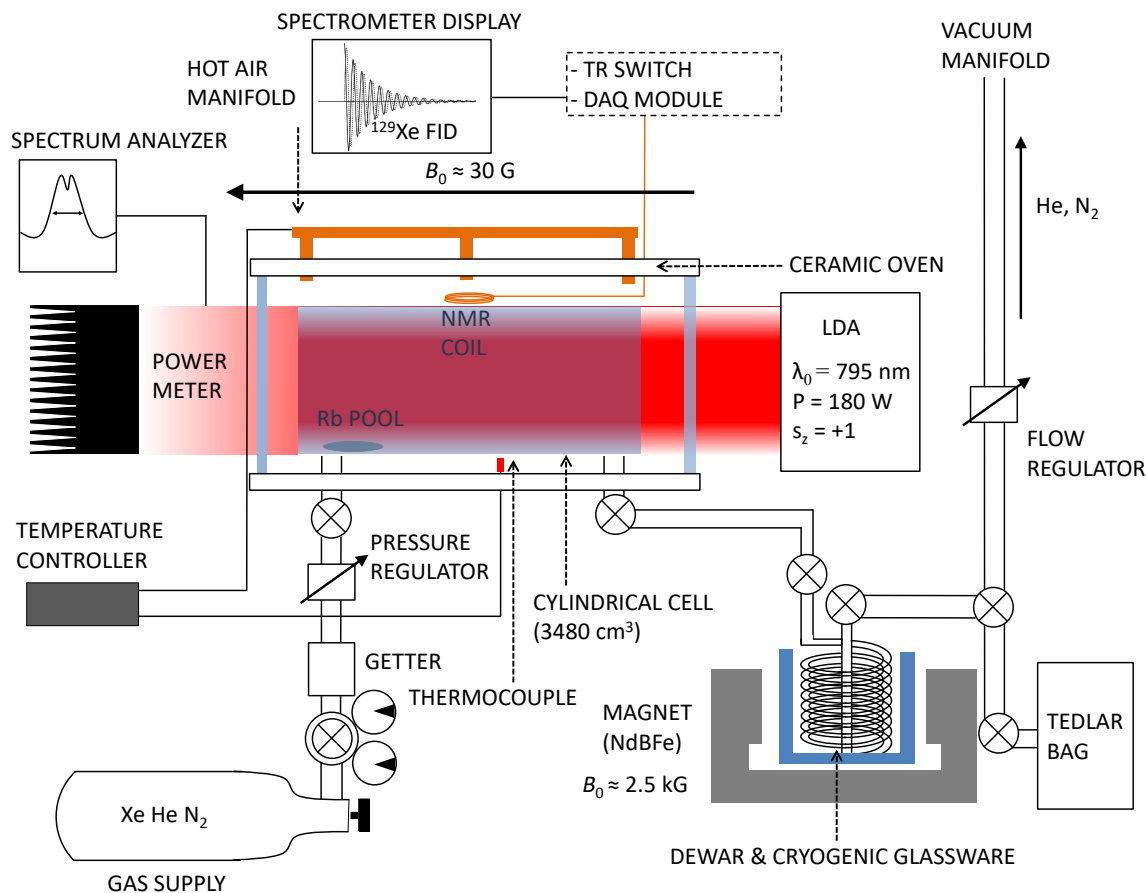


Figure 5.1: Schematic of the Sheffield ^{129}Xe -Rb continuous-flow polariser. Atomic absorption spectroscopy (AAS) apparatus is not shown. Figure adapted with permission from ref. [52]. Copyright 2023 by the American Physical Society.

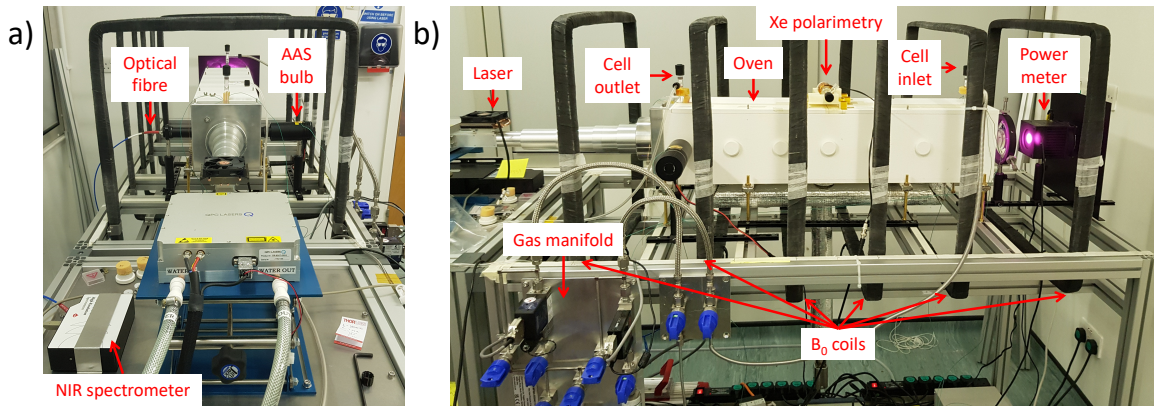


Figure 5.2: Labeled pictures of the polariser from (a) along the polariser and (b) side on to the polariser. The cryotrap and part of the gas manifold cannot be seen.

Laser

The laser diode array (LDA, QPC Lasers Inc model BrightLock Ultra-500 795nm-IG, 180W) and optical train is the optical pumping, left circularly polarised light source. An afocal telescope expands a 0.8 cm diameter beam from the fibre to a 7.5 cm diameter beam exiting the optical train, as shown in Fig. 5.3. The laser is characterised in terms of its output power, P_l , and Gaussian FWHM, as shown in Fig. 5.4. Operating at the maximum laser current of 38A produces $P_l = 184W$ output power and FWHM = 0.25nm.

Fig. 5.4d shows asymmetric deviation from a Gaussian line shape, which is due to different amounts of laser diode drift for each diode bar in the array. Over time with laser use, laser diodes increasingly drift apart reducing matching between the laser emission line shape and the Rb D₁ absorption line shape and optical pumping efficiency, as shown in Fig. 5.5.

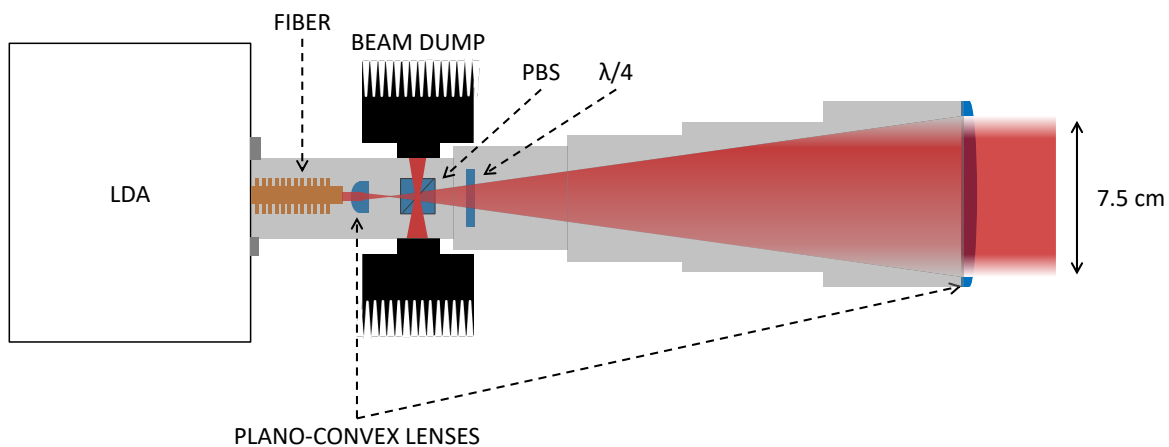


Figure 5.3: Schematic of the laser diode array (LDA) and optical train, consisting of the laser diode fibre, beam dumps, plano-convex lenses, polarising beam splitter (PBS) and quarter-wave plate ($\lambda/4$). Figure reproduced with permission from ref. [52]. Copyright 2023 by the American Physical Society.

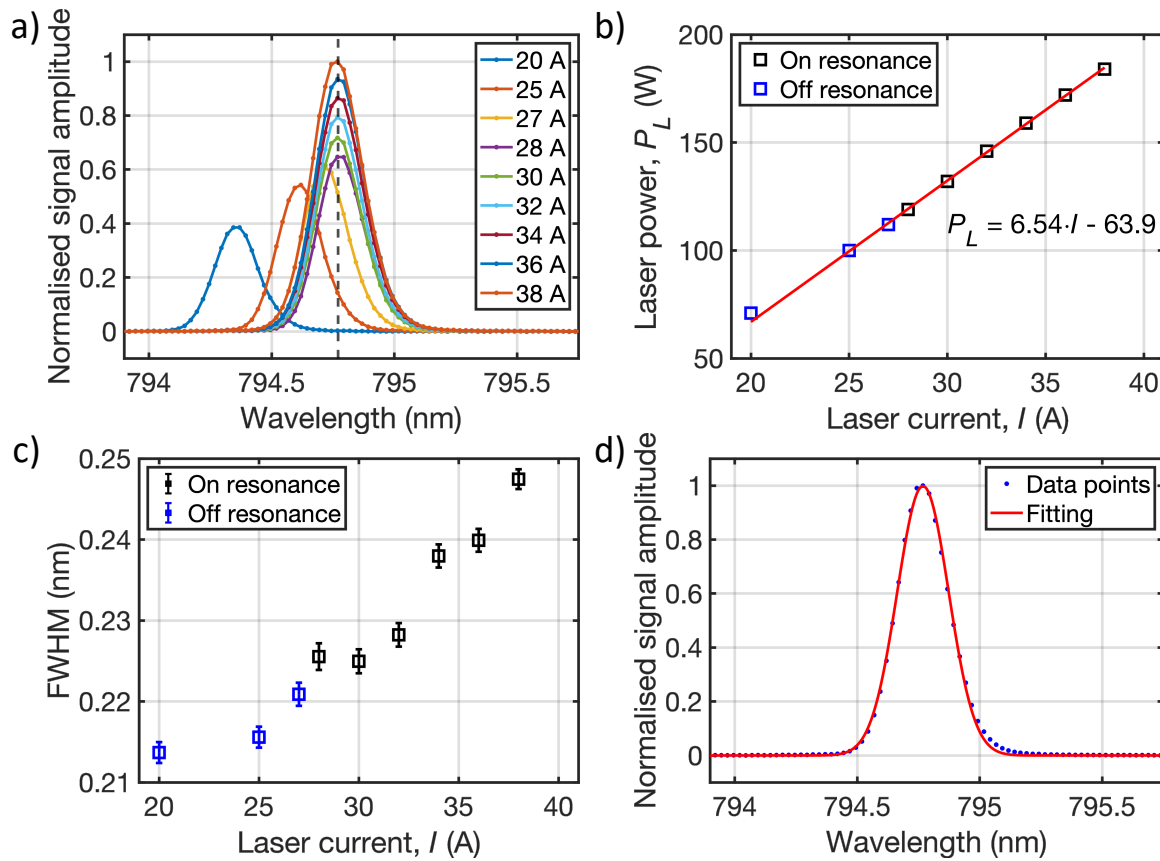


Figure 5.4: (a) Output laser optical spectra vs supplied laser current, I . Amplitudes are normalised to maximum signal intensity and integrals are normalised to output laser power, P_l . On-resonance ($\lambda_l = 794.768$ nm) spectra could not be acquired at $I \leq 27$ A due to the laser chiller maximum temperature (35°C) being reached. The vertical dashed line indicates D_1 resonance line (794.77nm). (b) P_l vs I . The red line is a linear fit to the on-resonance measurements. (c) Full width at half maximum (FWHM) determined from a Gaussian fit. (d) Gaussian fit of the $I = 38$ A spectra.

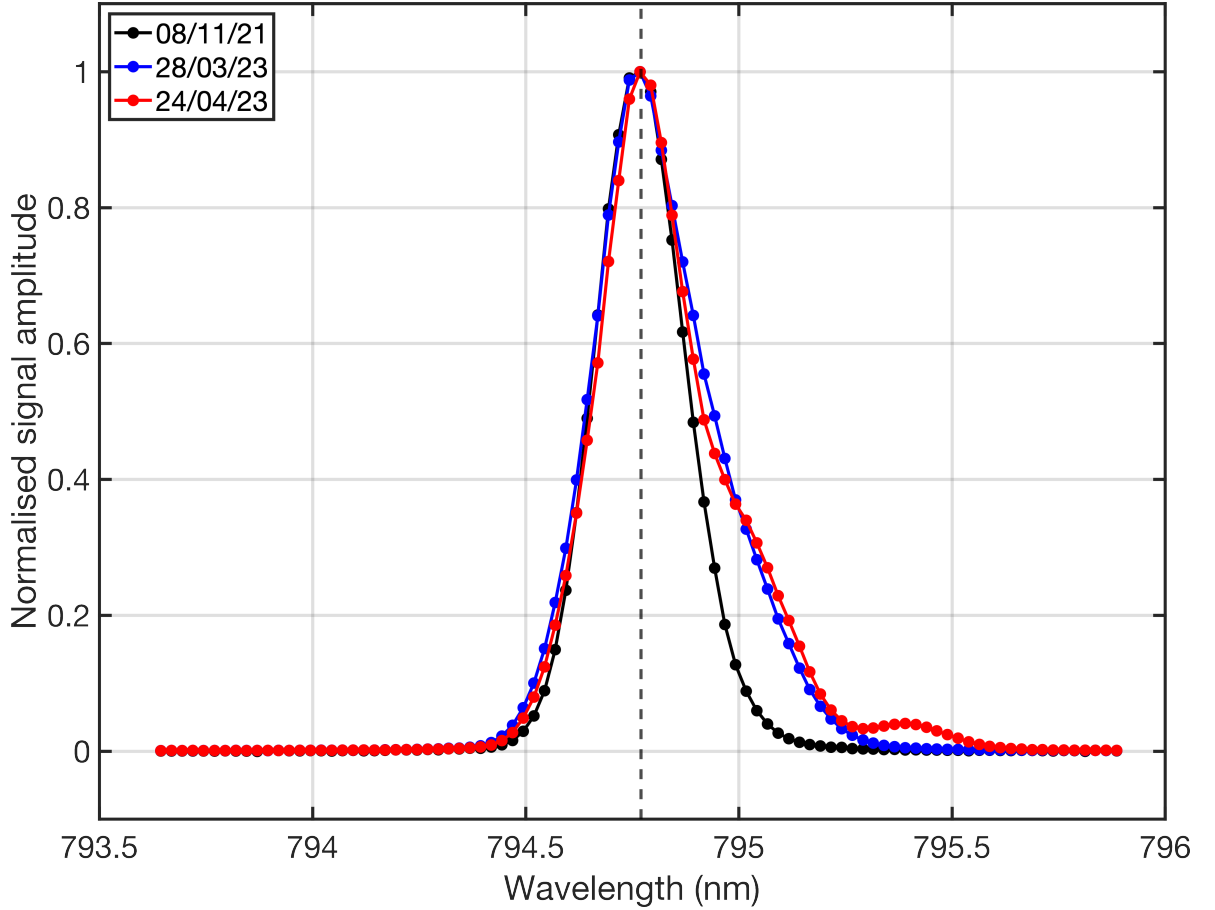


Figure 5.5: Laser spectra at maximum operating current (38A). Signal amplitudes are normalised to the maximum signal amplitude. 08/11/21: Gaussian fit FWHM = 0.25nm, $P_l = 184\text{W}$, acquired near the start of laser use. 28/03/23: Gaussian fit FWHM = 0.33nm (poor fit), P_l was not recorded. 24/04/23: Gaussian fit FWHM = 0.33nm (poor fit), $P_l = 179\text{W}$.

\mathbf{B}_0 field

Using a large optical cell, compared to a small optical cell, increases the volume over which the \mathbf{B}_0 field must be homogeneous for effective magnetic projection of the circularly polarised light for efficient optical pumping (see ref. [74]). In addition, good field homogeneity limits spin relaxation over the cell volume (see Section 3.3.3). θ defines the angle of \mathbf{B}_0 to the laser propagation direction z , and must be small for efficient optical pumping. Assuming $\theta \sim 0$, and in the high pressure regime¹, T_1 relaxation is dependent on B gradients transverse to \mathbf{B}_0 , $|\nabla B_\perp| = \sqrt{\nabla B_x^2 + \nabla B_y^2}$, according to Eq. 3.113. T_2 relaxation is affected by longitudinal B gradients, ∇B_z [23].

¹The high pressure regime is where the characteristic diffusion time, τ_d , is much longer than the characteristic precession time, τ_l [23]. For $\nu = 32.8\text{kHz}$, $D_{Xe} = 0.46\text{cm}^2\text{s}^{-1}$ and characteristic length equal to diameter of the cell = 7.5cm, $\tau_d/\tau_l = 2.5 \times 10^7$.

The B_0 field was produced previously in ref. [52] using a 4-square coil configuration based on ref. [137] with each coil side length = 1m (Acutran, Fombell, US). Although this produces a highly homogeneous B_0 field, a large footprint is required and the coils are heavy, reducing ease of transport and portability. A more compact, 6-square coil configuration, as used in ref. [138], was simulated and setup (MATLAB code supplied by Guilhem Collier). The simulations are based on the magnetic flux density in z -direction given by Eq. 2 of ref. [139]. A superposition of 9 infinitely small diameter square coils are simulated in order to simulate the width of the coils.

The square coils have a coil side length = 60cm. Inner, middle and outer coil-pairs consist of 51, 60 and 117 turns and are 1cm, 1.25cm and 2.5cm wide respectively. The separation of inner, middle and outer coils from the centre of the configuration are 9cm, 28.7cm and 55.6cm respectively. Simulated B_z field and B_z gradients along z are shown in Fig. 5.6.

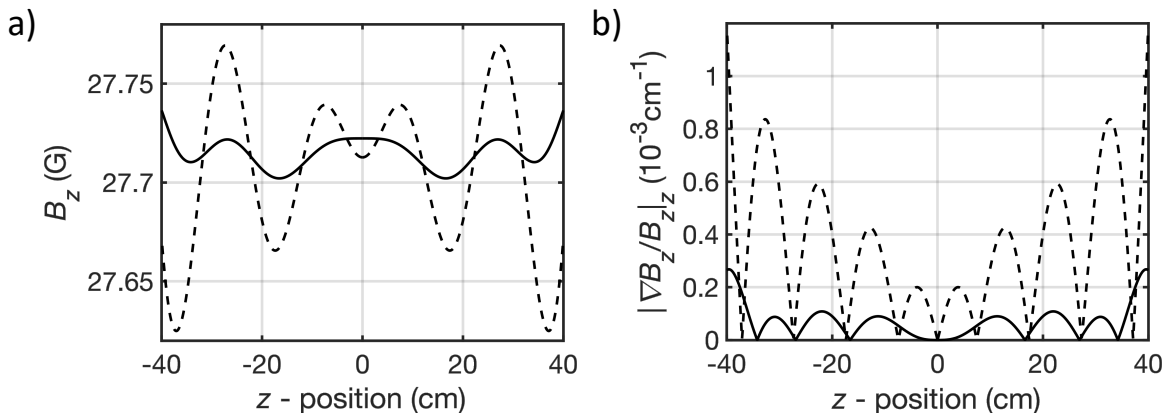


Figure 5.6: (a) Simulated magnetic flux density in z -direction, B_z , for the 6-coil configuration. (b) Corresponding B_z gradients in z , $|\nabla B_z/B_z|_z$. Solid and dashed lines are B_z field and gradients along the central ($x = y = 0$) and oven lid offset ($y = 95$ mm) longitudinal axes respectively. $z = 0$ corresponds to the centre of the coil setup.

Fig. 5.6 shows high B_z field homogeneity and small B_z gradients along the centre ($x = y = 0$) and offset oven lid ($y = 95$ mm). Limitations of these simulations include $\theta = 0$ assumed, only longitudinal B_z gradients were calculated (transverse B_z gradients were not calculated) and B_x and B_y gradients were also not simulated.

The B_0 field was experimentally measured using a three-axis magnetic field sensor (Bartington Instruments model Mag-03MS1000). The magnetic field sensor upper measurement limit is 10G, so measurements were performed at a coil current of $I = 0$ A (background) and $I = 2.5$ A. The background corrected $I = 2.5$ A field was then scaled for $I = 8.38$ A and background field added, as shown in Fig. 5.7.

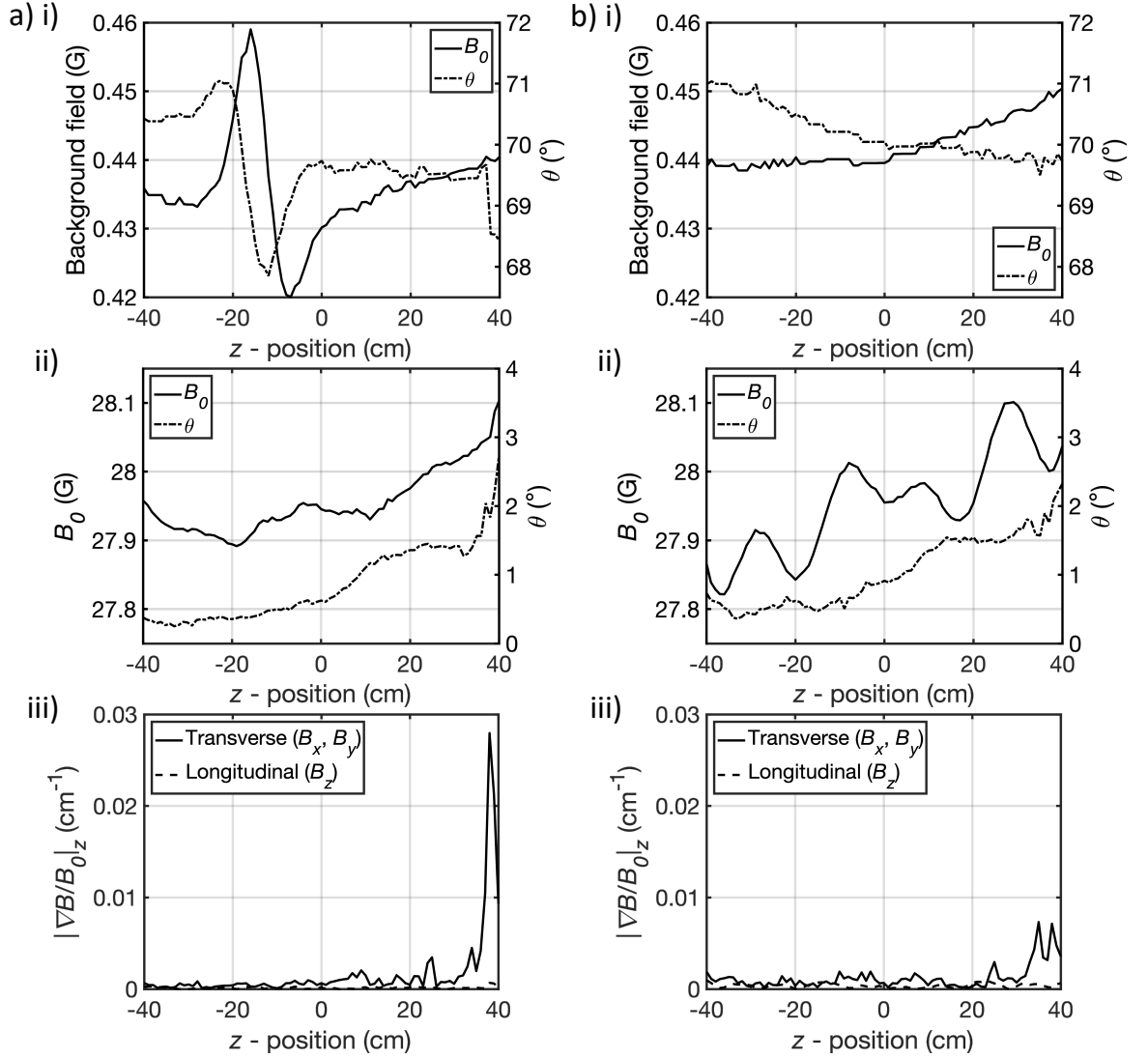


Figure 5.7: Measured B_0 field from 6-coil configuration (a) along the centre longitudinal axis and (b) along the longitudinal axis offset $y = 95\text{mm}$ equal to the top of the oven. (i) Background $I = 0\text{A}$ field, (ii) $I = 8.38\text{A}$ field, (iii) $I = 8.38\text{A}$ field gradients. The angle of B_0 to z -direction is $\theta = \arccos(B_z/B_0)$. $z = 0$ corresponds to the centre of the coil setup.

Fig. 5.7b shows that a coil current of $I = 8.38\text{A}$ produced $B_0 = 28\text{G}$ ($\nu_{129\text{Xe}} = 33\text{kHz}$) and $\theta < 3^\circ$. Using $R/\Gamma_{\text{SD}} \leq 83$ from simulations performed in Chapter 4, the expected effect of skewed light in our system on P_{Rb} and laser absorption, L_{abs} , can be calculated from factors given in ref. [74] and described in Section 3.3.1. Whilst $\theta < 3^\circ$ results in a negligible effect on P_{Rb} , with $\lesssim 0.1\%$ lower P_{Rb} expected compared to $\theta = 0^\circ$, L_{abs} will be up to $\sim 23\%$ higher in places compared to $\theta = 0^\circ$. This will have a detrimental effect on the photon efficiency and achievable Xe polarisation by reducing the fraction of absorbed photons that contribute to optical pumping. This was not accounted for

in this work, and may contribute the discrepancy in measured to simulated values seen in Chapters 5 and 6.

Magnetic field gradients are also very small ($< 0.03\text{cm}^{-1}$). The spike in gradients along the central axis at $z = 37$ to 40cm in Fig. 5.7 is suspected to be a probe mis-alignment anomaly, as it is not present in the top of the oven field measurements. Even so, $|\nabla B/B_0|_z = 0.028\text{cm}^{-1}$ calculated for $D_{\text{Xe}} = 0.46\text{cm}^2\text{s}^{-1}$ ($p = 1.25\text{bar}$, $T = 125^\circ\text{C}$, 3%Xe/10%N₂/87%He gas mix) using Eq. 3.113 gives $1/\Gamma_g = 46\text{min}$, which is longer than the contribution suspected from wall relaxation (order 1 to 10 mins).

SEOP cell Rb source distributions and Rb presaturation

Cylindrical Pyrex cells with internal diameter of $w_{\text{cell}} = 7.5\text{cm}$ and length of $L_{\text{cell}} = 79\text{ cm}$ (external diameter, $w_{\text{cell}}^{\text{ex}} = 8.5\text{ cm}$ and length, $L_{\text{cell}}^{\text{ex}} = 80\text{ cm}$) were used. All cells were cleaned with deionised water and isopropyl alcohol before drying at high temperature. Once dry, they were evacuated to an ultra-low pressure ($< 10^{-6}\text{ mbar}$) and placed in an argon glovebox for Rb filling. Three different Rb source distributions in the SEOP cells were produced, as shown in Figure 5.8. Two Rb distributions involved Rb placed inside the main body of the SEOP cell, whilst the third involved placing Rb only within a presaturation region upstream of the main body of the SEOP cell. The existing SEOP cell design was altered by extending the inlet to include a 72 cm presaturation region; this Rb source distribution and optical cell design was modelled in Chapter 4 to result in 92% Rb vapour saturation within the main cell body at $Q = 2\text{SLM}$. Heating tape (OMEGA, model DHT052060LD) with a maximum power output of 468 W was wrapped around a 53.5 cm section of the presaturation region in order to improve temperature control and provide a temperature gradient between the presaturator and the main body of the cell to increase Rb vapour diffusion into the main body of the cell during closed cell operation. A power supply of $\sim 21\text{ W}$ to the heating tape was used when using the presaturator.

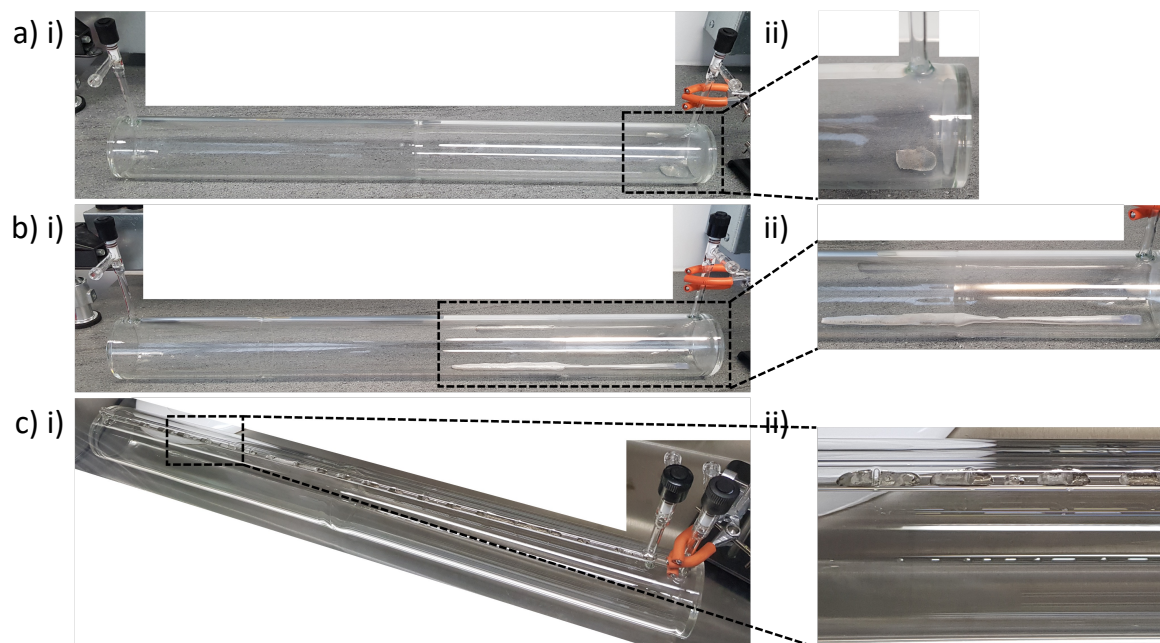


Figure 5.8: SEOP cells with different Rb source distributions; (a) 1g of Rb placed at the back of the cell, with an estimated surface area $\sim 10 \text{ cm}^2$, (b) 5 g of Rb placed in the cell, with an estimated surface area $\sim 64 \text{ cm}^2$ and (c) 2g of Rb distributed along the presaturator showing (i) the geometry of the cell and (ii) a close-up of the Rb distribution.

5.2.2 ^{129}Xe polarimetry and laser absorption

^{129}Xe polarimetry on a 1.5T MRI scanner

^{129}Xe polarisation can be calculated by measuring the signal from ^{129}Xe samples dispensed from the polariser on a 1.5T MRI scanner, as described in ref. [131]. The hyperpolarised signal is compared to the signal from a high-pressure thermally polarised ^{129}Xe sample acquired on the same setup. This has the advantage of reflecting the ^{129}Xe polarisation we would expect when performing *in vivo* scans on this scanner. However, potential polarisation losses between dispensing and acquisition on the scanner may occur. In addition, scanner time is often limited, as well as being expensive due to scanner running costs.

In-cell polarisation measurements could be performed, however ^{129}Xe number densities may be difficult to determine as gas temperatures are likely different to outer cell surface temperatures. Also, sampling the entire cell with homogeneous B_1 would require complex RF engineering. In addition, ^{129}Xe polarisation heterogeneity across the cell is likely high, making sampling a smaller region less useful. Sampling the front of the SEOP cell would be more suitable, however, laser heating and heterogeneous temper-

atures would alter the coil resistance, which would complicate correction for precise ^{129}Xe polarimetry. Consequently, a ^{129}Xe polarimetry system was implemented external to the SEOP cell but within the SEOP B_0 field for ease of dispensing ^{129}Xe gas and measuring its polarisation.

Coil, stand and sampling container

A 200 turn solenoid coil (CnC Tech Magnet Wire MW28-C SL AWG 26) with dimensions 47.0mm long and formed around a 34.6mm diameter PVC tube was constructed. B_1 maps obtained using an untuned probe coil are shown in Fig. 5.9. The well defined B_1 homogeneous region within the solenoid ($z \sim -1$ to 1cm) allowed flip angles to be measured via RF destruction.

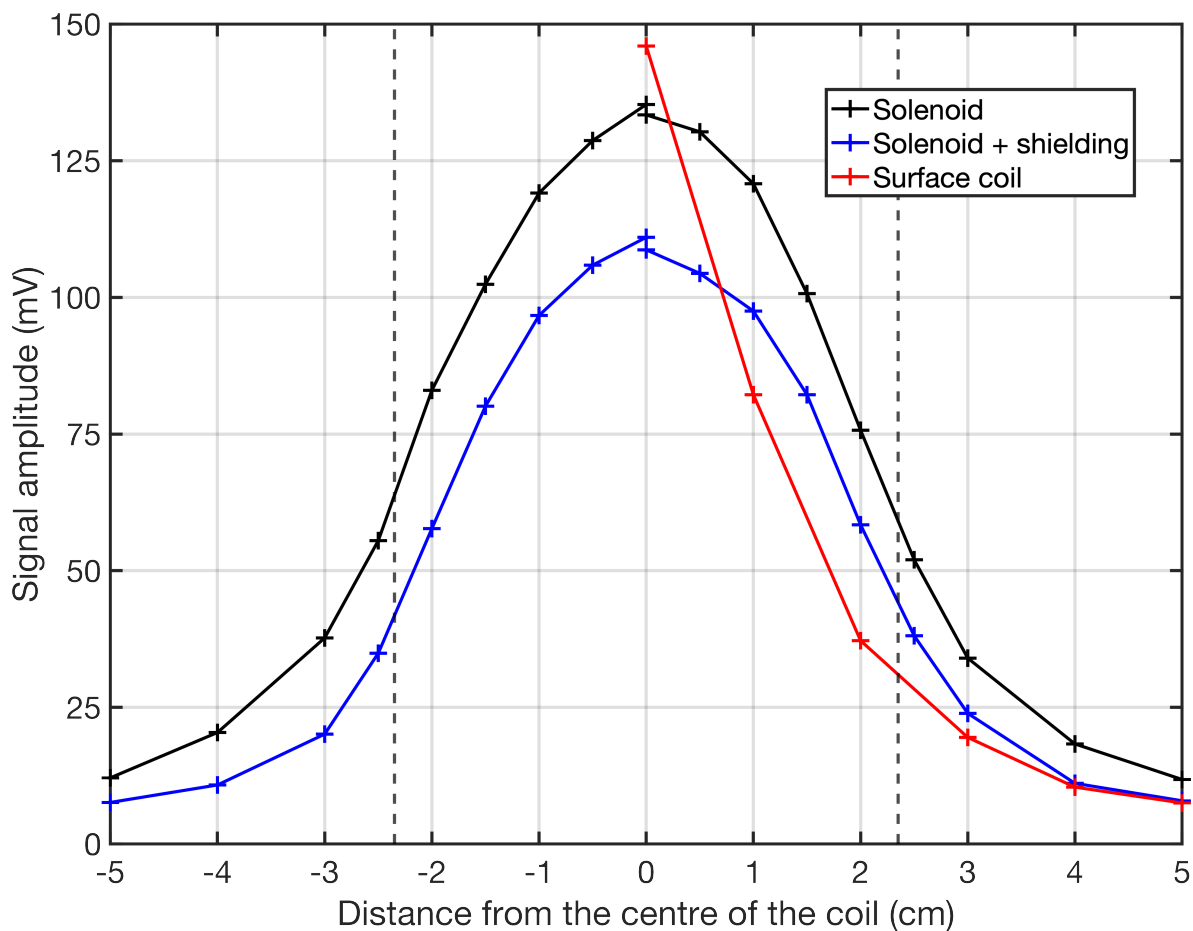


Figure 5.9: Coil B_1 map along the central z axis for the solenoid (black markers), with a copper shielding layer added (blue markers) and for a surface coil, as used on the surface of the optical cell (red markers). The connecting lines are to guide the eye only. Measurements in the opposite (negative) direction required re-orientating the probe coil, likely causing the slight change in centre measurements. The dashed lines indicate the ends of the solenoid.

At 32.8kHz, the solenoid coil Q was determined using an S_{11} measurement to be ~ 42 . A 3D printed stand was made to fix the position of the solenoid coil and sampling container within the B_0 field, as shown in Figure 5.10. The centre of the oven lid is the most homogeneous region of the B_0 coil outside the oven, as shown in Fig. 5.7biii and as such the most appropriate place to position the solenoid coil and stand. The solenoid configuration is oriented perpendicular to the optical pumping cell to ensure ^{129}Xe spins in the optical pumping cell are not sampled. The oven lid becomes warm during polariser operation, so the stand has feet which allow air flow around the stand, ensuring the solenoid and sample temperatures do not significantly change, whilst the room air conditioning and fans maintain air room temperature.

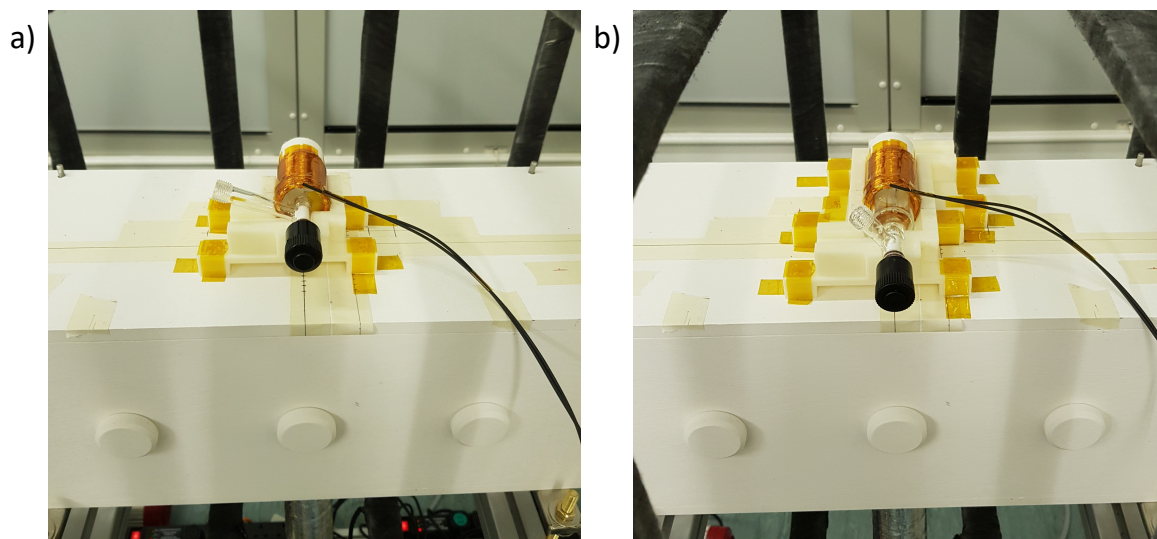


Figure 5.10: ^{129}Xe polarimetry setups with each container containing Xe gas mixture inside a solenoid coil, placed on the 3D printed stand(s). (a) The spherical container setup and (b) the cylindrical container setup.

Two sampling containers were used. A spherical (diameter = 23.9 mm) container was initially used which was positioned within the homogeneous region of the solenoid. However, low signal to noise with 3%Xe gas mixture and ^1H signals, even with thermal signal averaging, meant a larger cylindrical container was built, with a diameter and length of 28.1 mm and 95.5 mm respectively. Both sampling containers were made of Pyrex and cleaned before use. No anti-relaxation surface coatings were applied. The ^{129}Xe T_1 relaxation time constant was measured to be 63 ± 8 min for the spherical container and 76 ± 4 min for the cylindrical container at 32.8kHz. The T_1 of the cylinder is a factor 1.2 longer than the spherical container T_1 , which is similar to the factor 1.5 volume-to-surface ratio scaling of the cylinder ($V/S = 6.12$ mm) to the spherical container ($V/S = 3.98$ mm), as is expected from the relationship $T_1 \propto (V/S)$ given by Eq. 3.116. T_1 of both containers is sufficiently long for flip-angle measurements

using short repetition times to be performed. A Teflon stopcock and chem-thread on each container ensured leak-free connections to the gas manifold. The containers can then be filled, disconnected from the gas manifold and placed in the solenoid on the stand where a free induction decay (FID) is taken.

Radiation damping, if present, can lead to distortion in hyperpolarised ^{129}Xe FIDs, decreasing accuracy of Xe polarimetry. Radiation damping was investigated by observing T_2^* changes with successive pulses for different flip angles. The spherical container on the clinical polariser used in ref. [52] with higher B_0 homogeneity, and as such longer T_2^* , was used along with 100% enriched Xe (86% ^{129}Xe) samples collected following cryogenic separation after SEOP. No significant change in T_2^* was observed for flip angles up to 90° . Given the small number of pulses used (typically one 90° pulse) and short T_2^* , radiation damping effects did not have a noticeable effect on any of the recorded hyperpolarised ^{129}Xe FIDs.

Flip-angle calibration measurements were performed with 100% enriched Xe (86% ^{129}Xe) samples, in order to maximise NMR sensitivity when using low flip angles. Subsequent acquisitions with a 90° flip angle used lean gas mixture (3% enriched Xe) samples to reduce time and gas mixture usage. 100% enriched Xe samples were collected whilst under-flow for $Q = 2\text{NLPM}$ in the cryo-trap, during a 2 min freeze out. Lean Xe gas samples were dispensed directly from the SEOP cell into an evacuated tedlar bag, and then into the evacuated sampling container. The tedlar bag allows the sampling container pressure to be maintained at 1 atm during filling, without depolarising which can be caused by pressure regulator valves. Once the sampling container is filled, it is sealed, disconnected from the gas manifold and placed on the Xe polarimetry stand, inside the solenoid coil. For ^1H acquisitions, a twin container was filled with $\sim 10\text{ mM}$ of CuSO_4 to reduce the T_1 to allow thermal averaging with 400ms repetition times (TR) [99]. ^1H acquisitions with TR= 1 s and 400 ms were found to give consistent signal values, meaning that TR= 400 ms was sufficiently long for full longitudinal magnetisation recovery necessary for accurate signal measurements following thermal averaging.

NMR spectrometer

A home-built NMR spectrometer was used for acquisitions [140], as shown in Fig. 5.11. Some modifications were implemented in order to improve signal strength for ^1H acquisitions, namely (i) an updated DAQ card with a 2MHz sampling rate was used (National Instruments NI 6361) and (ii) a pre-amplifier (Stanford Research Systems SR560 Low-noise Voltage Preamplifier) and duplexer shown in Fig. 5.12, developed by Antonacci et al. [136]. The amplifier was set to a gain of 1000. Uncertainty in amplifier gain linearity is mitigated by using the same amplifier gain for ^{129}Xe and ^1H acquisitions. The dynamic range of the DAQ was set to match the expected signal, avoiding

saturating the DAQ and reducing noise. The amplifier gain is limited by the maximum output signal of the amplifier and the dynamic range of the DAQ. Timing of the acquisition process is performed via the internal trigger of the DAQ card. Parnell et al. [140] timed the transmit pulse and receive channel to begin successively and confirmed the synchronisation. Here, a pre-amplifier blanking pulse was included within this synchronisation, as shown in Fig. 5.13. Preamp blanking delay times up to 16 ms were achieved and 4 ms was typically used, which is sufficiently long for the transmit pulse width and coil ring down to occur in our setup with the acquisition parameters used. The spectrometer interface is shown in Fig. 5.14.

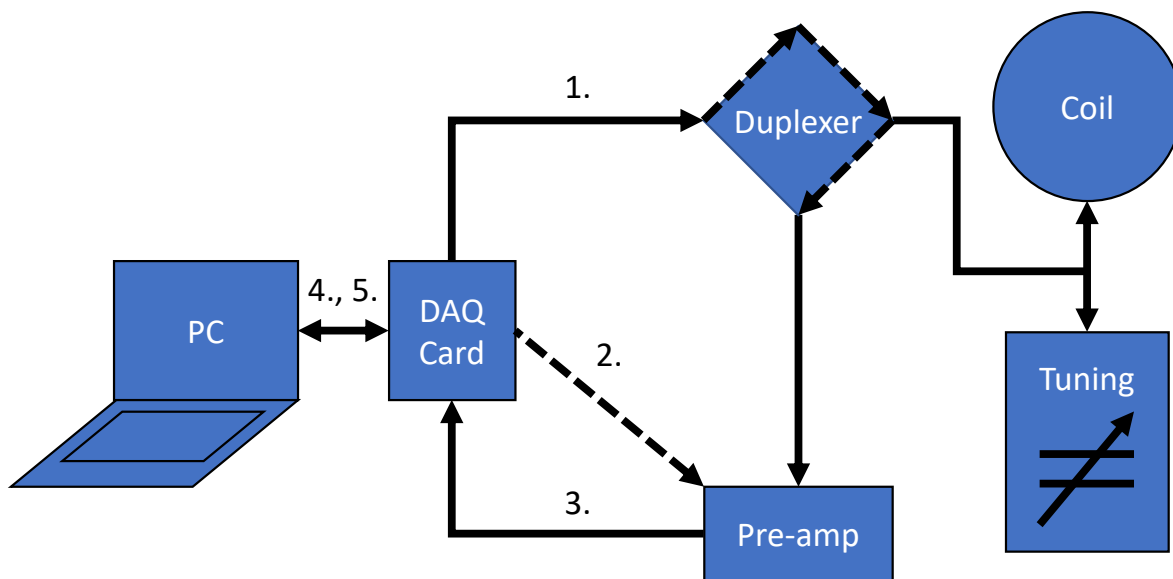


Figure 5.11: Diagram of the NMR circuit and FID acquisition, inspired by ref. [136]. **1.** Excitation pulse controlled by the PC is output by the DAQ card. **2.** Blanking pulse during this time isolates receiver pre-amp from the excitation pulse and coil ringdown. **3.** NMR signal from the coil is amplified through the pre-amp and read by the DAQ card. **4.** Demodulation and low-pass filter applied. **5.** Display or output FID for FID fitting to determine parameter values.

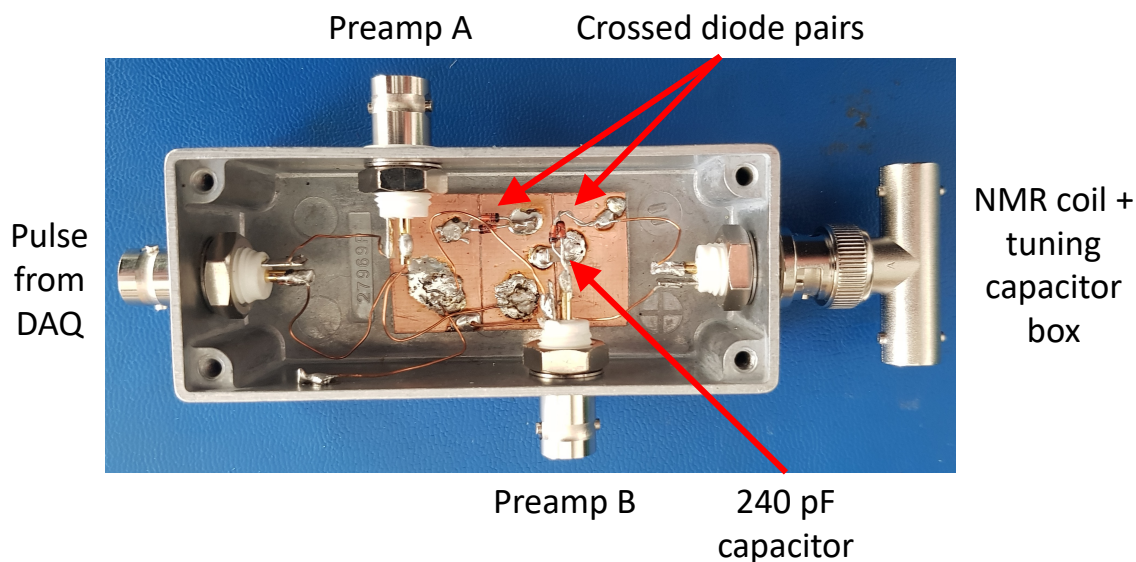


Figure 5.12: Duplexer inside aluminium housing, as designed by Antonacci et al. [136].

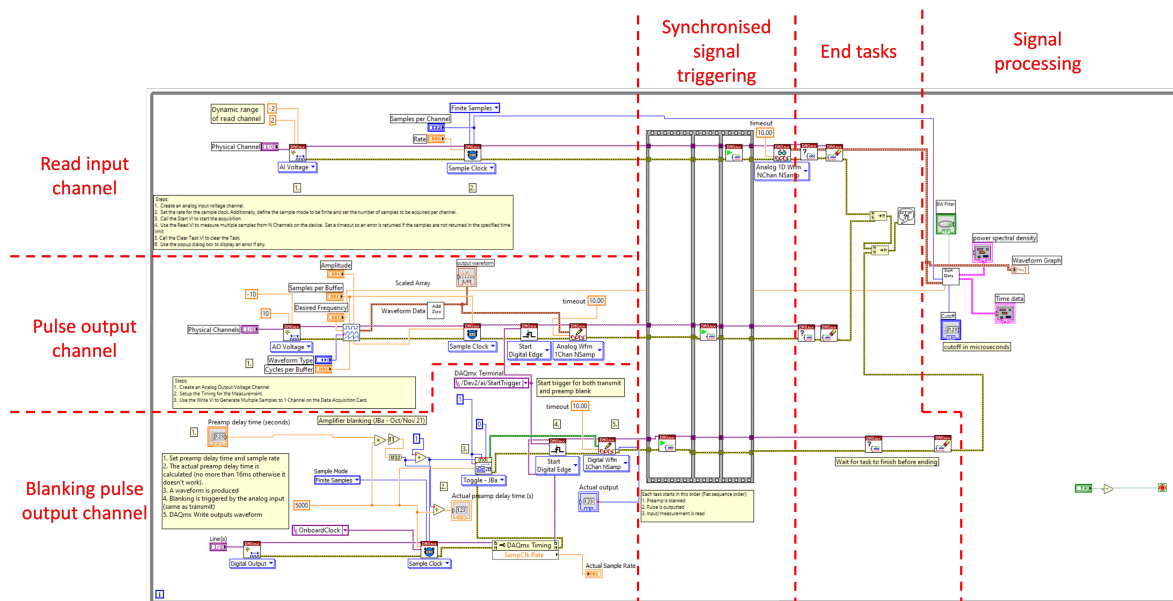


Figure 5.13: Screenshot of the block view of the NMR spectrometer program, developed in Labview (National Instruments), showing the blanking output for the pre-amplifier, which was added to the existing program.

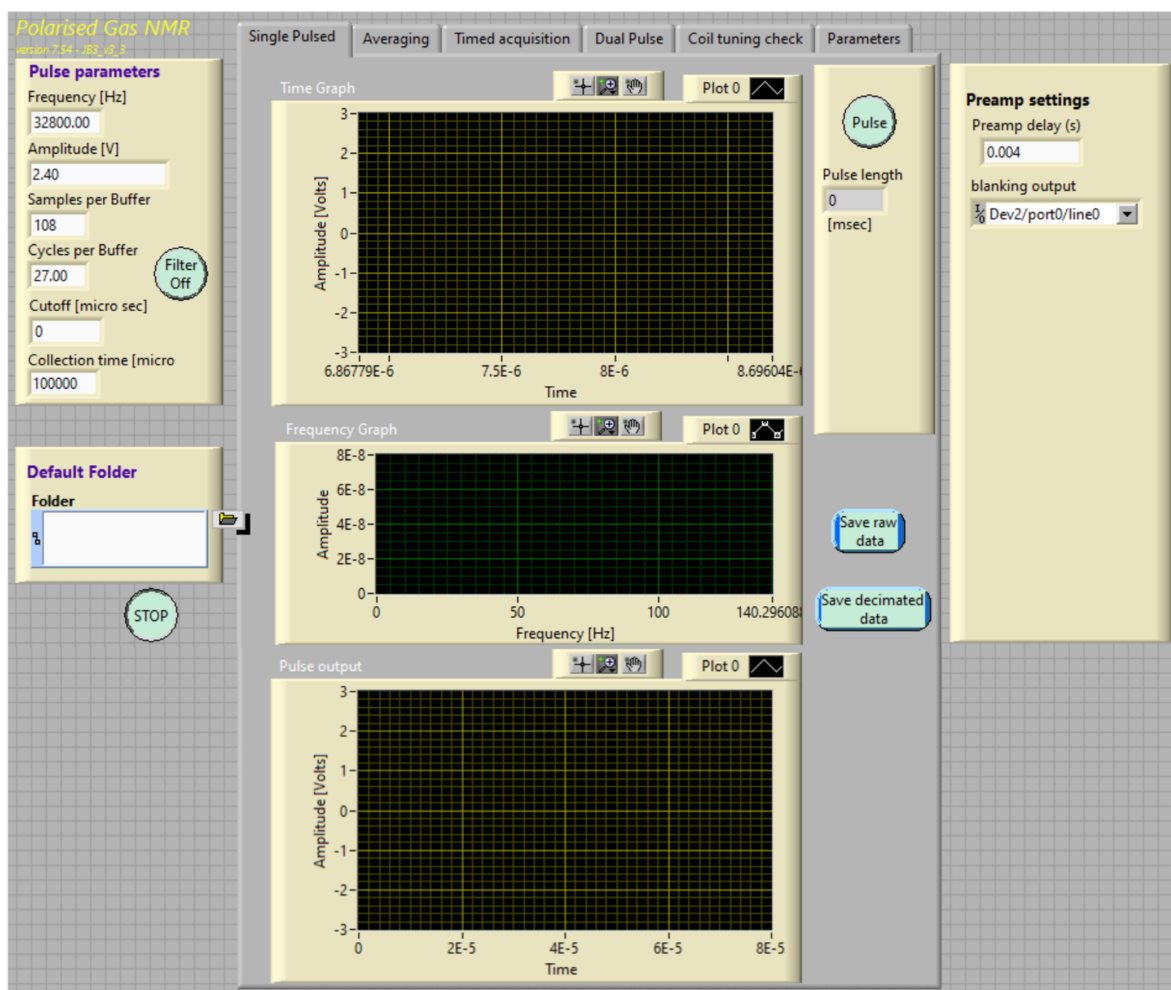


Figure 5.14: Screenshot of the NMR spectrometer user interface.

Xe polarisation calculation

^{129}Xe polarisation was measured by dispensing the flowing gas into the cylindrical container (Fig. 5.10). This was then placed inside a solenoid NMR coil located within the polariser B_0 field for FID acquisition. The signal was then compared to a ^1H reference signal acquired at the same frequency (32.8 kHz), within an identical cylinder filled with CuSO_4 -doped water.

The ^{129}Xe polarisation is calculated as

$$P_{^{129}\text{Xe}} = P_{^1\text{H}} \cdot \frac{V_{^{129}\text{Xe}}}{V_{^1\text{H}}} \cdot \frac{\sin \alpha_{^1\text{H}}}{\sin \alpha_{^{129}\text{Xe}}} \cdot \frac{I_{^1\text{H}}}{I_{^{129}\text{Xe}}} \cdot \frac{[^1\text{H}]}{[^{129}\text{Xe}]} \cdot \frac{\gamma_{^1\text{H}}}{\gamma_{^{129}\text{Xe}}} \cdot C_{T_2^*}, \quad (5.1)$$

where $P_{^1\text{H}}$ is the thermal polarisation of sampled ^1H nuclei, which is given by Eq. 3.14. $[\text{H}]$ and $[\text{Xe}]$ are the nuclei number densities. α , I , γ and V are the flip angle, nuclear spin, gyromagnetic ratio and initial signal amplitude for each nucleus. V and T_2^* are determined by FID fitting, as shown in Figure 5.15. Differences in pulse length

and T_2^* are accounted for using $C_{T_2^*} = \exp\left[\left(\frac{T_{AQ}}{T_2^*}\right)_{^{129}\text{Xe}} - \left(\frac{T_{AQ}}{T_2^*}\right)_{^1\text{H}}\right]$. For the purposes of our spectrometer, the pulse-acquire delay, $T_{AQ} = T_{CO} - \tau$, where τ is the pulse width and $T_{CO} = 5\text{ms}$ is the cutoff time.

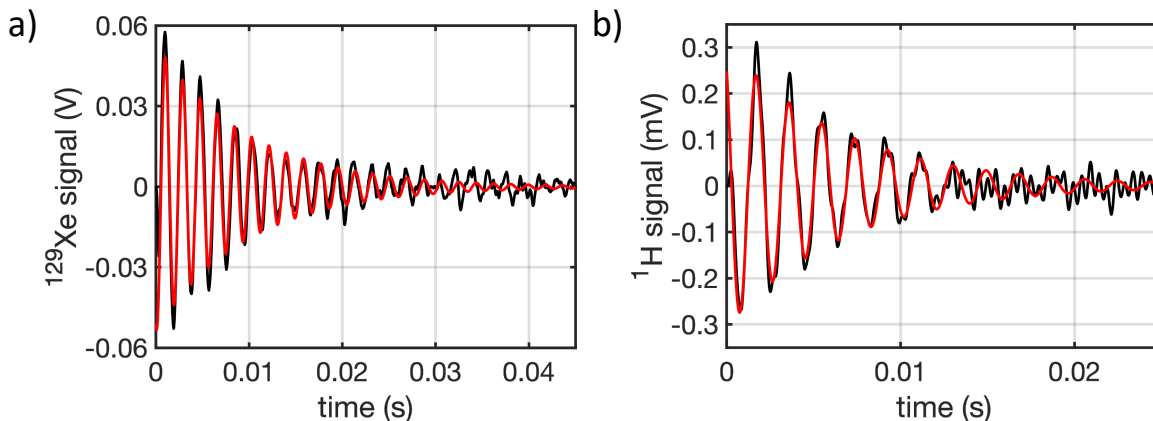


Figure 5.15: FIDs acquired on the polariser. The black line is the signal and the red line is the fitted FID. (a) 1 scan ^{129}Xe FID, with $V = 53.6\text{ mV}$ and $T_2^* = 9.76\text{ ms}$, using a pulse width of 0.89 ms . (b) 20,000 scan average ^1H FID, with $V = 0.307\text{ mV}$ and $T_2^* = 6.71\text{ ms}$, using a pulse width of 0.22 ms .

Laser absorption

Whilst AAS was used to measure regional $[\text{Rb}]$, laser absorption is proportional to the total amount of Rb vapour within the optical cell, or cell-averaged $[\text{Rb}]$, based on Eq. 3.78. Laser absorption measurements were performed by measuring the laser power at the back of the SEOP cell during continuous-flow SEOP and whilst at $20\text{ }^\circ\text{C}$ (i.e. $[\text{Rb}] = 0$) with a laser power meter (Gentec-EO UP55N-300F-H12-D0), as shown in Fig. 5.2.

5.2.3 Atomic absorption spectroscopy

$[\text{Rb}]$ was measured using AAS. This was performed using a similar setup to that described in previous work [82, 136, 141], as shown in Figure 5.16a. A 50W halogen bulb provided a broadband spectral light source from approximately 400 to 2200 nm, which was directed onto the SEOP cell with a beam width of 21.1 mm, transverse to the pump laser beam direction. Light is then collected by a 75 mm plano-convex lens (Thorlabs) and coupled to an optical fibre (OceanInsight) before being directed to the spectrometer (OceanInsight, model HR4000). Two spectrometers were used to observe Rb absorption lines in different frequency ranges, NIR and violet, at high resolution 7.8GHz to 16GHz and 34GHz to 78GHz respectively. The Rb D_1 ($5S_{1/2} \rightarrow 5P_{1/2}$) and D_2 ($5S_{1/2} \rightarrow 5P_{3/2}$) transitions, which lie within NIR, and the less attenuating

$5S_{1/2} \rightarrow 6P_{1/2}$ and $5S_{1/2} \rightarrow 6P_{3/2}$ transitions, which lie within violet, were probed. Transition properties are given in Table 3.3.

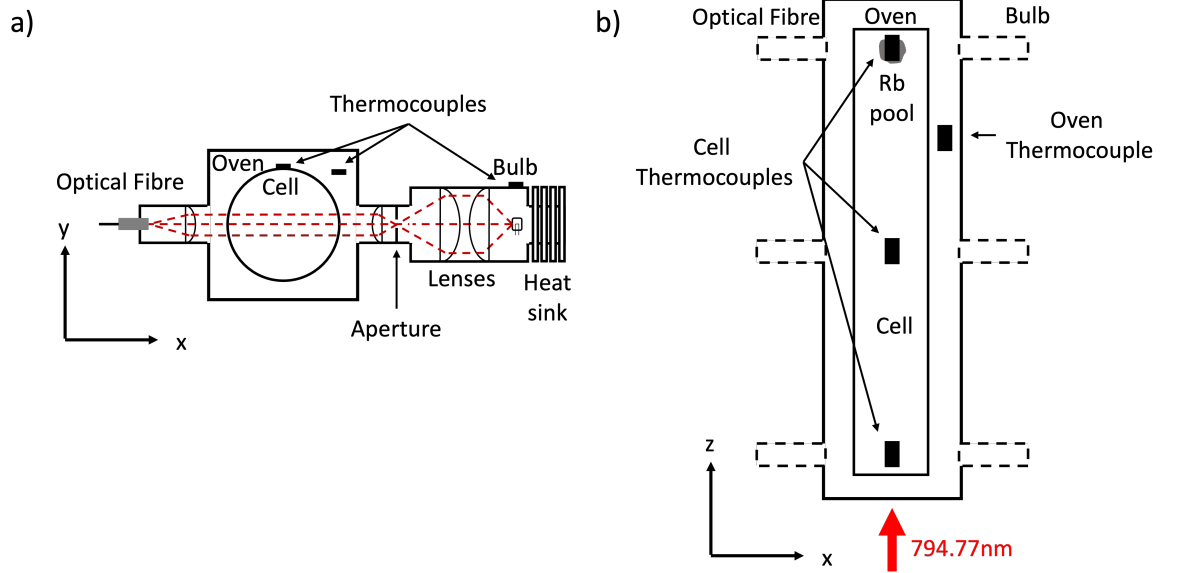


Figure 5.16: Experimental setup for AAS. (a) Optical setup consisting of a halogen bulb as the broad spectral light source. A thermocouple (OMEGA, model SA1XL K-type) is placed directly above the bulb on the housing to monitor bulb temperature and ensure the bulb has stabilised before measurements are taken. A series of plano-convex lenses ($f = 40$ mm, $f = 60$ mm, $f = 30$ mm) and aperture directs a parallel light beam onto the SEOP cell. A $f = 75$ mm plano-convex lens collects light and couples it to the optical fibre, which is connected to the spectrometer. (b) The optical setup was placed at 3 different positions along the length of the cell. At each position, cell temperature, T_{cell} , is measured by a thermocouple (OMEGA, model SA1XL K-type) adhered to the top of the external cell surface. Air passed through a heating element (OMEGA, model AHPF-122 1200W), controlled by a thermocouple (OMEGA, model SA1XL K-type) placed in the ambient oven space, regulates oven temperature, T_{oven} . The oven has three inlets for heated air, to maximise heated air coverage and oven temperature homogeneity across the cell. To ensure oven performance is not compromised, the oven port and lens tube fit compactly and the remaining oven ports are filled with ceramic plugs lined with insulation foam. The optics run on rails connected to the polariser chassis, ensuring precise optical alignment and fast re-positioning between oven ports. The direction of the optical pumping laser is shown, although this is switched off during AAS acquisitions to avoid emission due to energy pooling as mentioned in Section 5.2.4.

As described in Section 3.4, the absorbance spectra line shape has Gaussian and Lorentzian components due to Doppler and collisional broadening, respectively. Therefore, Pseudo-Voigt line shape fitting was applied to absorbance spectra $S(\nu)$ for each

transition, taking the form

$$S(\nu) + B = \ln \left(\frac{I_0(\nu)}{I(\nu)} \right) + B = A[\eta L(\nu) + (1 - \eta)G(\nu)] + B, \quad (5.2)$$

where η is the relation coefficient between $L(\nu)$ and $G(\nu)$, B is the baseline correction and A is the baseline corrected integral of $S(\nu)$ [106], as shown in Figure 5.17. $L(\nu)$ is the normalised Lorentzian,

$$L(\nu) = \frac{\Delta\nu/2\pi}{(\nu - \nu_0)^2 + \left(\frac{\Delta\nu}{2}\right)^2}, \quad (5.3)$$

and $G(\nu)$ is the normalised Gaussian,

$$G(\nu) = \frac{2}{\Delta\nu} \sqrt{\frac{\ln 2}{\pi}} \exp \left[-4 \ln 2 \left(\frac{\nu - \nu_0}{\Delta\nu} \right)^2 \right], \quad (5.4)$$

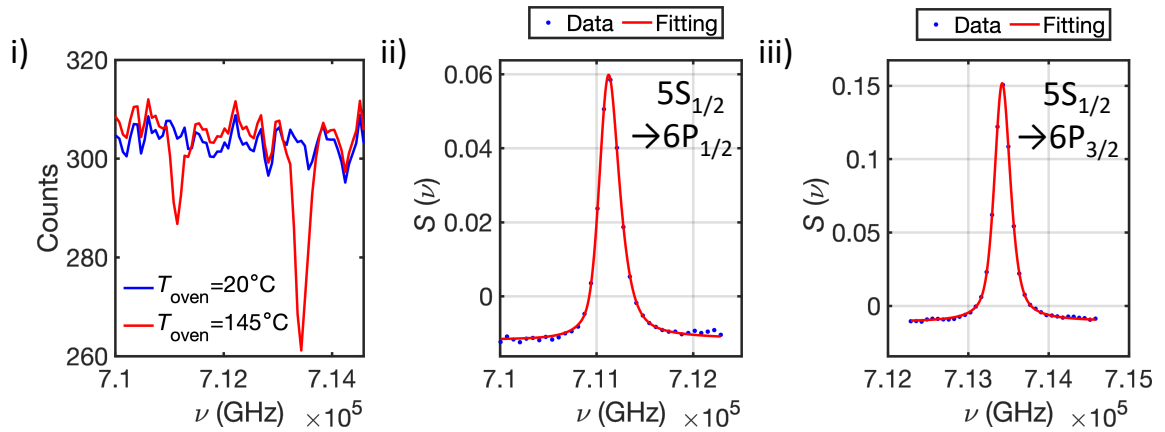
where ν_0 and $\Delta\nu$ are the temperature and pressure-dependent centre frequency and linewidth, respectively [82]. Line shape asymmetry is accounted for by defining $\Delta\nu$ as

$$\Delta\nu(\nu) = \frac{2\Delta\nu_0}{1 + \exp[a(\nu - \nu_0)]}, \quad (5.5)$$

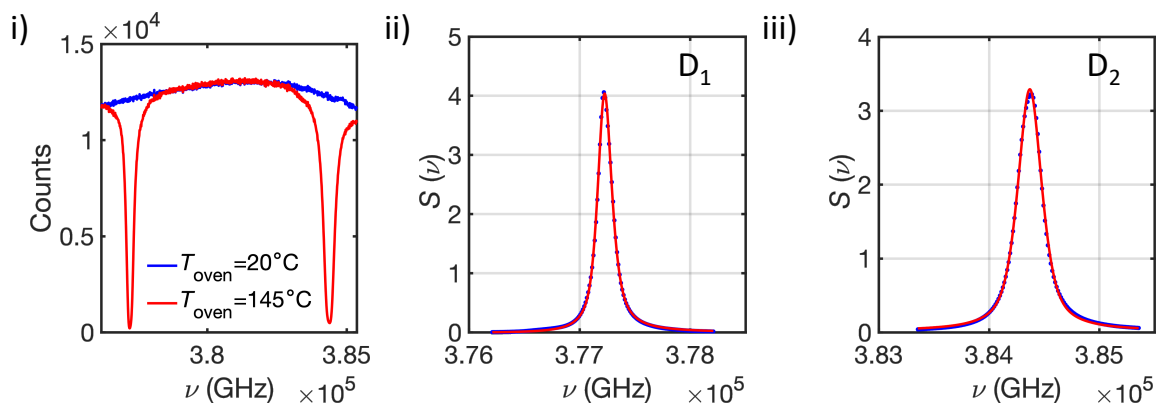
where a is the asymmetry parameter and $\Delta\nu_0$ is the symmetric FWHM (i.e. when $a = 0$) [106]. Differences in ^{85}Rb and ^{87}Rb absorption were not considered as ν_0 differences are smaller than $\Delta\nu$ (order 100GHz) for both near-IR (D_1 and D_2 , $|\nu_0^{85\text{Rb}} - \nu_0^{87\text{Rb}}| \sim 8\text{GHz}$ [62, 63]) and violet ($5^2\text{S}_{1/2} \rightarrow 6^2\text{P}_{1/2}$, $|\nu_0^{85\text{Rb}} - \nu_0^{87\text{Rb}}| = 110\text{MHz}$ and $5^2\text{S}_{1/2} \rightarrow 6^2\text{P}_{3/2}$, $|\nu_0^{85\text{Rb}} - \nu_0^{87\text{Rb}}| = 130\text{MHz}$ [142]) transitions. Using Eq. 3.117, 3.118, and 3.119, the Rb vapour density can then be calculated using

$$[\text{Rb}] = \frac{A}{\pi r_0 c f l}. \quad (5.6)$$

a) Above the Rb source (Beer-Lambert law holds)



b) Above the Rb source (Beer-Lambert law breakdown)



c) Far from Rb source (Beer-Lambert law holds)

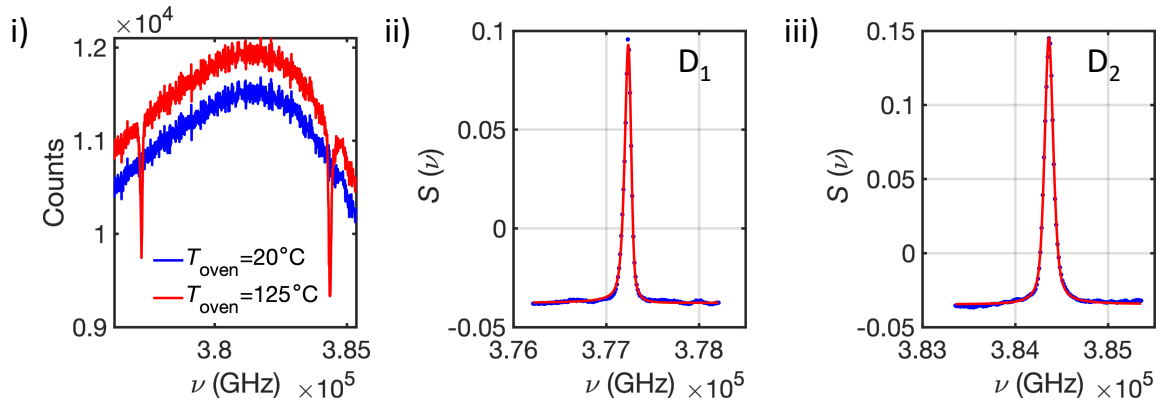


Figure 5.17: Example absorption spectra. **(ai)** Violet and **(bi)** NIR spectra acquired with the 1g Rb cell (Figure 5.8a), at cell position = 75.5cm, above the Rb source, at oven temperature, $T_{\text{oven}} \sim 20^\circ\text{C}$, $I_0(\nu)$ (blue) and $T_{\text{oven}} = 145^\circ\text{C}$, $I(\nu)$ (red). Corresponding pseudo-Voigt fitted absorbance spectra for the $5S_{1/2} \rightarrow$ **(aaii)** $6P_{1/2}$, **(aiii)** $6P_{3/2}$, **(bii)** $5P_{1/2}$ (D_1), **(biii)** $5P_{3/2}$ (D_2) transitions. Due to the high optical thickness for D_1 and D_2 absorption (deviation from the Beer-Lambert law), the line shape becomes less well defined and the quality of the fit worsens. **(c)** Example of NIR spectra acquired at cell position = 3.5cm, away from the Rb source, at $T_{\text{oven}} \sim 20^\circ\text{C}$ $I_0(\nu)$ (blue) and $T_{\text{oven}} = 125^\circ\text{C}$, where low [Rb] is observed (the Beer-Lambert law is obeyed).

The curvature of the SEOP cell leads to small changes in the path length of the probe beam off-centre of the cell. A fixed path length must be used for AAS as variation in the path length leads to systematic errors in the measured absorbance, as described in Section 3.4.1. Given that the geometry of the cell is fixed, and that the beam width must be balanced with the need for high signal, the variability in path length was evaluated. The path length is defined as the mean path length calculated from the chord in a circle as

$$\bar{l} = \frac{1}{r_b} \int_0^{r_b} 2\sqrt{(r_{\text{cell}}^2 - x^2)} dx. \quad (5.7)$$

Carrying out the integral in Equation (5.7) gives

$$\bar{l} = \frac{r_{\text{cell}}^2}{r_b} \arcsin\left(\frac{r_b}{r_{\text{cell}}}\right) + \sqrt{(r_{\text{cell}}^2 - r_b^2)}, \quad (5.8)$$

where r_b is the probe light beam radius and r_{cell} is the internal SEOP cell radius. For our setup, $r_b = 10.55\text{mm}$, $r_{\text{cell}} = 37.5\text{mm}$, so Eq. 5.8 gives $\bar{l} = 74\text{mm}$. The minimum path length sampled is only 4% shorter than the maximum path length, and the mean path length is 1.4% shorter than the maximum path length.

5.2.4 Acquisition procedure

A total acquisition time of 2 minutes was used for the violet spectrometer and 1 minute for the NIR spectrometer. The integration time was adjusted to closely match the dynamic range of the spectrometer, whilst being careful to avoid signal saturation. This was typically 20 ms with 6000 scan averages for violet acquisitions and 4 ms with 15000 scan averages for NIR spectra. Background spectra with the bulb switched off were also taken on the same day as cold and hot cell spectra. These were subtracted from the hot and cold spectra to reduce systematic uncertainties in absorbance measurements.

AAS spectra were acquired with the optical pumping laser switched off to avoid any possible emission due to energy pooling [143], as observed in NIR AAS of Rb during Rb- ^{129}Xe SEOP by Kelley and Branca [100]. With the pump laser off, laser heating would no longer be present, leading to changes in $[\text{Rb}]$ over time. To minimise $[\text{Rb}]$ distribution changes, the cell was closed during AAS acquisitions. This also limited the total acquisition time, limiting scan averages. Absorption spectra with an $\text{SNR} < 8$ were not included due to $> 20\%$ mean absolute percentage error determined from fitting known synthetic spectra, as detailed in Section 5.2.5, and results presented in Section 5.3.2.

$[\text{Rb}]$ measurements were performed on a closed cell in the absence of the optical pumping laser, for a range of oven temperatures, T_{oven} , in order to identify the range of accurate $[\text{Rb}]$ measurement for each absorption line. The cell was filled with 3% enriched Xe (86% ^{129}Xe), 10% N_2 , balanced with He for a total gas pressure, $p = 1.47$ bar at 20°C , which is

equivalent to the same number density for 2 bar at 125°C (nominal running conditions²). The cell containing 1g Rb in the main body of the cell was used, and AAS was performed with the probe beam positioned at the back of the cell, cell position = 75.5 cm, directly above the Rb source where [Rb] build up is expected to be greatest. Measurements were performed when oven and cell temperature measured at the Rb source where stable ($\leq 0.1^\circ\text{C}/\text{min}$). Time dependent changes in [Rb] were not measured.

For [Rb] measurements at different cell positions during continuous-flow SEOP, a flow rate of 2NLPM (normal litres per minute for conditions $T = 20^\circ\text{C}$ and $p = 1\text{ atm}$) at 2 bar was used. The SEOP cell was opened to allow gas flow and the power meter reading and cell temperatures, T_{cell} , from separate thermocouples (OMEGA, model SA1XL K-type) adhered to the top of the external cell surface (see Fig. 5.16), were recorded. The presaturator thermocouple (OMEGA, model SA1XL K-type) was positioned on the top surface of the presaturator that is within the back oven compartment, near the presaturator to main cell body junction. After 3 min, a small amount of gas was dispensed to measure P_{Xe} . The cell was then closed, the pump laser was powered off and violet ($5S_{1/2} \rightarrow 6P_{1/2}$ and $5S_{1/2} \rightarrow 6P_{3/2}$) absorption spectra were recorded. Immediately afterwards, the optical fibre was swapped from the violet spectrometer to the NIR spectrometer to record D_1 and D_2 absorption spectra.

5.2.5 Accuracy of AAS fitting at low SNR

In order to assess the accuracy of the AAS fitting routine, synthetic violet AAS spectra were produced. Voigt profiles were produced using Equation (5.2), with parameters $A_S = 22$, $a_S = -0.001\text{ GHz}^{-1}$, $B_S = 0$, $\Delta\nu_{0,S} = 212\text{ GHz}$, $\eta_S = 0.7$, $\nu_{0,S} = 711,134\text{ GHz}$ for the $5S_{1/2} \rightarrow 6P_{1/2}$ transition and $A_S = 57$, $a_S = 0\text{ GHz}^{-1}$, $B_S = 0$, $\Delta\nu_{0,S} = 237\text{ GHz}$, $\eta_S = 0.7$, $\nu_{0,S} = 713,414\text{ GHz}$ for the $5S_{1/2} \rightarrow 6P_{3/2}$ transition. The frequencies used were the same as the spectrometer in order to match the resolution of the synthetic violet spectra to the measured violet spectra. Gaussian noise was then added to the exponential of the Voigt profiles using the MATLAB (MathWorks) function “awgn”. The resulting synthetic spectra are then generated by taking the natural log of the result, as shown in Figure 5.18.

²The higher operating cell pressure used in this Chapter compared to Chapter 6 was due to the xenon volume recovery losses observed in Section 6.3.4 being initially and wrongly thought to be an issue with the mass flow regulator operating at 1.25 bar.

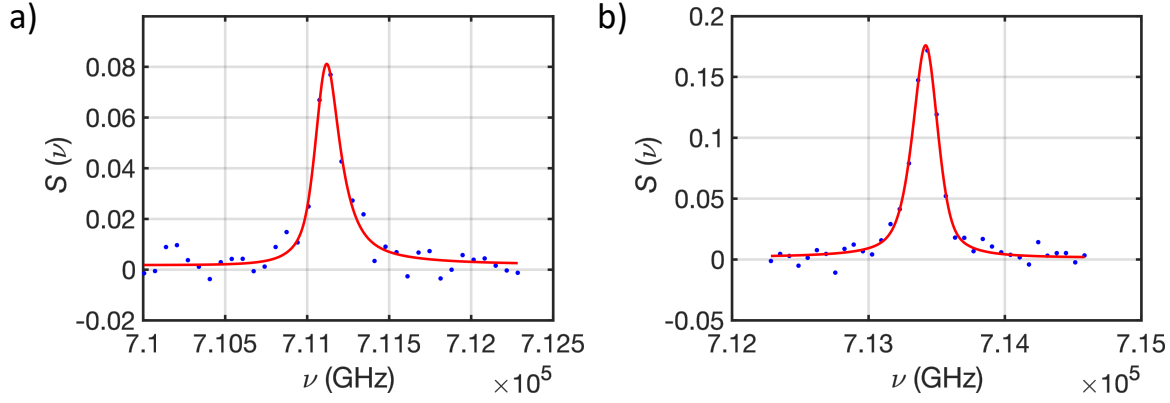


Figure 5.18: Example synthetic absorption spectra. (a) Voigt fitting parameters $A_F = 21.4246$, $a_F = -0.0032 \text{ GHz}^{-1}$, $B_F = 0.0018$, $\Delta\nu_{0,F} = 185.9509 \text{ GHz}$, $\eta_F = 0.8408$, $\nu_{0,F} = 711126 \text{ GHz}$, $M = 2.6154\%$, $\text{SNR} = 11.6648$ for the $5S_{1/2} \rightarrow 6P_{1/2}$ transition. (b) Voigt fitting parameters $A_F = 52.5141$, $a_F = 8.3817 \times 10^{-4} \text{ GHz}^{-1}$, $B_F = 0.0018$, $\Delta\nu_{0,F} = 221.2552 \text{ GHz}$, $\eta_F = 0.6765$, $\nu_{0,F} = 713415 \text{ GHz}$, $M = 7.87\%$, $\text{SNR} = 26.0774$ for the $5S_{1/2} \rightarrow 6P_{3/2}$ transition.

Different amounts of Gaussian noise were added to vary the signal-to-noise ratio (SNR) in each i absorbance spectrum, over n repeats. Pseudo-voigt fitting was then applied to calculate the integral, $A_{F,i}$, and the mean absolute percentage error was then calculated as

$$M = \frac{100\%}{n} \sum_{i=1}^n \left| \frac{A_{S,i} - A_{F,i}}{A_{S,i}} \right|, \quad (5.9)$$

where $A_{S,i}$ is the actual integral of the absorption line.

5.2.6 Spin-exchange cross section

The ability to measure [Rb] directly should improve the accuracy of γ' and Γ' determined from spin-up ($\Gamma_{\text{up}} = \gamma'_{(P_{\text{Rb}} > 0)}[\text{Rb}] + \Gamma'$) or spin-down ($\Gamma_{\text{down}} = \gamma'_{(P_{\text{Rb}} = 0)}[\text{Rb}] + \Gamma'$) measurements. While Γ' is primarily governed by cell wall relaxation, and can therefore determine the condition of the cell wall in terms of polariser performance, γ' should be a constant for fixed running conditions, and can be compared to the theoretical framework derived from the literature outlined in Section 3.3. The P_{Rb} dependence of γ'_{vdW} leads to differing γ' whether Γ_{up} or Γ_{down} measurements are performed. Γ_{down} is measured for $P_{\text{Rb}} = 0$ conditions, whilst Γ_{up} is measured for $P_{\text{Rb}} > 0$. Γ_{up} measurements require the pumping laser to be on, which would impact simultaneous AAS; consequently, these measurements were not performed.

At each T_{oven} , the centre of the SEOP cell was probed with AAS, directly below the NMR coil, to measure [Rb]. Once sufficient ^{129}Xe polarisation build up had occurred,

the pump laser diode was switched off and in-cell NMR acquisitions were taken periodically (TR=30 to 90s, 11 pulses per acquisition with the exception of the lowest [Rb] where 21 pulses were used) during ^{129}Xe relaxation. Where the acquisition was sufficiently long, mean [Rb] values were calculated from measurements taken at the start and end of each acquisition, in order to account for any changes in [Rb] during this time. Once complete, initial amplitudes, including correction for T_2^* relaxation during the pulse-acquire delay, were fitted to exponential decay in order to calculate Γ_{down} .

5.3 Results and Discussion

5.3.1 ^{129}Xe polarimetry

Flip angle calibration

^{129}Xe flip angles, $\alpha_{^{129}\text{Xe}}$, were measured with multiple pulses with TR= 1s (TR $\ll T_1$), so that RF destruction is the sole contribution to the decrease in signal between pulses, and fitted to $\ln [V_{^{129}\text{Xe}}(n) / V_{^{129}\text{Xe}}(n = 1)] = (n - 1) \cdot \ln [\cos(\alpha_{^{129}\text{Xe}})]$, where $V_{^{129}\text{Xe}}$ is the initial signal amplitude found using FID fitting and n is the pulse number. Due to the heterogeneous B_1 across the sample when using the cylindrical sampling container, flip angle measurements using RF destruction could not be performed directly on this container, however B_1 homogeneity was sufficient across the spherical container, shown in Fig. 5.9, to perform flip angle calibration measurements. For a fixed pulse amplitude of 2.4 V, a pulse width of 0.74 ms produced a flip angle closest to 90° , as shown in Figure 5.19. A pulse width of 0.89 ms, which gives a flip angle of 75.5° , was mistakenly used for measurements in this Chapter. As such, a correction factor of $\sin 90^\circ / \sin 75.5^\circ = 1.0329$ was multiplied to the calculated ^{129}Xe polarisation values.

^1H flip angle calibration was performed by taking pulse averaging scans for different pulse lengths. Initial amplitudes were then calculated from FID fitting, and then a correction factor applied to account for T_2^* relaxation during the pre-acquisition delay. Due to the low SNR of ^1H acquisitions, the cylindrical container was used for these measurements. During ^1H measurements, the number of pulses was scaled by $\frac{20,000}{\sqrt{\sin(\alpha_{^1\text{H}}/90^\circ)}}$, where $\alpha_{^1\text{H}}$ is the expected flip angle to maintain the same SNR. For a fixed pulse amplitude of 2.4 V, a pulse width of 0.22 ms produced the highest amplitude signal, corresponding to $\alpha_{^1\text{H}} = 90^\circ$, as shown in Figure 5.20. The ratio of the ^{129}Xe and ^1H pulse widths $\tau_{^{129}\text{Xe}}/\tau_{^1\text{H}} = 3.4$, which is slightly smaller than the ratio of the gyromagnetic ratios $\gamma_{^1\text{H}}/\gamma_{^{129}\text{Xe}} = 3.6$. This is due to the step size of the pulse width setting for 32.8kHz equal to 0.0305ms, which may introduce a small systematic

uncertainty due to V_{1H} being recorded at a flip angle slightly greater than 90° , leading to over prediction of P_{Xe} . We expect this to be only 0.6%. In future, lowering the pulse amplitude would improve the relative precision in determining 90° pulse widths and reduce the likelihood of introducing this systematic uncertainty.

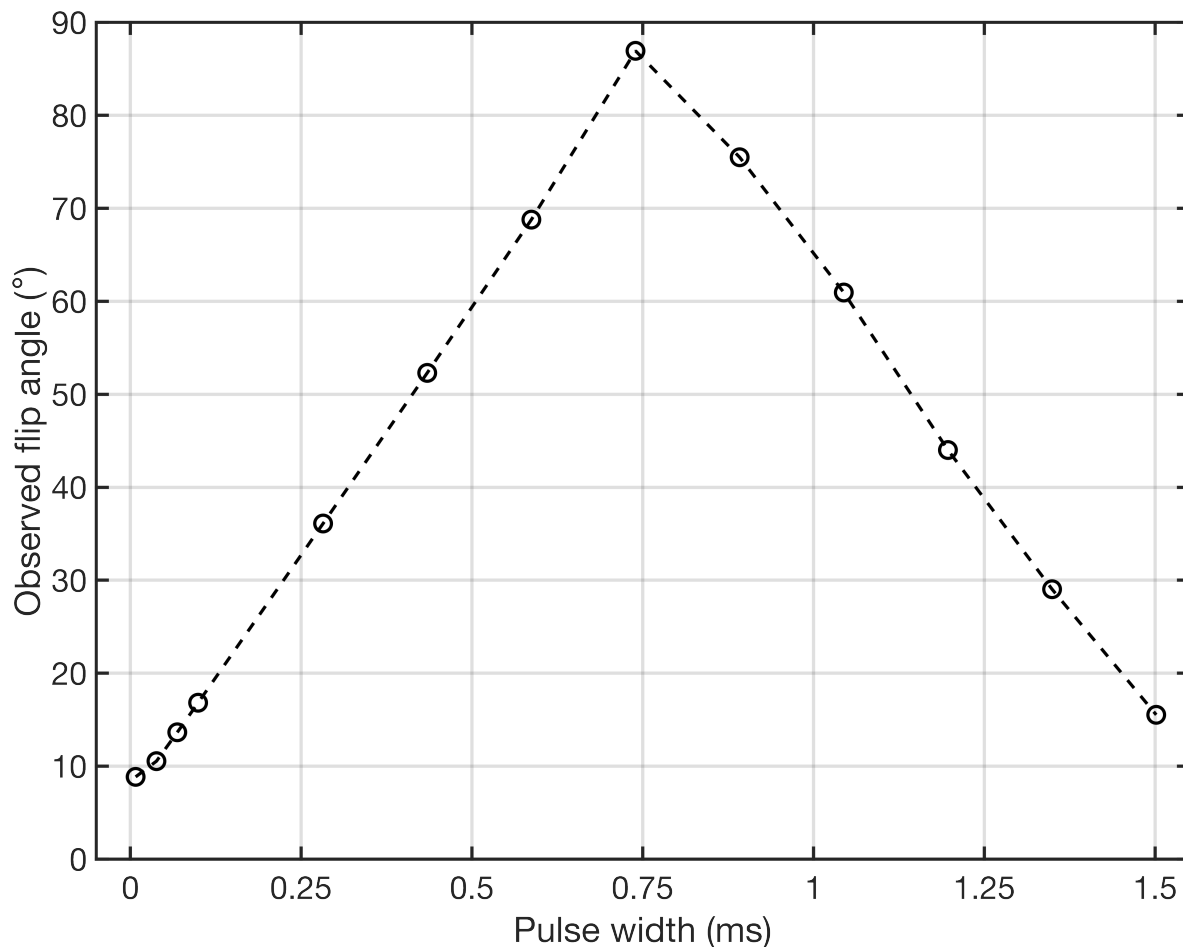


Figure 5.19: ^{129}Xe flip angle measurements for an amplitude of 2.4 V, at 32.8 kHz. Note that the observed flip angle is always $\leq 90^\circ$, as opposed to the true flip angle which can take any value. The observed and true flip angles are equal to 90° at the shortest pulse width that produces a 90° observed flip angle. Dashed lines are to guide the eye only.

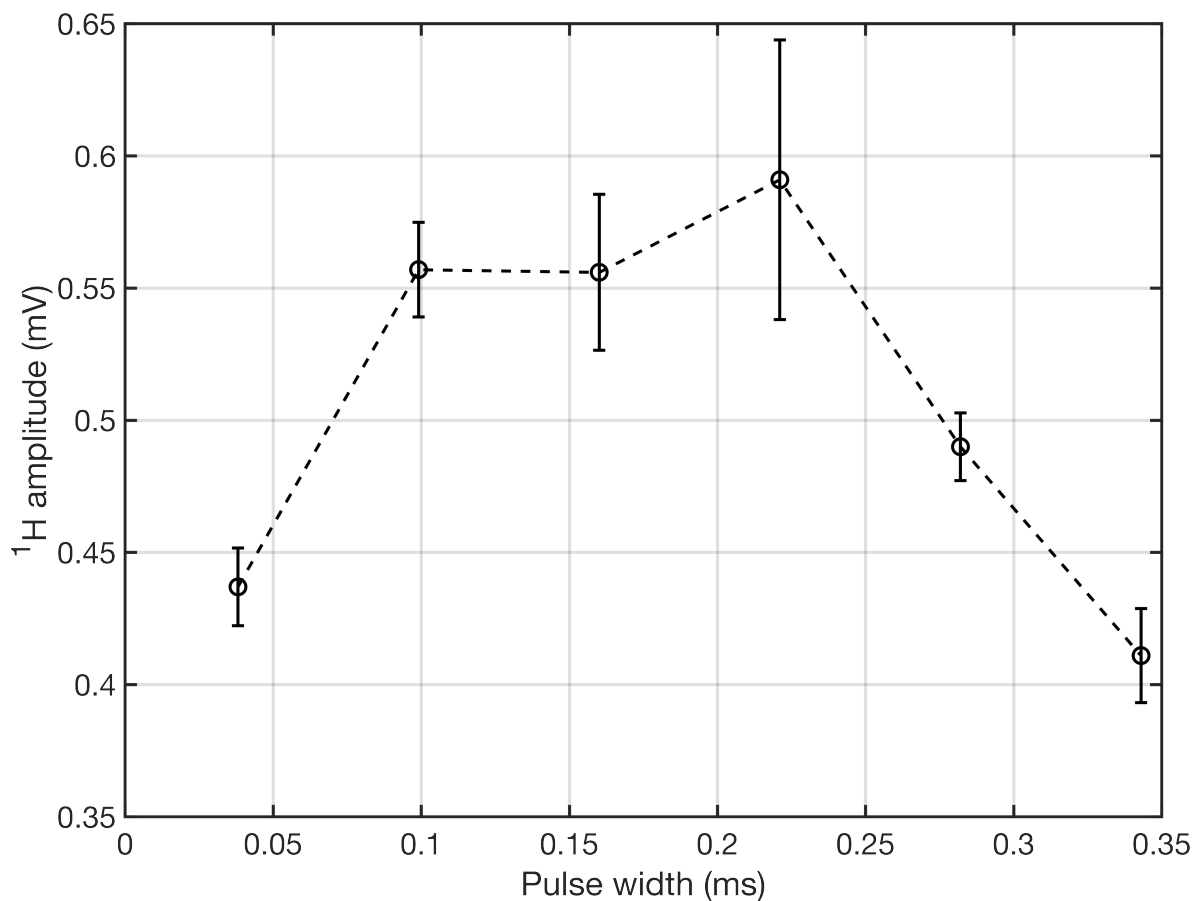


Figure 5.20: ^1H amplitude vs pulse width for a pulse amplitude of 2.4 V, at 32.8 kHz. Dashed lines are to guide the eye only.

Confirmation with 1.5T NMR measurements

In order to confirm the accuracy of the ^{129}Xe polarisation values measured on the polariser, ^{129}Xe polarisation was simultaneously measured on the 1.5T MRI scanner, as shown in Fig. 5.21.

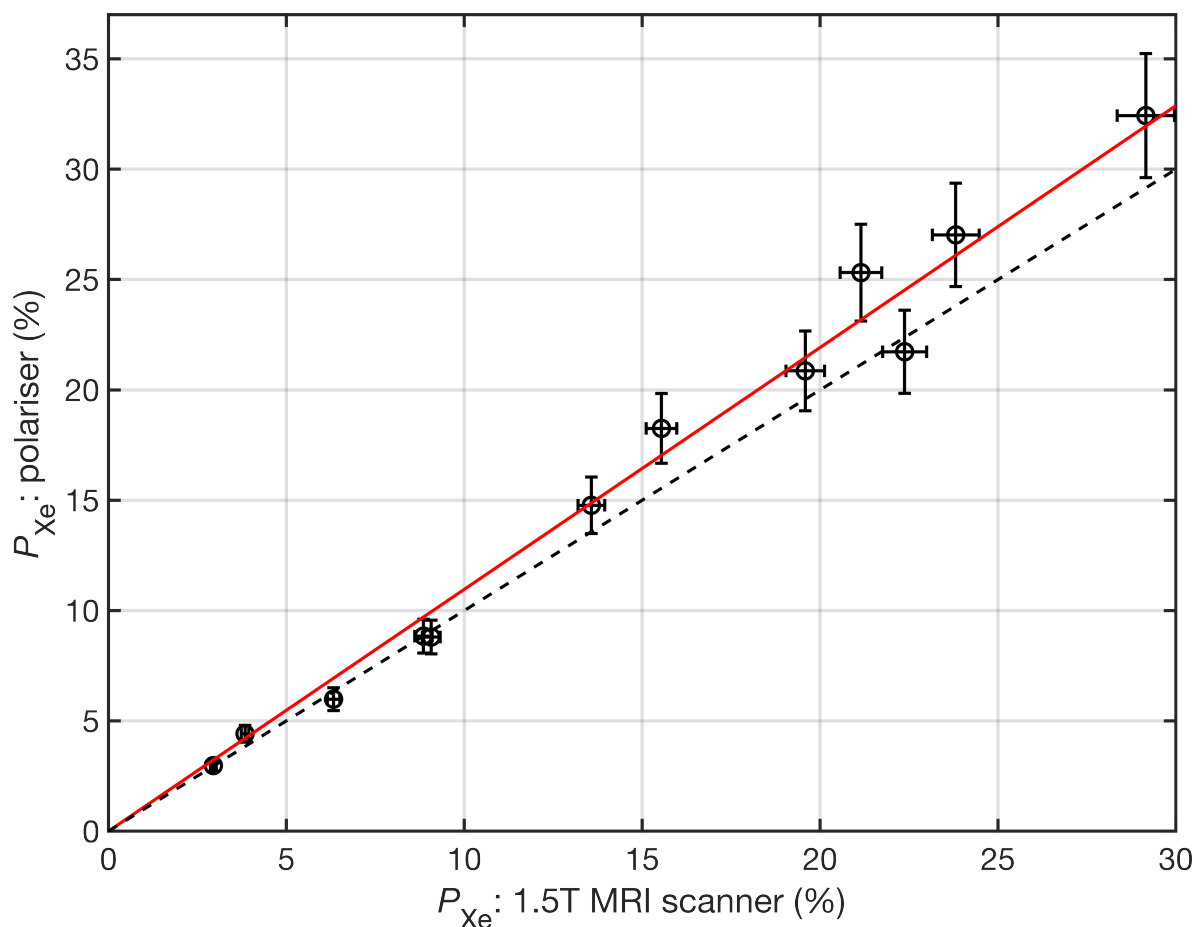


Figure 5.21: ^{129}Xe polarisation measured on the polariser ($P_{\text{Xe}}^{\text{pol}}$) vs on the MRI 1.5T scanner ($P_{\text{Xe}}^{\text{sc}}$). $P_{\text{Xe}}^{\text{pol}} = m * P_{\text{Xe}}^{\text{sc}}$ was fitted where $m = 1.10 \pm 0.02$, $R^2 = 0.9825$ (red). The dashed line indicates $P_{\text{Xe}}^{\text{pol}} = P_{\text{Xe}}^{\text{sc}}$, highlighting the gradient offset that may be the result of depolarisation between the polariser and the 1.5T scanner. The data points represent single measurements. The uncertainty in $P_{\text{Xe}}^{\text{pol}}$ is dominated by the uncertainty in ^1H amplitude. The uncertainty in $P_{\text{Xe}}^{\text{sc}}$ was determined separately as the standard deviation in repeat measurements on the 1.5T scanner from a single Xe sample from the polariser.

Figure 5.21 shows fair agreement between ^{129}Xe polarisation calculated by both methods over a range of ^{129}Xe polarisations. The higher Xe polarisations measured on the polariser compared to the 1.5T MRI scanner may be due to depolarisation between the polariser and the 1.5T MRI scanner, as the Xe sample travels through background magnetic field gradients.

5.3.2 Accuracy of AAS fitting

Synthetic violet spectra were produced and fitted to Voigt profiles. For each absorption line and fixed amount of added Gaussian noise, $n = 200$ repeats were performed. M

and mean SNR were then calculated, as shown in Figure 5.22.

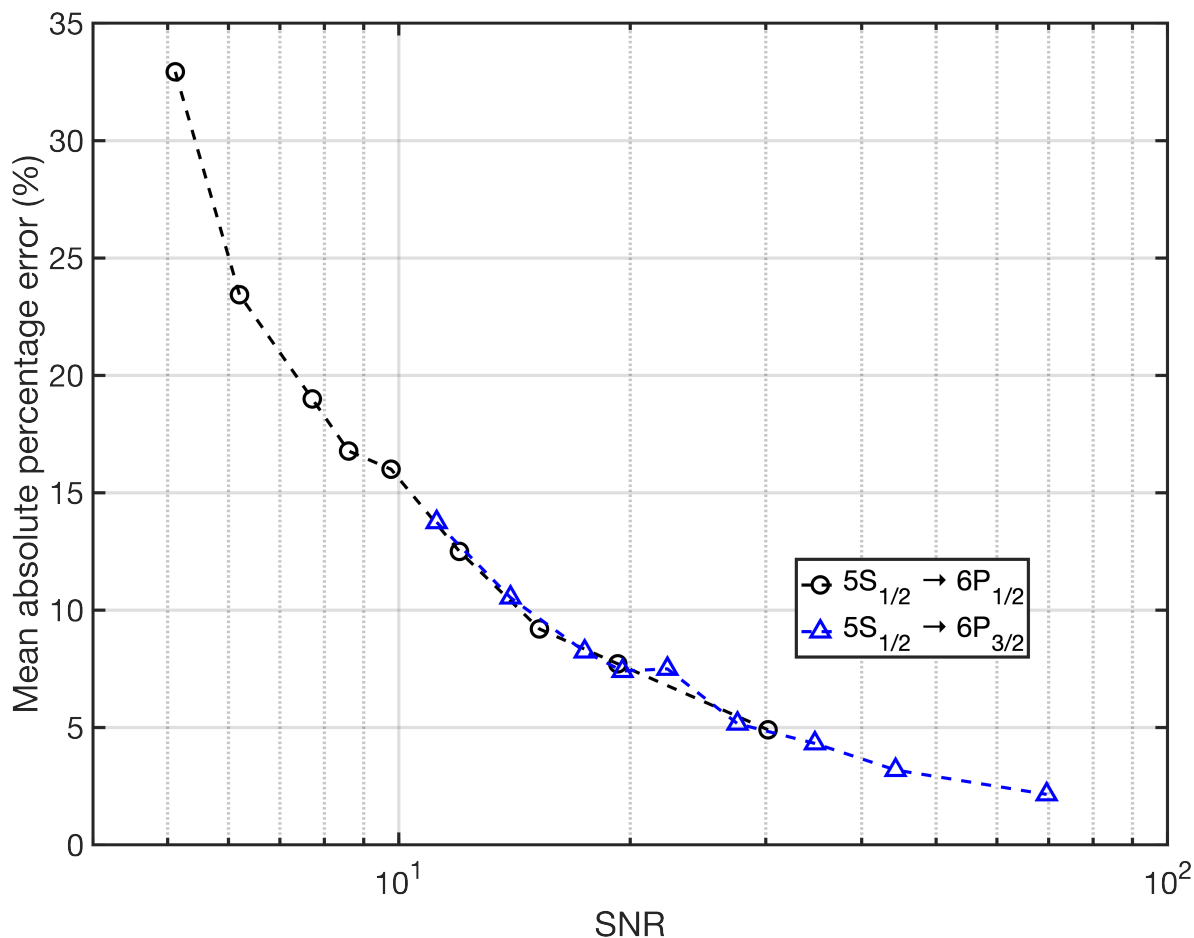


Figure 5.22: Mean absolute percentage error, M , vs signal-to-noise ratio (SNR) for $5S_{1/2} \rightarrow 6P_{1/2}$ (black circles), $6P_{3/2}$, (blue triangles) for $n = 200$ repeats. Dashed lines are to guide the eye only.

Figure 5.22 shows $\text{SNR} = 8$ corresponds to a mean absolute percentage error $\sim 20\%$. Therefore, violet spectra with $\text{SNR} < 8$ are not included in this work.

5.3.3 Closed cell Rb density for different oven temperatures

[Rb] measurements to identify the range of accurate [Rb] measurement are shown in Fig. 5.23. Three measurements were made at each T_{oven} . N.B. these measurements are not true repeats as they were performed successively at stable T_{oven} .

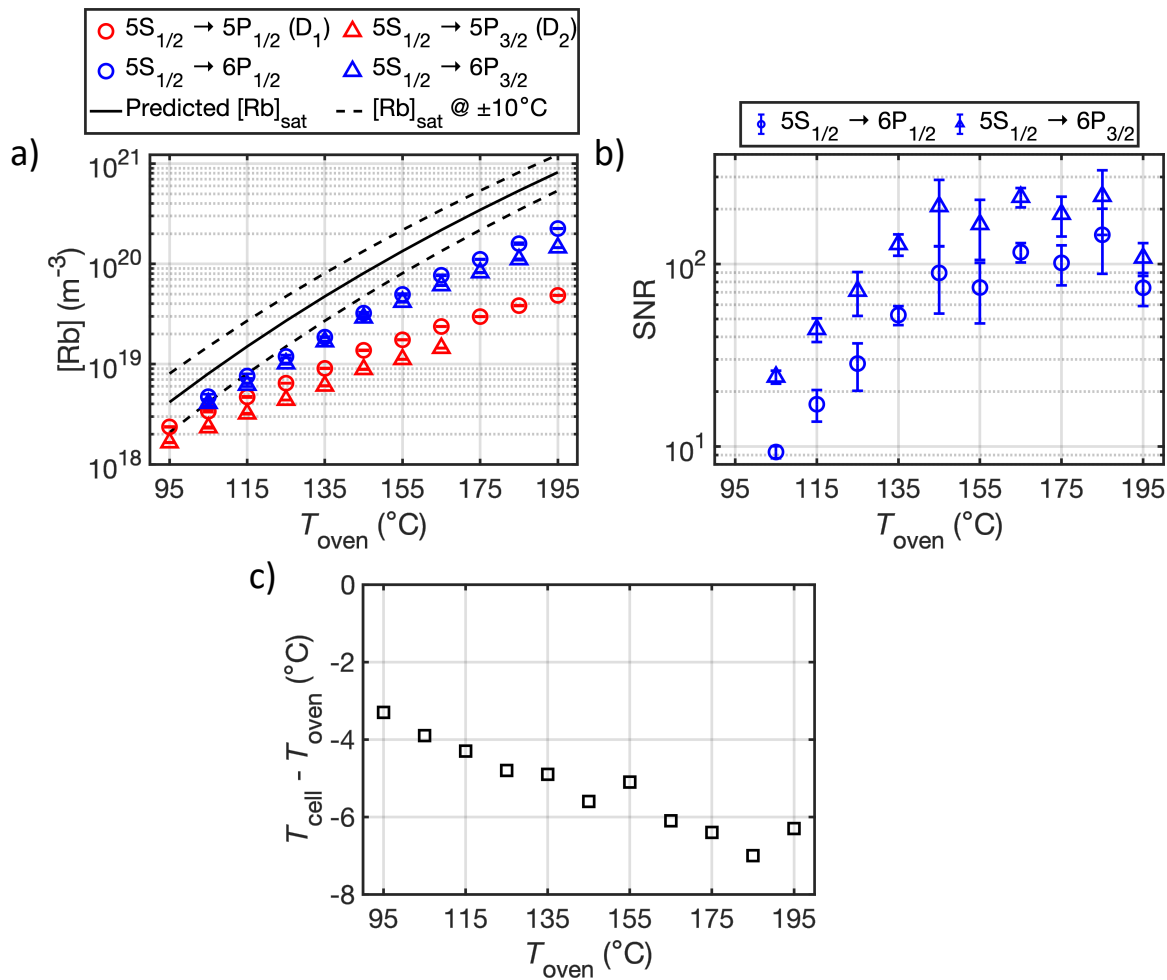


Figure 5.23: (a) Rb density, $[\text{Rb}]$, measured from the $5S_{1/2} \rightarrow 6P_{1/2}$ (blue circles), $6P_{3/2}$ (blue triangles), $5P_{1/2}$ (D₁) (red circles) and $5P_{3/2}$ (D₂) (red triangles) transitions vs T_{oven} . The black line is saturation Rb density, $[\text{Rb}]_{\text{sat}}$, calculated based on T_{oven} (see Table 3.1) and dashed lines indicate $T_{\text{oven}} \pm 10^{\circ}\text{C}$. (b) Corresponding SNR for violet absorbance spectrum. SNR in D₁ and D₂ absorbance spectra was high (> 100) and so was not included. (c) Difference in cell temperature, T_{cell} , to T_{oven} , vs T_{oven} . T_{cell} was measured directly above the Rb source.

By comparing the calculated $[\text{Rb}]$ for a given transition to $[\text{Rb}]$ calculated from the closest and higher absorption oscillator strength transition, it is possible to quantify $[\text{Rb}]$ measurement accuracy over a range of T_{oven} . A discrepancy suggests a breakdown in the Beer-Lambert law whereas agreement suggests accurate $[\text{Rb}]$ measurement. We define the Beer-Lambert law breakdown, our upper detection limit for accurate $[\text{Rb}]$ measurement, as a 20% difference between $[\text{Rb}]$ measurements for each transition, following the accuracy limits defined in the AAS line shape fitting shown in Section 5.3.2. Figure 5.23a shows that $[\text{Rb}]$ calculated from the D₁ and D₂ lines were consistently $> 28\%$ lower than those predicted by the $6P_{1/2}$ and D₁ absorption lines, respectively. This sug-

gests a breakdown in the Beer-Lambert law for the D_1 and D_2 lines, leading to under prediction of $[\text{Rb}]$ for these transitions over the range of temperatures evaluated. Incidentally, an upper accuracy limit for $[\text{Rb}]_{D_2}$, and correspondingly imposed on $[\text{Rb}]_{D_1}$, was determined in Section 5.3.5. At $T_{\text{oven}} = 155^\circ\text{C}$, $[\text{Rb}]_{6P_{3/2}} = (4.16 \pm 0.02) \times 10^{19} \text{ m}^{-3}$ calculated from $6P_{3/2}$ absorption was found to be 16% lower than calculated from $6P_{1/2}$ absorption, suggesting deviation from the Beer-Lambert law, and under prediction of $[\text{Rb}]$, for the $6P_{3/2}$ line at higher $[\text{Rb}]$.

The lowest measurable $[\text{Rb}]$ with $\text{SNR} \geq 8$ and $1 - [\text{Rb}]_{6P_{3/2}}/[\text{Rb}]_{6P_{1/2}} < 20\%$ was $[\text{Rb}]_{6P_{3/2}} = (4.1 \pm 0.2) \times 10^{18} \text{ m}^{-3}$, which is 84.8% lower than $[\text{Rb}]_{\text{sat}} = 2.70 \times 10^{19} \text{ m}^{-3}$ as defined in Table 3.1, for $T_{\text{oven}} = 125^\circ\text{C}$. This provides an order of magnitude range of sensitivity for $[\text{Rb}]_{6P_{3/2}}$ measurements and was expected to be sufficient in order to assess $[\text{Rb}]$ heterogeneity in our large SEOP cells.

Figure 5.23 shows experimentally measured $[\text{Rb}]$ lower than $[\text{Rb}]_{\text{sat}}$ for all T_{oven} investigated. Only at $T_{\text{oven}} = 105^\circ\text{C}$ was $[\text{Rb}]$ measured to be higher than $[\text{Rb}]_{\text{sat}}$ evaluated at 10°C lower than T_{oven} . T_{cell} was measured to be lower than T_{oven} , as shown in Fig 5.23c, but this did not account for lower measured $[\text{Rb}]$ than $[\text{Rb}]_{\text{sat}}$. This is similar to Shao et al. [87] and Shang et al. [144] who both observed lower than saturation Rb vapour densities over a range of temperatures. Adsorption of alkali metal to glass walls may lower alkali metal vapour densities [130]. In addition, the large volume of the SEOP cell in our setup likely leads to long $[\text{Rb}]$ build up times, highlighting the need to use a sufficiently long presaturator column to reach full Rb saturation at high gas flow rates through the SEOP cell, as shown in Chapter 4. The temperature difference between the top of the cell, where T_{cell} was measured, and the bottom of the cell, where the Rb source lies was not measured and so it is unclear if this contributes to the observed discrepancy.

5.3.4 AAS during continuous-flow SEOP

$[\text{Rb}]$ measurements during continuous-flow SEOP were performed at different cell positions for 3 different Rb source distributions. Measurements were repeated three times for each cell position probed. $[\text{Rb}]$ and T_{cell} distributions are presented in Figure 5.24, and P_{Xe} and optical pumping laser power absorbed are presented in Table 5.1.

In order to decouple laser heating and oven performance in cell temperature heterogeneity measurements, stable cell temperatures were recorded with the optical pumping laser switched off, as shown in Figure 5.24.

Table 5.1: Xe polarisation, P_{Xe} , and optical pumping laser power absorption for each Rb SEOP cell tested.

Rb distribution	P_{Xe} (%)	Power absorbed $= P_c - P_h$ (W)	Laser absorption $= \frac{P_c - P_h}{P_c}$ (%)
1g Rb main body	15 ± 2	46 ± 6	35 ± 5
5g Rb main body	18 ± 1	108 ± 4	80 ± 4
2g Rb presaturator	18 ± 2	121 ± 5	90 ± 3
2g Rb presaturator ¹	16 ± 3	100 ± 7	74 ± 4

¹Presaturator cell fluctuations resulted in every other acquisition showing lower optical pumping laser absorption, and corresponding cell temperature and [Rb] measurements were not included in Fig. 5.24.

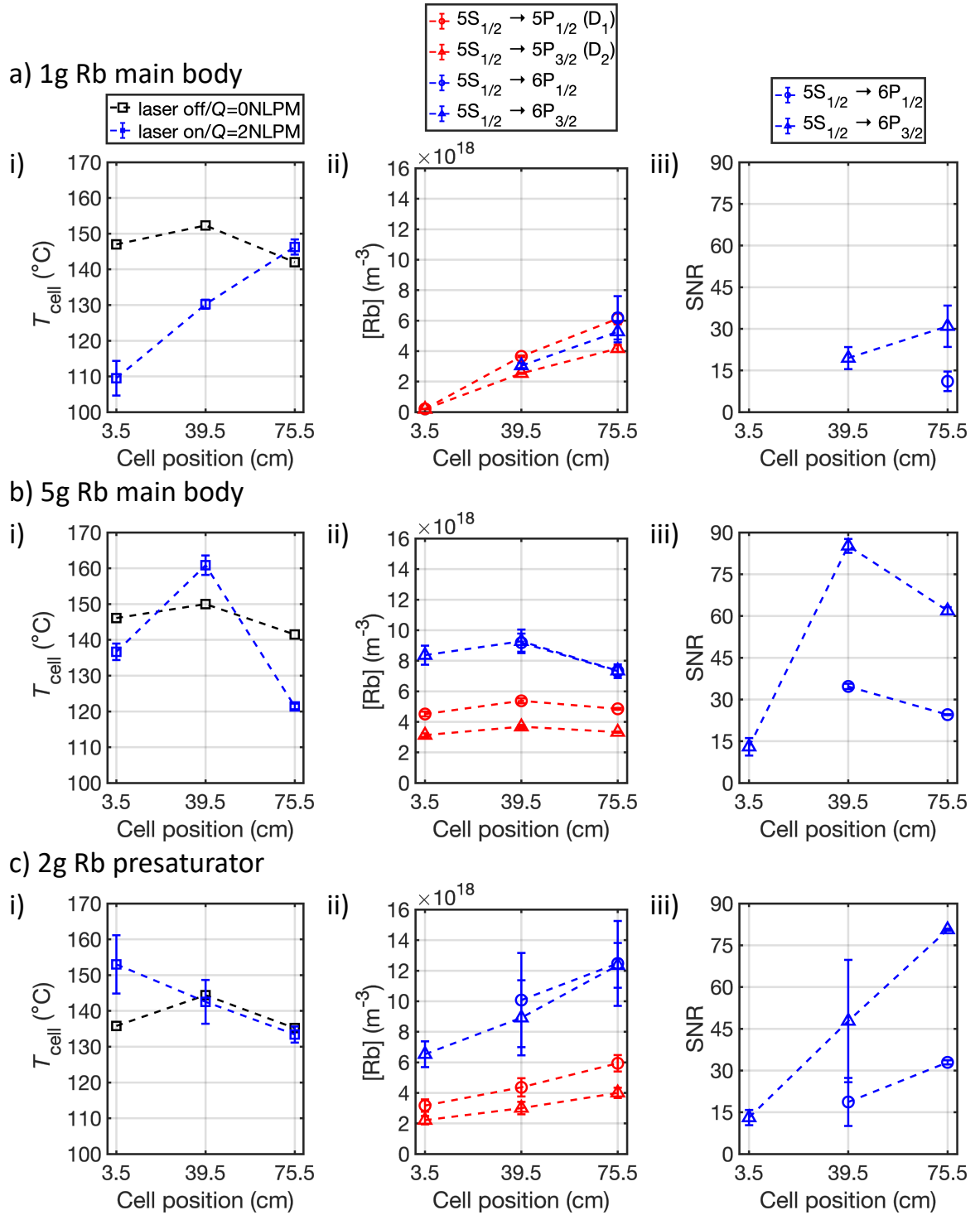


Figure 5.24: (i) T_{cell} , (ii) $[\text{Rb}]$ and (iii) SNR in violet absorbance spectra at different cell positions for (a) 1g Rb main body cell, (b) 5g Rb main body cell and (c) 2g Rb presaturator cell (see Figure 5.8). Dashed lines are to guide the eye only. The presaturator temperature was measured to be $164 \pm 2^\circ\text{C}$. SNR in D_1 and D_2 absorbance spectra was high (> 100) and so was not included in (iii) plots. N.B. in (ai), (bi) and (ci) T_{cell} measured without the pumping laser present do not have error bars due to only one measurement being taken.

Measurements from the first flow-through were typically discarded and subsequently repeated due to being outliers to subsequent measurements. The initial flow-through was considered necessary in order to disturb [Rb] and better match closed cell and under-flow thermal conditions to improve thermal stability. Even with this improvement in thermal stability, SEOP cell and oven temperatures, as well as laser power absorbed, fluctuated over long time scales (order 10 min) whilst the SEOP cell was closed. For the presaturator cell, fluctuations resulted in every other repeat acquisition showing lower absorption (see Table 5.1) and corresponding lower [Rb] at each cell position probed. This may be a result of reduced coupling of the Rb source in the presaturator from the oven ambient air temperature compared to SEOP cells with Rb sources in the main body of the cell, leading to non-replenishment of [Rb] in the main body of the cell once the cell has cooled and is reheated during closed cell conditions. However, further investigation into decoupling [Rb] from laser heating and the oven temperature controller in order to control [Rb] over a wider range of conditions is needed, as well as optimisation of closed cell [Rb] in between continuous-flow cycles.

Each run through of flowing gas through the cell was started when $T_{\text{oven}} = 125^{\circ}\text{C}$ and the transmitted power was increasing (power absorbed decreasing), suggesting decreasing [Rb], as a decreasing transmitted power may suggest Rb runaway conditions, which are unstable and difficult to reproduce.

Figure 5.24a shows that the 1g Rb cell under flow conditions produced maximum [Rb] at the back of the cell with $[\text{Rb}]_{6P_{1/2}} = (6 \pm 1) \times 10^{18} \text{ m}^{-3}$. This is 78% lower than $[\text{Rb}]_{\text{sat}}$ for $T_{\text{oven}} = 125^{\circ}\text{C}$. [Rb] decreases towards the front of the cell. The 9.4% lower $[\text{Rb}]_{D_2}$ than $[\text{Rb}]_{D_1}$ at cell position = 3.5cm compared to 31.8% at cell position = 75.5 cm suggests improved accuracy in $[\text{Rb}]_{D_1}$. This value suggests a 97% reduction in [Rb] from the back to the front of the cell. T_{cell} also follows this distribution with T_{cell} hottest at the back of the cell, $T_{\text{cell}} = 146 \pm 2^{\circ}\text{C}$, and decreasing towards the front of the cell, $T_{\text{cell}} = 110 \pm 5^{\circ}\text{C}$. This is due to the Rb source being located at the back of the cell, leading to a local build up in [Rb] at this position. Under flow, [Rb] should move towards the front of the cell, as seen in simulated [Rb] values for a 10cm^2 Rb pool in Fig. 4.6a, Section 4.3.2. However, the initial high [Rb] at the back of the cell leads to local heating in this region. As the oven can only control the global ambient air temperature within the oven, the effective heating from the oven reduces. This most likely results in lower heating of the cell in the region of the cell where laser heating is lower, which in this case is towards the front of the cell where there is no Rb source and [Rb] is low, leading to T_{cell} heterogeneity. This means that as gas with an initial high [Rb] flows from the back to the front of the cell, Rb will be deposited on the cell walls due to the lower T_{cell} , resulting in an unwanted reduction in [Rb]. This unexpectedly low [Rb] resulted in few violet transition points with a $\text{SNR} \geq 8$ that

could be processed.

Figure 5.24b shows that the 5g Rb cell produced maximum [Rb] at the centre of the cell with $[\text{Rb}]_{6P_{3/2}} = (9.3 \pm 0.8) \times 10^{18} \text{ m}^{-3}$. In addition, [Rb] heterogeneity is significantly lower for the 5g Rb cell than the 1g Rb cell, with a 21.5% difference in the maximum to lowest [Rb], which is $[\text{Rb}]_{6P_{3/2}} = (7.3 \pm 0.3) \times 10^{18} \text{ m}^{-3}$. This is due to the higher surface area of the Rb source that extends towards the centre of the SEOP cell, allowing for greater Rb evaporation and build up in [Rb] in the main body of the SEOP cell. In addition, the greater laser heating towards the front of the cell due to the location of Rb sources in this area results in higher T_{cell} , which reduces Rb deposition and maintains high [Rb] in this region. This differs from simulated [Rb] for a 70cm² Rb pool shown in Fig. 4.6a, where high [Rb] heterogeneity due to lower [Rb] at the back of the optical cell was observed. This may be as a result of the higher gas pressure used for the work in this chapter compared to simulations in Chapter 4 (2bar compared to 1.25bar), reducing volumetric gas flow rates in the optical cell and leading to lower disturbance of [Rb] build up at the back of the cell. It is worth noting, however, that the 5g Rb cell would often end up in Rb runaway, where total laser absorption would occur and the front of the SEOP cell would reach high T_{cell} ($> 200^\circ\text{C}$). This would most likely leave the majority of the cell unilluminated, resulting in low volume-averaged P_{Rb} and therefore low P_{Xe} of Xe gas exiting the SEOP cell.

Figure 5.24c shows that the 2g Rb presaturator cell produced maximum [Rb] at the back of the cell equal to $[\text{Rb}]_{6P_{1/2}} = (1.2 \pm 0.3) \times 10^{19} \text{ m}^{-3}$. This is 56% lower than $[\text{Rb}]_{\text{sat}}$ for $T_{\text{oven}} = 125^\circ\text{C}$. [Rb] decreases towards the front of the cell, similar to the 1g Rb cell, where at cell position = 3.5 cm, $[\text{Rb}]_{6P_{3/2}} = (6.5 \pm 0.8) \times 10^{18} \text{ m}^{-3}$, which is 46% lower than [Rb] measured at cell position = 75.5 cm. Therefore, [Rb] homogeneity in the 2g Rb presaturator cell is greater than in the 1g Rb cell, but less than in the 5g Rb cell.

Table 5.1 shows the 5g Rb cell and 2g Rb presaturator produced higher P_{Xe} than the 1g Rb cell, likely due to the more homogeneous and higher [Rb], increasing the spin-exchange rate and leading to a greater build up in P_{Xe} . Higher P_{Xe} values also corresponded with higher laser absorption. Measured P_{Xe} values were up to ~ 3.5 times lower than corresponding simulated P_{Xe} in Table 4.9, and up to \sim factor-2 lower than those measured from previous work with the same 1g Rb cell design [52]. This may be due to the higher temperature used in this work compared to the simulations in Chapter 4, or higher gas pressure of 2 bar used compared to 1.25 bar in previous work [52]. We would expect a 21-33% lower P_{Xe} when operating at 2 bar compared to 1.25 bar, for $1/\Gamma' = 44\text{min}$ to 80s, based on the modelling framework outlined in ref. [52]. Furthermore, T_{cell} measurements in the absence of the pumping laser revealed systematic T_{cell} differences to T_{oven} . T_{cell} measurements were not reported in the previous

study [52], making comparison of oven performance difficult. If we assume that the T_{cell} offset to T_{oven} was not present in ref. [52], then $T_{\text{oven}} = 125^\circ\text{C}$ in this work is likely far from the optimal to provide “peak” P_{Xe} , and as such P_{Xe} is significantly lower. In addition, skewed light in our setup, noted in Section 5.2.1, likely lowered measured P_{Xe} values compared to simulated values in Chapter 4. This, as well as other factors which limit optical pumping efficiency (see Section 3.3.1), were not accounted for in the simulations performed in Chapter 4, likely contributing to the P_{Xe} discrepancy.

A limitation of the oven is the single thermocouple used for global temperature control of the oven. For the work in Figure 5.24, the thermocouple was placed approximately halfway between the centre and the back of the oven, and for the work in Figure 5.23, the oven thermocouple was placed approximately halfway between the centre and the front of the oven. This is to be as far as possible from the oven heated air inlets which are located at the front, centre and back of the oven, where ambient oven temperature heterogeneity is suspected to be greatest and temperature stability to be the most challenging. However, this is likely to bias temperature control, both of the oven and the cell, to the thermocouple region. An improved thermal management solution may be to compartmentalise the oven, with independent local temperature control within each thermally isolated compartment of the oven. The greater the number of compartments used, the more local temperature control, at the expense of increased complexity. This oven design is explored in Chapter 6.

Additional limitations of this work are that measurements were only taken at 3 different cell positions and P_{Xe} measurements did not consider ^{129}Xe depolarisation due to dark Rb in outlet tubes. This depolarisation is likely to be more significant with higher [Rb] in the front of the cell and also dependent on Rb deposition in the outlet tubes.

Experiments using the 1g Rb cell were performed 2 to 6 months after the cell was installed on the polariser, in this time thermal cycling and other experiments, involving sparse polariser use, were performed. The 5g Rb cell and the 2g Rb presaturator cell were installed and ~ 3 days of thermal cycling was performed before experiments were carried out. Thermal cycling involves running the polariser at high and varying temperatures in order to evaporate and deposit Rb on the cell walls. The cells were then checked to see if reproducible laser power absorption, suggestive of stable [Rb], could be achieved before experiments were carried out. The cause of [Rb] changes and reduced P_{Xe} with extensive cell use are currently not well defined in the literature and require further investigation.

5.3.5 γ' and Γ' measurements

Using the 1g Rb cell, Γ_{down} was measured at different oven temperatures ($T_{\text{oven}} = 80$ °C to 125 °C). $[\text{Rb}]$ was measured simultaneously using AAS. Γ_{down} was plotted against $[\text{Rb}]$, and γ' and Γ' were determined from a linear fit, as shown in Figure 5.25.

Theoretical γ' was also calculated, using values in Table 3.1, and plotted as a function of P_{Rb} , as shown in Figure 5.26. Ranges of theoretical binary and vdW spin-exchange contributions were included in this plot to reflect the variation in the literature.

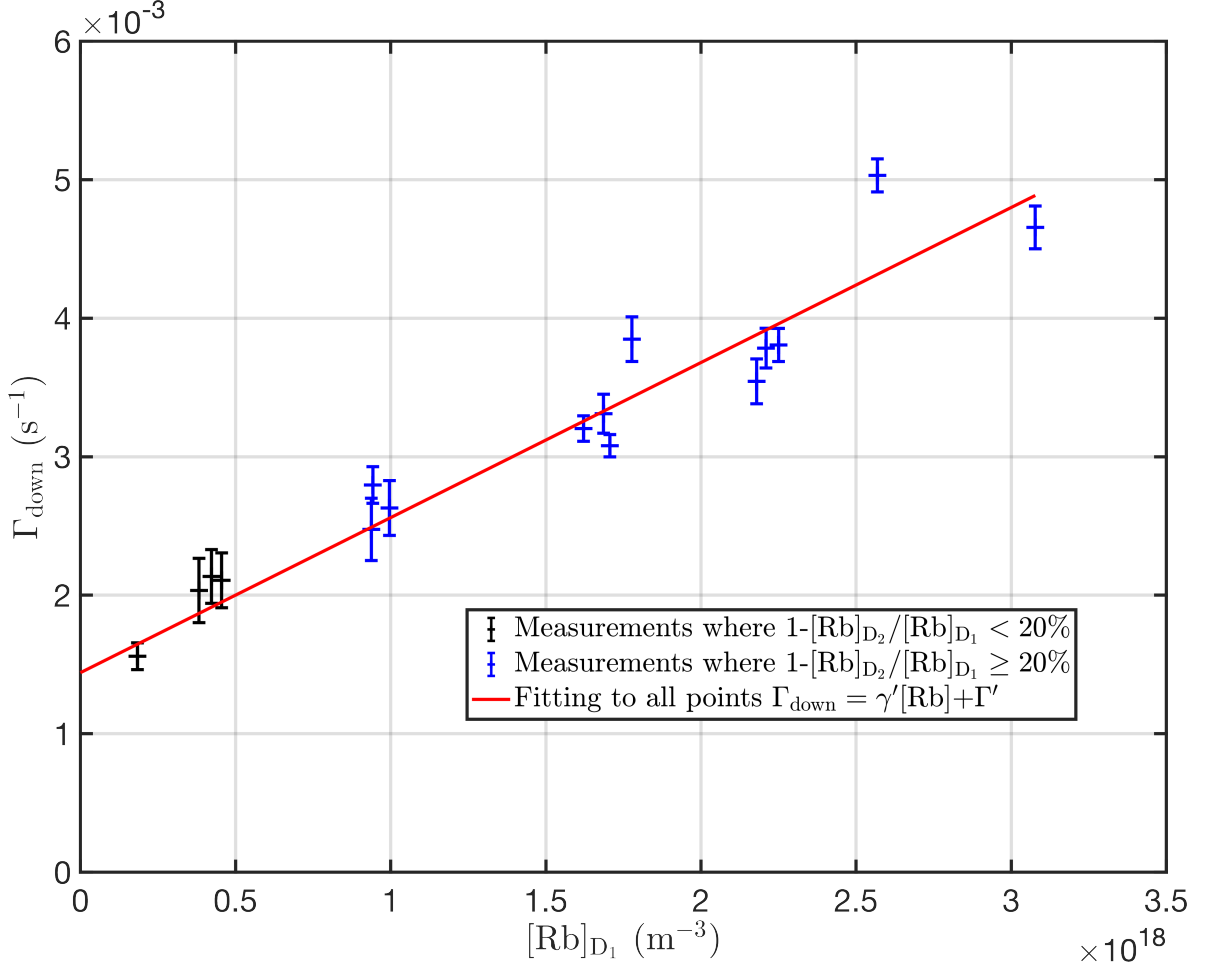


Figure 5.25: ^{129}Xe relaxation rate, Γ_{down} , as a function of $[\text{Rb}]$ measured from D_1 line absorption for 1g Rb main body cell. $\gamma' = (1.1 \pm 0.1) \times 10^{-21} \text{ m}^3\text{s}^{-1}$ and $1/\Gamma' = 12 \pm 1$ min. $> 20\%$ difference in $[\text{Rb}]_{\text{D}_1}$ and $[\text{Rb}]_{\text{D}_2}$, suggestive of deviation from the Beer-Lambert law for D_2 absorption, occurs at $[\text{Rb}]_{\text{D}_2} \gtrsim 4 \times 10^{17} \text{ m}^{-3}$ and correspondingly $[\text{Rb}]_{\text{D}_1} \gtrsim 5 \times 10^{17} \text{ m}^{-3}$, which is our current limit of accurate $[\text{Rb}]_{\text{D}_1}$ measurement.

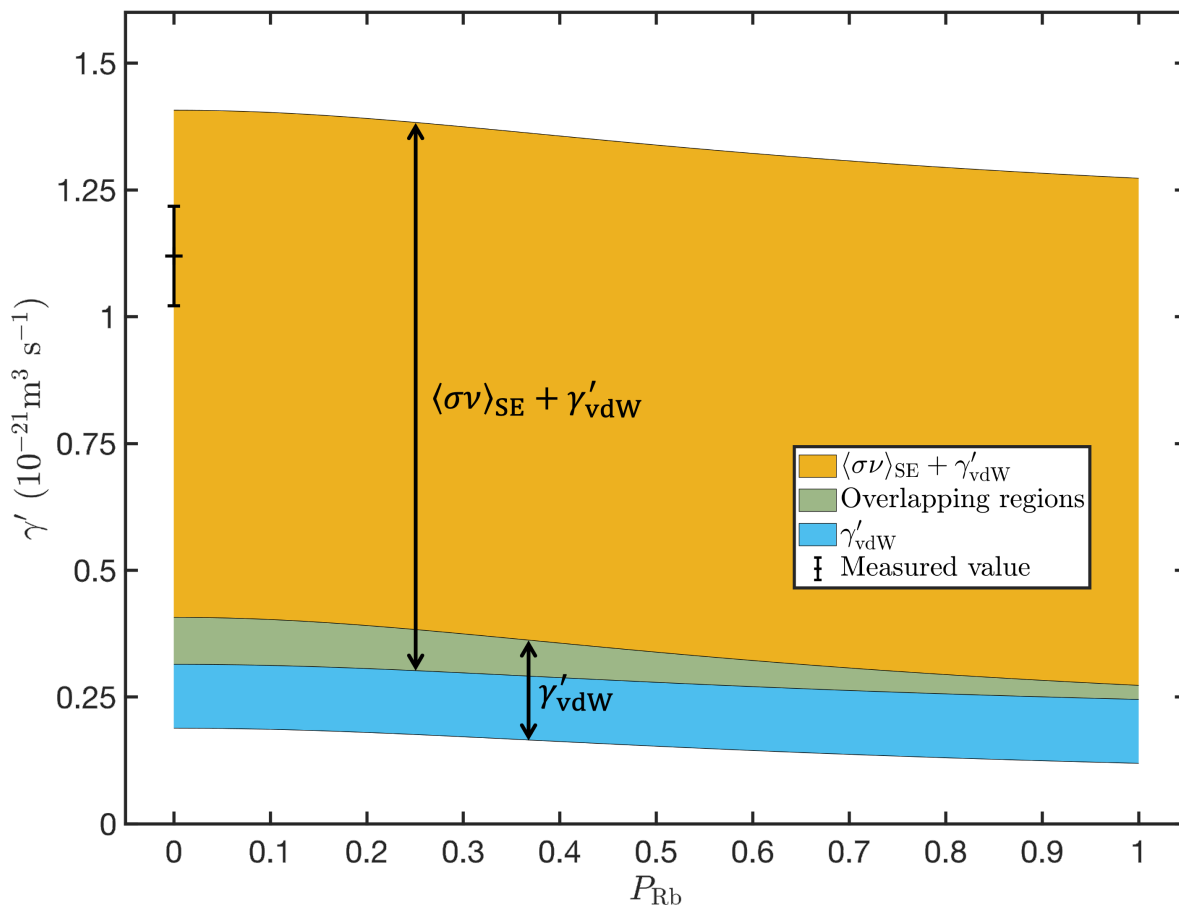


Figure 5.26: Theoretical Rb- ^{129}Xe spin-exchange cross section, γ' , as a function of Rb polarisation, P_{Rb} , as calculated for our conditions ($p = 2$ bar, $T = 125$ °C and 3%Xe, 10%N₂, 87%He). The blue region is the range of contribution due to three-body van der Waals interactions, and the yellow region is the added range of contribution due to measured binary spin-exchange cross sections from the literature. The green region is where the derived ranges of each spin-exchange cross section contribution from the literature overlap. Our measured value is plotted at $P_{Rb} = 0$, as the optical pumping laser was not on during Γ_{down} measurements.

Figure 5.26 shows that γ' is within the range of predicted spin-exchange rates. Our measurement is likely an overestimation due to $> 20\%$ difference in $[\text{Rb}]_{D_1}$ and $[\text{Rb}]_{D_2}$, suggestive of deviation from the Beer-Lambert law for D₂ absorption, which occurs at $[\text{Rb}]_{D_2} \gtrsim 4 \times 10^{17} \text{m}^{-3}$ and correspondingly $[\text{Rb}]_{D_1} \gtrsim 5 \times 10^{17} \text{m}^{-3}$. This is our current limit of accurate $[\text{Rb}]_{D_1}$ measurement, as an upper accuracy limit for $[\text{Rb}]_{D_1}$ cannot be determined due to $\text{SNR} < 8$ in violet absorption spectra. Thus we expect the true γ' value to be lower and true Γ' to be higher. Figure 5.26 also shows the P_{Rb} dependence for our conditions, thus we expect a 10% to 22% decrease in the spin-exchange cross section during optical pumping conditions. It is also shown that for $P_{Rb} = 0$, there is an up to 5 times difference in the total spin-exchange cross section depending on which

values from the literature are used, suggesting further investigation into spin-exchange parameters is needed.

We note that when $[\text{Rb}]_{\text{sat}}$ calculated from T_{oven} were used instead of those measured using AAS, $\gamma' = (7 \pm 4) \times 10^{-23} \text{ m}^3\text{s}^{-1}$ and $1/\Gamma' = (8 \pm 3) \text{ min}$. This highlights the issues with measuring γ' and Γ' assuming saturation Rb densities in systems where actual $[\text{Rb}]$ differs significantly. Given that temperature dependence of wall relaxation is not currently well defined in the literature, a limitation with this method of measuring γ' and Γ' is that it assumes cell wall relaxation is temperature and/or $[\text{Rb}]$ independent, which may not be a valid assumption as reported in studies of both ^3He -Rb [95] and ^{129}Xe -Rb [96] SEOP.

5.4 Conclusions

In this chapter, the accuracy limits of AAS in measuring $[\text{Rb}]$ within a high throughput ^{129}Xe -Rb polariser over a range of running conditions was systematically evaluated. Violet Rb electronic transitions were found to be valid for calculating $[\text{Rb}]$ of the order $< 5 \times 10^{19} \text{ m}^{-3}$, whereas the D_1 and D_2 NIR transitions were found to underpredict $[\text{Rb}]$ for $[\text{Rb}]$ of the order $> 5 \times 10^{17} \text{ m}^{-3}$. In future, SNR in violet AAS could be improved by using a dedicated LED or laser diode violet light source, extending the lower limit of detectable $[\text{Rb}]$ and improving accuracy of γ' and Γ' measurements.

$[\text{Rb}]$ heterogeneity was found to be greatest within a cell containing a localised drop of 1g Rb. $[\text{Rb}]$ homogeneity was improved within the cell containing a line of 5g Rb covering half the total cell length, as well as within a cell containing a 2g Rb presaturator region. $[\text{Rb}]$ was lower than saturation for all Rb source distributions tested and at high laser absorption values. Cell temperature heterogeneity appeared to play a role in $[\text{Rb}]$ heterogeneity. In addition, Rb runaway conditions observed in the 5g Rb cell suggest thermal management design changes warrant investigation if $[\text{Rb}]$ homogeneity is to be improved by using spread out Rb sources across the main cell body.

While γ' was measured and shown to be in line with current theory from the literature, it is worth noting the large range of published values of constants used to estimate both binary and molecular spin exchange rates.

In the next chapter, the oven design is altered to improve cell temperature homogeneity and reduce Rb runaway susceptibility. The optimal Rb source distribution is determined with this oven design. Optimisation of this setup for HP- ^{129}Xe production for clinical and research use is performed.

Chapter 6

Optimisation of the large-scale Rb-¹²⁹Xe hyperpolariser

6.1 Introduction

In Chapter 5, it was observed that Rb vapour density, [Rb], homogeneity in the optical cell was improved by using a larger 5g Rb pool source or 2g Rb presaturator distribution compared to the previously used 1g Rb pool. This also led to higher laser absorption and correspondingly higher ¹²⁹Xe polarisation, P_{Xe} . Whilst the 5g Rb pool source produced the most homogeneous [Rb], it is more susceptible to Rb runaway than the other Rb source configurations. In addition, temperature heterogeneity over the cell was high, likely due to laser heating as a result of heterogeneous [Rb] distribution and the single point of oven temperature control.

The aim of the work in this chapter was to implement a compartmentalised oven in order to improve cell temperature regulation, so that the Rb source distribution in the cell main body could be increased to improve [Rb] levels and homogeneity whilst avoiding Rb runaway. Once completed, the aim was to optimise HP-¹²⁹Xe production on the upgraded polariser to be used for routine and research HP-¹²⁹Xe gas MRI.

The multi-compartment oven was tested by recording cell temperatures and laser absorption with different amounts of Rb source in the main cell body in order to see which gave the highest and most stable laser absorption, whilst avoiding Rb runaway. The utility of the Rb presaturator was also assessed with the optimal main body Rb source distribution.

The setup with the ideal Rb source distribution was then optimised for HP-¹²⁹Xe production. In order to aid optimisation efforts and compare experimental and theoretical values, 1D simulations were performed. Many continuous-flow polarisers have used the-

oretical SEOP models in order to aid optimisation work [52–55,94,117]. The parameter often used to characterise performance is the cell or oven temperature, as this adjusts [Rb] within the cell. However, as seen in Chapters 4 and 5, [Rb] distribution is also dependent on Rb source distribution, gas flow dynamics and laser heating reducing the proportionality between temperature and [Rb] and therefore leading to variability in actual [Rb] values.

Whilst AAS allows us to directly probe [Rb], it is a cumbersome technique in its current form, necessitating setup at different cell positions that is difficult to be performed “on-demand”, and therefore impractical to monitor [Rb] in real-time. On the other hand, laser absorption is easily monitored throughout polariser operation and will be proportional to global, cell-averaged [Rb], $\langle[\text{Rb}]\rangle$, based on Eq. 3.78, assuming optical pumping and Rb spin destruction are realistically modelled. Although [Rb] heterogeneity was investigated in Chapter 4 and shown to lead to lowering of P_{Xe} and laser absorption levels, this was only performed at a single temperature. It is unclear how [Rb] heterogeneity affects laser absorption and P_{Xe} build up across a large range of cell temperatures. Therefore, [Rb] heterogeneity was simulated and its effect on laser absorption and P_{Xe} build up determined for a large range of cell temperatures.

Two models of P_{Xe} have been used in 1D modelling, a numerical model based on Eq. 3.104, or an analytical model based on Eq. 3.103. Both approaches have been used throughout the literature, for greatly varying SEOP setups (numerical [53], analytical [25, 52–55]). The reasoning for the choice of model in these works are not always explained. In Chapter 4, P_{Xe} build up was simulated using the numerical model, due to the high gas flow rates ($Q = 2$ SLM and 2 NLPM). However, in this Chapter, static ($Q = 0$) P_{Xe} was measured, and so assumptions of the numerical model must be revisited.

The key difference in the models is the cell-position dependence of SEOP parameters in the numerical model, whilst the analytical model uses cell-averaged parameters and assumes P_{Xe} build up is always exponential. The choice of model is important for defining expectations of achievable P_{Xe} , production rates and optimal running conditions. Eq. 3.103 will be valid for high P_{Rb} homogeneity, which will occur at low [Rb], however it is unclear at which [Rb] this will no longer hold and the role of [Rb] heterogeneity in this. In addition, it is unclear the role of flow rate, Q , in the deviation between models. Turbulent gas flow and significant Xe diffusion at low Q have been given as reasons to use the analytical model [55], whereas the numerical model often neglects D_{Xe} , as can be done at high Q . Therefore, both models were simulated and compared to assess under which conditions they deviate from each other. Experimental measurements were compared to values predicted by each model in order to assess the suitability of each model for explaining P_{Xe} build up in our high-throughput polariser. Cryogenic accumu-

lation was investigated in more detail in order to characterise Xe volume recovery, and a larger spiral was introduced to reduce Xe volume losses during this process at high Q and low pressure where the residency time of Xe in the spiral is reduced. Finally, HP-Xe production maps were produced in order to determine optimal polariser running conditions for routine and research HP-¹²⁹Xe gas MRI.

6.2 Methods

6.2.1 Oven modification

As discussed in Chapter 5, an enhancement to the oven design was proposed, involving the regulation of temperature based on cell position to reduce susceptibility to Rb runaway in cells with large surface area Rb pools.

The existing ceramic oven was divided into three compartments using two layers of foam insulation as shown in Fig. 6.1. The heating element (OMEGA, model AHPF-122 1200W), PID controller (OMEGA, model CN7523) and manifold were replaced with three independent heating elements (OMEGA, model AHP-7562 750W) and PID controllers (OMEGA, model CN7523) connected to each of the existing oven inlets. Each element was regulated with independent thermocouples (OMEGA, model SA1XL K-type), placed in the airspace of each oven compartment. The compressed air supply was divided among each heating element. The cell stem openings in the oven were used as exhausts for the front and back oven compartments and an exhaust for the centre compartment was created by removing an oven plug designed for atomic absorption spectroscopy and adding insulation foam to reduce the diameter of the opening.

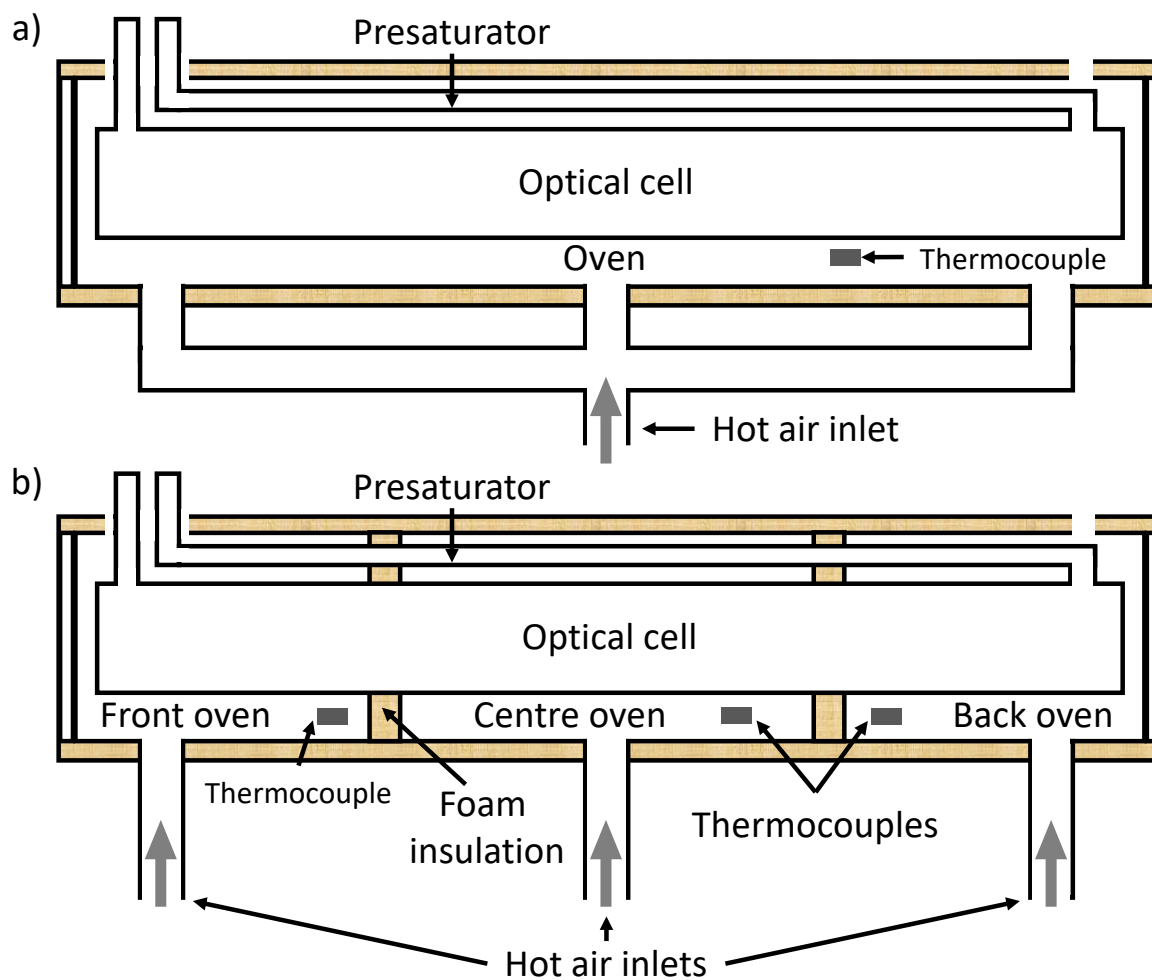


Figure 6.1: (a) The single compartment oven, as used in Chapter 5, and (b) the multi-compartment oven. Foam insulation is used to separate compartments. Each compartment has an independent heating element, PID controller and thermocouple in the ambient oven compartment space.

Each oven design was characterised in terms of oven temperature to cell or presaturator temperature, with presaturator heating tape power set to different amounts. The cell and presaturator thermocouples were positioned in the same positions as used in Chapter 5 where the cell thermocouples are at the centre of the cell and $\pm 36\text{cm}$ from the centre and the presaturator thermocouple is placed near the presaturator to main cell body junction.

For the multi-compartment oven, thermal isolation between compartments is important for independent control of the oven compartment temperatures and precise cell temperature control. This was tested by measuring temperatures with a 50°C set temperature differential between compartments.

These tests were performed with the optical pumping laser off in order to assess oven heating only. Tests with the pumping laser on are described in the subsequent section.

6.2.2 Laser absorption for different Rb source distributions

In addition to the multi-compartment oven modification, Rb source distributions were further investigated. The aim of this was to evaluate the optimal size of the Rb pool within the main cell body to achieve high laser absorption, whilst preventing Rb run-away or heterogeneous cell temperatures, indicating [Rb] heterogeneity, as observed in Chapter 5. Additionally, the goal was to closely match laser absorption in both static (no gas flow or standby mode) and under-flow conditions, which indicates a consistent [Rb] distribution between static and under-flow polariser operation. Static polariser operation was not explored in the previous chapters. When transitioning from static to under-flow operation, the goal is for conditions to remain approximately the same. This is to (i) avoid having initial low P_{Xe} gas that would need to be removed before cryogenic accumulation, (ii) improve stability by reducing the need for conditions to be adjusted in order to achieve maximum P_{Xe} , (iii) reduce operating time and the amount of user input and monitoring required for optimal polariser operation and (iv) most theoretical models assume static and under-flow conditions are the same so to better match experimental and theoretical conditions. To avoid changing conditions, stable [Rb] distribution in the optical cell, unaltered by gas dynamics, must be present. Here, stable conditions are characterised by a constant laser absorption value.

Laser transmission was measured from initially static to under-flow ($Q = 2\text{NLPM}$) conditions and vice versa for each amount of Rb source in the main body. The amount of Rb in the main cell body was varied from no Rb to many Rb pools and dry-ice Rb spreading treatment, as described by Birchall and colleagues [99, 145]. After the cell with no Rb in the main body was tested, $\sim 1/4$ to $1/3$ of the 2g Rb in the presaturator was heated and tipped into the main cell body. The remaining Rb in the presaturator was then re-distributed evenly. The same amount of Rb ($\sim 0.5\text{g}$ to 0.67g) was used for all Rb pools in the main body. Rb pools were positioned symmetrically $\sim 9\text{cm}$ and $\sim 28\text{cm}$ from the centre of the cell. A small amount of Rb was situated at the bottom of the back cell window, within a small trench where the cell body meets the cell window, and could not be removed which resulted in $\sim 3\%$ lower laser transmission. Laser absorption measurements assumed that laser absorption through the unhindered cross section were representative of laser absorption in the cross section blocked by Rb. The tested Rb source distributions with respect to the oven are shown in Fig. 6.2 and pictured before installation on the polariser in Fig. 6.3. The Rb presaturator cell was used throughout testing, although a non-presaturator cell was also tested, as shown

in Fig. 6.2e and Fig. 6.3e, as well as within the single-compartment oven, to directly compare laser absorption with and without the oven modification and the addition of the presaturator.

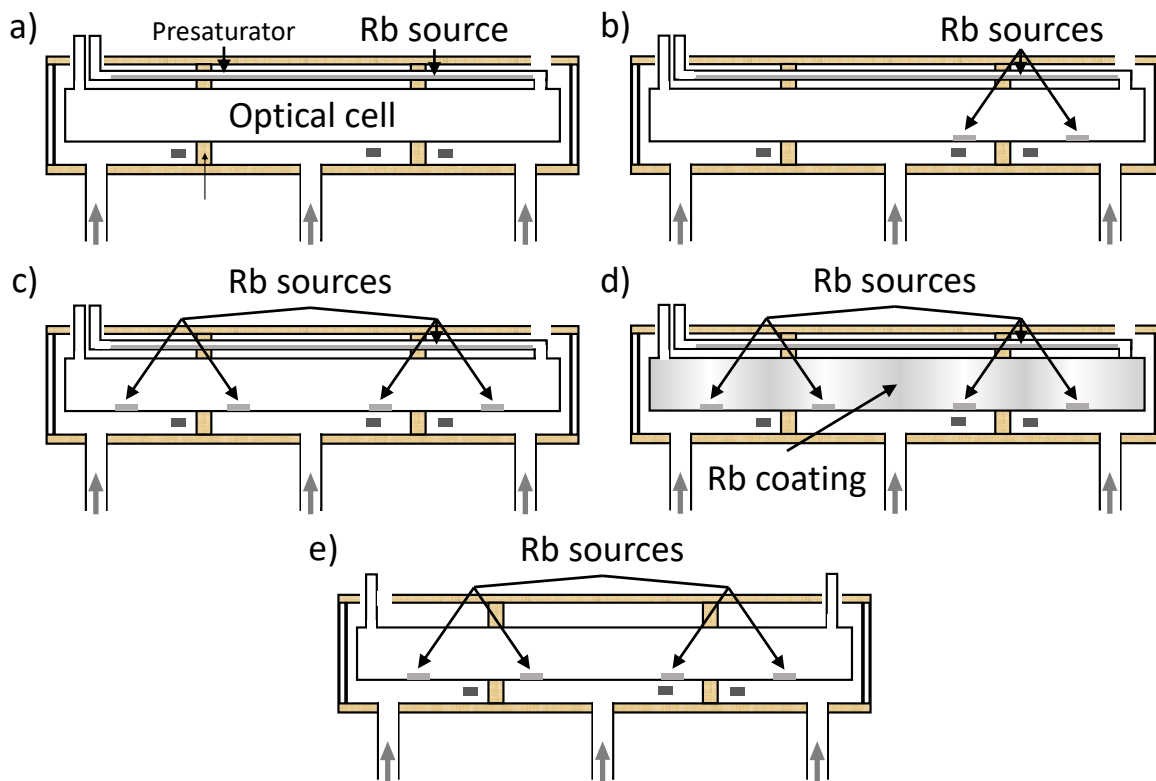


Figure 6.2: Multi-compartment oven setup, showing the approximate location of the Rb droplets/Rb source distributions in the optical cells. Rb distributions are (a) Rb in the presaturator only, (b) Rb in the presaturator and 2 Rb pools in the main cell body, (c) Rb in the presaturator and 4 Rb pools in the main cell body, (d) Rb in the presaturator, 4 Rb pools in the main body and dry-ice Rb coating and (e) 4 Rb pools in the main body, no Rb presaturator. Corresponding photos of the optical cells are in Fig. 6.3.

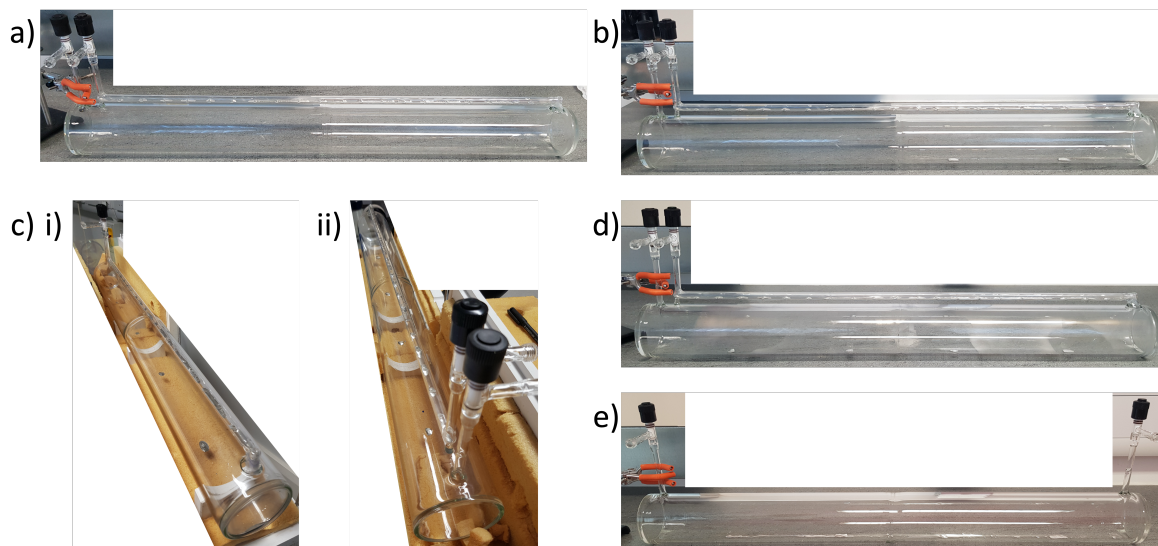


Figure 6.3: Optical cells (before installation) with Rb in the presaturator and (a) no Rb in the main body, corresponding to Fig. 6.2a; (b) 2 Rb pools in the main cell body corresponding to Fig. 6.2b; (c) 4 Rb pools in the main cell body, without dry-ice coating treatment, corresponding to Fig. 6.2c as viewed from (i) near the back of the cell and (ii) near the front of the cell; (d) 4 Rb pools in the main cell body, with dry-ice coating treatment, corresponding to Fig. 6.2d; (e) no presaturator and 4 Rb pools in the main cell body, without dry-ice coating treatment, corresponding to Fig. 6.2e. There are Rb trails between the Rb pools, due to the tendency for the Rb to stick to the cell walls. When installed on the polariser and heated, the Rb aggregated together reducing the size of the Rb trails. (b), (c) and (d) show Rb also by the back cell window due to collecting in the trench between the window and walls.

6.2.3 1D simulations of Rb density heterogeneity and laser absorption

Numerical and analytical P_{Xe} build up models

In this chapter, P_{Xe} build up was modelled using two different methods; a numerical and analytical approach. A summary of these methods is given in Table 6.1.

The numerical model is based on Eq. 3.104 and assumes Xe enters the optical cell through the back cell window. Xe then travels with plug flow ($\mathbf{v} = -v_z$) through the optical cell to the front cell window where it is extracted. Within any short time period, δt , Xe is confined to a cell position, δz . This means that the spatial variation of parameters is considered. In this model, Rb is assumed to be static, thus the variation in SEOP parameters such as $[Rb]$ and P_{Rb} are considered. Diffusion of Rb and Xe are neglected.

The analytical model is based on Eq. 3.103. In this model, diffusion is assumed to be extremely fast, i.e. the diffusion length in the spin-up time, τ_{up} , is much longer than the cell length, $L_D(t = \tau_{\text{up}}) \gg L_{\text{cell}}$. Therefore, within any short time period, δt , Xe nuclei move through all parts of the optical cell $z = L_{\text{cell}}$. This results in a global-averaged effect of SEOP parameters and the spatial distribution of SEOP parameters is ignored. We may also think of this occurring if convection due to sufficient temperature gradients, which alters \mathbf{v} , is present.

At high flow rates, Q , we expect the numerical model to be applicable due to $\mathbf{v} \cdot \nabla \mathbf{P}_{\text{Xe}} \gg \nabla \cdot (-\mathbf{D}_{\text{Xe}} \cdot \nabla \mathbf{P}_{\text{Xe}})$, as observed in Chapter 4. Under static conditions, $\mathbf{v} = 0$ ignoring convection. Diffusion can be neglected if $L_D(t = \tau_{\text{up}}) \ll L_{\text{cell}}$. Therefore τ_{up} must be sufficiently short for this to be true, $\tau_{\text{up}} \ll \frac{L_{\text{cell}}^2}{2D_{\text{Xe}}}$, where the 1D diffusion length is used due to $r_{\text{cell}} \ll L_{\text{cell}}$. For $D_{\text{Xe}} = 0.46 \text{cm}^2 \text{s}^{-1}$ and $L_{\text{cell}} = 78.7 \text{cm}$, $\tau_{\text{up}} \ll 112 \text{min}$. This is true for most polariser running conditions and we expect the numerical model to be the appropriate model. We expect the analytical model to only be applicable where homogeneous SEOP parameter distributions exist, such as low, homogeneous [Rb] distribution, where low laser absorption resulting in high homogeneous P_{Rb} and homogeneous temperatures due to low laser heating exists.

The limitations of both models are they neglect convection. Convection will alter \mathbf{v} , which will depend on cell orientation [71,112] and temperature gradients within the cell. We expect this to be insignificant at high flow rates based on simulations performed in Chapter 4, however it is unknown how it may affect P_{Xe} build up under static conditions.

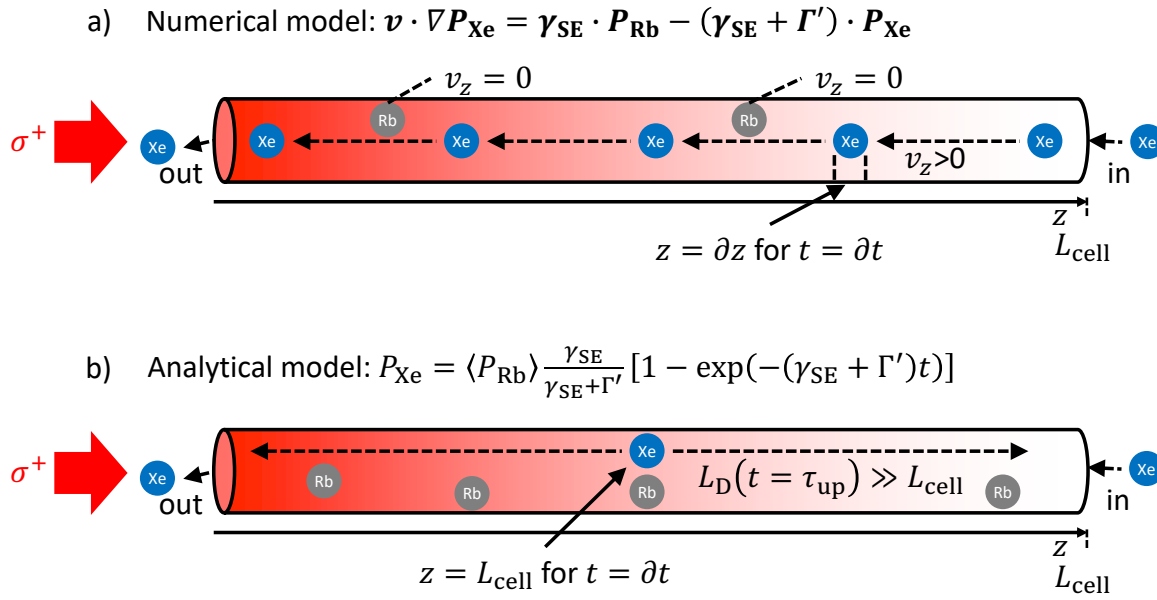


Figure 6.4: Diagram showing the differences between the (a) numerical and (b) analytical P_{Xe} build up models.

1D simulations were performed in MATLAB (MathWorks). Fixed $P_{\text{Rb}} = 0.8$ was assumed to calculate Γ_{SD} , as similarly performed in Chapter 4. Photon attenuation was simulated, as opposed to optical pumping attenuation used in Chapters 4. The initial photon flux is the laser output flux and the spectral line shape is Gaussian, defined by the laser FWHM. Photon attenuation, given by Eq. 3.78, was calculated numerically using Euler's first-order method. The optical pumping rate, R , was then calculated using Eq. 3.72, and P_{Rb} calculated using Eq. 3.71. P_{Xe} build up was modelled using both the numerical model (Eq. 3.104), and the analytical model (Eq. 3.103). Cell-averaged parameters for P_{Rb} , $\langle P_{\text{Rb}} \rangle$, and spin-exchange cross section, $\langle \gamma' \rangle$, were used in the analytical model.¹ Critical flow rates, Q_c , as described later on in Section 6.2.4, were also calculated for both models.

¹ $\langle \gamma' \rangle$ is the cell-averaged γ' as opposed to γ' evaluated for $\langle P_{\text{Rb}} \rangle$.

Table 6.1: 1D numerical vs analytical P_{Xe} build up models.

Model	Numerical model		Analytical model	
	Method	Equation	Method	Equation
Photon attenuation	Same for both models	Eq. 3.78	Same for both models	Eq. 3.78
Optical pumping	Same for both models	Eq. 3.72	Same for both models	Eq. 3.72
P_{Rb}	Spatially dependent	Eq. 3.71	Cell-averaged	Mean of Eq. 3.71 over the cell
Static P_{Xe}	Evaluated at $z = 0$	$P_{Rb}(z = 0) \frac{\gamma_{SE}(z=0)}{\gamma_{SE}(z=0)+\Gamma'}$	Cell-averaged	$\langle P_{Rb} \rangle \frac{\langle \gamma_{SE} \rangle}{\langle \gamma_{SE} \rangle + \Gamma'}$
P_{Xe} build up	Partial differential equation	Eq. 3.104	Exponential build-up equation	Eq. 3.103
Gas flow	Plug flow	$\mathbf{v} = -v_z$	Complete gas mixing	$L_D(t = \tau_{up}) \gg L_{cell}$
Diffusion	Neglected	$L_D(t = \tau_{up}) \ll L_{cell}$	Very fast diffusion	$L_D(t = \tau_{up}) \gg L_{cell}$

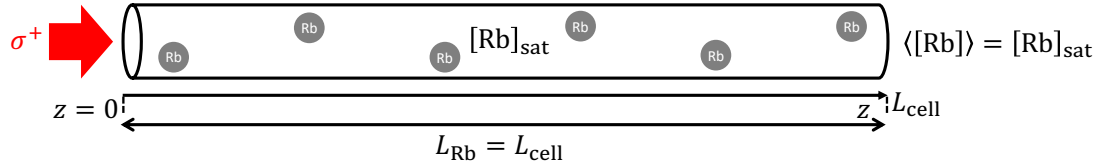
Modelling Rb density heterogeneity

[Rb] heterogeneity was simulated in Chapter 4, however its effect on P_{Xe} and Q_c values was not determined for different cell temperatures. This was performed in this Chapter. A 1D simulation framework, as opposed to a FEM framework was used as run times for the FEM framework are too long for large multi-parameter parametric sweeps. [Rb] heterogeneity in this 1D simulation framework was modelled by assuming two optical cell regions: one region within a length L_{Rb} from the front of the cell where finite $[Rb] > 0$ exists, and the region in the remaining portion of the cell where $[Rb] = 0$. This is the worst-case scenario of [Rb] heterogeneity and is shown in Fig. 6.5b. [Rb] heterogeneity increases with decreasing L_{Rb} . For the numerical model, as SEOP will not occur in the $[Rb] = 0$ volume, the effective cell length is reduced to just the L_{Rb} region. The effective reduction in cell length also reduces the Xe residency time, t_{res} . Effective cell length therefore decreases with increasing [Rb] heterogeneity. For the analytical model, [Rb] heterogeneity cannot be modelled as a parameter distribution and instead leads to a lowering of the cell-averaged Rb density, $\langle [Rb] \rangle$.

The limitation of modelling $[\text{Rb}]$ heterogeneity in this way is that it does not consider the case where the region of $[\text{Rb}] > 0$ exists at the back of the cell as opposed to the front of the cell. Both cases can be considered as identical if depolarisation in the area of $[\text{Rb}] = 0$ is low, i.e. $\Gamma' t_{\text{res}} \approx 0$, where Γ' is Xe relaxation in the absence of Rb and t_{res} is the Xe residency time in the area of $[\text{Rb}] = 0$. This may not be the case for rapid Γ' , or slow flow rates, Q .

Simulations were performed using $\Gamma' = 44\text{min}$, as determined in ref. [52]. Laser FWHM was set to 0.25nm , as measured in Section 5.2.1. Laser power was set to 160W , to account for 10% transmission losses at the front cell window. $p = 1.25\text{bar}$ was used. Simulations were performed for different temperatures and Q . $[\text{Rb}] = [\text{Rb}]_{\text{sat}}$ was used, as given in Table 3.1. The absolute percentage difference between P_{Xe} and Q_c calculated by each model was determined.

a) Homogeneous $[\text{Rb}]$



b) Heterogeneous $[\text{Rb}]$



Figure 6.5: Simulated Rb density, $[\text{Rb}]$, distributions. (a) Homogeneous $[\text{Rb}]$ across the full cell length $L_{\text{Rb}} = L_{\text{cell}}$. (b) Heterogeneous $[\text{Rb}]$ where $[\text{Rb}] = [\text{Rb}]_{\text{sat}}$ only within the L_{Rb} region. Beyond this region $[\text{Rb}] = 0$. For the numerical model, this results in a reduction in the effective cell length, whereas for the analytical model, the cell-averaged Rb density, $\langle [\text{Rb}] \rangle$ changes by a factor $L_{\text{Rb}}/L_{\text{cell}}$ compared to the homogeneous case in (a).

6.2.4 HP-¹²⁹Xe production optimisation

For the optimal Rb source distribution, HP-¹²⁹Xe production optimisation was performed.

Firstly, γ' and Γ' were measured using spin-down and $[\text{Rb}]$ measurements, as described in Section 5.2.6. These values were incorporated into the theoretical model for direct comparison with experimentally determined P_{Xe} , Q_c and efficiency values.

P_{Xe} and laser absorption were measured for different oven temperatures, both under flow ($Q = 2\text{NLPM}$) and static operation, in order to determine optimal running conditions. Under flow measurements were performed by firstly allowing gas flow for $1.2t_{\text{res}}$ before taking measurements. This was to make sure Xe sampled was not present within the optical cell before flow through started, and $+0.2t_{\text{res}}$ to account for the time taken for the pressure and flow regulator to stabilise and any possible unconsidered systematic time considerations. t_{res} is given by

$$t_{\text{res}} = \frac{V_{\text{cell}}}{Q_V} = \frac{V_{\text{cell}}}{Q[\text{NLPM}]} \cdot \frac{p}{1\text{atm}} \cdot \frac{293.15\text{K}}{T_{\text{oven}}}. \quad (6.1)$$

Static measurements were performed once stable static polariser conditions were attained, waiting a time $6/\Gamma_{\text{down}}$ before taking measurements, where Γ_{down} was measured previously at similar oven temperatures for the same cell. This long wait ensures P_{Xe} has reached its $t \rightarrow \infty$ value ($= P_{\text{Xe}}^{\text{eq}}$). A Xe volume of ~ 100 to 400ml , i.e. only Xe at the front of the cell, was collected for measurements.

Production rates

We have characterised the HP-¹²⁹Xe production rate as being equal to the critical flow rate, Q_c . This is the flow rate at which the residency time of Xe, t_{res} , equals the spin-up time, τ_{up} i.e.

$$Q_c = \frac{t_{\text{res}}Q}{\tau_{\text{up}}}. \quad (6.2)$$

Equilibrium, or static gas flow, P_{Xe} from Eq. 3.103 is

$$P_{\text{Xe}}^{\text{eq}} = P_{\text{Xe}}(Q = 0) = \langle P_{\text{Rb}} \rangle \frac{\gamma_{\text{SE}}}{\gamma_{\text{SE}} + \Gamma'}. \quad (6.3)$$

Substituting $(\gamma_{\text{SE}} + \Gamma')t = t_{\text{res}}/\tau_{\text{up}} = Q_c/Q$, as well as $P_{\text{Xe}}^{\text{eq}}$ into Eq. 3.103 gives

$$P_{\text{Xe}}(Q) = P_{\text{Xe}}^{\text{eq}} \left[1 - \exp\left(\frac{-Q_c}{Q}\right) \right]. \quad (6.4)$$

Q_c was determined by rearranging Eq. 6.4, which gives

$$Q_c = -Q \log\left(1 - \frac{P_{\text{Xe}}(Q)}{P_{\text{Xe}}^{\text{eq}}}\right). \quad (6.5)$$

Q_c could therefore be determined for different laser absorption from the static ($Q = 0$) and $Q = 2\text{NLPM}$ P_{Xe} measurements. In order to verify this, for confidence in Q_c determined from only two P_{Xe} measurements, P_{Xe} was measured for a range of Q and fitted to Eq. 6.4, at two different laser absorption values.

Photon and spin-exchanges efficiencies

Photon efficiency, η_γ , is the ratio of ¹²⁹Xe polarisation rate to photon absorption rate $\Delta\Phi$, given by [146]

$$\begin{aligned}\eta_\gamma(t) &= \frac{[^{129}\text{Xe}]_{\text{cell}} V_{\text{cell}}}{\Delta\Phi} \cdot \frac{dP_{\text{Xe}}}{dt} \\ &= \frac{[^{129}\text{Xe}]_{\text{cell}} V_{\text{cell}}}{\Delta\Phi} \cdot \frac{(P_{\text{Xe}}^{\text{eq}} - P_{\text{Xe}}(t))}{\tau_{\text{up}}} \\ &= \frac{Q_c [^{129}\text{Xe}]_{\text{NTP}}}{\Delta\Phi} \cdot (P_{\text{Xe}}^{\text{eq}} - P_{\text{Xe}}(t)),\end{aligned}\tag{6.6}$$

where $[^{129}\text{Xe}]_{\text{cell}}$ is the ¹²⁹Xe number density in the optical cell, V_{cell} is the cell volume and $[^{129}\text{Xe}]_{\text{NTP}} = f_{^{129}\text{Xe}} n_0 \frac{273.15\text{K}}{293.15\text{K}}$ is ¹²⁹Xe number density at normal temperature and pressure ($p = 1\text{atm}$, $T = 293.15\text{K}$), n_0 is the Loschmidt number, $f_{^{129}\text{Xe}}$ is the fraction of ¹²⁹Xe in the gas mixture and Q_c is in units of nominal litres per minute (NLPM). Maximum photon efficiency occurs when $P_{\text{Xe}}(t = 0) = 0$, given by

$$\eta_\gamma(t = 0) = \frac{Q_c [^{129}\text{Xe}]_{\text{NTP}}}{\Delta\Phi} \cdot P_{\text{Xe}}^{\text{eq}}.\tag{6.7}$$

During HP-¹²⁹Xe production, (where $t = t_{\text{res}} > 0$) photon efficiency decreases by a factor $P_{\text{Xe}}^{\text{eq}} / (P_{\text{Xe}}^{\text{eq}} - P_{\text{Xe}}(Q))$ as t_{res} increases, due to the lowering availability of ¹²⁹Xe nuclei in the low energy state that can undergo a spin flip. For operating at flow rate Q , the production efficiency, η_{pr} , is the mean η_γ during t_{res} defined as

$$\eta_{\text{pr}} = \frac{1}{t_{\text{res}}} \int_0^{t_{\text{res}}} \eta_\gamma(t) dt = \frac{Q [^{129}\text{Xe}]_{\text{NTP}}}{\Delta\Phi} \cdot P_{\text{Xe}}(Q).\tag{6.8}$$

The photon efficiency upper limit is the spin-exchange efficiency, η_{SE} , which is the ratio of the ¹²⁹Xe to Rb spin-exchange rate and the Rb spin-destruction rate, given by

$$\eta_{\text{SE}} = \frac{\gamma_{\text{SE}} [^{129}\text{Xe}]_{\text{cell}}}{[\text{Rb}] \Gamma_{\text{SD}}} = \frac{\gamma' [^{129}\text{Xe}]_{\text{cell}}}{\Gamma_{\text{SD}}}.\tag{6.9}$$

$\eta_\gamma(t = 0) = \eta_{\text{SE}}$ when all absorbed photons contribute to optical pumping in the system, otherwise $\eta_\gamma(t = 0) < \eta_{\text{SE}}$ due to skewed light effects [74], imperfect left-circularly polarised pumping light, circular dichroism [75, 76] or incomplete N₂ quenching [64].

Maximum photon efficiency was determined for different laser absorption values using Q_c and $P_{\text{Xe}}^{\text{eq}}$ measurements. Photon absorption is typically measured as $\Delta\Phi = (P_c - P_h) / E_p$, where P_c is the cold cell transmission, P_h is the hot cell transmission and E_p is the photon energy. However, this does not account for transmission losses at the front and back of the cell. The cell windows (75mm Diameter x 6.5mm Thickness, Uncoated, BOROFLOAT® Window, SCHOTT) are rated for 90% transmission, and cold cell transmissions with polariser use are lower than brand-new or unused cold cell transmission. We suspect this is due to the observed Rb deposition on the back cell

window, which might occur at high laser absorption, or due to oven design and heat losses at the oven windows, which are close to the cell windows. Therefore an alternative form was used to account for transmission reduction and therefore avoid systematic overestimation of photon efficiency values,

$$\Delta\Phi = \frac{(P_c - P_h)}{P_c} \cdot \frac{P_l f_{\text{tran}}}{E_p}, \quad (6.10)$$

where P_l is the laser power measured in the absence of the cell and $f_{\text{tran}} = 0.9$ is the front cell window transmission rating. For $\lambda_l = 794.77\text{nm}$, $E_p = 2.50 \times 10^{-19}\text{J}$.

In this work, η_{pr} was determined for $Q = 2\text{NLPM}$. Theoretical η_{SE} and $\eta_\gamma(t = 0)$ were calculated using the numerical and analytical P_{Xe} build up models which incorporated measured γ' and Γ' values.

Xe cryogenic separation and recovery

Cryogenic accumulation is used to produce concentrated Xe doses. The accumulation process consists of spiral glassware, downstream of the optical cell, and permanent magnets on each side producing a spin-preserving magnetic field in the enclosing volume, as shown in Fig. 6.6. The spiral is submerged in a dewar of liquid N₂. Together this is known as the cryotrap. As the gas mixture flows through the cryotrap, Xe freezes and is deposited on the spiral walls as Xe snow, whilst the buffer gases N₂ and He are evacuated. Once accumulation is complete, the spiral is submerged in a container of warm water, Xe snow thaws and is dispensed into a tedlar bag.

The volume of Xe recovered is

$$V_{\text{Xe}}(Q, t_a) = V_{\text{Xe}}^{\text{theo}}(Q, t_a) - V_{\text{loss}}(Q, t_a), \quad (6.11)$$

where $V_{\text{Xe}}^{\text{theo}} = (Q \cdot t_a \cdot f_{\text{Xe}})$ is the theoretical maximum volume of Xe recovered, $f_{\text{Xe}} = 0.03$ is the fraction of Xe in the gas mixture and V_{loss} is the volume of Xe lost to the system during the accumulation process, due to the enclosed volume of the spiral², V^{CT} , or unfrozen Xe that is not deposited on the spiral over the spiral length and is evacuated, V_{evac} , given by

$$V_{\text{loss}}(Q, t_a) = V^{\text{CT}} + V_{\text{evac}}(Q, t_a). \quad (6.12)$$

V_{evac} can be written as

$$V_{\text{evac}}(Q, t_a) = f_{\text{evac}}(Q) \cdot V_{\text{Xe}}^{\text{theo}}(Q, t_a), \quad (6.13)$$

²To eliminate the V^{CT} contribution to V_{loss} , the spiral can be washed through with N₂, however, due to possible Xe and N₂ gas mixing, this increases uncertainty in the volume of Xe in the dose and cannot be performed for 100% Xe doses. The time that thawed Xe is out of the polariser field is also increased, which may increase polarisation losses.

where f_{evac} is the fraction of Xe gas lost due to being evacuated compared to the theoretical maximum volume of Xe recovered. Whilst the Q dependence of f_{evac} is difficult to continuously quantify, $t_a \propto V_{\text{evac}}$. f_{evac} was determined by measuring V_{Xe} using a gas syringe (1.5L Super Syringe, Hamilton Company). Eq. 6.11 was used to calculate V_{loss} . V^{CT} was measured and Eq. 6.12 was used to determine V_{evac} . f_{evac} was then calculated using Eq. 6.13. V^{CT} for each spiral was measured by weighing them dry and filled with DI-water.

Eq. 6.12 shows that a cryotrap which minimises V^{CT} and f_{evac} is optimal for high Xe volume recovery, V_{Xe} . Ideally $f_{\text{evac}} \approx 0$ if all Xe that flows through the cryotrap is deposited in the spiral during cryogenic accumulation. As will be discussed later in Section 6.3.4, $f_{\text{evac}} > 0$ for the existing 5-turn spiral (Fig. 6.6a) at $p = 1.25\text{bar}$ and $Q = 2\text{NLPM}$. Therefore, a larger 8.5-turn spiral and correspondingly larger permanent magnet was installed and f_{evac} determined, as shown in Fig. 6.6b.

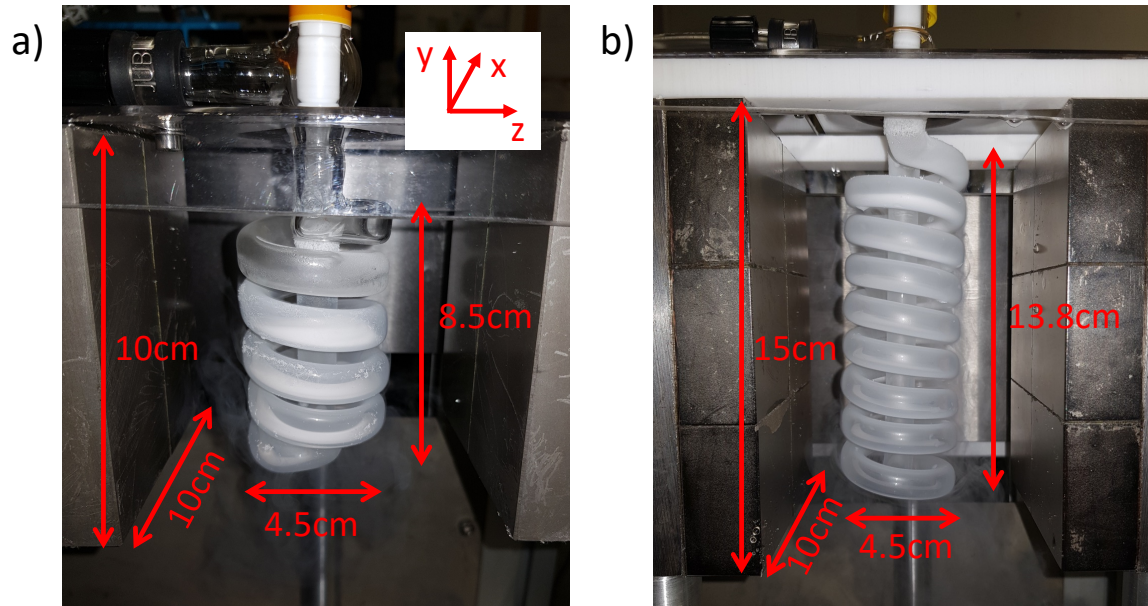


Figure 6.6: Cryogenic accumulation setups consisting of the spiral glassware and permanent magnets on each side. Xe snow (white) can be seen within the spiral. Not pictured are the liquid N_2 dewars in which the spirals are submerged. (a) Existing 5-turn spiral setup. (b) New 8.5-turn spiral setup, which is larger in order to improve Xe volume recovery at high flow rate.

Unlike the optical pumping B-field, the cryotrap magnetic field does not require high homogeneity as frozen Xe will not travel through flux lines causing depolarisation. However, gaseous Xe before freeze and after thaw will travel through flux lines causing depolarisation, so a gradual decrease in field in the direction of gas flow is desirable. The field must be $\gtrsim 500\text{G}$ across the liquid- N_2 cooled spiral for the frozen Xe relaxation

rate to be approximately field-independent [147].

The absolute magnetic field in the horizontal direction, $|B_z|$, was measured at different positions along the centre of the cryotrap (y displacement) up to the top and bottom of the spiral ($y = \pm 69\text{mm}$) as well at the edges of the cryotrap ($x = -22.5\text{mm}$, $z = 22.5\text{mm}$).

HP-¹²⁹Xe production mapping

HP-¹²⁹Xe production maps are produced by considering P_{Xe} losses during cryogenic accumulation. During cryogenic accumulation, Xe snow forms in the cryotrap and will relax over time as fresh Xe straight from the optical cell is continuously accumulated, described by

$$\begin{aligned} P_{\text{Xe}}^{\text{acc}}(Q, t_a) &= P_{\text{Xe}}(Q) \frac{T_1}{t_a} \left[1 - \exp\left(\frac{-t_a}{T_1}\right) \right] \\ &= P_{\text{Xe}}^{\text{eq}} \left[1 - \exp\left(\frac{-Q_c}{Q}\right) \right] \frac{T_1}{t_a} \left[1 - \exp\left(\frac{-t_a}{T_1}\right) \right], \end{aligned} \quad (6.14)$$

where t_a is the accumulation time and T_1 is the HP-¹²⁹Xe snow relaxation rate.

Mapping $P_{\text{Xe}}^{\text{acc}}(Q, t_a)$ to V_{Xe} and t_a allows achievable P_{Xe} and maximum V_{Xe} that can be produced per accumulation cycle with $P_{\text{Xe}} > 20\%$ for $Q = 2\text{NLPM}$ (maximum set Q) to be determined. These measures are important for polariser operation during clinical studies where t_a should be as short as possible.

For research studies where short t_a is less important, and SNR is limited such as dissolved phase imaging in organs beyond the lungs, the maximum polarisation achievable for a $V_{\text{Xe}} = 1\text{L}$ dose and its running conditions (Q, t_a) are determined.

Dose equivalence rate

The performance of large-scale polarisers is compared using dose equivalence (DE) rate [148], which is given by

$$\Delta\text{DE} = \frac{P_{^{129}\text{Xe}} \cdot f_{^{129}\text{Xe}} \cdot V_{\text{Xe}}}{t_a}, \quad (6.15)$$

where $f_{^{129}\text{Xe}}$ is fraction of ¹²⁹Xe in the Xe dose, which is set to $f_{^{129}\text{Xe}} = 1$, i.e. 100% isotopically enriched ¹²⁹Xe. This was calculated using the HP-¹²⁹Xe production maps for a range of polariser operating conditions.

6.3 Results and Discussion

6.3.1 Oven characterisation

Single compartment oven

Cell and presaturator temperatures were measured for different oven set temperatures, as shown in Fig. 6.7, with the presaturator heating tape switched off and pumping laser switched off. Presaturator and cell temperatures were then measured for different presaturator tape heating powers, at fixed oven temperatures, as shown in Fig. 6.8.

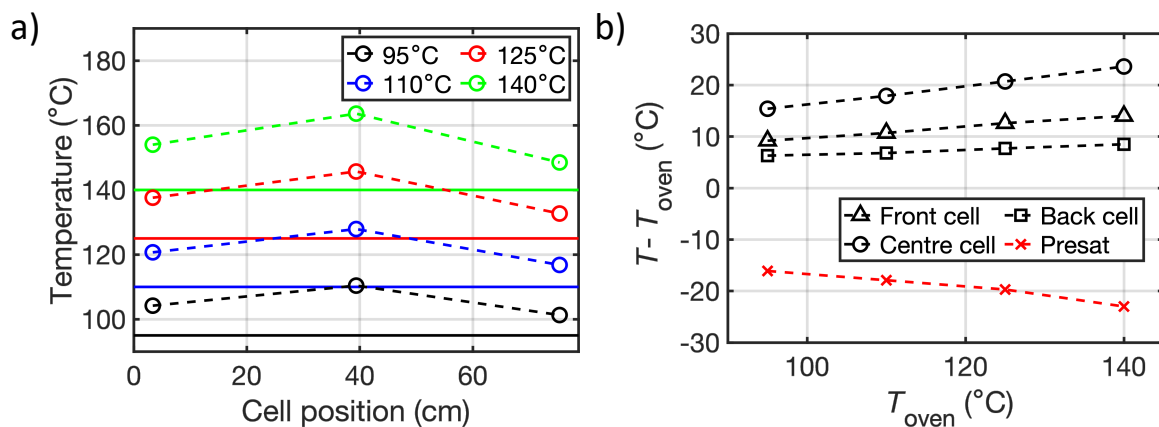


Figure 6.7: Single-compartment oven - Oven to cell and presaturator temperature differential, $T - T_{\text{oven}}$, with the presaturator heating tape switched off. (a) Cell temperature for different oven temperatures, T_{oven} . (b) $T - T_{\text{oven}}$ for different T_{oven} . Dashed lines are to guide the eye only.

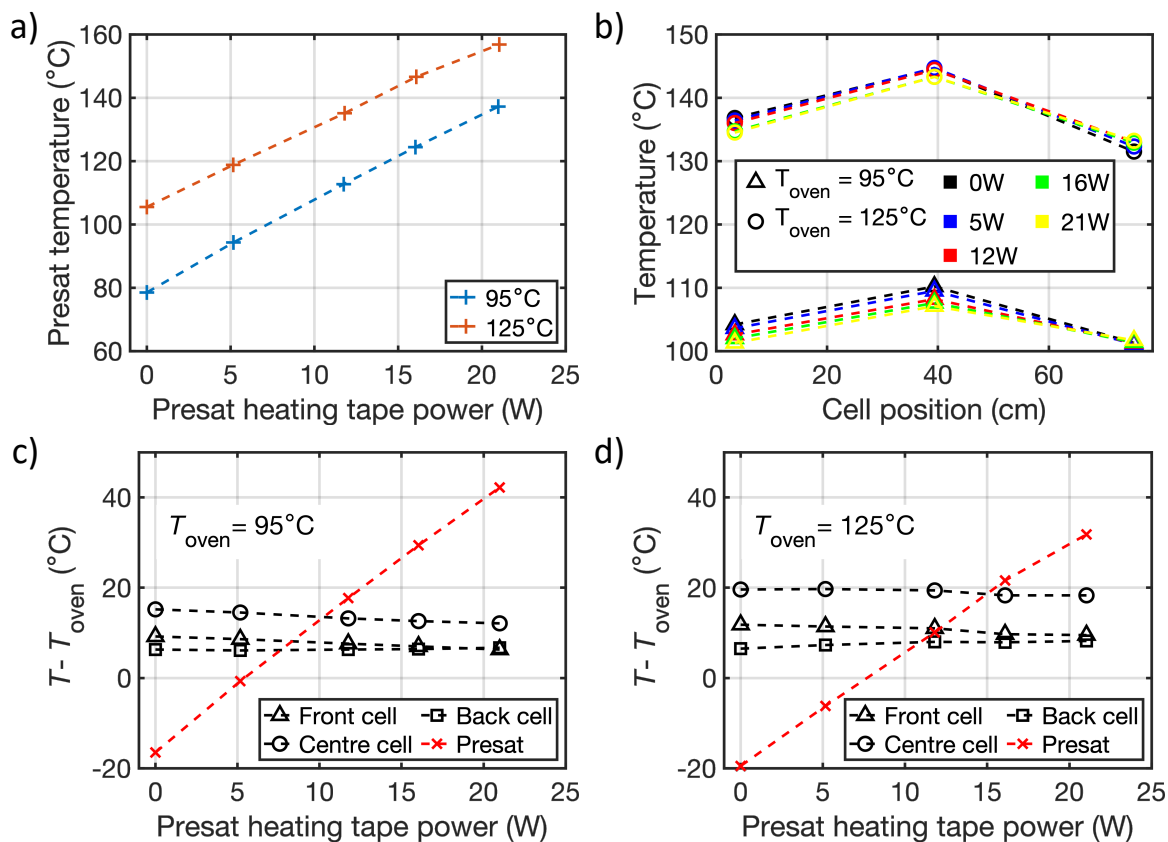


Figure 6.8: Single-compartment oven - $T - T_{\text{oven}}$ with the presaturator heating tape switched on. (a) Presaturator temperature vs heating tape power for $T_{\text{oven}} = 95^{\circ}\text{C}$ and 125°C . (b) Cell temperature for presaturator heating tape powers, where triangles and circles are for $T_{\text{oven}} = 95^{\circ}\text{C}$ and $T_{\text{oven}} = 125^{\circ}\text{C}$ respectively. (c) $T - T_{\text{oven}}$ vs presaturator heating tape power for $T_{\text{oven}} = 95^{\circ}\text{C}$ and (d) for $T_{\text{oven}} = 125^{\circ}\text{C}$. Dashed lines are to guide the eye only.

Fig. 6.7b shows that the oven to cell temperature differential gradually increases with increasing oven temperature, whereas the oven to presaturator temperature differential gradually decreases with increasing oven temperature, with the heating tape switched off. The centre cell position exhibited the greatest temperature differential, suggesting preferential heating to the centre. This may be due to the oven air exhausts being the openings for the cell inlet and outlet, positioned near the front and back of the cell, as well as the oven windows, which are not insulated, contributing to oven heat losses in these regions.

Fig. 6.8 shows that the presaturator temperature increases approximately linearly with heating tape power, however the gradient is lower with higher oven temperature. As the presaturator heating tape power is increased, oven to cell temperature differential remains approximately stable, with a small decrease in front and centre cell temperature

differentials and small increase in back cell temperature differential. This is due to heat from the heating tape dispersing within the oven and contributing to the oven temperature, reducing heating to the cell slightly. Overall, the presaturator heating tape is well isolated from the main body of the optical cell.

Fig. 6.7b and Fig. 6.8c and d can be used to set the oven temperature and presaturator heating tape power to achieve desired presaturator and cell temperatures, by using approximate linear fits. The accuracy of these fits will potentially be reduced under running conditions which are different to the tested conditions. In addition, laser heating will cause these values to vary and make achieving desired cell and presaturator temperatures more complex (see Section 6.3.2).

Multi-compartment oven testing

To test the thermal isolation between compartments, a single compartment was set to 120°C with the other compartments set to 70°C, and with the optical pumping laser switched off. The cell temperatures were then recorded once oven temperatures had stabilised. Results are shown in Table 6.2. In addition, cell and presaturator temperatures were measured for different presaturator heating tape powers, as shown in Fig. 6.9.

Table 6.2: Cell temperatures with a single oven compartment set to $T_{\text{oven}} = 120^\circ\text{C}$ whilst the other oven compartments are set to $T_{\text{oven}} = 70^\circ\text{C}$. The presaturator heating tape was switched off throughout.

Hot compartment ($T_{\text{oven}} = 120^\circ\text{C}$)	Front cell temperature ($^\circ\text{C}$)	Centre cell temperature ($^\circ\text{C}$)	Back cell temperature ($^\circ\text{C}$)	Presaturator temperature ($^\circ\text{C}$)
None	74.7 ± 0.8	75.7 ± 1.6	73.7 ± 0.9	58.9 ± 0.6
Front	140.5 ± 0.3	75.6 ± 0.4	72.03 ± 0.06	58.7 ± 0.3
Centre	71.1 ± 0.3	127.3 ± 0.5	68.6 ± 0.3	73.5 ± 0.5
Back	74.0 ± 0.5	75.8 ± 0.2	133.0 ± 0.3	97.6 ± 0.5
All	132.2 ± 0.2	126.8 ± 0.4	125.4 ± 0.2	98.7 ± 0.3

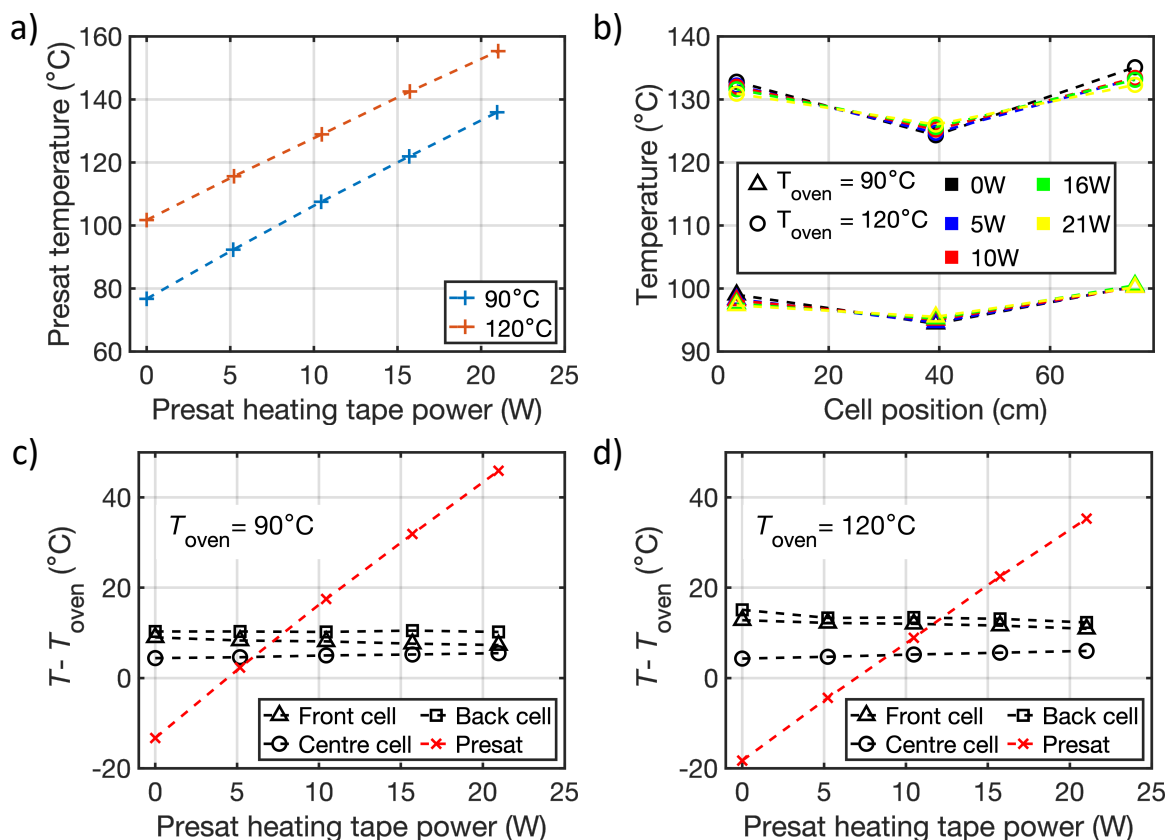


Figure 6.9: Multi-compartment oven - $T - T_{\text{oven}}$ with the presaturator heating tape switched on. (a) Presaturator temperature vs heating tape power for $T_{\text{oven}} = 90^\circ\text{C}$ and 120°C . (b) Cell temperatures for different presaturator heating tape powers, where triangles and circles are for $T_{\text{oven}} = 90^\circ\text{C}$ and $T_{\text{oven}} = 120^\circ\text{C}$ respectively. $T - T_{\text{oven}}$ vs presaturator heating tape power for (c) $T_{\text{oven}} = 90^\circ\text{C}$ and (d) $T_{\text{oven}} = 120^\circ\text{C}$. Dashed lines are to guide the eye only. Discrepancy between back cell temperature (cell position = 75.5cm) here and in Table 6.2 was investigated but no cell or oven setup differences were observed.

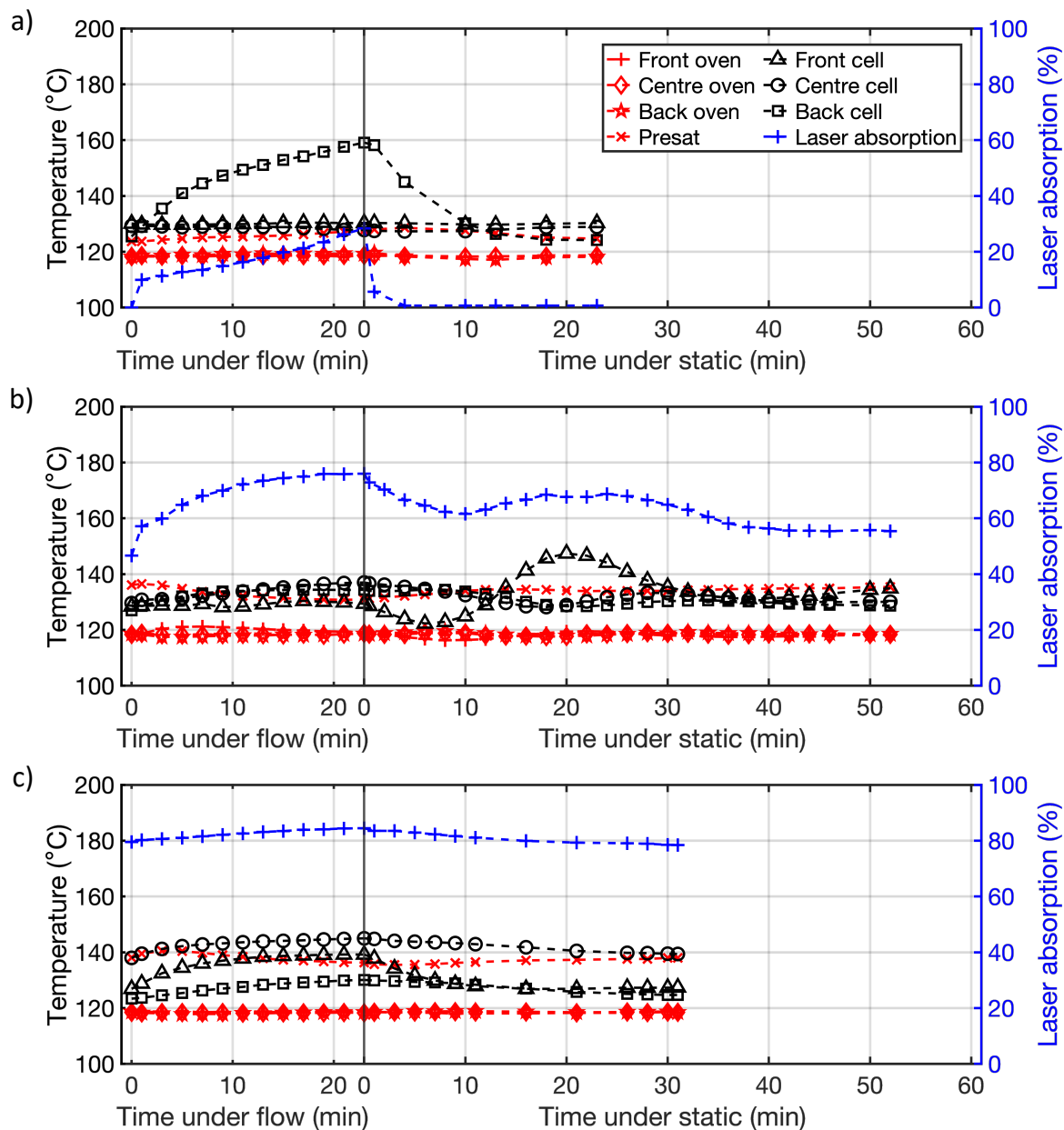
Table 6.2 shows minimal changes in cell temperature within a given compartment for a 50°C temperature differential between compartments. The centre cell temperature remained the most consistent, with a 0.1°C absolute change in temperature. The back cell temperature was the least consistent, with a 5.1°C decrease in temperature when the centre compartment was hot. This could suggest higher air flow rate to the central oven compartment, or preferential air or heat flow through the oven partitions out of the central oven compartment. Glassware conduction of heat could also contribute to this. For a 50°C temperature differential between compartments, it was concluded that the observed change in cell temperature indicated acceptable thermal isolation between compartment, therefore allowing us to proceed with this oven design.

The presaturator temperature was observed to decrease with the hot compartment going from the back compartment to the front compartment. This is because the presaturator thermocouple is located within the back oven compartment, near the presaturator-main cell body junction. In addition, the presaturator is small and wrapped in heating tape so thermal conduction along the presaturator is likely more significant than along the cell.

From Table 6.2, it can be seen that the difference in temperature between the oven temperature and the cell temperature increases with oven temperature, and is greatest for the front oven compartment, similar to observed in Fig. 6.7 for the single-compartment oven. Therefore this design change has not removed the oven-to-cell temperature differential, and must be considered when setting the oven temperature to achieve a desired cell temperature. Fig. 6.9 shows reasonable thermal isolation from the heated presaturator to the cell main body, similar to the single-compartment setup (Fig. 6.8).

6.3.2 Laser absorption for different Rb source distributions

Laser absorption and cell and presaturator temperatures were measured under static and under flow ($Q = 2\text{NLPM}$) for the different Rb source distributions. The laser was set to maximum operating current $I = 38\text{A}$. All ovens were set to 118.5°C and the Rb presaturator heating tape was set to 9.4W . The polariser under static operation was allowed to stabilise, a condition met when there was $\leq 0.1^\circ\text{C}/\text{min}$ change for oven, cell and presaturator temperatures. The optical cell was then opened with a flow rate set to $Q = 2\text{NLPM}$. Temperatures and laser absorption were recorded every 2 mins from 1 min to 23 mins under flow. After 23 mins under flow, the cell valves were closed. The time taken for the polariser under static conditions to stabilise was then recorded. Results are given in Table 6.3, and measurements of temperatures and laser absorption during acquisitions for the 2nd repeat are shown in Fig. 6.10.



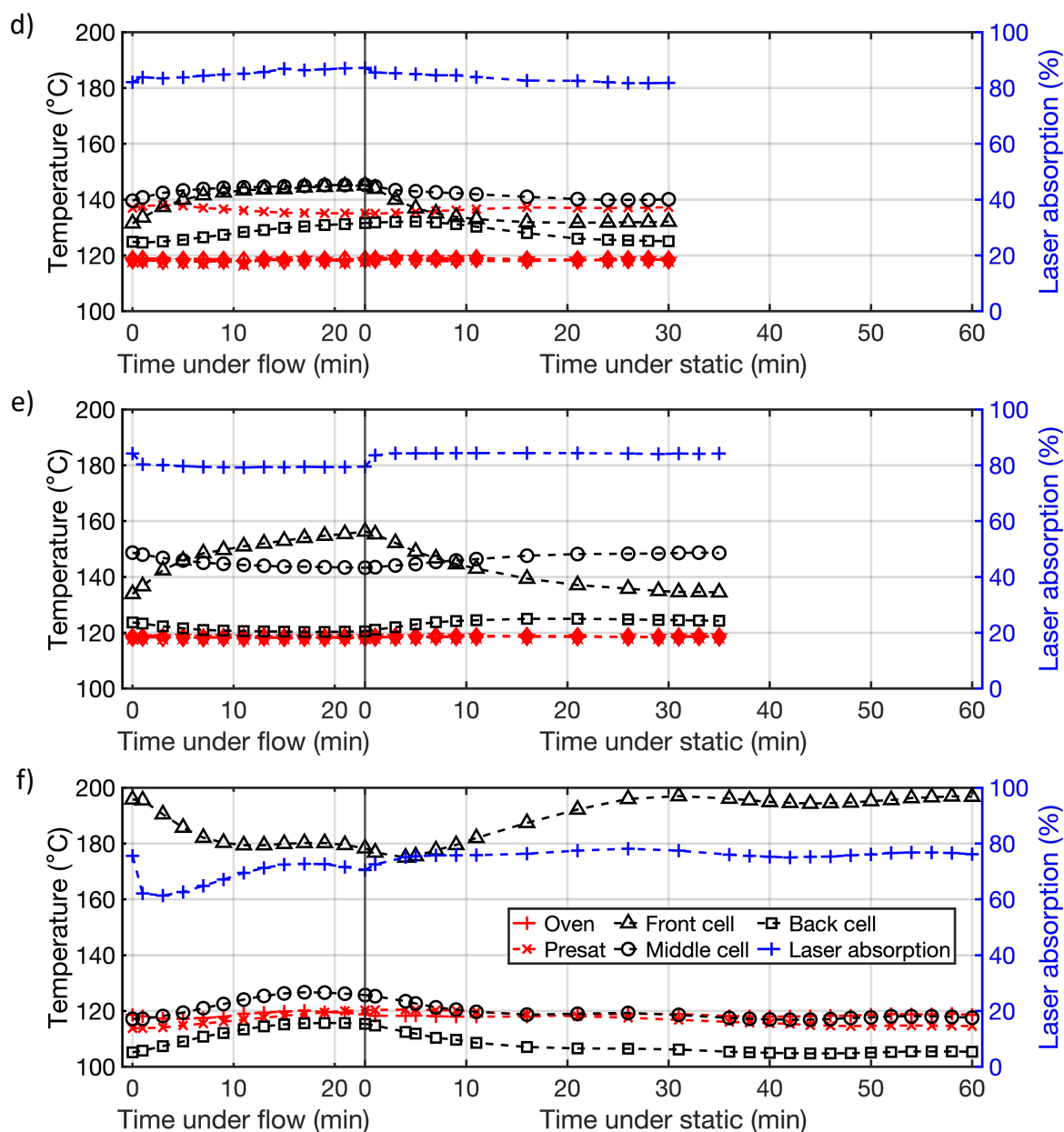


Figure 6.10: 2nd repeat of temperatures and laser absorption static to under flow ($Q = 2\text{NLPM}$) and under flow to static gas for the following Rb distributions; (a) no Rb in the main body, Rb in the presaturator (presat) only, (b) 2 Rb pools in the main cell body (c) 4 Rb pools in the main cell body (d) 4 Rb pools in the main cell body and with dry-ice Rb coating, (e) no presaturator, 4 Rb pools in the main cell body and performed for $Q = 1.7\text{NLPM}$ due to a mass flow regulator issue, (f) 4 Rb pools in the main cell body and presaturator in a single compartment oven.

Table 6.3: Temperatures and laser absorption for static to under flow ($Q = 2\text{NLPM}$) and under flow to static gas for different Rb source distributions, using the multi-compartment oven.

Rb distribution		Static: Temperature ($^{\circ}\text{C}$)				Under flow: Temperature ($^{\circ}\text{C}$)				Time to return to static (min)		
Rb in the pre-sat?	Rb pools in the main body?	Laser absorption (%)	front	centre	back	presat	Laser absorption (%)	front	centre	back	presat	
yes	no	1.2 ± 1.5	130.1 ± 0.2	129.1 ± 0.2	126 ± 2	125 ± 1	22 ± 14	130.3 ± 0.4	129.0 ± 0.8	148 ± 10	126 ± 3	37 ± 27
yes	2 pools	57 ± 12	135 ± 6	131 ± 2	128 ± 1	135 ± 2	69 ± 8	132 ± 6	134 ± 3	133 ± 3	133 ± 2	49 ± 11
yes	4 pools	78 ± 1	127 ± 1	139.3 ± 0.9	125 ± 1	138.0 ± 0.3	83 ± 2	137 ± 4	143 ± 2	127 ± 2	138 ± 2	34 ± 6
yes	4 pools + coating	81.5 ± 0.9	131.5 ± 0.7	139.9 ± 0.2	125.1 ± 0.1	137.2 ± 0.1	85 ± 1	142 ± 4	144 ± 1	128 ± 2	136 ± 1	30.7 ± 0.6
no*	4 pools	84.2 ± 0.3	134.3 ± 0.3	148.7 ± 0.3	124.3 ± 0.4	n/a	79.7 ± 0.7	150 ± 6	145 ± 2	121 ± 1	n/a	37 ± 3
yes	4 pools + coating†	75.9 ± 0.5	196 ± 2	117.4 ± 0.3	105.2 ± 0.3	114.9 ± 0.5	68 ± 4	183 ± 5	123 ± 4	112 ± 3	117 ± 2	49 ± 10

* $Q = 1.7\text{NLPM}$ used as opposed to 2NLPM due to a mass flow regulator issue, which could not be diagnosed.

†Coating due to dry-ice no longer visible on cell and the single compartment oven used.

Table 6.3 shows that static and under-flow laser absorption increases with increasing number of Rb pools in the main cell body. This is due to the higher Rb pool surface area allowing [Rb] to build up locally in different parts of the cell, leading to overall greater [Rb] across the cell and increasing laser absorption. The difference between static and under-flow laser absorption also decreases with increasing number of Rb pools in the main cell body. This suggests more uniform [Rb] build up occurs, so as gas flows through the optical cell, carrying [Rb] with it, regional [Rb] values neither decrease nor increase significantly.

In addition, front and centre cell temperatures increase whilst the back cell temperature decreases with increasing Rb sources in the main body. The greater [Rb] build up towards the front of the cell leads to high laser absorption, and correspondingly higher cell temperature due to laser heating and higher front cell temperature. This higher absorption at the front of the cell also leads to lower photon flux at the back of the cell and correspondingly lower laser heating and cell temperatures at the back of the cell.

Fig. 6.10e and Table 6.3 show that the removal of the Rb presaturator leads to lower laser absorption under flow compared to static operation. This is due to [Rb]=0 gas flowing into the cell main body at the cell inlet, which depletes [Rb] at the back of the cell. As a result, the laser absorption and back cell temperature are both reduced. Also, later in Section 6.3.4, the optimal laser absorption during flow was shown to be higher than the optimal laser absorption during static operation. Therefore, it is beneficial to be able to increase the laser absorption using a presaturator under-flow without having to adjust the oven temperature.

Fig. 6.10f and Table 6.3 show that higher laser absorption and more homogeneous cell temperatures (lower front cell temperature and higher centre and back cell temperatures) were recorded with the 3-compartment oven compared to the single-compartment oven.

Overall, these results suggest 4 Rb pools and coating is the desirable Rb distribution. However, we note that the Rb coating on the cell walls quickly disappeared with polariser use; the coating was likely thin and a fast rate of evaporation occurred due to the higher temperatures used here compared to the batch-mode polariser systems in refs. [99, 145], so this step may be not needed for our system.

Rb runaway

An incident of Rb runaway occurring was recorded to illustrate the phenomenon. Rb runaway occurred in the presaturator cell with 4 Rb pools in the single-compartment oven, as shown in Fig. 6.11. In this setup, the oven thermocouple was placed between the centre and back oven inlets.

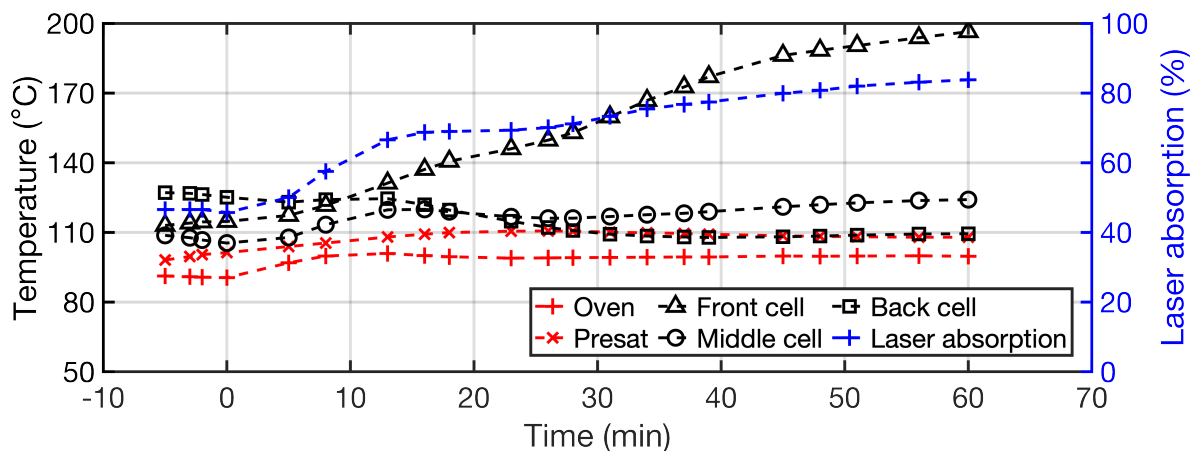


Figure 6.11: Rb runaway occurring in the single compartment oven. The oven thermocouple was placed towards the back of oven. At time = 0 min, the set oven temperature was changed from 90°C to 100°C.

Fig. 6.11 shows that even after the oven temperature had stabilised at 100°C, the front cell temperature and laser absorption continued to increase. This likely indicates a build up of [Rb] at the front of the cell, leading to higher laser heating at the front of the cell. The nearby Rb pool at the front of the cell liberated more Rb vapour as the temperature increased and the poor coupling between the front cell temperature and the global oven temperature meant the oven heating did not adjust for the increase in front cell temperature, as shown in Fig. 6.11 by the stable oven temperature. Therefore, [Rb] continued to build up, which is an example of unwanted Rb runaway. In addition, this resulted in low photon flux at the back of the cell, lowering laser heating in this region as indicated by the decrease in back cell temperature. The nearby positioning of the oven thermocouple may have resulted in an increase in oven heating, further exacerbating the [Rb] build up and laser heating at the front of the cell.

For measurements using the single-compartment oven shown in Table 6.3 and Fig. 6.10f, the oven thermocouple was moved to near the front of the cell to see if this could improve front-of-cell thermal regulation by coupling the oven thermocouple to the high laser heating near the front of the cell. This resulted in stable front cell temperature, although cell temperatures were very heterogeneous, suggesting photon absorption heterogeneity and overall lower power absorption than seen with the same cell using the

multi-compartment oven.

6.3.3 1D simulations of Rb density heterogeneity and laser absorption

Perfect [Rb] homogeneity, $L_{\text{Rb}} = L_{\text{cell}}$, and three levels of [Rb] heterogeneity, corresponding to three L_{Rb} values, were simulated. $\langle[\text{Rb}]\rangle$, P_{Xe} and Q_c were calculated for different temperatures and corresponding laser absorption for each L_{Rb} value. $Q = 2\text{NLPM}$ and saturation [Rb] were used as given in Table 3.1. P_{Xe} and Q_c were determined using both the numerical (spatially dependent) and the analytical (cell-averaged) models. The optimal temperature/laser absorption for maximum P_{Xe} was then determined for each L_{Rb} value. Spatial P_{Xe} , P_{Rb} and laser absorption along the cell length for $L_{\text{Rb}} = L_{\text{cell}}$, i.e. perfect [Rb] homogeneity, for each optimal temperature were plotted as shown in Fig. 6.13.

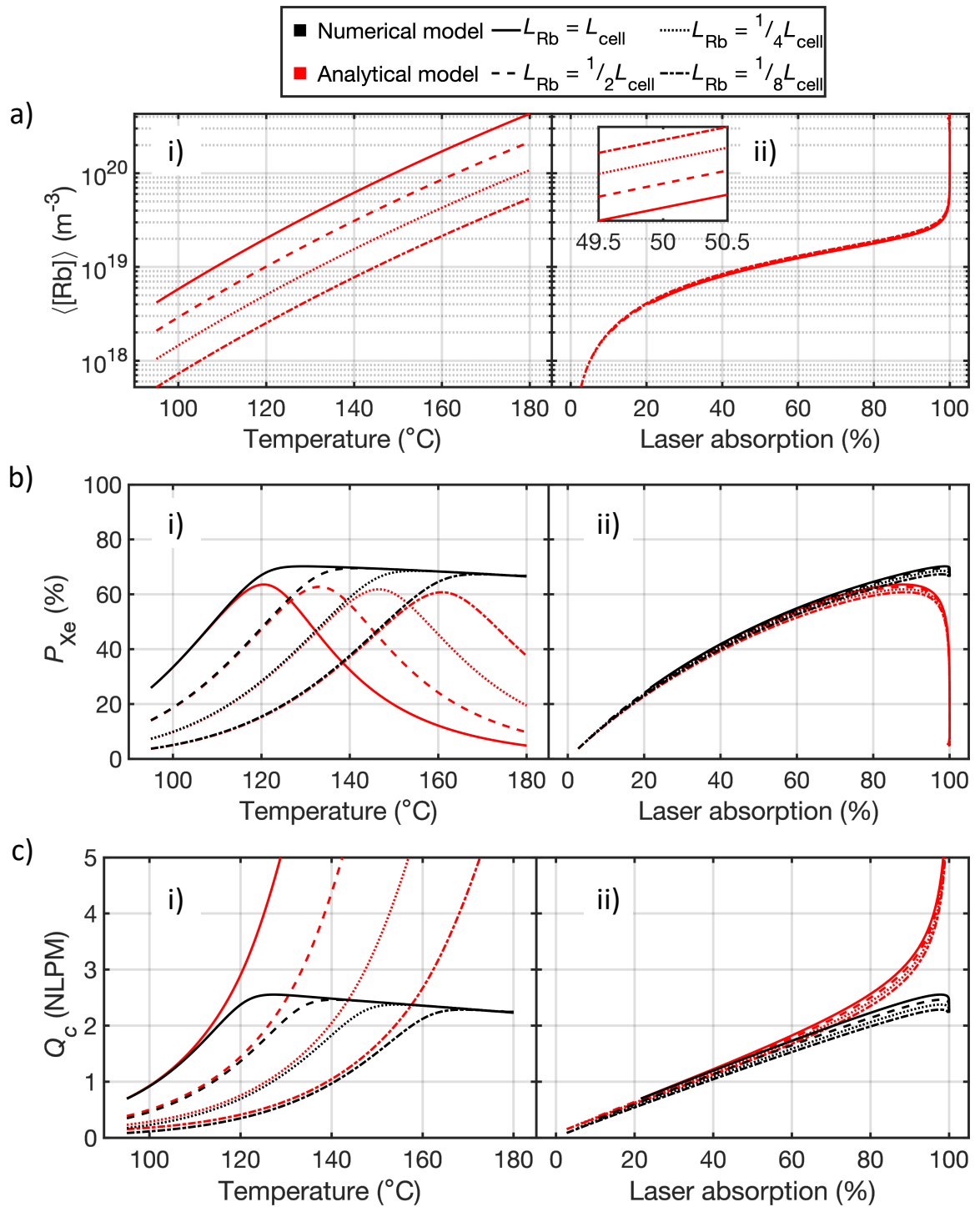


Figure 6.12: (a) Cell-averaged Rb density, $\langle [\text{Rb}] \rangle$, (b) Xe polarisation, P_{Xe} and (c) critical flow rate, Q_c , vs (i) temperature and (ii) laser absorption for different L_{Rb} . Cell lengths tested were $L_{\text{Rb}} = L_{\text{cell}}$ (solid lines), $L_{\text{Rb}} = L_{\text{cell}}/2$ (dashed lines), $L_{\text{Rb}} = L_{\text{cell}}/4$ (dotted lines) and $L_{\text{Rb}} = L_{\text{cell}}/8$ (dash-dotted lines), corresponding to increasing $[\text{Rb}]$ heterogeneity. Black and red lines indicate the numerical model and analytical models respectively.

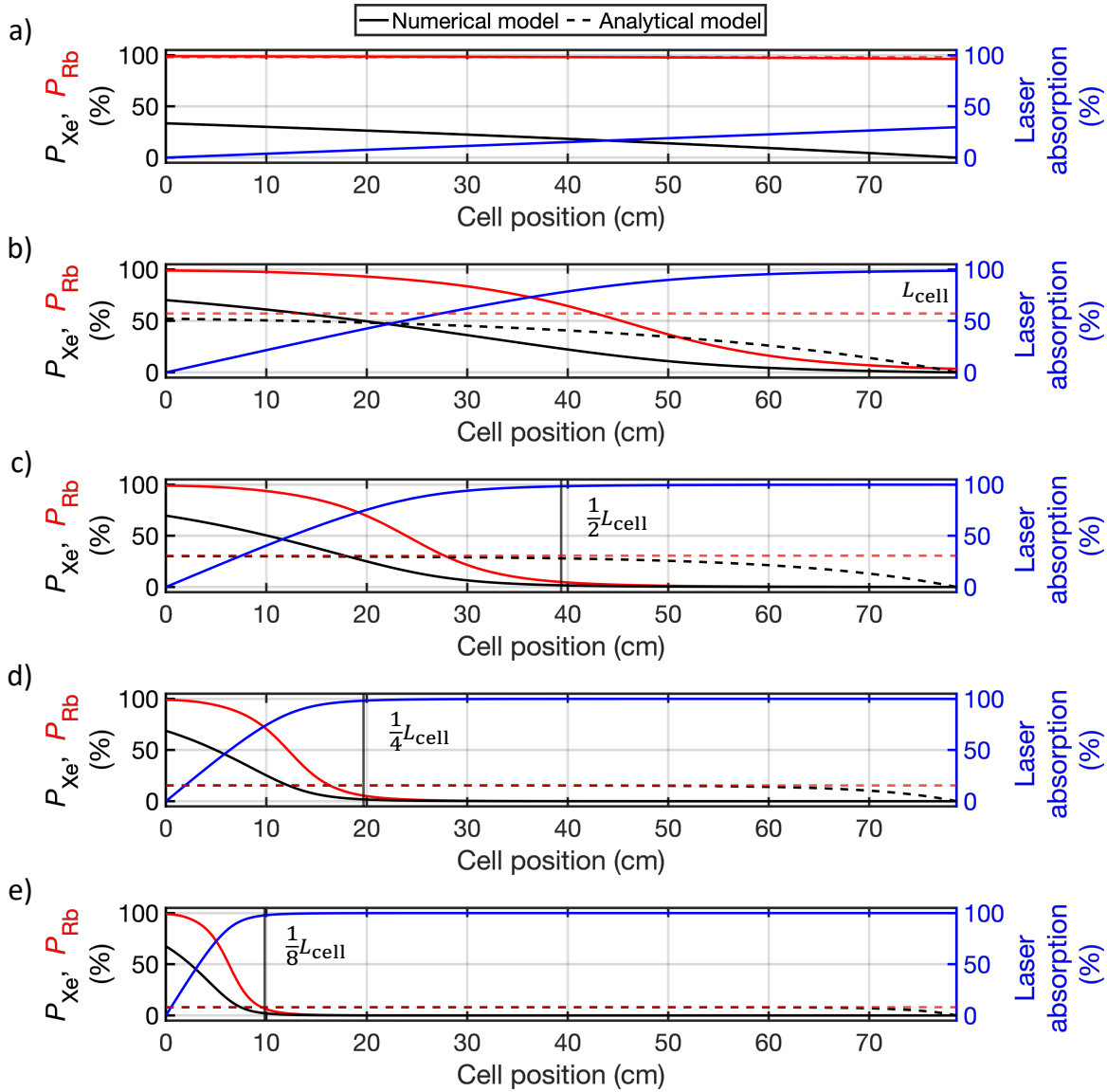


Figure 6.13: Modelled P_{Xe} , Rb polarisation, P_{Rb} , and laser absorption vs cell position using the numerical (solid lines) and analytical (dashed lines) models for $Q = 2\text{NLPM}$ and $L_{Rb} = L_{cell}$ (homogeneous [Rb]). This was performed at different temperatures corresponding to optimal temperatures for different L_{Rb} values. (a) $T = 100^\circ\text{C}$ where low laser absorption occurs. (b) $T = 129.5^\circ\text{C}$, optimal T for $L_{Rb} = L_{cell}$. (c) $T = 141.5^\circ\text{C}$, optimal T for $L_{Rb} = L_{cell}/2$. (d) $T = 155^\circ\text{C}$, optimal T for $L_{Rb} = L_{cell}/4$. (e) $T = 169^\circ\text{C}$, optimal T for $L_{Rb} = L_{cell}/8$.

Fig. 6.12ai shows that $\langle[\text{Rb}]\rangle$ varied significantly with temperature for different levels of $[\text{Rb}]$ heterogeneity, as expected. This corresponded to greatly varying optimal temperatures for maximum P_{Xe} , as well as Q_c values as shown in Fig. 6.12bi and ci respectively. The relationship between the laser absorption dependence of $\langle[\text{Rb}]\rangle$ (Fig. 6.12aii), P_{Xe} (Fig. 6.12bii) and Q_c (Fig. 6.12cii) are mostly unaffected by the level of $[\text{Rb}]$ heterogeneity, regardless of P_{Xe} model used. This is also true for the optimal laser absorption for maximum P_{Xe} (Fig. 6.12bii). This shows that the optimal value of laser absorption is a more robust parameter than optimal temperature, which is helpful for optimisation efforts as well as comparing modelling to experimental measurements.

In addition, the direct relationship between $\langle[\text{Rb}]\rangle$ and laser absorption unaffected by $[\text{Rb}]$ heterogeneity seen in Fig. 6.12aii, and the relatively small change in P_{Xe} and Q_c for different amounts of $[\text{Rb}]$ heterogeneity across all laser absorption values seen in Fig. 6.12bii and cii shows that optimal $\langle[\text{Rb}]\rangle$ level is more significant than $[\text{Rb}]$ homogeneity for P_{Xe} build up. On the surface this appears to discount our efforts to improve $[\text{Rb}]$ homogeneity in our setup, however simulated maximum P_{Xe} increased slightly with $[\text{Rb}]$ homogeneity. Also, optimal temperature decreased with $[\text{Rb}]$ homogeneity, as shown in Fig. 6.12bi. Therefore high $[\text{Rb}]$ homogeneity is still desirable as thermal regulation is less demanding and more easily achieved at low operating temperatures. Also, for future work, anti-relaxation surface coatings, which have been shown to reduce Γ' [21, 149], can only be used at low temperatures where the coating does not react with Rb. n-octadecyltrichlorosilane (OTS) surface coating reacts with Rb at 190°C [149], although elevated internal cell gas temperatures due to laser heating, as seen in Fig. 4.8b, must also be considered.

From Fig. 6.12bii and 6.13a, at low laser absorption, P_{Xe} determined from the analytical and numerical models are equal. This is due to the high homogeneous P_{Rb} across the optical cell so average and spatial P_{Rb} values are approximately equal.

From Fig. 6.13b, at the laser absorption which maximises P_{Xe} in the numerical model, P_{Rb} is heterogeneous across the cell, $\langle P_{\text{Rb}} \rangle$ is significantly different to P_{Rb} across the cell and P_{Xe} differs between models. The optimal laser absorption for maximum P_{Xe} for the numerical model is higher than that for the analytical model, due to the inverse sigmoid shape of P_{Rb} heterogeneity which lowers $\langle[\text{Rb}]\rangle$. This P_{Rb} distribution is due to mismatch in laser and Rb absorption line shapes. Precise matching would result in a steeper curve and analytical and numerical models would more closely match at the numerical optimal laser absorption.

Fig. 6.13 shows that for $L_{\text{Rb}} = L_{\text{cell}}$, i.e. cell with perfect $[\text{Rb}]$ homogeneity, at optimal temperature/laser absorption for maximum P_{Xe} for the different L_{Rb} values explored in Fig. 6.12, L_{Rb} approximately corresponds to the cell position at which P_{Rb} is near zero.

Beyond this cell position, $P_{\text{Rb}} \sim 0$, and so there is no initial build up in P_{Xe} for the numerical model. Furthermore, in Fig. 6.12bi and ci, where at the optimal temperature for maximum P_{Xe} for a given L_{Rb} value, numerical P_{Xe} and Q_c values are equal for all higher L_{Rb} simulation values up to $L_{\text{Rb}} = L_{\text{cell}}$. Therefore, the distribution of P_{Rb} heterogeneity across the cell has a similar effect on P_{Xe} build up to [Rb] heterogeneity described by Fig. 6.5b and modelled in Fig. 6.12, where at higher than optimal laser absorption there is an effective reduction in the cell length which lowers P_{Xe} .

Although in the numerical model the effective cell length is reduced at high laser absorptions, the higher [Rb] means that fast γ_{SE} occurs in the high P_{Rb} towards the front of cell, meaning P_{Xe} at the front of the cell is still very high. This is different to the analytical model, where the large $P_{\text{Rb}} \sim 0$ region results in low $\langle P_{\text{Rb}} \rangle$, and $\langle P_{\text{Rb}} \rangle \sim P_{\text{Xe}}$ at the front of the cell.

This also helps explain the laser absorption dependence of Q_c for both models shown in Fig. 6.12cii. For the analytical model, $\tau_{\text{up}}^{-1} \propto [\text{Rb}]$ increases with increasing laser absorption, and t_{res} is assumed to be constant, leading to $Q_c \propto [\text{Rb}]$ (Eq. 6.2). However for the numerical model, the effective reduction in the cell length (or V_{cell}) as laser absorption increases beyond its optimal value also corresponds to an effective reduction in t_{res} (Eq. 6.1). The decrease in effective t_{res} is greater than the decrease in τ_{up} and so Q_c gradually decreases beyond its optimal value.

Flow rate dependence

Simulations performed for $L_{\text{Rb}} = L_{\text{cell}}$ were extended to model for different Q values, as shown in Fig. 6.14. P_{Xe} and Q_c values were determined for each Q and laser absorption value. The absolute percentage difference between the two models for P_{Xe} , $|\% \text{diff}|_{P_{\text{Xe}}}$, and Q_c , $|\% \text{diff}|_{Q_c}$, were also determined, as shown in Fig. 6.14ci and cii, respectively.

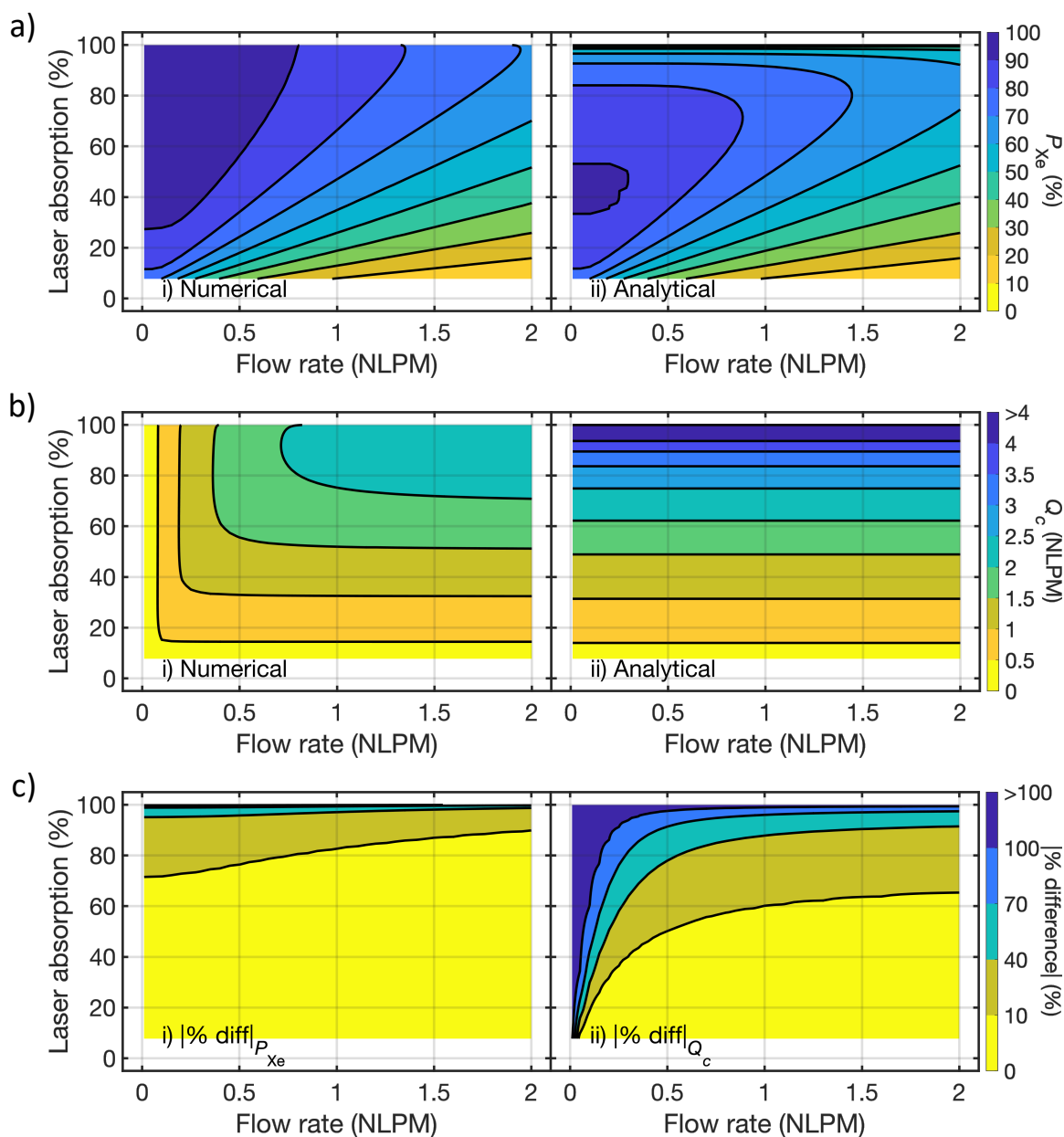


Figure 6.14: Contours of laser absorption vs flow rate vs (a) P_{Xe} and (b) Q_c . This was performed for (ai, bi) the numerical P_{Xe} build up model and (aii, bii) the analytical P_{Xe} build up model. (c) The absolute percentage difference between the numerical and analytical models, $|\% \text{ difference}|$, was determined for (ci) P_{Xe} values, $|\% \text{ diff}|_{P_{Xe}}$, and (cii) Q_c values, $|\% \text{ diff}|_{Q_c}$.

Fig. 6.14ci and cii show that P_{Xe} and Q_c values produced by the numerical and analytical models agree ($|\%difference| < 10\%$) at low to moderate laser absorption ($L_{abs} < 60\%$) and high Q values ($Q \geq 1.1\text{NLPM}$). Disagreement ($|\%difference| \geq 10\%$) is greatest at low Q and high laser absorption values. $|\%diff|_{Q_c} > |\%diff|_{P_{Xe}}$ for all simulated values due to $P_{Xe}(Q = 0)$ values, where high $|\%diff|_{P_{Xe}}$ occurs, being used to calculate Q_c values.

The deviation in models at low Q and high laser absorption is due to the non-exponential P_{Xe} build up that occurs in the numerical model, compared to exponential P_{Xe} build up defined by Eq. 6.4 for the analytical model. High laser absorption results in short τ_{up} and low Q results in long t_{res} . Under these conditions, $\tau_{up} < t_{res}$ and $1 - \exp(-t_{res}/\tau_{up}) \sim 1$, so P_{Xe} build up in the numerical model is highly dependent on the inverse sigmoidal spatial distribution of P_{Rb} , and leads to lower Q_c values than predicted by the analytical model, which are also Q dependent. At high Q and/or low laser absorption, $\tau_{up} > t_{res}$ and so $1 - \exp(-t_{res}/\tau_{up}) \ll 1$, therefore P_{Rb} is always much higher than $P_{Xe}(Q)$ (Eq. 6.4), at a given cell position where P_{Rb} is non-zero and P_{Xe} behaves exponentially, with no Q dependence of Q_c .

The other cause of the discrepancy in P_{Xe} values is the difference in $P_{Xe}(Q = 0)$ between the models. This is due to the difference between $\langle P_{Rb} \rangle$ used by the analytical model and $P_{Rb}(z = 0)$, as $P_{Rb}(z = 0) > \langle P_{Rb} \rangle$ for all laser absorption values, $P_{Xe}(Q = 0)$ values predicted by the numerical model will always be greater than those predicted by the analytical model. This discrepancy increases with laser absorption due to the increase in P_{Rb} heterogeneity across the cell.

Fig. 6.14ai shows that the numerical model predicts near-100% laser absorption for maximum P_{Xe} at a given Q value, for $0 \leq Q \leq 2\text{NLPM}$. Whereas the analytical model (Fig. 6.14aii) predicts a gradual increase in optimal laser absorption with increasing Q , from 44% for $Q = 0.01\text{NLPM}$. Optimal laser absorption for maximum Q_c differs for each model, with the analytical model predicting 100% laser absorption for all values of Q , as shown in Fig. 6.14bii, and the numerical model (Fig. 6.14bi) predicting an increase in optimal laser absorption for maximum Q_c with increasing Q . This means selection of the appropriate model is important for optimisation efforts. Experimental measurements are needed to assess model suitability under varying conditions.

P_{Xe} is always predicted to be greater, and Q_c always lower, for the numerical model than the analytical model. Given the discrepancy in P_{Xe} build up from the literature has shown lower P_{Xe} and Q_c than expected from simulations [55], the choice of model cannot explain both P_{Xe} and Q_c under performance. We would suggest that the choice of model may explain lower Q_c than expected, but measured P_{Xe} may be lower than simulations due to other factors such as an incomplete optical pumping model (see

Section 3.3.1) or temperature dependent Γ' (see Section 3.3.3).

The limitations of both models are that plug flow was assumed. Also the output P_{Xe} was sampled as a single thin ‘slab’ at the front of the cell, whereas in practice, the sampled gas is likely extracted over a thicker ‘slab’ at the front of the cell, which would result in lower P_{Xe} values. In addition, elevated internal gas temperatures observed in Chapter 4, which lower P_{Xe} and laser absorption (Table 4.9), were not included in these simulations. However this contribution is small compared to P_{Xe} and laser absorption changes with [Rb].

6.3.4 HP-¹²⁹Xe production optimisation

Determination of cell-specific γ' and Γ'

The cell was filled with 3%Xe/10%N₂/87%He gas mix at $T = 20^\circ\text{C}$ to $p = 0.92\text{bar}$, corresponding to the same number density at $T = 125^\circ\text{C}$ for 1.25bar. Γ_{down} and [Rb] were measured for four different oven temperatures (111°C, 118.5°C, 122.5°C, 126°C). γ' and Γ' were then determined by a linear fit of Γ_{down} against [Rb], as shown in Fig. 6.15.

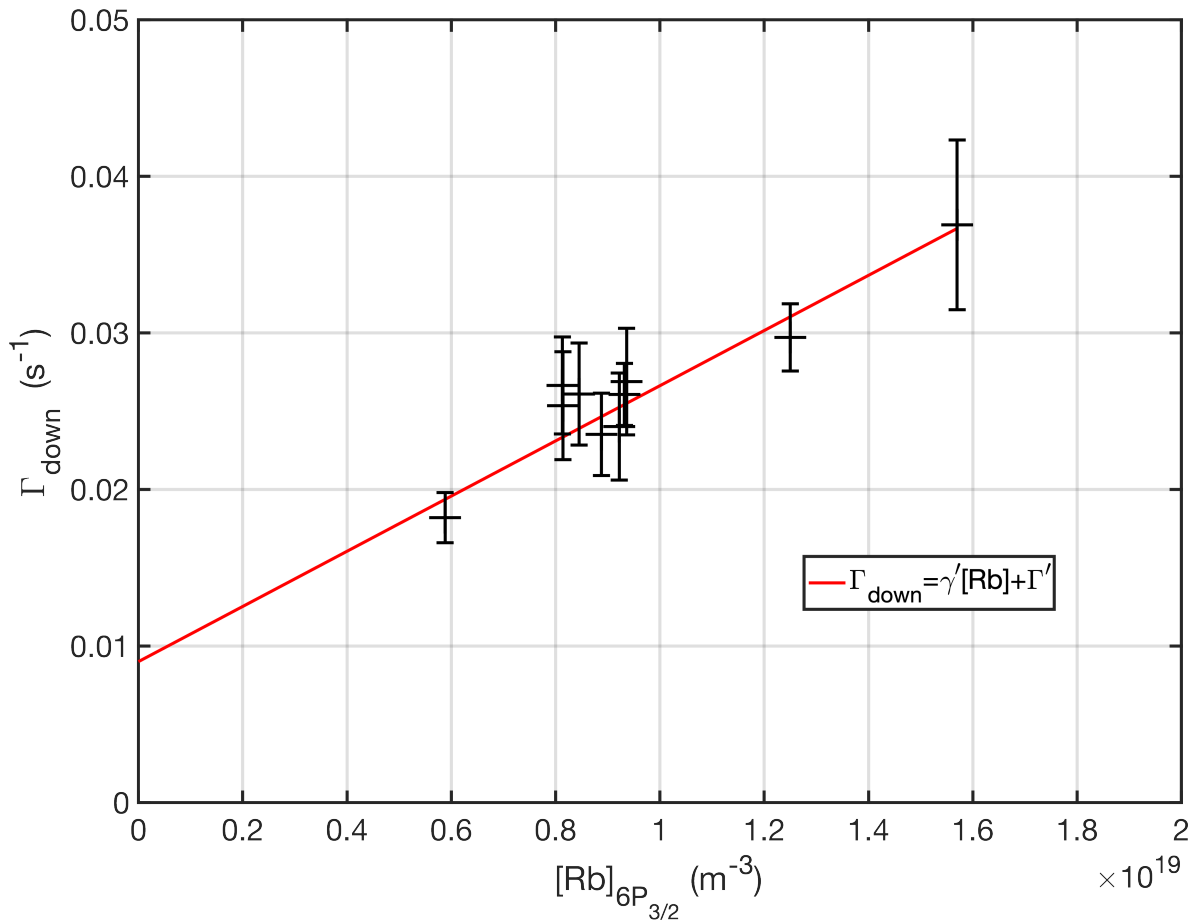


Figure 6.15: Spin-down, Γ_{down} , vs $[\text{Rb}]$ measured with the $5S_{1/2} \rightarrow 6P_{3/2}$ Rb transition, for the Rb coated, 4 Rb pools cell. From the linear fit, $\gamma' = (1.8 \pm 0.2) \times 10^{-21} \text{ m}^3\text{s}^{-1}$ and $1/\Gamma' = 111 \pm 27 \text{ s}$.

From Fig. 6.15, $\gamma' = (1.8 \pm 0.2) \times 10^{-21} \text{ m}^3\text{s}^{-1}$, which is larger than the value determined in Chapter 5, likely due to the lower gas number density used, which increases the molecular lifetime, defined in Eq. 3.92, increasing the fraction of short regime interactions, f_F , which enhances the vdW contribution to the spin-exchange cross section defined in Eq. 3.107.

$1/\Gamma' = 111 \pm 27 \text{ s}$ was also determined, which is smaller than determined in Chapter 5. This may be due to the larger Rb pool surface area on the cell walls, increasing Xe relaxation due to collisions with the cell walls.

P_{Xe} and Q_c laser absorption dependence measurements

P_{Xe} was measured at $Q = 2\text{NLPM}$ and static gas flow for different oven temperatures are shown in Fig. 6.16a. P_{Xe} measurements were performed on the polariser Xe polarimetry setup described in Section 5.2.2. Flip angle calibration and ¹H signal reference

were repeated, negating the use of a flip angle correction factor used in Chapter 5. Corresponding laser absorption measurements are shown in Fig. 6.16b, and are used to plot P_{Xe} laser absorption dependence in Fig. 6.16c. These P_{Xe} values were used to calculate Q_c using Eq. 6.5, and are shown in Fig. 6.16d. Simulations were also performed, which incorporated measured γ' and Γ' values from Fig. 6.15 to compare theoretical and experimental values.

To validate the use of two measurements and Eq. 6.5 to determine Q_c , Q_c values were also determined by measuring P_{Xe} for different Q values and fitting to Eq. 6.4, as shown in Fig. 6.17. This was performed for optimal $T_{oven} = 111^\circ\text{C}$ as well as $T_{oven} = 126^\circ\text{C}$ corresponding to high laser absorption.

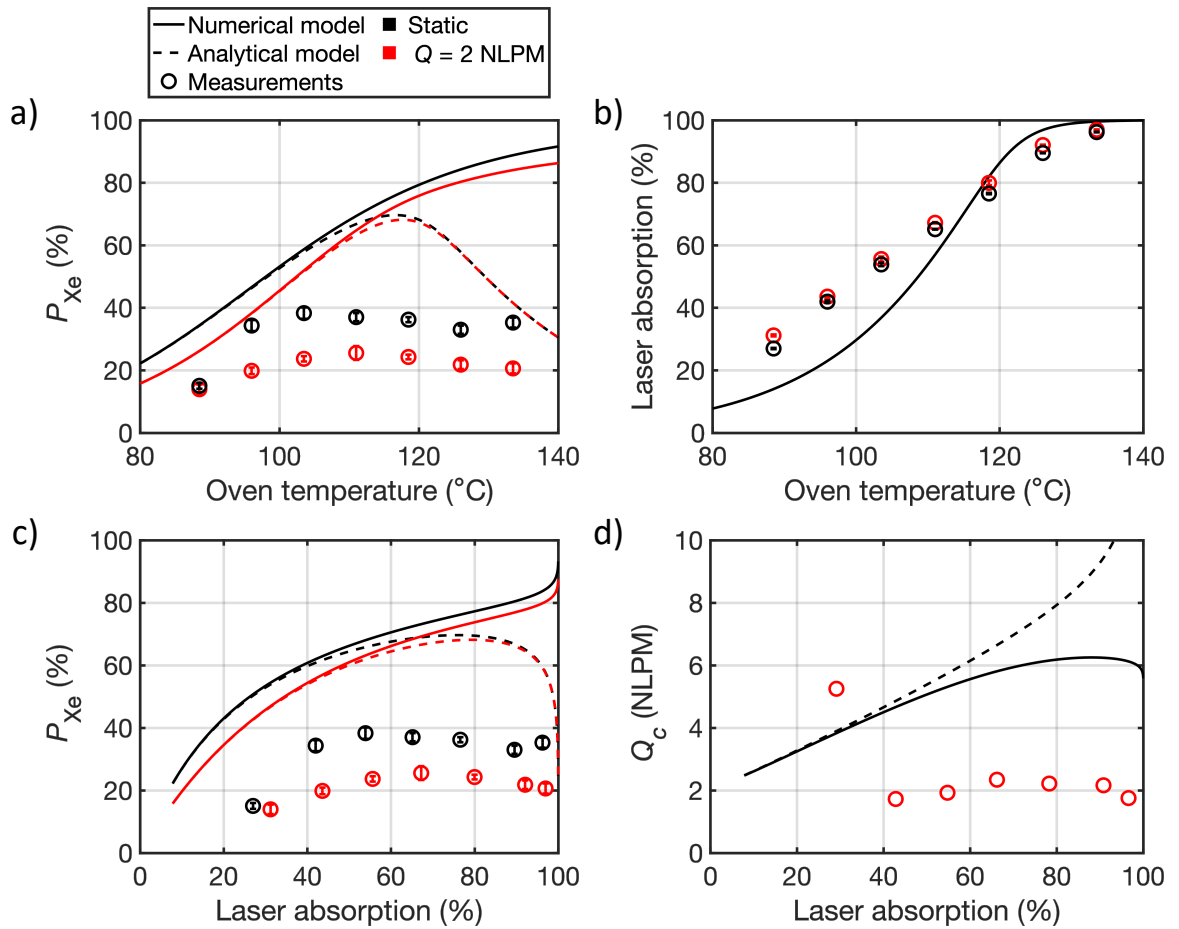


Figure 6.16: (a) P_{Xe} vs T_{oven} , (b) laser absorption vs T_{oven} , (c) P_{Xe} vs laser absorption and (d) critical flow rate, Q_c , vs mean laser absorption. Black lines correspond to static gas measurements and red lines to $Q = 2$ NLPM measurements. Solid lines are from the numerical model and dashed lines from the analytical model. Theoretical curves incorporated spin-exchange cross section and Xe relaxation in absence of Rb values from Fig. 6.15, neglecting Rb polarisation dependence of the ¹²⁹Xe-Rb spin-exchange cross section. Dashed lines are to guide the eye only.

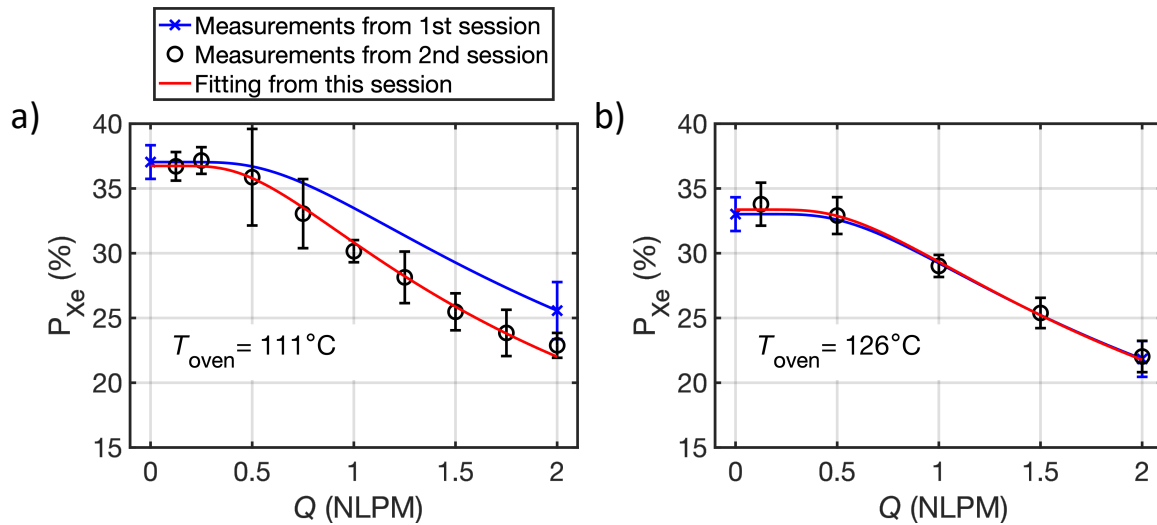


Figure 6.17: P_{Xe} , vs gas flow rate, Q , for (a) $T_{oven} = 111^\circ\text{C}$ and (b) $T_{oven} = 126^\circ\text{C}$. The red line is the fitting of data points to Eq. 6.4 giving (a) $P_{Xe}^{eq} = (36.7 \pm 0.4)\%$ and $Q_c = (1.83 \pm 0.06)\text{NLPM}$, and (b) $P_{Xe}^{eq} = (33.4 \pm 0.4)\%$ and $Q_c = (2.11 \pm 0.08)\text{NLPM}$. Blue data points are the values collected in a different session at the same T_{oven} in Fig. 6.16. The blue line is also of the form of Eq. 6.4, but uses the value of Q_c determined using the blue data points and Eq. 6.5. Red and blue lines show comparable Q dependence of P_{Xe} for both methods of deriving Q_c .

Fig. 6.16b, shows that for $T_{oven} > 126^\circ\text{C}$, measured laser absorption (both static and under-flow) begins to level off towards 100%. Measured laser absorption was observed to increase approximately linearly from 88.5°C to 126°C . Below $T_{oven} < 118.5^\circ\text{C}$, measured laser absorption was consistently higher than theory. This is surprising as the theoretical model assumes saturation Rb densities given by Killian [81], whereas [Rb] have been consistently measured to be lower than saturation levels in our setup, as seen in Chapter 5. Thus we would expect measured laser absorption to be consistently lower than the theoretical model. This may suggest actual optical pumping deviates from the modelling. As mentioned throughout this thesis, optical pumping efficiency may be limited by the factors given in Section 3.3.1, such as non-unity circularly polarised light [68], skewed light effects [74] and circular dichroism [75, 76], as well as surface Rb spin-destruction [150]. An important future work aim is to investigate P_{Rb} as a possible factor limiting P_{Xe} .

Fig. 6.16c, shows that both measured static and under flow P_{Xe} values increase with laser absorption to a maximum value, before gradually decreasing. Maximum measured static P_{Xe} occurs at laser absorption = 54% while the maximum $P_{Xe}(Q = 2\text{NLPM})$ occurs at laser absorption = 67%. Theoretical maxima predicted by the analytical model for P_{Xe}^{eq} and $P_{Xe}(Q = 2\text{NLPM})$ are 75% and 79% respectively. Higher optimal laser absorption for maximum under flow P_{Xe} than for maximum P_{Xe}^{eq} is consistent with

the analytical model, whilst the numerical model suggests that both maxima should occur at near 100% laser absorption.

Fig. 6.16 shows optimal laser absorption and oven temperatures for $Q = 2\text{NLPM}$ of $T_{\text{oven}} = 111^\circ\text{C}$ and laser absorption = $(67.2 \pm 0.2)\%$, produced maximum $P_{\text{Xe}} = (26 \pm 2)\%$. For static measurements, maximum $P_{\text{Xe}} = (38 \pm 2)\%$ for $T_{\text{oven}} = 103.5^\circ\text{C}$ and laser absorption = $(53.9 \pm 0.5)\%$. These values are lower than measured previously for $T_{\text{oven}} = 125^\circ\text{C}$ and laser absorption = 87.5% , $P_{\text{Xe}}(Q = 0\text{SLM}) = 41\%$ and $P_{\text{Xe}}(Q = 2\text{SLM}) = 29\%$ [52]. Fig. 6.16 shows under similar operating conditions of $T_{\text{oven}} = 126^\circ\text{C}$, static laser absorption = 89.5% and $Q = 2\text{NLPM}$ laser absorption = 92.1% , previously measured P_{Xe} could not be reproduced. Although the polariser used in this work and in ref. [52] are similar, a key difference is the higher B_0 homogeneity produced by the larger coil configuration in ref. [52], which may improve optical pumping efficiency and reduce Xe relaxation due to B_0 field gradients.

We did not observe the steep decrease in static and under flow P_{Xe} predicted by the analytical model. Nevertheless, to definitively validate the models, additional P_{Xe} measurements at near 100% laser absorption are necessary. The large discrepancy between measured and theoretical P_{Xe} was not resolved by inclusion of cell-specific measured γ' and Γ' . This suggests that there could be other SEOP factors, such as P_{Rb} variation, which were not explored in this thesis, that might contribute to the observed discrepancy.

Fig. 6.16d shows Q_c increases with laser absorption, up to a maximum at laser absorption = 66% . At higher laser absorptions, Q_c decreases, although the values remain reasonably consistent for all laser absorption values tested. This trend is more similar to the numerical model than the analytical model, which we expect given the high Q used. The $> 2\times$ higher Q_c value at laser absorption = 29% compared to all other measured values is an outlier from the trend and may be explained if [Rb] heterogeneity resulted in lower [Rb], and so lower P_{Xe} build up, at the front of the cell. As the static sample is only taken from the front of the cell, whereas the under-flow sample is from gas that has passed through the entire length of the cell, the under flow sample will undergo higher than expected P_{Xe} build up compared to the static sample, resulting in a higher than expected Q_c value. This may occur at low laser absorption if heterogeneous laser heating results in cell temperature heterogeneity. The $> 2\times$ lower Q_c observed than calculated by the numerical model is likely due to unaccounted for detrimental processes affecting optical pumping and Rb spin-destruction leading to higher measured laser absorption than simulated values at the same [Rb] value. In addition, the presence of elevated internal gas temperatures due to laser heating would reduce t_{res} and Q_c compared to modelled values.

Fig. 6.17a and b show $P_{\text{Xe}}^{\text{eq}} = (36.7 \pm 0.4)\%$ and $P_{\text{Xe}}^{\text{eq}} = (33.4 \pm 0.4)\%$ respectively, which is in good agreement with the static values in Fig. 6.16, where $P_{\text{Xe}}^{\text{eq}} = (37 \pm 1)\%$ and $P_{\text{Xe}}^{\text{eq}} = (33 \pm 1)\%$ respectively. This confirms the static procedure for obtaining $P_{\text{Xe}}^{\text{eq}}$ used for measurements in Fig. 6.16.

Although in Fig. 6.17b, $Q_c = 2.11 \pm 0.08\text{NLPM}$ agree with the measurement from Fig. 6.16 ($Q_c = 2.17\text{NLPM}$), $Q_c = 1.83 \pm 0.06\text{NLPM}$ in Fig. 6.17a does not agree with corresponding measurements from Fig. 6.16 ($Q_c = 2.34\text{NLPM}$). In both Fig. 6.17a and b, laser absorption was slightly lower than at the same T_{oven} in Fig. 6.16 by 1% and 2.6% respectively. This may have been due to laser degradation, as described in Section 5.2.1, which was observed to occur during P_{Xe} vs T_{oven} experiments. These results gave us confidence that Q_c measurements determined using Eq. 6.5 were accurate, although more susceptible to measurement variability.

In summary, neither theoretical model entirely accounts for the trend in measured values. The numerical model seems to describe the laser absorption dependence of Q_c more closely. However, the analytical model gives optimal laser absorptions at which peak P_{Xe} values occur which are more in line with experimental measurements than the numerical model. Future work should focus on measurements at near-100% laser absorption where models deviate the most.

Photon and spin-exchanges efficiencies

Modelled values of $\eta_\gamma(t = 0)$, η_{SE} and η_{pr} were calculated for different laser absorption values as shown in Fig. 6.18. Values for both numerical and analytical models were determined, as performed throughout the work in this chapter. Measured $\eta_\gamma(t = 0)$ and η_{pr} were determined from P_{Xe} values in Fig. 6.16.

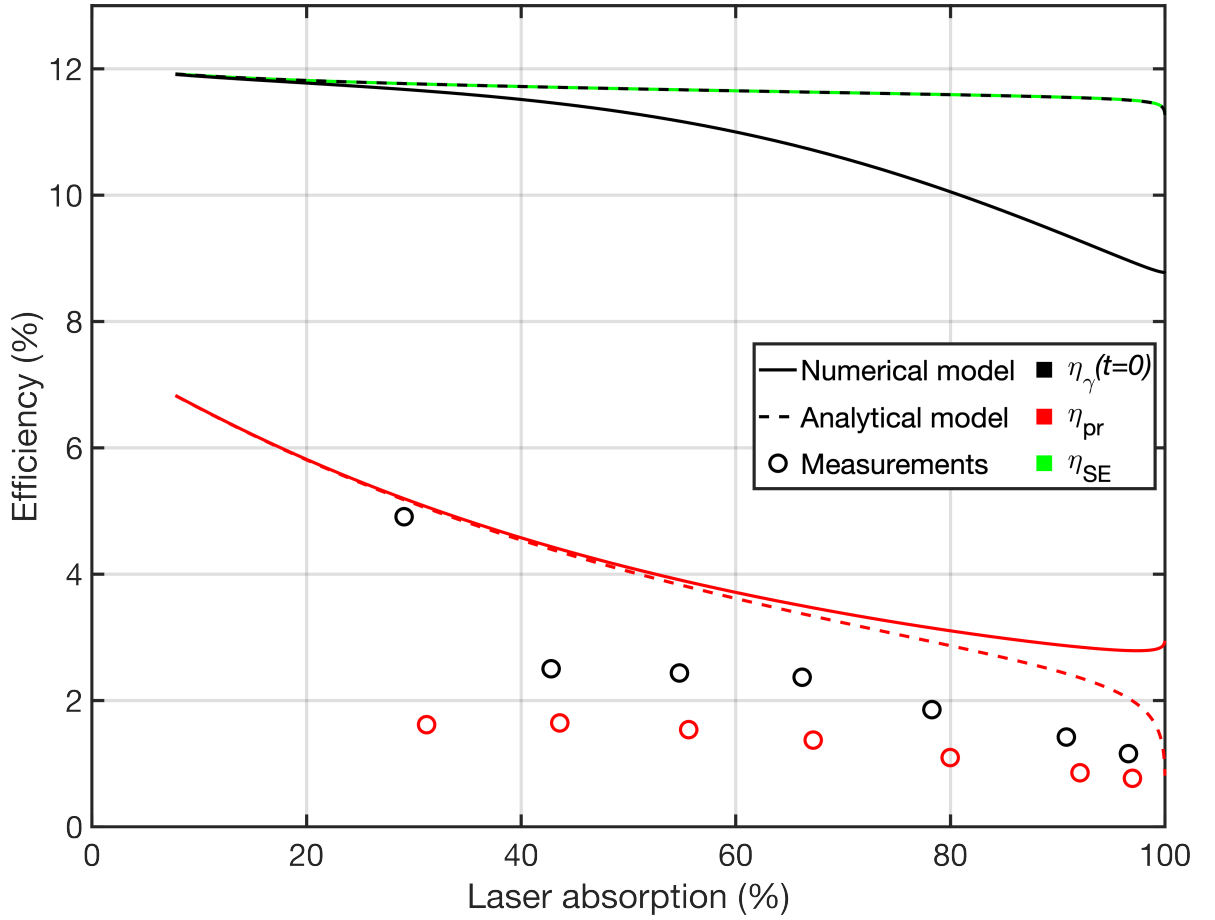


Figure 6.18: Photon, $\eta_\gamma(t=0)$, spin-exchange, η_{SE} , and production rate, η_{pr} , efficiencies vs mean laser absorption. Solid lines are values produced using the numerical model and dashed lines are produced using the analytical model. $\eta_\gamma(t=0) = \eta_{SE}$ for values produced using the analytical model. Circles correspond to experimentally measured values.

Fig. 6.18 shows that $\eta_{SE} = \eta_\gamma(t=0)$ for the analytical model and is fairly consistent across all laser absorption values, whereas $\eta_\gamma(t=0)$ for the numerical model decreases with increasing laser absorption. This is due to non-exponential P_{Xe} build up ($\frac{dP_{Xe}}{dt}(t=0) \neq \frac{P_{Xe}^{eq}}{\tau_{up}}$) that occurs at high laser absorption. Lower Q_c for the numerical model than the analytical model at high laser absorption leads to lower $\eta_\gamma(t=0)$. $\eta_\gamma(t=0)$ measurements follow the same trend as the numerical model, decreasing with laser absorption.

η_{pr} calculated using Eq. 6.8 for the numerical model decreases slowly with increasing laser absorption compared to η_{pr} given by the analytical model which decreases rapidly. This is because P_{Xe} is predicted to be higher for the numerical model than the analytical model, due to the higher P_{Rb} values towards the front of the cell than $\langle P_{Rb} \rangle$. Similar to $\eta_\gamma(t=0)$, the general trend in η_{pr} measurements is more similar to the numerical

model than the analytical model.

Measured efficiencies are significantly lower than theoretical efficiencies. As γ' was measured and incorporated into theoretical efficiencies, this suggests that simulated Γ_{SD} values used to determine theoretical efficiencies are much faster in reality, or higher laser absorption occurs in practice, both of which could be the result of inefficient optical pumping processes described in Section 3.3.1. Elevated internal gas temperatures, which were observed in simulations in Chapter 4, may also be present, which reduces t_{res} leading to overestimation in Q_c and efficiency values. Directly measuring P_{RB} would be insightful for investigating low η_{pr} .

For optimal mean laser absorption = 66%, $\eta_{\gamma}(t = 0) = 0.024$ and $\eta_{\text{pr}} = 0.014$. These values are lower than previously measured in ref. [52] ($\eta_{\gamma}(t = 0) = 0.033$ and $\eta_{\text{pr}} = 0.018$). This is largely due to the higher Q_c and P_{Xe} values reported in ref. [52] than in this work. $\Delta\Phi$ calculation in Eq. 6.10, to account for transmission losses at the back cell window, was not performed in ref. [52], which would contribute to a decrease in their reported efficiency values ($\eta_{\gamma}(t = 0) = 0.029$ and $\eta_{\text{pr}} = 0.016$).

Theoretical efficiencies were higher in this work than reported in ref. [12] and [54]. This is due to the lower gas pressure operation in this work which enhances the vdW contribution to γ' defined in Eq. 3.107, increasing η_{SE} in Eq. 6.9. The large range of γ' from the literature, as seen in Fig. 5.26, indicates that $\eta_{\gamma}(t = 0)$ values determined from the literature will significantly vary also.

Cryogenic Xe volume recovery

The 5-turn spiral volume was measured using water to be $V_{5\text{t}}^{\text{CT}} = (50.0 \pm 0.1)\text{mL}$ and the 8.5-turn spiral volume was measured to be $V_{8.5\text{t}}^{\text{CT}} = (71.2 \pm 0.1)\text{mL}$, where the uncertainty arises from the precision of the weighing scales. $V_{8.5\text{t}}^{\text{CT}}/V_{5\text{t}}^{\text{CT}} = 1.42$ which is less than the scaling of the number of turns $8.5/5 = 1.7$ which may suggest the spiral turns are smaller in diameter or the volume of the spiral above the turns, which is not submerged in liquid N_2 , contributes more greatly to the overall spiral volume than expected. The spirals measured were the same design, but not the exact spirals installed on the experimental polariser, so manufacturer variation has not been accounted for in V^{CT} values.

f_{evac} was determined for both spiral setups for $Q = 1\text{NLPM}$ and 2NLPM , as presented in Table 6.4. The dominant source of uncertainty was from the precision of the gas syringe ($\pm 10\text{mL}$).

Table 6.4: Mass recovery performed on both cryotrap. For the 8.5-turn spiral, the first quoted uncertainty is the standard deviation and the second quoted uncertainty is due to the precision of the gas syringe. Where standard deviation = 0 was due to identical values from repeat measurements. < 3 repeat measurements were taken for the 5-turn spiral, so only the uncertainty due to the precision of the gas syringe is quoted.

Cryo-trap	Pressure (bar)	Q (NLPM)	t _a (min)	V _{Xe} ^{theo} (mL)	V _{Xe} (mL)	V _{loss} (mL)	V _{evac} (mL)	f _{evac} (10 ⁻²)
5-turn spiral	2	1	4	120	80 ± 10	40 ± 10	-10 ± 10	-8 ± 8
	2	2	4	240	200 ± 10	40 ± 10	-10 ± 10	-4 ± 4
	1.25	1	4	120	80 ± 10	40 ± 10	-10 ± 10	-8 ± 8
	1.25	2	4	240	140 ± 10	100 ± 10	50 ± 10	21 ± 4
8.5-turn spiral	1.25	1	8	240	170 ± 0 ± 10	70 ± 0 ± 10	-1.2 ± 0 ± 10	-1 ± 0 ± 4
	1.25	2	4	240	147 ± 12 ± 10	93 ± 12 ± 10	22 ± 12 ± 10	9 ± 5 ± 4

Table 6.4 shows that for all $Q = 1\text{NLPM}$, determined f_{evac} values were within experimental uncertainty of $f_{\text{evac}} = 0$. This means that all Xe flowing through the cryotrap spiral is deposited within the spiral.

The 5-turn spiral for $p = 1.25\text{bar}$, $Q = 2\text{NLPM}$ gave $f_{\text{evac}} = 0.21 \pm 0.04$. This means that a large fraction of Xe flowing through the cryotrap was not deposited, due to the lower residency time of the gas in the spiral compared to operating at higher gas pressures or slow flow rates. The 8.5-turn spiral, with a longer gas flow path increases the distance over which Xe can be deposited. As such f_{evac} was smaller, $f_{\text{evac}} = 0.09 \pm 0.05 \pm 0.04$. However this was still non-zero, which means a small amount of Xe is still not deposited. This may suggest that the volume of the spiral turns is lower than expected and would need to be increased further to achieve $f_{\text{evac}} = 0$.

A disadvantage of the larger cryotrap is the larger V^{CT} contribution to V_{loss} . As such, the 8.5-turn spiral is only worth using over the 5-turn spiral when operating at $Q = 2\text{NLPM}$ and producing $V_{\text{Xe}} \geq 90\text{mL}$, which is the case for most clinical and research Xe

dose requirements. In addition, a larger liquid N₂ dewar is required, leading to higher liquid N₂ boil off and usage. Whilst reducing the spiral tubing diameter may decrease V^{CT} and/or f_{evac} by increasing the overall surface area of the spiral, gas flow path blockages due to frozen Xe may occur [30]. Alternatively, cryotrap designs that are non-spiral, such as the squared-helical design developed by Freeman [132] and utilised in the Polarean 9820-A polariser system (Polarean, Durham, NC, USA) described in ref. [94] may lower V_{loss} , by minimising V^{CT} and f_{evac} . We speculate that designs which increase the Xe coldfinger wall contact time by disrupting the gas flow path with high angle bends in the tubing may improve Xe volume recovery. These cryotrap design considerations will be particularly important if $Q > 2\text{NLPM}$ operation to improve HP-Xe production rates is to be explored.

For simplicity of producing the HP-¹²⁹Xe production maps shown in Fig. 6.21, as the continuous dependence of V_{Xe} on Q is unknown, for $Q \leq 1\text{NLPM}$, $f_{\text{evac}} = 0$ and for $Q > 1\text{NLPM}$, $f_{\text{evac}} = 0.09$ were used.

B field map

The cryotrap B-field was measured for the 8.5-turn spiral setup (Fig. 6.6b), as shown in Fig. 6.19.

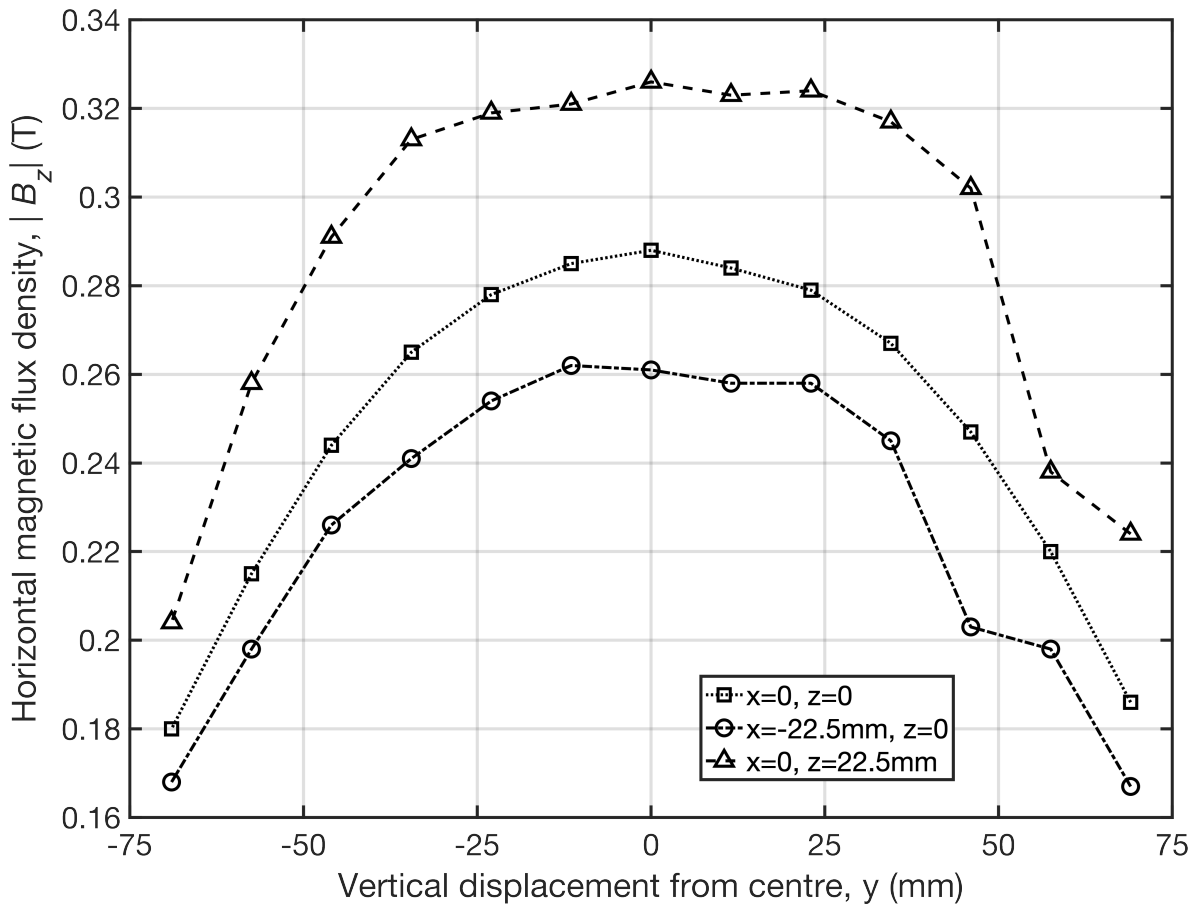


Figure 6.19: B-field map for the cryotrap permanent magnet. Squares are measurements taken at zero x and z-displacement; circles were taken at 22.5mm x-displacement, zero z-displacement; and triangles were taken -22.5mm z-displacement, zero x-displacement.

Fig. 6.19 shows that the cryotrap B-field is much higher than 500G across all values tested, so Xe snow relaxation should be sufficiently suppressed. In addition, the flux gradually decreases towards the vertical displacement +75mm, where the gas enters and exits the spiral, which should help minimise gaseous Xe depolarisation once thawed.

Cryotrap T_1 relaxation

T_1 relaxation of ¹²⁹Xe snow in the cryotrap was measured by accumulating Xe for $Q = 1\text{NLPM}$. After accumulation time $t_a = 4\text{mins}$, the optical cell was closed, the spiral was evacuated and also closed. Xe snow was then held in the spiral, submerged in the liquid N₂ dewar. The dewar was frequently filled to replace liquid N₂ that had boiled off to keep the spiral fully submerged. After an amount of time had passed (frozen time = 30, 60, 90 mins), the spiral was opened, the liquid N₂ dewar removed and replaced with a cup of warm water to thaw the Xe snow. The thawed Xe was

collected in the spherical container (Fig. 5.10a), before being transferred to the Xe polarimetry setup to measure NMR signal. For measurements at frozen time = 0, the Xe was thawed immediately after Xe accumulation was completed.

This method involved independent measurements for each time point, as the signal could not be sampled in Xe snow directly, or re-frozen after thawing and measurement as performed in ref. [30]. This more than doubled the time taken to complete measurements compared to performing multiple measurements in a single Xe snow acquisition. This meant that large numbers of repeats could not be taken. Therefore, per day of measurements, two measurements for frozen time = 0 and one measurement for frozen time > 0 were taken. Three days of measurements in total were completed. Results are shown in Fig. 6.20.

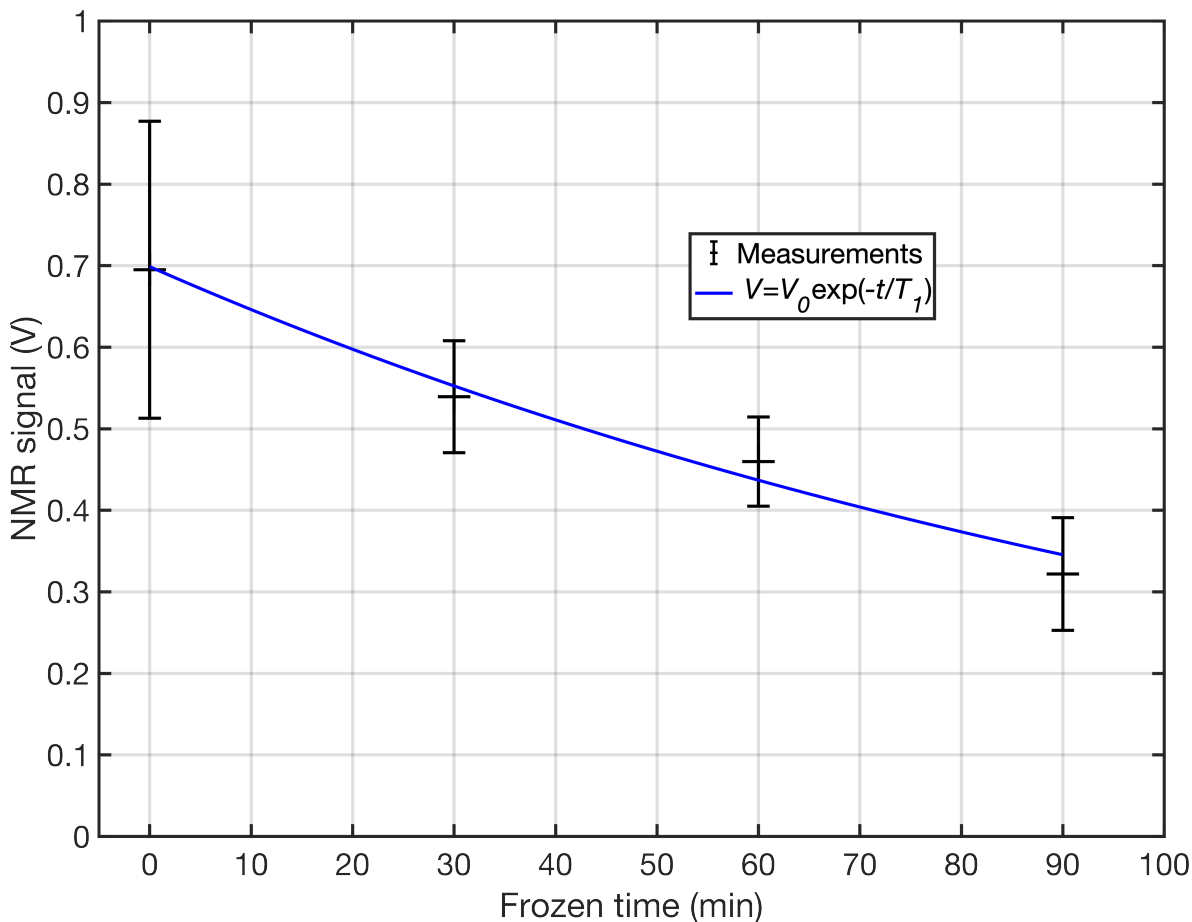


Figure 6.20: Relaxation of frozen Xe snow in the cryotrap. Fitting to $V = V_0 \exp(-t/T_1)$ where $V_0 = 0.70 \pm 0.06\text{V}$ and $T_1 = 128 \pm 27\text{min}$.

Fig. 6.20 shows the relaxation of frozen Xe over time in the cryotrap. T_1 was measured to be $T_1 = 128 \pm 27\text{min}$. This value is comparable to others taken in similar cryotrap setups, 150mins [151], 150mins [30], 87mins [54], 84mins [94], noting that methods used

to measure values varied. The measured cryotrap T_1 is sufficiently high to perform accumulation times of 10s mins, with limited P_{Xe} losses.

The high uncertainty in T_1 is due to each time point measurement being independent. Therefore, the uncertainty in T_1 is not only due to the variation in Xe snow relaxation but also additionally due to the variation in initial P_{Xe} of gas straight from the polariser and variation in depolarisation due to freeze-thaw. The higher relative uncertainty in the $t = 0$ measurement compared to $t > 0$ measurements may be an hysteresis effect whereby it was noticed that the initial measurement, taken at the start of the session was always lower than the 2nd measurement, taken at the end of the session. Further investigation is needed as to the cause of this effect.

Optimal HP-¹²⁹Xe production

Measured values of cryotrap $T_1 = 128\text{min}$, $P_{Xe}^{\text{eq}} = 37\%$ and $Q_c = 2.34\text{NLPM}$ were incorporated into Eq. 6.2.4 to produce the P_{Xe} , t_a , Q contour plot, as shown in Fig. 6.21a. V_{Xe} was then calculated for the 8.5-turn spiral using Eq. 6.11, to produce the P_{Xe} , V_{Xe} , t_a contour plot shown in Fig. 6.21b. Fig. 6.21a represents the user controlled parameters, Q and t_a , whilst Fig. 6.21b represents end-user key parameters which inform planning experiments and clinical scans which use HP-¹²⁹Xe.

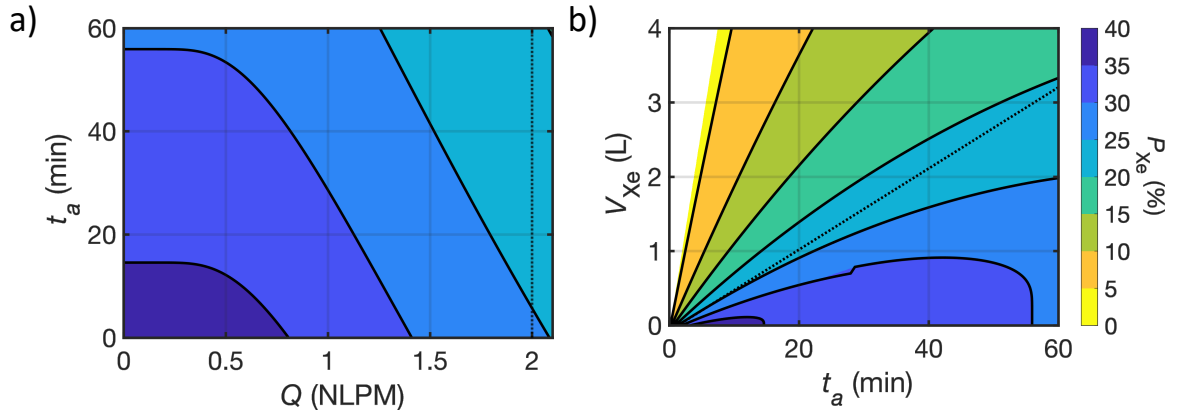


Figure 6.21: (a) P_{Xe} contour plot for accumulation time, t_a vs total gas flow rate, Q . (b) P_{Xe} contour plot for volume of Xe recovered, V_{Xe} vs t_a . The black dashed line represents $Q = 2\text{NLPM}$, so volumes of Xe per accumulation time above this line are not currently achievable with our setup as they would require $Q > 2\text{NLPM}$. The discontinuities in the contours and coloured regions is due to the f_{evac} condition discontinuity at $Q = 1\text{NLPM}$.

Figure 6.21b shows the polariser is able to generate $V_{Xe} = 250\text{mL}$, $P_{Xe} = 25.0\%$ in $t_a = 5\text{mins } 54\text{s}$, $V_{Xe} = 500\text{mL}$, $P_{Xe} = 24.5\%$ in $t_a = 10\text{mins } 30\text{s}$ and $V_{Xe} = 1\text{L}$, $P_{Xe} = 23.7\%$ in $t_a = 19\text{mins } 36\text{s}$. DE rates calculated using Eq. 6.15 are $\Delta\text{DE} = 637\text{ml/hr}$,

704ml/hr and 725ml/hr respectively. These P_{Xe} values are all $> 20\%$ and are reasonably consistent for different V_{Xe} , which is good for clinical studies where reproducible HP-¹²⁹Xe doses are important.

The maximum V_{Xe} that can be collected to $P_{Xe} > 20\%$ in one accumulation is 3.5L, which means multiple Xe doses can be acquired in one accumulation, which reduces the total V_{Xe} lost due to V^{CT} and the total time spent thawing Xe and preparing the polariser between accumulation cycles. In my experience, this is typically 5-10 mins.

The maximum P_{Xe} for $V_{Xe} = 1L$ dose is $P_{Xe} = 29.6\%$ in $t_a = 45$ mins, corresponding to $Q = 0.8NLPM$, with $\Delta DE = 398ml/hr$. Whilst ~ 2.3 times longer to accumulate than operating at $Q = 2NLPM$, a 25% increase in P_{Xe} , and so image SNR, is expected, which is particularly important for imaging on the limits of SNR, such as dissolved-phase imaging in well-perfused organs beyond the lungs.

These P_{Xe} values and DE rates are not improvements over previous measurements in ref. [52]. In ref. [52], V_{loss} was not accounted for. In addition, SLM may have been mistaken for NLPM (flow regulator calibration conditions), as was initially the case when performing this work. Mistaking SLM for NLPM leads to a $(293.15K - 273.15K)/273.15K = 7\%$ over estimation in V_{Xe}^{theo} . Γ' is remarkably slower in ref [52] ($1/\Gamma' = 44$ mins) compared to our measurement, which would contribute to higher P_{Xe} values as seen in Section 4.3.1, although saturation $[Rb]$ was assumed, lowering confidence in their Γ' value. Laser degradation (see Section 5.2.1), and differing cell condition may also contribute to the discrepancy.

Fig. 6.21 indicates installing a higher maximum mass flow rate regulator would be able to produce $P_{Xe} > 20\%$ $V_{Xe} = 1L$ doses in as little as $t_a = 14$ mins 12s, 28% shorter than the current fastest achievable t_a . Although we note that f_{evac} would likely increase, decreasing V_{Xe} , without further design modifications to the cryotrap.

Limitations of this work are the high cryotrap T_1 uncertainty increasing uncertainty in P_{Xe} production maps, particularly at long t_a values. A possible unaccounted systematic error was depolarisation as a result of freeze/thaw. Only relaxation of Xe snow during accumulation was considered in P_{Xe} production maps.

6.4 Conclusions

The effect of different amounts of Rb sources in the main cell body on overall laser absorption was shown, with increasing spread out of Rb sources contributing to high laser absorption and better matching between static and under-flow laser absorption. The presaturator was shown to improve laser absorption under flow, likely due to non-depletion of [Rb] at the back of the cell.

A multi-compartment oven was shown to be necessary when using a large number of Rb pools to improve cell temperature homogeneity and reduce susceptibility to Rb runaway.

Using 1D simulations, it was shown that the effects of [Rb] heterogeneity on polariser optimisation could be reduced by focusing on laser absorption as opposed to operating temperature. This should also aid comparison of literature values.

The analytical and numerical models investigated were shown to deviate at high laser absorption and/or low Q . Experimental measurements could not distinguish between models, however in general the numerical model better match the laser absorption dependence of P_{Xe} and Q_c . Mean optimal laser absorption for maximum P_{Xe} at $Q = 2\text{NLPM}$ was determined to be 66%, which differs to both theoretical models used. γ' and Γ' measurements were incorporated into modelling, however this did not lead to agreement with experimental measurements of P_{Xe} and Q_c , suggesting other limiting factors are responsible for the discrepancy. Low measured $\eta_\gamma(t = 0)$ and η_{pr} compared to theoretical values suggest factors affecting P_{Rb} may be responsible for the discrepancy and should be investigated in the future.

Xe volume loss during cryogenic accumulation was characterised and the need for a sufficiently large volume cryotrap at high gas flow rates and/or low total gas pressures was demonstrated. Xe volume recovery was improved by implementing a larger volume cryotrap setup, which improves HP-Xe DE rates.

HP-¹²⁹Xe production maps were produced, and optimal running conditions for clinical studies, where short accumulation time is prioritised, and research-use, where high P_{Xe} for high SNR is prioritised, were determined. The setup is capable of producing $P_{Xe} > 20\%$, 1L doses in $< 20\text{mins}$ for clinical studies, and $P_{Xe} = 29.6\%$ for research scans. In future, $Q > 2\text{NLPM}$ optimisation will be carried out in order to reduce accumulation times. In addition, high gas pressures, or differing gas compositions will be tested to reduce required cryotrap volume at high Q and reduce Xe volume losses, further increasing achievable HP-Xe DE rates.

Chapter 7

Summary and future work

This thesis explored SEOP on a large-scale ^{129}Xe -Rb polariser system, utilising a combination of theoretical models and experimental measurements to study the SEOP parameters governing the behaviour of ^{129}Xe -Rb spin systems. Informed polariser design modifications have been implemented and assessed. The updated polariser system was then characterised and optimised for large-scale hyperpolarised ^{129}Xe production. In this chapter, the findings from the work in this thesis are summarised, and future work directions are discussed.

7.1 Summary

In **Chapter 4**, FEM simulations were performed to model realistic gas flow-dynamics and thermal transfer within the SEOP polariser. It was found that [Rb] level increases with increasing Rb sources across the optical cell. The length of Rb presaturator for sufficient level of [Rb] was shown to be approximately linearly dependent on gas flow rate. Implementation of a Rb presaturator led to homogeneous, near-saturation [Rb] across the optical cell and optimal P_{Xe} build up.

In **Chapter 5**, AAS was developed for direct [Rb] measurements. Simultaneous [Rb] measurements over multiple violet and infrared Rb transitions were performed and measurement accuracy limits were determined. Direct [Rb] measurements showed that [Rb] level and homogeneity was greatest for a spread out Rb source across the optical cell and for Rb placed only within the presaturator. However, it was found that cell temperature measurements and observations of Rb runaway when using the large Rb source surface area indicated the need for an improved thermal management design for high, homogeneous [Rb] and low Rb runaway susceptibility. [Rb] was measured to be consistently lower than saturation [Rb], even at high laser absorption.

In **Chapter 6**, a multi-compartment oven, highly spread Rb source distribution and Rb presaturator were shown to be optimal for achieving high laser absorption and improved cell temperature homogeneity for both under-flow and static system operation. Incorporation of measured spin-exchange and ^{129}Xe relaxation rates in theoretical models did not account for the discrepancy between theoretical and experimentally measured polariser performance. In addition, the choice of theoretical model did not account for the observed discrepancy. Future investigations should therefore focus on factors affecting optical pumping and Rb spin-destruction. The upgraded polariser was optimised for clinical-scale HP- ^{129}Xe production. Dose production characteristics for the fastest production rate of $V_{\text{Xe}} = 1\text{L}$ doses was shown to be $P_{\text{Xe}} = 23.7\%$, $\Delta\text{DE} = 725\text{ml/hr}$, and for maximum P_{Xe} , $P_{\text{Xe}} = 29.6\%$ and $\Delta\text{DE} = 398\text{ml/hr}$ were shown to be achievable. It is hoped that these design improvements will lead to more consistent, stable polariser performance in a clinical and research setting.

7.2 Future work

Whilst the production rates and P_{Xe} levels are sufficient for the use of enriched Xe (86% ^{129}Xe) doses, they are still too low for the wider adoption of natural abundance Xe (26.4% ^{129}Xe). Improved MRI hardware, pulse sequences and reconstruction methods have helped with the gradual introduction of natural abundance Xe for ventilation hyperpolarised gas MRI scans within the POLARIS group at the University of Sheffield. However dissolved-phase imaging still requires enriched Xe doses prepared at high concentration and P_{Xe} . Therefore, further polariser optimisation warrants investigation. Highlighted below are potential areas for gains in P_{Xe} and HP- ^{129}Xe production rates.

As seen in **Chapter 4**, reduction in the ^{129}Xe spin-destruction rate Γ' would lead to improved P_{Xe} and production rates. In **Chapter 6**, a relatively short T_1 ($1/\Gamma' = 111 \pm 27\text{ s}$) was measured. This may have been due to the cell walls being untreated with an anti-relaxation coating, cleaned using less thorough methods and the high distribution of Rb present across them [21]. Initial work is underway into more systematic cleaning methods, as well as the use of anti-relaxation surface coatings to lower Γ' . In particular, we are interested in the use of the surface coating n-octadecyltrichlorosilane (OTS), due to its higher operating temperature ($< 190^\circ\text{C}$) than other surface coatings such as Surfasil [149]. The OTS binding process to the cell wall is shown in Fig. 7.1. Piranha solution cleaning is performed in order to prepare the cell surface by removal of impurities and hydroxylation of the surface as shown in Fig. 7.2. However, scaling up this technique to clean the larger optical cell volumes used in our polariser is difficult, as piranha solution is highly corrosive and reactions are exothermic, posing an explosion

risk. Therefore alternative cleaning methods which provide surface hydroxylation, or safe scaling up of piranha solution cleaning, are being investigated. In addition, the possible temperature dependence of Γ' is worth investigating to accurately simulate SEOP and aid efforts to reduce Γ' to maximise P_{Xe} and HP-Xe production rates.

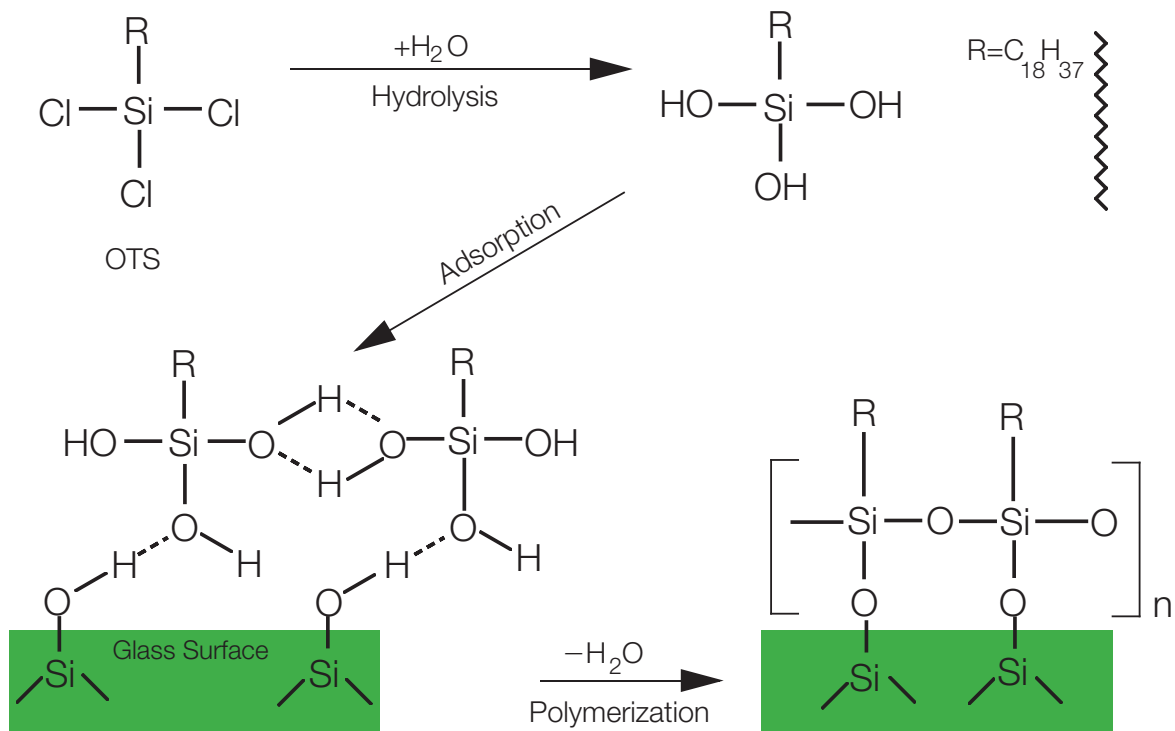


Figure 7.1: The chemical process of coating glass with n-octadecyltrichlorosilane (OTS). Figure reproduced with permission of the author from ref. [73]. Copyright 2023 by Matthew S. Rosen.

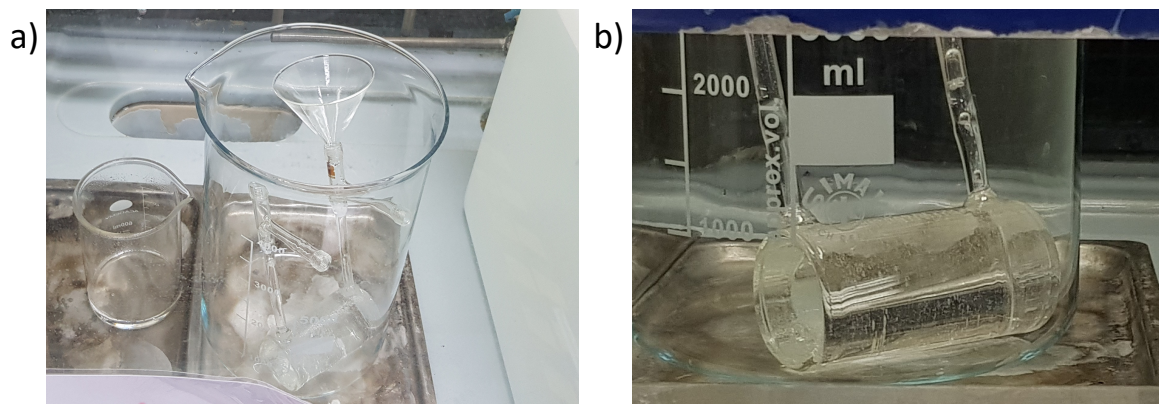


Figure 7.2: Piranha solution cleaning of a small optical cell (Cell volume $\sim 140\text{cm}^3$). (a) The optical cell filled with piranha solution placed in the fume cupboard. (b) Close up picture showing bubbling due to the release of gas (likely CO_2 , O_2) as piranha solution reacts with organic impurities on the cell wall, as well as the decomposition of H_2O_2 .

Secondly, investigating optimising polariser performance at higher mass flow rate ($Q > 2\text{NLPM}$) polariser operation is worthwhile for improving production rates. Based on the optimisation work in **Chapter 6**, it appears that $Q > 2\text{NLPM}$, $P_{\text{Xe}} > 20\%$ operation is likely to be achieved with the current setup. Gas composition and pressure optimisation may provide additional improvements in polariser performance. In another similar CF-SEOP polariser reported in ref. [94], gas composition optimisation led to significant improvements in P_{Xe} and production rates.

While low gas pressures increase the vdW spin-exchange cross section, as well as decreasing the Rb spin-destruction rate and Xe relaxation rate in the absence of Rb, there are advantages of increasing total gas pressure, including (i) increased Xe residency time within the optical cell and (ii) better matching between the Rb absorption linewidth and the laser linewidth, especially given the observed laser broadening with polariser-use seen in **Chapter 5**. At $p = 1.25\text{bar}$ and $T = 125^\circ\text{C}$, $\Delta\nu_a = 1.52 \times 10^{10}\text{Hz}$ whereas at $p = 3\text{bar}$, $\Delta\nu_a = 3.66 \times 10^{10}\text{Hz}$, increasing the absorption-transmission linewidth overlap, respectively, from $\sim 10\%$ to $\sim 30\%$ for a laser transmission linewidth of $\Delta\nu_l = 1.187 \times 10^{11}\text{Hz}$. Investigating different gas compositions and pressures is also worthwhile for exploring ways of limiting Xe volume losses during cryogenic accumulation, especially at higher gas flow rates. In **Chapter 6**, it was seen that Xe volume losses due to incomplete freeze-out of Xe increased with gas flow rate. This was reduced by implementing a sufficiently large spiral, at the expense of increasing Xe volume losses due to the cryotrap volume itself. This balancing act favours slower total volumetric gas flow rates in the cryotrap, which are possible at higher gas pressure or Xe partial pressures, whilst maintaining or extending Xe mass flow rates.

For future investigation of the on-going discrepancy between theoretical and experimentally measured polariser performance, direct P_{Rb} measurements to explore optical pumping and Rb spin-destruction over a long optical cell is needed, as well as further investigation into Γ' discussed above. Optically detected electron paramagnetic (or spin) resonance (EPR/ESR) methods [53, 83, 134, 152] can be used to measure P_{Rb} across the optical cell for different conditions. We also suspect optical pumping efficiency to be improved by addressing the non-zero angle between B_0 field and laser propagation directions measured in Section 5.2.1. This would allow $[\text{Rb}]$ to be increased for the same amount of laser absorption, and without a lowering of P_{Rb} occurring, leading to faster spin-exchange rates and likely improving P_{Xe} and production rates.

Ideally, accurately mapping P_{Xe} within the cell as well as P_{Rb} would allow for a precise determination of the influence of cell position on SEOP dynamics. This approach could provide deeper understanding of the cell-specific variations in optical pumping and P_{Xe} accumulation, aiding in the development of suitable P_{Xe} buildup models for large optical cell CF-SEOP polarisers. Mapping P_{Xe} could potentially be performed

with a low-field ^{129}Xe imaging setup similar to what was done for ^3He [153]. Using this method would also enable quantification of ^{129}Xe gas density, required for accurate absolute ^{129}Xe polarisation, by probing the internal cell temperature with diffusion measurements.

A final comment is that whilst large optical cell polariser systems have performed better than small cell compact polarisers, compact polarisers are still desirable where hospital space is limited. Exploring varying cell sizes with near-100% laser absorption in an effort to distinguish between theoretical models exhibiting the most significant disparities between numerical and analytical approaches is expected to provide valuable insights into enhancing compact polariser design.

Appendix A

List of publications

A.1 List of publications from this thesis

Journal articles

1. **J. E. Ball**, J. M. Wild, G. Norquay, “Investigating Rubidium Density and Temperature Distributions in a High-Throughput ^{129}Xe -Rb Spin-Exchange Optical Pumping Polarizer”, *Molecules*, 28(1), 2023. DOI: 10.3390/molecules28010011

Conference proceedings

1. **J. Ball**, J. M. Wild, G. Norquay, “Investigating Rb vapor density and temperature distributions in a high throughput ^{129}Xe -Rb polarizer”, *Proceedings of the Annual Meeting of the International Society for Magnetic Resonance in Medicine (ISMRM), Toronto, Canada, 2023*, Poster presentation.
2. **J. Ball**, J. M. Wild, G. Norquay, “Evaluating Absorption Spectroscopy for Measuring Rubidium Vapour Densities in a ^{129}Xe -Rb Polariser”, *Proceedings of the 63rd Experimental Nuclear Magnetic Resonance Conference, Orlando, Florida, USA, 2022*, Poster presentation.
3. **J. Ball**, J. M. Wild, G. Norquay, “Experimental considerations of absorption spectroscopy of rubidium”, *Proceedings of the Polarization in Noble Gases (PiNG) workshop, virtual, 2021*, Poster presentation.
4. **J. Ball**, J. M. Wild, G. Norquay, “Modelling realistic Rb density and temperature distributions in a high throughput xenon-129 polariser”, *Proceedings of the Annual Meeting of the International Society for Magnetic Resonance in Medicine (ISMRM), virtual, 2021*, Poster presentation.

5. **J. Ball**, J. M. Wild, G. Norquay, “Modelling Realistic Rubidium Density Distributions in a High Throughput Continuous-Flow Xenon-129 Polariser”, *Proceedings of the 62nd Experimental Nuclear Magnetic Resonance Conference, virtual*, 2021, Poster presentation.

A.2 Other co-authored publications

Journal articles

1. L. C. Saunders, G. J. Collier, H.-F. Chan, P. J. C. Hughes, L. J. Smith, J. G. R. Watson, J. E. Meiring, Z. Gabriel, T. Newman, M. Plowright, P. Wade, J. A. Eaden, S. Thomas, S. Strickland, L. Gustafsson, J. Bray, H. Marshall, D. A. Capener, L. Armstrong, J. Rodgers, M. Brook, A. M. Biancardi, M. R. Rao, G. Norquay, O. Rodgers, R. Munro, **J. E. Ball**, N. J. Stewart, A. Lawrie, R. G. Jenkins, J. T. Grist, F. Gleeson, R. F. Schulte, K. M. Johnson, F. J. Wilson, A. Cahn, A. J. Swift, S. Rajaram, G. H. Mills, L. Watson, P. J. Collini, R. Lawson, A. A. Roger Thompson, J. M. Wild. “Longitudinal Lung Function Assessment of Patients Hospitalized With COVID-19 Using ^1H and ^{129}Xe Lung MRI”. *CHEST*, 2023 DOI: 10.1016/j.chest.2023.03.024
2. G. J. Collier, R. F. Schulte, M. Rao, G. Norquay, **J. Ball**, J. M. Wild, “Imaging gas-exchange lung function and brain tissue uptake of hyperpolarized ^{129}Xe using sampling density-weighted MRSI”, *Magnetic Resonance in Medicine*, 89(6):2217-2226, 6, 2023. DOI: 10.1002/mrm.29602

Conference proceedings

1. L. J. Smith, H. Marshall, A. Biancardi, G. J. Collier, H.-F. Chan, D. Capener, J. Bray, D. Jakymelen, L. Saunders, J. Astley, B. A. Tahir, R. Munro, O. Rodgers, **J. Ball**, P. J. C. Hughes, S. Rajaram, A. J. Swift, N. J. Stewart, G. Norquay, M. L. Brook, L. Armstrong, L. Hardaker, T. Fihn-Wikander, R. Hughes, J. M. Wild, “Xe-MRI bronchodilator response to assess disease severity in patients with asthma and/or COPD”, *Proceedings of the European Respiratory Society (ERS) International Conference*, 2023, Poster presentation.
2. L. J. Smith, H. Marshall, A. Biancardi, G. J. Collier, H.-F. Chan, D. Capener, J. Bray, D. Jakymelen, L. Saunders, J. Astley, B. A. Tahir, R. Munro, O. Rodgers, **J. Ball**, P. J. C. Hughes, S. Rajaram, A. J. Swift, N. J. Stewart, G. Norquay, M. L. Brook, L. Armstrong, L. Hardaker, T. Fihn-Wikander, R. Hughes, J. M. Wild, “Bronchodilator response discordance in patients with asthma and/or COPD using Xe-MRI and spirometry”, *Proceedings of the European Respiratory Society*

- (ERS) International Conference, 2023, Oral presentation.
3. H. Marshall, L. J. Smith, A. Biancardi, G. J. Collier, H.-F. Chan, D. Capener, J. Bray, D. Jakymelen, L. Saunders, J. Astley, B. A. Tahir, R. Munro, O. Rodgers, **J. Ball**, P. J. C. Hughes, S. Rajaram, A. J. Swift, N. J. Stewart, G. Norquay, M. L. Brook, L. Armstrong, L. Hardaker, T. Fihn-Wikander, R. Hughes, J. M. Wild, “Longitudinal change in lung physiology and ^{129}Xe MRI over 1 year in patients with asthma and/or COPD”, *Proceedings of the European Respiratory Society (ERS) International Conference*, 2023, Oral presentation.
 4. A. Biancardi, H. Marshall, L. J. Smith, G. J. Collier, H.-F. Chan, P. J. C. Hughes, M. L. Brook, J. Astley, R. Munro, S. Rajaram, A. J. Swift, D. Capener, J. Bray, **J. Ball**, O. Rodgers, D. Jakymelen, I. Smith, B. A. Tahir, M. Rao, G. Norquay, N. D. Weatherley, L. Armstrong, L. Hardaker, T. Fihn-Wikander, R. Hughes, J. M. Wild, “Lung physiology and ^{129}Xe MRI data driven clustering of patients with asthma and/or COPD”, *Proceedings of the European Respiratory Society (ERS) International Conference*, 2023, Poster presentation.
 5. L. Saunders, G. Collier, H.-F. Chan, P. Hughes, L. Smith, N. Stewart, J. Brooke, J. Watson, J. Meiring, Z. Gabriel, T. Newman, M. Plowright, P. Wade, J. Eaden, J. Bray, H. Marshall, D. Capener, L. Armstrong, J. Rodgers, M. Brook, A. Biancardi, M. Rao, G. Norquay, O. Rodgers, R. Munro, **J. Ball**, N. Stewart, G. Jenkins, J. Grist, K. Lik Ng, L.-p. Ho, F. Gleeson, I. Hall, T. Meersmann, G. Pavlovskaya, A. Harrison, J. Brooke, J. Jacob, A. Swift, S. Rajaram, G. Mills, L. Watson, P. Collini, R. Lawson, A. A. R. Thompson, and J. Wild, “Impaired Xenon Gas Transfer Observed One Year After Hospitalisation Due To COVID-19 In Patients With Signs Of Interstitial Lung Disease”, *Proceedings of the Annual Meeting of the International Society for Magnetic Resonance in Medicine (ISMRM)*, Toronto, Canada, 2023, Oral presentation.
 6. H. Marshall, G. J. Collier, H.-F. Chan, L. J. Smith, P. J. C. Hughes, D. Capener, J. Bray, S. Joseph, R. Munro, O. Rodgers, **J. Ball**, N. J. Stewart, G. Norquay, M. L. Brook, L. Armstrong, L. Hardaker, T. Fihn-Wikander, R. Hughes, J. M. Wild, “Longitudinal ^{129}Xe MRI assessment of lung gas transfer and microstructure over 1 year in patients with asthma and/or COPD”, *Proceedings of the Annual Meeting of the International Society for Magnetic Resonance in Medicine (ISMRM)*, Toronto, Canada, 2023, Poster presentation.
 7. P. J. C. Hughes, H. Marshall, L. Smith, D. Jakymelen, A. Biancardi, G. Collier, H.-F. Chan, M. Brook, J. Astley, R. Munro, S. Rajaram, A. Swift, D. Capener, J. Bray, **J. Ball**, O. Rodgers, B. Tahir, M. Rao, G. Norquay, N. Weatherley, L. Armstrong, L. Hardaker, T. Fihn-Wikander, R. Hughes, J. Wild, “Differenti-

- ating patients with asthma and/or chronic obstructive pulmonary disease using lung T_1 and M_0 ”, *Proceedings of the Annual Meeting of the International Society for Magnetic Resonance in Medicine (ISMRM)*, Toronto, Canada, 2023, Poster presentation.
8. H. Marshall, G. J. Collier, L. J. Smith, H.-F. Chan, P. J. C. Hughes, D. Capener, J. Bray, S. Joseph, R. Munro, O. Rodgers, **J. Ball**, N. J. Stewart, G. Norquay, M. L. Brook, L. Armstrong, L. Hardaker, T. Fihn-Wikander, R. Hughes, J. M. Wild, “ ^{129}Xe gas transfer lung MRI before and after bronchodilator inhalation in patients with asthma and/or COPD”, *Proceedings of the Annual Meeting of the International Society for Magnetic Resonance in Medicine (ISMRM)*, Toronto, Canada, 2023, Poster presentation.
 9. L. Smith, H. Marshall, D. Jakymelen, A. Biancardi, G. J. Collier, H. Chan, P. J. C. Hughes, M. L. Brook, J. Astley, R. Munro, S. Rajaram, A. J. Swift, D. Capener, J. Bray, **J. Ball**, O. Rodgers, I. Smith, B. A. Tahir, M. Rao, G. Norquay, N. D. Weatherley, L. Armstrong, L. Hardaker, T. Fihn-Wikander, R. Hughes, J. M. Wild, “Physiological assessment of patients with airways dysanapsis using ^{129}Xe MRI”, *Proceedings of the European Respiratory Society (ERS) International Conference, Barcelona, Spain*, 2022, Oral presentation.
 10. L. Smith, H. Marshall, D. Jakymelen, A. Biancardi, G. Collier, H. Chan, P. Hughes, M. Brook, J. Astley, R. Munro, S. Rajaram, A. Swift, D. Capener, J. Bray, **J. Ball**, O. Rodgers, I. Smith, B. Tahir, M. Rao, G. Norquay, N. Weatherly, L. Armstrong, L. Hardaker, T. Fihn-Wikander, R. Hughes, J. Wild, “ ^{129}Xe -MRI and lung function to phenotype ventilation heterogeneity in asthma and/or COPD”, *Proceedings of the European Respiratory Society (ERS) International Conference, Barcelona, Spain*, 2022, Poster presentation.
 11. H. Marshall, L. J. Smith, A. Biancardi, G. J. Collier, H.-F. Chan, P. J. C. Hughes, M. L. Brook, J. Astley, R. Munro, and S. Rajaram, A. J. Swift, D. Capener, J. Bray, **J. Ball**, O. Rodgers, I. Smith, B. A. Tahir, M. Rao, G. Norquay, N. D. Weatherley, L. Armstrong, L. Hardaker, T. Fihn-Wikander, R. Hughes, J. M. Wild, “Physiological Phenotypes of Patients with Asthma and/or COPD Using ^{129}Xe MRI”. *Proceedings of the American Thoracic Society (ATS) International Conference, San Francisco, California, USA*, 2022, Oral presentation.
 12. H. Marshall, L. J. Smith, A. Biancardi, G. J. Collier, H.-F. Chan, P. J. C. Hughes, M. L. Brook, J. Astley, R. Munro, S. Rajaram, A. J. Swift, D. A. Capener, J. Bray, A. Hussain, **J. Ball**, O. Rodgers, D. Jakymelen, I. Smith, B. A. Tahir, M. Rao, G. Norquay, N. D. Weatherly, L. Armstrong, L. Hardaker, T. Fihn-Wikander, F.X. Blé, R. Hughes, J. M. Wild, “ ^{129}Xe MRI patterns of lung function

- in patients with asthma and/or COPD in the NOVELTY study”, *Proceedings of the Annual Meeting of the International Society for Magnetic Resonance in Medicine (ISMRM), London, UK, 2022*, Poster presentation.
13. D. Jakymelen, L. J. Smith, H. Marshall, A. Biancardi, G. J. Collier, H.-F. Chan, P. J. C. Hughes, M. L. Brook, J. Astley, R. Munro, S. Rajaram, A. J. Swift, D. Capener, J. Bray, **J. Ball**, O. Rodgers, I. Smith, B. A. Tahir, M. Rao, G. Norquay, N. D. Weatherley, L. Armstrong, L. Hardaker, T. Fihn-Wikander, R. Hughes, J. M. Wild, “Differentiating COPD and asthma using ^{129}Xe ventilation MRI, lung clearance index and spirometry”, *Proceedings of the Association for Respiratory Technology & Physiology (ARTP) Conference, Hinckley, UK, 2022*, Poster presentation.
 14. L. J. Smith, H. Marshall, D. Jakymelen, A. Biancardi, G. J. Collier, H.-F. Chan, P. J. C. Hughes, M. L. Brook, J. Astley, R. Munro, S. Rajaram, A. J. Swift, D. Capener, J. Bray, **J. Ball**, O. Rodgers, I. Smith, B. A. Tahir, M. Rao, G. Norquay, N. D. Weatherley, L. Armstrong, L. Hardaker, T. Fihn-Wikander, R. Hughes, J. M. Wild, “The impact of airway dysanapsis in patients with asthma and/or COPD on ^{129}Xe ventilation MRI”, *Proceedings of the Association for Respiratory Technology & Physiology (ARTP) Conference, Hinckley, UK, 2022*, Oral presentation.
 15. R. F. Schulte, G. J. Collier, **J. Ball**, G. Norquay, M. Rao, J. M. Wild, “Imaging Gas-Exchange Lung Function using Density-Weighted MRSI and Hyperpolarised ^{129}Xe Gas”, *Proceedings of the Annual Meeting of the International Society for Magnetic Resonance in Medicine (ISMRM), virtual, 2021*, Poster presentation.

List of Figures

3.1	Zeeman splitting for spin half-integer systems. (a) $I = 1/2$, (b) $I = 3/2$, (c) $I = 5/2$	6
3.2	(a) Laboratory frame and (b) Rotating frame. Figure adapted with permission of John Wiley & Sons, from Ref. [57] 2023; permission conveyed through Copyright Clearance Center, Inc.	9
3.3	Spectral density vs frequency. $\omega_0 = 1$ was used. $\omega_0\tau_c = 0.1, 1$ and 10 are the dashed, solid and dotted lines respectively.	13
3.4	Transition probabilities in a homonuclear AX system.	15
3.5	T_1 (solid line) and T_2 (dashed line) relaxation times due to dipole-dipole relaxation vs correlation time, τ_c . $\omega_0 = 1$ was used.	16
3.6	FID, $S(t)$, and NMR spectrum after fourier transform, $\mathcal{F}[S(t)]$. The solid and dashed lines represent the real (absorption) and imaginary (dispersion) parts respectively.	18
3.7	Coil designs showing the direction of the current, I , through the wire for (a) a surface coil, (b) a Helmholtz coil-pair and (c) a solenoid. The direction of \mathbf{B} , in blue, is given by the right-hand rule.	20
3.8	Rb energy level diagram of the orbital, fine and hyperfine structure. Diagram not to scale. Hyperfine transition energies are given by Steck [62, 63]. The hyperfine structure of $5^2P_{3/2}$ is not shown.	21
3.9	Optical pumping of the Rb D_1 line with left-circularly polarised light parallel to a static field B_z (σ^+).	23
3.10	Schematic of photon or optical pumping attenuation along the optical cell. As circularly-polarised photons are absorbed by Rb in the optical cell, the photon flux, Φ , and optical pumping rate, R , decrease with cell position, z , represented by the red shading.	25
3.11	Angular momentum vectors associated with the Rb- ^{129}Xe van der Waals molecule or colliding pair.	29
3.12	Spin-exchange between Rb and ^{129}Xe during (a) binary collisions and (b) the presence of the third body mediates spin exchange in van der Waals molecules.	31

3.13	(a) Rb spin-destruction due to spin-exchange and (b) Xe polarisation build up due to spin-exchange. The arrows indicate polarisation transfer (spin-exchange interaction between S and K) whilst dashed lines without arrows indicates interactions without a transfer of polarisation.	32
3.14	Grotrian Rubidium energy level diagram. Transition parameters are given in Table 3.3.	38
3.15	Transmission of incident light, I_0 , through the sample of Rb vapour, of path length l , during AAS, based on Eq. 3.117. The arrow indicates the direction of transmission and the violet shading represents the attenuation of I_0 through the sample.	40
3.16	Beer-Lambert law deviation in absorbance, A , vs Rb vapour density, $[\text{Rb}]$, defined by the amount of unabsorbed (stray) light, f_{stray} . Asymptotes occur at $A = -\ln(f_{\text{stray}})$	42
4.1	CAD models of four optical cell geometries, where the Rb source is highlighted in violet. (a) The small (10cm^2) Rb source placed within the cell main body, (b) the large (194cm^2) Rb source placed within the cell main body, (c) Rb placed only within the 72cm presaturator and (d) Rb within a 1m presaturator only (not to scale). The Rb source boundary condition is applied to all internal cell outlet walls outside of the oven, where Rb deposition is typically observed. The optical pumping laser propagates along z , from the front to the back of the main cell body, and the gas flows counter to this from the inlet to the outlet.	48
4.2	Rb flux boundary condition geometry in the main cell body viewed from (a) the rear optical cell window and (b) the side. The Rb pool edge is aligned with the centre of the cell inlet and extends a length L_{pool} towards the front of the cell. θ_{pool} is the angle of the boundary condition.	53
4.3	Meshes of the 10cm^2 Rb pool optical cell geometry shown in Fig. 4.1a. (a) ‘Coarser’ mesh and (b) ‘Finer’ mesh. Only the external surface mesh shown, however the mesh extends in 3D space within the object.	55
4.4	Xe polarisation, P_{Xe} vs temperature for different values of laser absorption, P_l , and Xe relaxation rate in the absence of Rb, Γ' . $p = 1.25\text{bar}$, $Q = 2\text{SLM}$ and $[\text{Rb}] = [\text{Rb}]_{\text{sat}}$ were used.	59
4.5	(a) Rb polarisation, P_{Rb} , and (b , c) P_{Xe} vs laser power for different (b) Rb vapour densities, $[\text{Rb}]$, and (c) Γ' . $T = 120^\circ\text{C}$, $p = 1.25\text{bar}$ and $Q = 2\text{SLM}$ were used.	61

4.6 Simulations for different Rb pool sizes for $Q = 2\text{SLM}$, $p = 1.25\text{bar}$ and Rb pool angle $\theta_{\text{pool}} = 20^\circ$. The dashed line indicates the results of the 1D simulation, showing parameter cell position dependence for (a) normalised Rb density, $[\text{Rb}]/[\text{Rb}]_{\text{sat}}$, (b) cell internal gas temperature, (c) Xe polarisation, P_{Xe} , (d) optical pumping rate, R , (e) z gas velocities. 64

4.7 1m Rb presaturator only simulations for $p = 1.25\text{bar}$ and $T = 125^\circ\text{C}$. (a) $[\text{Rb}]/[\text{Rb}]_{\text{sat}}$ vs presaturator position for different Q . (b) $[\text{Rb}]/[\text{Rb}]_{\text{sat}}$ at the end of the presaturator vs Q for different presaturator lengths. (c) $[\text{Rb}]/[\text{Rb}]_{\text{sat}}$ contour plot for presaturator length vs Q 68

4.8 Simulations for different Rb pool sizes ($\theta_{\text{pool}} = 20^\circ$) and the Rb presaturator for $Q = 2\text{SLM}$ and $p = 1.25\text{bar}$. The dashed line indicates the results of the 1D simulation, showing parameter cell position dependence for (a) $[\text{Rb}]/[\text{Rb}]_{\text{sat}}$, (b) cell internal gas temperature, (c) P_{Xe} , (d) R , (e) z gas velocities. 70

4.9 $[\text{Rb}]/[\text{Rb}]_{\text{sat}}$ distributions for $P_l = 160\text{W}$, $Q = 2\text{SLM}$ and $p = 1.25\text{bar}$ for the optical cells given in Fig. 4.1. (a) Small (10cm^2) Rb source placed within the cell main body. (b) Large (194cm^2) Rb source placed within the cell main body. (c) Rb placed only within the 72cm presaturator. (d) Rb within a 1m presaturator only (not to scale). 72

5.1 Schematic of the Sheffield ^{129}Xe -Rb continuous-flow polariser. Atomic absorption spectroscopy (AAS) apparatus is not shown. Figure adapted with permission from ref. [52]. Copyright 2023 by the American Physical Society. 77

5.2 Labelled pictures of the polariser from (a) along the polariser and (b) side on to the polariser. The cryotrap and part of the gas manifold cannot be seen. 78

5.3 Schematic of the laser diode array (LDA) and optical train, consisting of the laser diode fibre, beam dumps, plano-convex lenses, polarising beam splitter (PBS) and quarter-wave plate ($\lambda/4$). Figure reproduced with permission from ref. [52]. Copyright 2023 by the American Physical Society. 79

- 5.4 (a) Output laser optical spectra vs supplied laser current, I . Amplitudes are normalised to maximum signal intensity and integrals are normalised to output laser power, P_l . On-resonance ($\lambda_l = 794.768\text{nm}$) spectra could not be acquired at $I \leq 27\text{A}$ due to the laser chiller maximum temperature (35°C) being reached. The vertical dashed line indicates D_1 resonance line (794.77nm). (b) P_l vs I . The red line is a linear fit to the on-resonance measurements. (c) Full width at half maximum (FWHM) determined from a Gaussian fit. (d) Gaussian fit of the $I = 38\text{A}$ spectra. 80
- 5.5 Laser spectra at maximum operating current (38A). Signal amplitudes are normalised to the maximum signal amplitude. 08/11/21: Gaussian fit FWHM = 0.25nm , $P_l = 184\text{W}$, acquired near the start of laser use. 28/03/23: Gaussian fit FWHM = 0.33nm (poor fit), P_l was not recorded. 24/04/23: Gaussian fit FWHM = 0.33nm (poor fit), $P_l = 179\text{W}$ 81
- 5.6 (a) Simulated magnetic flux density in z -direction, B_z , for the 6-coil configuration. (b) Corresponding B_z gradients in z , $|\nabla B_z/B_z|_z$. Solid and dashed lines are B_z field and gradients along the central ($x = y = 0$) and oven lid offset ($y = 95\text{mm}$) longitudinal axes respectively. $z = 0$ corresponds to the centre of the coil setup. 82
- 5.7 Measured B_0 field from 6-coil configuration (a) along the centre longitudinal axis and (b) along the longitudinal axis offset $y = 95\text{mm}$ equal to the top of the oven. (i) Background $I = 0\text{A}$ field, (ii) $I = 8.38\text{A}$ field, (iii) $I = 8.38\text{A}$ field gradients. The angle of B_0 to z -direction is $\theta = \arccos(B_z/B_0)$. $z = 0$ corresponds to the centre of the coil setup. . 83
- 5.8 SEOP cells with different Rb source distributions; (a) 1g of Rb placed at the back of the cell, with an estimated surface area $\sim 10\text{ cm}^2$, (b) 5 g of Rb placed in the cell, with an estimated surface area $\sim 64\text{ cm}^2$ and (c) 2g of Rb distributed along the presaturator showing (i) the geometry of the cell and (ii) a close-up of the Rb distribution. 85
- 5.9 Coil B_1 map along the central z axis for the solenoid (black markers), with a copper shielding layer added (blue markers) and for a surface coil, as used on the surface of the optical cell (red markers). The connecting lines are to guide the eye only. Measurements in the opposite (negative) direction required re-orientating the probe coil, likely causing the slight change in centre measurements. The dashed lines indicate the ends of the solenoid. 86
- 5.10 ^{129}Xe polarimetry setups with each container containing Xe gas mixture inside a solenoid coil, placed on the 3D printed stand(s). (a) The spherical container setup and (b) the cylindrical container setup. 87

5.11	Diagram of the NMR circuit and FID acquisition, inspired by ref. [136]. 1. Excitation pulse controlled by the PC is output by the DAQ card. 2. Blanking pulse during this time isolates receiver pre-amp from the excitation pulse and coil ringdown. 3. NMR signal from the coil is amplified through the pre-amp and read by the DAQ card. 4. Demodulation and low-pass filter applied. 5. Display or output FID for FID fitting to determine parameter values.	89
5.12	Duplexer inside aluminium housing, as designed by Antonacci et al. [136].	90
5.13	Screenshot of the block view of the NMR spectrometer program, developed in Labview (National Instruments), showing the blanking output for the pre-amplifier, which was added to the existing program.	90
5.14	Screenshot of the NMR spectrometer user interface.	91
5.15	FIDs acquired on the polariser. The black line is the signal and the red line is the fitted FID. (a) 1 scan ^{129}Xe FID, with $V = 53.6$ mV and $T_2^* = 9.76$ ms, using a pulse width of 0.89 ms. (b) 20,000 scan average ^1H FID, with $V = 0.307$ mV and $T_2^* = 6.71$ ms, using a pulse width of 0.22 ms.	92

- 5.16 Experimental setup for AAS. **(a)** Optical setup consisting of a halogen bulb as the broad spectral light source. A thermocouple (OMEGA, model SA1XL K-type) is placed directly above the bulb on the housing to monitor bulb temperature and ensure the bulb has stabilised before measurements are taken. A series of plano-convex lenses ($f = 40$ mm, $f = 60$ mm, $f = 30$ mm) and aperture directs a parallel light beam onto the SEOP cell. A $f = 75$ mm plano-convex lens collects light and couples it to the optical fibre, which is connected to the spectrometer. **(b)** The optical setup was placed at 3 different positions along the length of the cell. At each position, cell temperature, T_{cell} , is measured by a thermocouple (OMEGA, model SA1XL K-type) adhered to the top of the external cell surface. Air passed through a heating element (OMEGA, model AHPF-122 1200W), controlled by a thermocouple (OMEGA, model SA1XL K-type) placed in the ambient oven space, regulates oven temperature, T_{oven} . The oven has three inlets for heated air, to maximise heated air coverage and oven temperature homogeneity across the cell. To ensure oven performance is not compromised, the oven port and lens tube fit compactly and the remaining oven ports are filled with ceramic plugs lined with insulation foam. The optics run on rails connected to the polariser chassis, ensuring precise optical alignment and fast re-positioning between oven ports. The direction of the optical pumping laser is shown, although this is switched off during AAS acquisitions to avoid emission due to energy pooling as mentioned in Section 5.2.4. 93
- 5.17 Example absorption spectra. **(ai)** Violet and **(bi)** NIR spectra acquired with the 1g Rb cell (Figure 5.8a), at cell position = 75.5cm, above the Rb source, at oven temperature, $T_{\text{oven}} \sim 20^\circ\text{C}$, $I_0(\nu)$ (blue) and $T_{\text{oven}} = 145^\circ\text{C}$, $I(\nu)$ (red). Corresponding pseudo-Voigt fitted absorbance spectra for the $5S_{1/2} \rightarrow$ **(aia)** $6P_{1/2}$, **(aib)** $6P_{3/2}$, **(aib)** $5P_{1/2}$ (D_1), **(aib)** $5P_{3/2}$ (D_2) transitions. Due to the high optical thickness for D_1 and D_2 absorption (deviation from the Beer-Lambert law), the line shape becomes less well defined and the quality of the fit worsens. **(c)** Example of NIR spectra acquired at cell position = 3.5cm, away from the Rb source, at $T_{\text{oven}} \sim 20^\circ\text{C}$ $I_0(\nu)$ (blue) and $T_{\text{oven}} = 125^\circ\text{C}$, where low [Rb] is observed (the Beer-Lambert law is obeyed). 95

- 5.18 Example synthetic absorption spectra. **(a)** Voigt fitting parameters $A_F = 21.4246$, $a_F = -0.0032 \text{ GHz}^{-1}$, $B_F = 0.0018$, $\Delta\nu_{0,F} = 185.9509 \text{ GHz}$, $\eta_F = 0.8408$, $\nu_{0,F} = 711126 \text{ GHz}$, $M = 2.6154\%$, $\text{SNR} = 11.6648$ for the $5S_{1/2} \rightarrow 6P_{1/2}$ transition. **(b)** Voigt fitting parameters $A_F = 52.5141$, $a_F = 8.3817 \times 10^{-4} \text{ GHz}^{-1}$, $B_F = 0.0018$, $\Delta\nu_{0,F} = 221.2552 \text{ GHz}$, $\eta_F = 0.6765$, $\nu_{0,F} = 713415 \text{ GHz}$, $M = 7.87\%$, $\text{SNR} = 26.0774$ for the $5S_{1/2} \rightarrow 6P_{3/2}$ transition. 98
- 5.19 ^{129}Xe flip angle measurements for an amplitude of 2.4 V, at 32.8 kHz. Note that the observed flip angle is always $\leq 90^\circ$, as opposed to the true flip angle which can take any value. The observed and true flip angles are equal to 90° at the shortest pulse width that produces a 90° observed flip angle. Dashed lines are to guide the eye only. 100
- 5.20 ^1H amplitude vs pulse width for a pulse amplitude of 2.4 V, at 32.8 kHz. Dashed lines are to guide the eye only. 101
- 5.21 ^{129}Xe polarisation measured on the polariser ($P_{\text{Xe}}^{\text{pol}}$) vs on the MRI 1.5T scanner ($P_{\text{Xe}}^{\text{sc}}$). $P_{\text{Xe}}^{\text{pol}} = m * P_{\text{Xe}}^{\text{sc}}$ was fitted where $m = 1.10 \pm 0.02$, $R^2 = 0.9825$ (red). The dashed line indicates $P_{\text{Xe}}^{\text{pol}} = P_{\text{Xe}}^{\text{sc}}$, highlighting the gradient offset that may be the result of depolarisation between the polariser and the 1.5T scanner. The data points represent single measurements. The uncertainty in $P_{\text{Xe}}^{\text{pol}}$ is dominated by the uncertainty in ^1H amplitude. The uncertainty in $P_{\text{Xe}}^{\text{sc}}$ was determined separately as the standard deviation in repeat measurements on the 1.5T scanner from a single Xe sample from the polariser. 102
- 5.22 Mean absolute percentage error, M , vs signal-to-noise ratio (SNR) for $5S_{1/2} \rightarrow 6P_{1/2}$ (black circles), $6P_{3/2}$, (blue triangles) for $n = 200$ repeats. Dashed lines are to guide the eye only. 103
- 5.23 **(a)** Rb density, $[\text{Rb}]$, measured from the $5S_{1/2} \rightarrow 6P_{1/2}$ (blue circles), $6P_{3/2}$ (blue triangles), $5P_{1/2}$ (D_1) (red circles) and $5P_{3/2}$ (D_2) (red triangles) transitions vs T_{oven} . The black line is saturation Rb density, $[\text{Rb}]_{\text{sat}}$, calculated based on T_{oven} (see Table 3.1) and dashed lines indicate $T_{\text{oven}} \pm 10^\circ\text{C}$. **(b)** Corresponding SNR for violet absorbance spectrum. SNR in D_1 and D_2 absorbance spectra was high (> 100) and so was not included. **(c)** Difference in cell temperature, T_{cell} , to T_{oven} , vs T_{oven} . T_{cell} was measured directly above the Rb source. 104

- 5.24 (i) T_{cell} , (ii) [Rb] and (iii) SNR in violet absorbance spectra at different cell positions for (a) 1g Rb main body cell, (b) 5g Rb main body cell and (c) 2g Rb presaturator cell (see Figure 5.8). Dashed lines are to guide the eye only. The presaturator temperature was measured to be $164 \pm 2^\circ\text{C}$. SNR in D_1 and D_2 absorbance spectra was high (> 100) and so was not included in (iii) plots. N.B. in (ai), (bi) and (ci) T_{cell} measured without the pumping laser present do not have error bars due to only one measurement being taken. 107
- 5.25 ^{129}Xe relaxation rate, Γ_{down} , as a function of [Rb] measured from D_1 line absorption for 1g Rb main body cell. $\gamma' = (1.1 \pm 0.1) \times 10^{-21} \text{ m}^3\text{s}^{-1}$ and $1/\Gamma' = 12 \pm 1 \text{ min}$. $> 20\%$ difference in $[\text{Rb}]_{D_1}$ and $[\text{Rb}]_{D_2}$, suggestive of deviation from the Beer-Lambert law for D_2 absorption, occurs at $[\text{Rb}]_{D_2} \gtrsim 4 \times 10^{17} \text{ m}^{-3}$ and correspondingly $[\text{Rb}]_{D_1} \gtrsim 5 \times 10^{17} \text{ m}^{-3}$, which is our current limit of accurate $[\text{Rb}]_{D_1}$ measurement. 111
- 5.26 Theoretical Rb- ^{129}Xe spin-exchange cross section, γ' , as a function of Rb polarisation, P_{Rb} , as calculated for our conditions ($p = 2 \text{ bar}$, $T = 125^\circ\text{C}$ and 3%Xe, 10%N₂, 87%He). The blue region is the range of contribution due to three-body van der Waals interactions, and the yellow region is the added range of contribution due to measured binary spin-exchange cross sections from the literature. The green region is where the derived ranges of each spin-exchange cross section contribution from the literature overlap. Our measured value is plotted at $P_{\text{Rb}} = 0$, as the optical pumping laser was not on during Γ_{down} measurements. 112
- 6.1 (a) The single compartment oven, as used in Chapter 5, and (b) the multi-compartment oven. Foam insulation is used to separate compartments. Each compartment has an independent heating element, PID controller and thermocouple in the ambient oven compartment space. 117
- 6.2 Multi-compartment oven setup, showing the approximate location of the Rb droplets/Rb source distributions in the optical cells. Rb distributions are (a) Rb in the presaturator only, (b) Rb in the presaturator and 2 Rb pools in the main cell body, (c) Rb in the presaturator and 4 Rb pools in the main cell body, (d) Rb in the presaturator, 4 Rb pools in the main body and dry-ice Rb coating and (e) 4 Rb pools in the main body, no Rb presaturator. Corresponding photos of the optical cells are in Fig. 6.3.119

6.3 Optical cells (before installation) with Rb in the presaturator and **(a)** no Rb in the main body, corresponding to Fig. 6.2a; **(b)** 2 Rb pools in the main cell body corresponding to Fig. 6.2b; **(c)** 4 Rb pools in the main cell body, without dry-ice coating treatment, corresponding to Fig. 6.2c as viewed from **(i)** near the back of the cell and **(ii)** near the front of the cell; **(d)** 4 Rb pools in the main cell body, with dry-ice coating treatment, corresponding to Fig. 6.2d; **(e)** no presaturator and 4 Rb pools in the main cell body, without dry-ice coating treatment, corresponding to Fig. 6.2e. There are Rb trails between the Rb pools, due to the tendency for the Rb to stick to the cell walls. When installed on the polariser and heated, the Rb aggregated together reducing the size of the Rb trails. **(b)**, **(c)** and **(d)** show Rb also by the back cell window due to collecting in the trench between the window and walls. 120

6.4 Diagram showing the differences between the **(a)** numerical and **(b)** analytical P_{Xe} build up models. 122

6.5 Simulated Rb density, $[Rb]$, distributions. **(a)** Homogeneous $[Rb]$ across the full cell length $L_{Rb} = L_{cell}$. **(b)** Heterogeneous $[Rb]$ where $[Rb] = [Rb]_{sat}$ only within the L_{Rb} region. Beyond this region $[Rb] = 0$. For the numerical model, this results in a reduction in the effective cell length, whereas for the analytical model, the cell-averaged Rb density, $\langle [Rb] \rangle$ changes by a factor L_{Rb}/L_{cell} compared to the homogeneous case in **(a)**. 124

6.6 Cryogenic accumulation setups consisting of the spiral glassware and permanent magnets on each side. Xe snow (white) can be seen within the spiral. Not pictured are the liquid N_2 dewars in which the spirals are submerged. **(a)** Existing 5-turn spiral setup. **(b)** New 8.5-turn spiral setup, which is larger in order to improve Xe volume recovery at high flow rate. 128

6.7 Single-compartment oven - Oven to cell and presaturator temperature differential, $T - T_{oven}$, with the presaturator heating tape switched off. **(a)** Cell temperature for different oven temperatures, T_{oven} . **(b)** $T - T_{oven}$ for different T_{oven} . Dashed lines are to guide the eye only. 130

6.8 Single-compartment oven - $T - T_{oven}$ with the presaturator heating tape switched on. **(a)** Presaturator temperature vs heating tape power for $T_{oven} = 95^\circ C$ and $125^\circ C$. **(b)** Cell temperature for presaturator heating tape powers, where triangles and circles are for $T_{oven} = 95^\circ C$ and $T_{oven} = 125^\circ C$ respectively. **(c)** $T - T_{oven}$ vs presaturator heating tape power for $T_{oven} = 95^\circ C$ and **(d)** for $T_{oven} = 125^\circ C$. Dashed lines are to guide the eye only. 131

- 6.9 Multi-compartment oven - $T - T_{\text{oven}}$ with the presaturator heating tape switched on. **(a)** Presaturator temperature vs heating tape power for $T_{\text{oven}} = 90^\circ\text{C}$ and 120°C . **(b)** Cell temperatures for different presaturator heating tape powers, where triangles and circles are for $T_{\text{oven}} = 90^\circ\text{C}$ and $T_{\text{oven}} = 120^\circ\text{C}$ respectively. $T - T_{\text{oven}}$ vs presaturator heating tape power for **(c)** $T_{\text{oven}} = 90^\circ\text{C}$ and **(d)** $T_{\text{oven}} = 120^\circ\text{C}$. Dashed lines are to guide the eye only. Discrepancy between back cell temperature (cell position = 75.5cm) here and in Table 6.2 was investigated but no cell or oven setup differences were observed. 133
- 6.10 2nd repeat of temperatures and laser absorption static to under flow ($Q = 2\text{NLPM}$) and under flow to static gas for the following Rb distributions; **(a)** no Rb in the main body, Rb in the presaturator (presat) only, **(b)** 2 Rb pools in the main cell body **(c)** 4 Rb pools in the main cell body **(d)** 4 Rb pools in the main cell body and with dry-ice Rb coating, **(e)** no presaturator, 4 Rb pools in the main cell body and performed for $Q = 1.7\text{NLPM}$ due to a mass flow regulator issue, **(f)** 4 Rb pools in the main cell body and presaturator in a single compartment oven. 136
- 6.11 Rb runaway occurring in the single compartment oven. The oven thermocouple was placed towards the back of oven. At time = 0 min, the set oven temperature was changed from 90°C to 100°C 139
- 6.12 **(a)** Cell-averaged Rb density, $\langle[\text{Rb}]\rangle$, **(b)** Xe polarisation, P_{Xe} and **(c)** critical flow rate, Q_c , vs **(i)** temperature and **(ii)** laser absorption for different L_{Rb} . Cell lengths tested were $L_{\text{Rb}} = L_{\text{cell}}$ (solid lines), $L_{\text{Rb}} = L_{\text{cell}}/2$ (dashed lines), $L_{\text{Rb}} = L_{\text{cell}}/4$ (dotted lines) and $L_{\text{Rb}} = L_{\text{cell}}/8$ (dash-dotted lines), corresponding to increasing $[\text{Rb}]$ heterogeneity. Black and red lines indicate the numerical model and analytical models respectively. 141
- 6.13 Modelled P_{Xe} , Rb polarisation, P_{Rb} , and laser absorption vs cell position using the numerical (solid lines) and analytical (dashed lines) models for $Q = 2\text{NLPM}$ and $L_{\text{Rb}} = L_{\text{cell}}$ (homogeneous $[\text{Rb}]$). This was performed at different temperatures corresponding to optimal temperatures for different L_{Rb} values. **(a)** $T = 100^\circ\text{C}$ where low laser absorption occurs. **(b)** $T = 129.5^\circ\text{C}$, optimal T for $L_{\text{Rb}} = L_{\text{cell}}$. **(c)** $T = 141.5^\circ\text{C}$, optimal T for $L_{\text{Rb}} = L_{\text{cell}}/2$. **(d)** $T = 155^\circ\text{C}$, optimal T for $L_{\text{Rb}} = L_{\text{cell}}/4$. **(e)** $T = 169^\circ\text{C}$, optimal T for $L_{\text{Rb}} = L_{\text{cell}}/8$ 142

6.14 Contours of laser absorption vs flow rate vs **(a)** P_{Xe} and **(b)** Q_c . This was performed for **(ai, bi)** the numerical P_{Xe} build up model and **(aii, bii)** the analytical P_{Xe} build up model. **(c)** The absolute percentage difference between the numerical and analytical models, $|\%difference|$, was determined for **(ci)** P_{Xe} values, $|\%diff|_{P_{Xe}}$, and **(cii)** Q_c values, $|\%diff|_{Q_c}$. 145

6.15 Spin-down, Γ_{down} , vs [Rb] measured with the $5S_{1/2} \rightarrow 6P_{3/2}$ Rb transition, for the Rb coated, 4 Rb pools cell. From the linear fit, $\gamma' = (1.8 \pm 0.2) \times 10^{-21} \text{ m}^3\text{s}^{-1}$ and $1/\Gamma' = 111 \pm 27 \text{ s}$ 148

6.16 **(a)** P_{Xe} vs T_{oven} , **(b)** laser absorption vs T_{oven} , **(c)** P_{Xe} vs laser absorption and **(d)** critical flow rate, Q_c , vs mean laser absorption. Black lines correspond to static gas measurements and red lines to $Q = 2$ NLPM measurements. Solid lines are from the numerical model and dashed lines from the analytical model. Theoretical curves incorporated spin-exchange cross section and Xe relaxation in absence of Rb values from Fig. 6.15, neglecting Rb polarisation dependence of the ^{129}Xe -Rb spin-exchange cross section. Dashed lines are to guide the eye only. 149

6.17 P_{Xe} , vs gas flow rate, Q , for **(a)** $T_{oven} = 111^\circ\text{C}$ and **(b)** $T_{oven} = 126^\circ\text{C}$. The red line is the fitting of data points to Eq. 6.4 giving **(a)** $P_{Xe}^{eq} = (36.7 \pm 0.4)\%$ and $Q_c = (1.83 \pm 0.06)\text{NLPM}$, and **(b)** $P_{Xe}^{eq} = (33.4 \pm 0.4)\%$ and $Q_c = (2.11 \pm 0.08)\text{NLPM}$. Blue data points are the values collected in a different session at the same T_{oven} in Fig. 6.16. The blue line is also of the form of Eq. 6.4, but uses the value of Q_c determined using the blue data points and Eq. 6.5. Red and blue lines show comparable Q dependence of P_{Xe} for both methods of deriving Q_c 150

6.18 Photon, $\eta_\gamma(t=0)$, spin-exchange, η_{SE} , and production rate, η_{pr} , efficiencies vs mean laser absorption. Solid lines are values produced using the numerical model and dashed lines are produced using the analytical model. $\eta_\gamma(t=0) = \eta_{SE}$ for values produced using the analytical model. Circles correspond to experimentally measured values. 153

6.19 B-field map for the cryotrap permanent magnet. Squares are measurements taken at zero x and z-displacement; circles were taken at 22.5mm x-displacement, zero z-displacement; and triangles were taken -22.5mm z-displacement, zero x-displacement. 157

6.20 Relaxation of frozen Xe snow in the cryotrap. Fitting to $V = V_0 \exp(-t/T_1)$ where $V_0 = 0.70 \pm 0.06\text{V}$ and $T_1 = 128 \pm 27\text{min}$ 158

-
- 6.21 (a) P_{Xe} contour plot for accumulation time, t_a vs total gas flow rate, Q .
(b) P_{Xe} contour plot for volume of Xe recovered, V_{Xe} vs t_a . The black dashed line represents $Q = 2\text{NLPM}$, so volumes of Xe per accumulation time above this line are not currently achievable with our setup as they would require $Q > 2\text{NLPM}$. The discontinuities in the contours and coloured regions is due to the f_{evac} condition discontinuity at $Q = 1\text{NLPM}$. 159
- 7.1 The chemical process of coating glass with n-octadecyltrichlorosilane (OTS). Figure reproduced with permission of the author from ref. [73]. Copyright 2023 by Matthew S. Rosen. 164
- 7.2 Piranha solution cleaning of a small optical cell (Cell volume $\sim 140\text{cm}^3$).
(a) The optical cell filled with piranha solution placed in the fume cupboard. (b) Close up picture showing bubbling due to the release of gas (likely CO_2 , O_2) as piranha solution reacts with organic impurities on the cell wall, as well as the decomposition of H_2O_2 164

List of Tables

3.1	SEOP Parameters. A range of values is given where multiple, differing, applicable values are present in the literature.	32
3.2	In-cell ^{129}Xe relaxation times in the absence of Rubidium, $T_1 = 1/\Gamma'$, measured in different SEOP cells. BM = batch-mode and CF = continuous-flow.	37
3.3	Rubidium electronic transition parameters.	39
4.1	Table of gas molar heat capacity coefficients given by ref. [124].	50
4.2	Xe diffusion coefficient parameters, given by ref. [125].	51
4.3	1D vs 3D simulation methods.	56
4.4	3D simulation boundary conditions.	57
4.5	Mesh elements corresponding to Table 4.6.	62
4.6	Mesh dependent parameters for the 10cm ² Rb pool cell, pressure $p = 1.25\text{bar}$, flow rate $Q = 2\text{SLM}$, $T_{\text{oven}} = 120^\circ\text{C}$. Highlighted values are where maximum absolute percentage change compared to ‘finer’ mesh solution occurs.	63
4.7	Mesh parameters for presaturator-only simulations, $p = 1.25\text{bar}$, $Q = 2\text{SLM}$, $T = 125^\circ\text{C}$. Highlighted values are where maximum absolute percentage change compared to ‘finer’ mesh solution occurs.	66
4.8	Mesh elements corresponding to Table 4.7.	67
4.9	Output P_{Xe} for different modelled Rb distributions, $p = 1.25\text{bar}$, $Q = 2\text{SLM}$	71
5.1	Xe polarisation, P_{Xe} , and optical pumping laser power absorption for each Rb SEOP cell tested.	106
6.1	1D numerical vs analytical P_{Xe} build up models.	123
6.2	Cell temperatures with a single oven compartment set to $T_{\text{oven}} = 120^\circ\text{C}$ whilst the other oven compartments are set to $T_{\text{oven}} = 70^\circ\text{C}$. The presaturator heating tape was switched off throughout.	132

6.3	Temperatures and laser absorption for static to under flow ($Q = 2\text{NLPM}$) and under flow to static gas for different Rb source distributions, using the multi-compartment oven.	137
6.4	Mass recovery performed on both cryotrap. For the 8.5-turn spiral, the first quoted uncertainty is the standard deviation and the second quoted uncertainty is due to the precision of the gas syringe. Where standard deviation = 0 was due to identical values from repeat measurements. < 3 repeat measurements were taken for the 5-turn spiral, so only the uncertainty due to the precision of the gas syringe is quoted.	155

Bibliography

- [1] I. I. Rabi, "Space Quantization in a Gyating Magnetic Field," *Physical Review*, vol. 51, pp. 652–654, 4 1937.
- [2] E. M. Purcell, H. C. Torrey, and R. V. Pound, "Resonance Absorption by Nuclear Magnetic Moments in a Solid," *Physical Review*, vol. 69, pp. 37–38, 1 1946.
- [3] F. Bloch, W. W. Hansen, and M. Packard, "The Nuclear Induction Experiment," *Physical Review*, vol. 70, pp. 474–485, 10 1946.
- [4] W. G. Proctor and F. C. Yu, "The Dependence of a Nuclear Magnetic Resonance Frequency upon Chemical Compound," *Physical Review*, vol. 77, p. 717, 3 1950.
- [5] W. C. Dickinson, "Dependence of the F^{19} Nuclear Resonance Position on Chemical Compound," *Physical Review*, vol. 77, pp. 736–737, 3 1950.
- [6] P. C. Lauterbur, "Image Formation by Induced Local Interactions: Examples Employing Nuclear Magnetic Resonance," *Nature*, vol. 242, no. 5394, pp. 190–191, 1973.
- [7] P Mansfield, "Multi-planar image formation using NMR spin echoes," *Journal of Physics C: Solid State Physics*, vol. 10, no. 3, p. L55, 1977.
- [8] A. Kastler, "Quelques suggestions concernant la production optique et la détection optique d'une inégalité de population des niveaux de quantification spatiale des atomes. Application à l'expérience de Stern et Gerlach et à la résonance magnétique," *J. phys. radium*, vol. 11, no. 6, pp. 255–265, 1950.
- [9] J. Brossel, A. Kastler, and J. Winter, "Gréation optique d'une inégalité de population entre les sous-niveaux Zeeman de l'état fondamental des atomes," *Journal de Physique et le Radium*, vol. 13, no. 12, p. 668, 1952.
- [10] M. A. Bouchiat, T. R. Carver, and C. M. Varnum, "Nuclear Polarization in He^3 Gas Induced by Optical Pumping and Dipolar Exchange," *Physical Review Letters*, vol. 5, pp. 373–375, 10 1960.

-
- [11] C. H. Volk, T. M. Kwon, and J. G. Mark, "Measurement of the ^{87}Rb – ^{129}Xe spin-exchange cross section," *Physical Review A*, vol. 21, no. 5, pp. 1549–1555, 1980.
- [12] N. D. Bhaskar, W. Happer, and T. McClelland, "Efficiency of Spin Exchange between Rubidium Spins and ^{129}Xe Nuclei in a Gas," *Physical Review Letters*, vol. 49, pp. 25–28, 7 1982.
- [13] W. Happer, E. Miron, S. Schaefer, D. Schreiber, W. A. van Wijngaarden, and X. Zeng, "Polarization of the nuclear spins of noble-gas atoms by spin exchange with optically pumped alkali-metal atoms," *Physical Review A*, vol. 29, pp. 3092–3110, 6 1984.
- [14] T. G. Walker, "Estimates of spin-exchange parameters for alkali-metal–noble-gas pairs," *Physical Review A*, vol. 40, pp. 4959–4964, 11 1989.
- [15] G. D. Cates, R. J. Fitzgerald, A. S. Barton, P. Bogorad, M. Gatzke, N. R. Newbury, and B. Saam, " Rb – ^{129}Xe spin-exchange rates due to binary and three-body collisions at high Xe pressures," *Physical Review A*, vol. 45, pp. 4631–4639, 4 1992.
- [16] W. Franzen, "Spin Relaxation of Optically Aligned Rubidium Vapor," *Physical Review*, vol. 115, pp. 850–856, 8 1959.
- [17] C. C. Bouchiat, M. A. Bouchiat, and L. C. L. Pottier, "Evidence for Rb-Rare-Gas Molecules from the Relaxation of Polarized Rb Atoms in a Rare Gas. Theory," *Physical Review*, vol. 181, pp. 144–165, 5 1969.
- [18] M. A. Bouchiat, J. Brossel, and L. C. Pottier, "Evidence for Rb-Rare-Gas Molecules from the Relaxation of Polarized Rb Atoms in a Rare Gas. Experimental Results," *The Journal of Chemical Physics*, vol. 56, pp. 3703–3714, 4 1972.
- [19] F. A. Franz and C. Volk, "Spin relaxation of rubidium atoms in sudden and quasimolecular collisions with light-noble-gas atoms," *Physical Review A*, vol. 14, pp. 1711–1728, 11 1976.
- [20] N. D. Bhaskar, W. Happer, M. Larsson, and X. Zeng, "Slowing Down of Rubidium-Induced Nuclear Spin Relaxation of ^{129}Xe Gas in a Magnetic Field," *Physical Review Letters*, vol. 50, pp. 105–108, 1 1983.
- [21] X. Zeng, E. Miron, W. A. Van Wijngaarden, D. Schreiber, and W. Happer, "Wall relaxation of spin polarized ^{129}Xe nuclei," *Physics Letters A*, vol. 96, no. 4, pp. 191–194, 1983.

- [22] X. Zeng, Z. Wu, T. Call, E. Miron, D. Schreiber, and W. Happer, “Experimental determination of the rate constants for spin exchange between optically pumped K, Rb, and Cs atoms and ^{129}Xe nuclei in alkali-metal–noble-gas van der Waals molecules,” *Physical Review A*, vol. 31, pp. 260–278, 1 1985.
- [23] G. D. Cates, S. R. Schaefer, and W. Happer, “Relaxation of spins due to field inhomogeneities in gaseous samples at low magnetic fields and low pressures,” *Physical Review A*, vol. 37, pp. 2877–2885, 4 1988.
- [24] C. J. Jameson, A. K. Jameson, and J. K. Hwang, “Nuclear spin relaxation by intermolecular magnetic dipole coupling in the gas phase. ^{129}Xe in oxygen,” *The Journal of Chemical Physics*, vol. 89, pp. 4074–4081, 10 1988.
- [25] B. Driehuys, G. D. Cates, E. Miron, K. Sauer, D. K. Walter, and W. Happer, “High-volume production of laser-polarized ^{129}Xe ,” *Applied Physics Letters*, vol. 69, pp. 1668–1670, 9 1996.
- [26] M. S. Albert, G. D. Cates, B. Driehuys, W. Happer, B. Saam, C. S. Springer, and A. Wishnia, “Biological magnetic resonance imaging using laser-polarized ^{129}Xe ,” *Nature*, vol. 370, no. 6486, pp. 199–201, 1994.
- [27] J. P. Mugler III, B. Driehuys, J. R. Brookeman, G. D. Cates, S. S. Berr, R. G. Bryant, T. M. Daniel, E. E. De Lange, J. H. Downs, C. J. Erickson, W. Happer, D. P. Hinton, N. F. Kassel, T. Maier, C. D. Phillips, B. T. Saam, K. L. Sauer, and M. E. Wagshul, “MR imaging and spectroscopy using hyperpolarized ^{129}Xe gas: Preliminary human results,” *Magnetic Resonance in Medicine*, vol. 37, pp. 809–815, 6 1997.
- [28] M. Ebert, T. Grossmann, W. Heil, E. W. Otten, R. Surkau, M. Thelen, M. Leduc, P. Bachert, M. V. Knopp, and L. R. Schad, “Nuclear magnetic resonance imaging with hyperpolarised helium-3,” *The Lancet*, vol. 347, no. 9011, pp. 1297–1299, 1996.
- [29] D. A. Shea and D. L. Morgan, “The helium-3 shortage: Supply, demand, and options for congress,” tech. rep., Congressional Research Service, Washington D.C., 2010.
- [30] I. C. Ruset, *Hyperpolarized ^{129}Xe Production and Applications*. PhD thesis, University of New Hampshire, Durham, 2005.
- [31] F. W. Hersman, I. C. Ruset, S. Ketel, I. Muradian, S. D. Covrig, J. Distelbrink, W. Porter, D. Watt, J. Ketel, J. Brackett, A. Hope, and S. Patz, “Large Production System for Hyperpolarized ^{129}Xe for Human Lung Imaging Studies,” *Academic Radiology*, vol. 15, no. 6, pp. 683–692, 2008.

- [32] P. Nikolaou, A. M. Coffey, L. L. Walkup, B. M. Gust, N. Whiting, H. Newton, S. Barcus, I. Muradyan, M. Dabaghyan, G. D. Moroz, M. S. Rosen, S. Patz, M. J. Barlow, E. Y. Chekmenev, and B. M. Goodson, “Near-unity nuclear polarization with an open-source ^{129}Xe hyperpolarizer for NMR and MRI,” *Proceedings of the National Academy of Sciences*, vol. 110, pp. 14150 LP – 14155, 8 2013.
- [33] S. S. Kaushik, Z. I. Cleveland, G. P. Cofer, G. Metz, D. Beaver, J. Nouis, M. Kraft, W. Auffermann, J. Wolber, H. P. McAdams, and B. Driehuys, “Diffusion-weighted hyperpolarized ^{129}Xe MRI in healthy volunteers and subjects with chronic obstructive pulmonary disease,” *Magnetic Resonance in Medicine*, vol. 65, pp. 1154–1165, 4 2011.
- [34] M. Kirby, S. Svenningsen, A. Owrangi, A. Wheatley, A. Farag, A. Ouriadov, G. E. Santyr, R. Etemad-Rezai, H. O. Coxson, D. G. McCormack, and G. Parraga, “Hyperpolarized ^3He and ^{129}Xe MR Imaging in Healthy Volunteers and Patients with Chronic Obstructive Pulmonary Disease,” *Radiology*, vol. 265, pp. 600–610, 11 2012.
- [35] L. Myc, K. Qing, M. He, N. Tustison, Z. Lin, A. W. Manichaikul, J. Patrie, J. Cassani, R. N. Nunoo-Asare, Y. Huang, Z. Obaida, S. Tafti, A. M. Ropp, G. W. Miller, J. Mata, T. Altes, J. Mugler, and Y. M. Shim, “Characterisation of gas exchange in COPD with dissolved-phase hyperpolarised xenon-129 MRI,” *Thorax*, vol. 76, pp. 178 LP – 181, 2 2021.
- [36] S. Svenningsen, M. Kirby, D. Starr, D. Leary, A. Wheatley, G. N. Maksym, D. G. McCormack, and G. Parraga, “Hyperpolarized ^3He and ^{129}Xe MRI: Differences in asthma before bronchodilation,” *Journal of Magnetic Resonance Imaging*, vol. 38, pp. 1521–1530, 12 2013.
- [37] K. Qing, J. P. Mugler III, T. A. Altes, Y. Jiang, J. F. Mata, G. W. Miller, I. C. Ruset, F. W. Hersman, and K. Ruppert, “Assessment of lung function in asthma and COPD using hyperpolarized ^{129}Xe chemical shift saturation recovery spectroscopy and dissolved-phase MRI,” *NMR in Biomedicine*, vol. 27, pp. 1490–1501, 12 2014.
- [38] L. L. Walkup, R. P. Thomen, T. G. Akinyi, E. Watters, K. Ruppert, J. P. Clancy, J. C. Woods, and Z. I. Cleveland, “Feasibility, tolerability and safety of pediatric hyperpolarized ^{129}Xe magnetic resonance imaging in healthy volunteers and children with cystic fibrosis,” *Pediatric Radiology*, vol. 46, no. 12, pp. 1651–1662, 2016.
- [39] J. C. Woods, J. M. Wild, M. O. Wielpütz, J. P. Clancy, H. Hatabu, H.-U. Kauczor, E. J. R. van Beek, and T. A. Altes, “Current state of the art MRI for the

- longitudinal assessment of cystic fibrosis,” *Journal of Magnetic Resonance Imaging*, vol. 52, pp. 1306–1320, 11 2020.
- [40] L. J. Smith, A. Horsley, J. Bray, P. J. C. Hughes, A. Biancardi, G. Norquay, M. Wildman, N. West, H. Marshall, and J. M. Wild, “The assessment of short- and long-term changes in lung function in cystic fibrosis using ^{129}Xe MRI,” *European Respiratory Journal*, vol. 56, p. 2000441, 12 2020.
- [41] S. S. Kaushik, M. S. Freeman, S. W. Yoon, M. G. Liljeroth, J. V. Stiles, J. E. Roos, W. S. Michael Foster, C. R. Rackley, H. P. McAdams, and B. Driehuys, “Measuring diffusion limitation with a perfusion-limited gas—Hyperpolarized ^{129}Xe gas-transfer spectroscopy in patients with idiopathic pulmonary fibrosis,” *Journal of Applied Physiology*, vol. 117, pp. 577–585, 7 2014.
- [42] N. J. Stewart, G. Leung, G. Norquay, H. Marshall, J. Parra-Robles, P. S. Murphy, R. F. Schulte, C. Elliot, R. Condliffe, P. D. Griffiths, D. G. Kiely, M. K. Whyte, J. Wolber, and J. M. Wild, “Experimental validation of the hyperpolarized ^{129}Xe chemical shift saturation recovery technique in healthy volunteers and subjects with interstitial lung disease,” *Magnetic Resonance in Medicine*, vol. 74, pp. 196–207, 7 2015.
- [43] J. M. Wang, S. H. Robertson, Z. Wang, M. He, R. S. Virgincar, G. M. Schrank, R. M. Smigla, T. G. O’Riordan, J. Sundry, L. Ebner, C. R. Rackley, P. McAdams, and B. Driehuys, “Using hyperpolarized ^{129}Xe MRI to quantify regional gas transfer in idiopathic pulmonary fibrosis,” *Thorax*, vol. 73, pp. 21 LP – 28, 1 2018.
- [44] J. G. Mammarrappallil, L. Rankine, J. M. Wild, and B. Driehuys, “New Developments in Imaging Idiopathic Pulmonary Fibrosis With Hyperpolarized Xenon Magnetic Resonance Imaging,” *Journal of Thoracic Imaging*, vol. 34, no. 2, 2019.
- [45] N. D. Weatherley, N. J. Stewart, H.-F. Chan, M. Austin, L. J. Smith, G. Collier, M. Rao, H. Marshall, G. Norquay, S. A. Renshaw, S. M. Bianchi, and J. M. Wild, “Hyperpolarised xenon magnetic resonance spectroscopy for the longitudinal assessment of changes in gas diffusion in IPF,” *Thorax*, vol. 74, pp. 500 LP – 502, 5 2019.
- [46] K. Qing, T. A. Altes, J. P. Mugler, J. F. Mata, N. J. Tustison, K. Ruppert, J. Bueno, L. Flors, Y. M. Shim, L. Zhao, J. Cassani, W. G. Teague, J. S. Kim, Z. Wang, I. C. Ruset, F. W. Hersman, and B. Mehrad, “Hyperpolarized Xenon-129: A New Tool to Assess Pulmonary Physiology in Patients with Pulmonary Fibrosis,” *Biomedicines*, vol. 11, no. 6, 2023.
- [47] J. T. Grist, M. Chen, G. J. Collier, B. Raman, G. Abueid, A. McIntyre, V. Matthews, E. Fraser, L.-P. Ho, J. M. Wild, and F. Gleeson, “Hyperpolar-

- ized ^{129}Xe MRI Abnormalities in Dyspneic Patients 3 Months after COVID-19 Pneumonia: Preliminary Results,” *Radiology*, vol. 301, pp. E353–E360, 5 2021.
- [48] L. Haidong, Z. Xiuchao, W. Yujin, L. Xin, C. Shizhen, D. He, S. Lei, X. Junshuai, T. Dazhong, Z. Jianping, B. Louis-S., X. Liming, and Z. Xin, “Damaged lung gas exchange function of discharged COVID-19 patients detected by hyperpolarized ^{129}Xe MRI,” *Science Advances*, vol. 7, p. eabc8180, 2 2022.
- [49] M. Rao, N. Stewart, P. Griffiths, G. Norquay, and J. Wild, “Imaging Human Brain Perfusion with Inhaled Hyperpolarized ^{129}Xe MR Imaging,” *Radiology*, vol. 286, no. 2, pp. 659–665, 2018.
- [50] J. Chacon-Caldera, A. Maunder, M. Rao, G. Norquay, O. I. Rodgers, M. Clemence, C. Puddu, L. R. Schad, and J. M. Wild, “Dissolved hyperpolarized xenon-129 MRI in human kidneys,” *Magnetic Resonance in Medicine*, vol. 83, pp. 262–270, 1 2020.
- [51] O. Doganay, M. Chen, T. Matin, M. Rigolli, J.-A. Phillips, A. McIntyre, and F. V. Gleeson, “Magnetic resonance imaging of the time course of hyperpolarized ^{129}Xe gas exchange in the human lungs and heart,” *European Radiology*, vol. 29, no. 5, pp. 2283–2292, 2019.
- [52] G. Norquay, G. J. Collier, M. Rao, N. J. Stewart, and J. M. Wild, “ ^{129}Xe -Rb Spin-Exchange Optical Pumping with High Photon Efficiency,” *Physical Review Letters*, vol. 121, p. 153201, 10 2018.
- [53] G. Schrank, Z. Ma, A. Schoeck, and B. Saam, “Characterization of a low-pressure high-capacity ^{129}Xe flow-through polarizer,” *Physical Review A*, vol. 80, p. 63424, 12 2009.
- [54] G. Norquay, S. R. Parnell, X. Xu, J. Parra-Robles, and J. M. Wild, “Optimized production of hyperpolarized ^{129}Xe at 2 bars for in vivo lung magnetic resonance imaging,” *Journal of Applied Physics*, vol. 113, p. 44908, 1 2013.
- [55] M. S. S. Freeman, K. Emami, and B. Driehuys, “Characterizing and modeling the efficiency limits in large-scale production of hyperpolarized ^{129}Xe ,” *Physical Review A*, vol. 90, p. 23406, 8 2014.
- [56] A. Abragam, *The principles of nuclear magnetism*. Oxford: Clarendon Press, 1961.
- [57] D. Canet, *Nuclear magnetic resonance: concepts and methods*. Chichester: Wiley, 1996.
- [58] M. H. Levitt, *Spin dynamics: basics of nuclear magnetic resonance*. Wiley, 2001.

- [59] R. K. R. K. Harris, *Nuclear magnetic resonance spectroscopy : a physicochemical view*. Harlow: Longman Scientific & Technical, rev ed., 1986.
- [60] I. Solomon, “Relaxation Processes in a System of Two Spins,” *Physical Review*, vol. 99, pp. 559–565, 7 1955.
- [61] J. Mispelter, M. Lupu, and A. Briguet, *NMR probeheads for biophysical and biomedical experiments: theoretical principles and practical guidelines*. World Scientific Publishing Company, 2015.
- [62] D. Steck, “Rubidium 87 D line data, Oregon Center for Optics and Department of Physics, University of Oregon.” <https://steck.us/alkalidata/>, 2003. revision 1.6, 14 October 2003.
- [63] D. Steck, “Rubidium 85 D line data, Oregon Center for Optics and Department of Physics, University of Oregon.” <https://steck.us/alkalidata/>, 2021. revision 2.2.3, 9 July 2021.
- [64] M. E. Wagshul and T. E. Chupp, “Optical pumping of high-density Rb with a broadband dye laser and GaAlAs diode laser arrays: Application to ^3He polarization,” *Physical Review A*, vol. 40, pp. 4447–4454, 10 1989.
- [65] E. S. Hrycyszyn and L. Krause, “Inelastic collisions between excited alkali atoms and molecules. VII. Sensitized fluorescence and quenching in mixtures of rubidium with H_2 , HD, D_2 , N_2 , CH_4 , CD_4 , C_2H_4 , and C_2H_6 ,” *Canadian Journal of Physics*, vol. 48, pp. 2761–2768, 11 1970.
- [66] E. Brunner, “Enhancement of surface and biological magnetic resonance using laser-polarized noble gases,” *Concepts in Magnetic Resonance*, vol. 11, no. 5, pp. 313–335, 1999.
- [67] S. Appelt, A. Ben-Amar Baranga, A. R. Young, and W. Happer, “Light narrowing of rubidium magnetic-resonance lines in high-pressure optical-pumping cells,” *Physical Review A*, vol. 59, pp. 2078–2084, 3 1999.
- [68] S. Appelt, A. B.-A. Baranga, C. J. Erickson, M. V. Romalis, A. R. Young, and W. Happer, “Theory of spin-exchange optical pumping of ^3He and ^{129}Xe ,” *Physical Review A*, vol. 58, pp. 1412–1439, 8 1998.
- [69] S. Appelt, T. Ünlü, K. Zilles, N. J. Shah, S. Baer-Lang, and H. Halling, “Experimental studies of rubidium absolute polarization at high temperatures,” *Applied Physics Letters*, vol. 75, pp. 427–429, 7 1999.
- [70] I. A. Nelson, *Physics of practical spin-exchange optical pumping*. PhD thesis, University of Wisconsin-Madison, Madison, 2001.

- [71] A. Fink, D. Baumer, and E. Brunner, "Production of hyperpolarized xenon in a static pump cell: Numerical simulations and experiments," *Physical Review A*, vol. 72, p. 53411, 11 2005.
- [72] M. G. Mortuza, S. Anala, G. E. Pavlovskaya, T. J. Dieken, and T. Meersmann, "Spin-exchange optical pumping of high-density xenon-129," *The Journal of Chemical Physics*, vol. 118, pp. 1581–1584, 1 2003.
- [73] M. S. Rosen, *Laser-polarized xenon-129 magnetic resonance spectroscopy and imaging. The development of a method for in vivo perfusion measurement*. PhD thesis, University of Michigan, Ann Arbor, 2001.
- [74] B. Chann, E. Babcock, L. W. Anderson, and T. G. Walker, "Skew light propagation in optically thick optical pumping cells," *Physical Review A*, vol. 66, p. 33406, 9 2002.
- [75] B. Lancor, E. Babcock, R. Wyllie, and T. G. Walker, "Breakdown of Angular Momentum Selection Rules in High Pressure Optical Pumping Experiments," *Physical Review Letters*, vol. 105, p. 83003, 8 2010.
- [76] B. Lancor, E. Babcock, R. Wyllie, and T. G. Walker, "Circular dichroism of RbHe and RbN₂ molecules," *Physical Review A*, vol. 82, p. 43435, 10 2010.
- [77] T. G. Walker and M. S. Larsen, "Chapter Eight - Spin-Exchange-Pumped NMR Gyros," vol. 65, pp. 373–401, Academic Press, 2016.
- [78] I. A. Nelson and T. G. Walker, "Rb-Xe spin relaxation in dilute Xe mixtures," *Physical Review A*, vol. 65, p. 12712, 12 2001.
- [79] Z. Wu, T. G. Walker, and W. Happer, "Spin-Rotation Interaction of Noble-Gas Alkali-Metal Atom Pairs," *Physical Review Letters*, vol. 54, pp. 1921–1924, 4 1985.
- [80] N. Ramsey, E. Miron, X. Zeng, and W. Happe, "Formation and breakup rates of RbXe van der Waals molecules in He and N₂ gas," *Chemical Physics Letters*, vol. 102, no. 4, pp. 340–343, 1983.
- [81] T. J. Killian, "Thermionic Phenomena Caused by Vapors of Rubidium and Potassium," *Physical Review*, vol. 27, pp. 578–587, 5 1926.
- [82] M. V. Romalis, E. Miron, and G. D. Cates, "Pressure broadening of Rb D₁ and D₂ lines by ³He, ⁴He, N₂, and Xe: Line cores and near wings," *Physical Review A - Atomic, Molecular, and Optical Physics*, vol. 56, pp. 4569–4578, 12 1997.

- [83] A. B.-A. Baranga, S. Appelt, C. J. Erickson, A. R. Young, and W. Happer, “Alkali-metal-atom polarization imaging in high-pressure optical-pumping cells,” *Physical Review A*, vol. 58, pp. 2282–2294, 9 1998.
- [84] W. C. Chen, T. R. Gentile, T. G. Walker, and E. Babcock, “Spin-exchange optical pumping of ^3He with Rb-K mixtures and pure K,” *Physical Review A*, vol. 75, p. 13416, 1 2007.
- [85] L. Chen and Y. Ren, “Rapid ^{129}Xe –Rb spin-exchange rate measurement by using an atomic magnetometer,” *Applied Optics*, vol. 59, no. 13, pp. 3967–3970, 2020.
- [86] B. Song, Y. Wang, and N. Zhao, “Spin-polarization dependence of the Rb-Xe spin-exchange optical pumping process,” *Physical Review A*, vol. 104, p. 23105, 8 2021.
- [87] W. Shao, G. Wang, and E. W. Hughes, “Measurement of spin-exchange rate constants between ^{129}Xe and alkali metals,” *Physical Review A - Atomic, Molecular, and Optical Physics*, vol. 72, p. 22713, 8 2005.
- [88] E. R. Hunt and H. Y. Carr, “Nuclear Magnetic Resonance of Xe^{129} in Natural Xenon,” *Physical Review*, vol. 130, pp. 2302–2305, 6 1963.
- [89] B. Chann, I. A. Nelson, L. W. Anderson, B. Driehuys, and T. G. Walker, “ ^{129}Xe -Xe Molecular Spin Relaxation,” *Physical Review Letters*, vol. 88, p. 113201, 2 2002.
- [90] L. A. Pedros, *Diffusion of laser polarized gases in MRI*. PhD thesis, Johannes Gutenberg-Universität Mainz, Mainz, 2008.
- [91] T. G. Walker and W. Happer, “Spin-exchange optical pumping of noble-gas nuclei,” *Reviews of Modern Physics*, vol. 69, pp. 629–642, 4 1997.
- [92] G. Zhang, L. Wei, M. Wang, and K. Zhao, “Effects of water concentration in the coating solution on the wall relaxation rate of octadecyltrichlorosilane coated rubidium vapor cells,” *Journal of Applied Physics*, vol. 117, p. 43106, 1 2015.
- [93] S. R. Breeze, S. Lang, I. Moudrakovski, C. I. Ratcliffe, J. A. Ripmeester, B. Simard, and G. Santyr, “Coatings for optical pumping cells and extending the lifetime of hyperpolarized xenon,” *Journal of Applied Physics*, vol. 86, pp. 4040–4042, 9 1999.
- [94] J. W. Plummer, K. Emami, A. Dummer, J. C. Woods, L. L. Walkup, and Z. I. Cleveland, “A semi-empirical model to optimize continuous-flow hyperpolarized ^{129}Xe production under practical cryogenic-accumulation conditions,” *Journal of Magnetic Resonance*, vol. 320, p. 106845, 2020.

- [95] E. Babcock, B. Chann, T. G. Walker, W. C. Chen, and T. R. Gentile, “Limits to the Polarization for Spin-Exchange Optical Pumping of ^3He ,” *Physical Review Letters*, vol. 96, p. 83003, 3 2006.
- [96] N. Shah, T. Ünlü, H.-P. Wegener, H. Halling, K. Zilles, and S. Appelt, “Measurement of rubidium and xenon absolute polarization at high temperatures as a means of improved production of hyperpolarized ^{129}Xe ,” *NMR in Biomedicine*, vol. 13, no. 4, pp. 214–219, 2000.
- [97] M. Repetto, E. Babcock, P. Blümmler, W. Heil, S. Karpuk, and K. Tullney, “Systematic T_1 improvement for hyperpolarized ^{129}Xe ,” *Journal of Magnetic Resonance*, vol. 252, pp. 163–169, 2015.
- [98] S. R. Breeze, S. Lang, I. Moudrakovski, C. I. Ratcliffe, J. A. Ripmeester, G. Santyr, B. Simard, and I. Zuger, “Coatings for optical pumping cells and short-term storage of hyperpolarized xenon,” *Journal of Applied Physics*, vol. 87, pp. 8013–8017, 5 2000.
- [99] J. R. Birchall, P. Nikolaou, A. M. Coffey, B. E. Kidd, M. Murphy, M. Molway, L. B. Bales, B. M. Goodson, R. K. Irwin, M. J. Barlow, and E. Y. Chekmenev, “Batch-Mode Clinical-Scale Optical Hyperpolarization of Xenon-129 Using an Aluminum Jacket with Rapid Temperature Ramping,” *Analytical Chemistry*, 2 2020.
- [100] M. Kelley and R. T. Branca, “Theoretical models of spin-exchange optical pumping: Revisited and reconciled,” *Journal of Applied Physics*, vol. 129, p. 154901, 4 2021.
- [101] C. E. Moore, *Atomic energy levels as derived from the analyses of optical spectra : volume II. ^{24}Cr to ^{41}Nb* . U.S. Department of Commerce, National Bureau of Standards, 1971.
- [102] J. Migdalek and Y.-K. Kim, “Core polarization and oscillator strength ratio anomaly in potassium, rubidium and caesium,” *Journal of Physics B: Atomic, Molecular and Optical Physics*, vol. 31, no. 9, pp. 1947–1960, 1998.
- [103] D. R. Bates, A. Damgaard, and H. S. W. Massey, “The calculation of the absolute strengths of spectral lines,” *Philosophical Transactions of the Royal Society of London. Series A, Mathematical and Physical Sciences*, vol. 242, pp. 101–122, 1 1949.
- [104] E. Caliebe and K. Niemax, “Oscillator strengths of the principal series lines of Rb,” *Journal of Physics B: Atomic and Molecular Physics*, vol. 12, no. 2, p. L45, 1979.

- [105] G. D. Christian and F. J. Feldman, *Atomic absorption spectroscopy : applications in agriculture, biology and medicine*. New York: Chichester : Wiley-Interscience, 1970.
- [106] A. L. Stancik and E. B. Brauns, “A simple asymmetric lineshape for fitting infrared absorption spectra,” *Vibrational Spectroscopy*, vol. 47, no. 1, pp. 66–69, 2008.
- [107] W. Price, *Spectrochemical analysis by atomic absorption*. London: Heyden, 1979.
- [108] J. Speight, *Lange’s handbook of chemistry*. McGraw-Hill Education, 2005.
- [109] M. E. Wagshul and T. E. Chupp, “Laser optical pumping of high-density Rb in polarized ^3He targets,” *Physical Review A*, vol. 49, pp. 3854–3869, 5 1994.
- [110] K. Ranta, *Clinical-scale hyperpolarization of ^{129}Xe and ^{131}Xe via stopped-flow spin-exchange optical pumping*. PhD thesis, Southern Illinois University Carbondale, Carbondale, 2016.
- [111] J. G. Skinner, K. Ranta, N. Whiting, A. M. Coffey, P. Nikolaou, M. S. Rosen, E. Y. Chekmenev, P. G. Morris, M. J. Barlow, and B. M. Goodson, “High Xe density, high photon flux, stopped-flow spin-exchange optical pumping: Simulations versus experiments,” *Journal of Magnetic Resonance*, vol. 312, p. 106686, 3 2020.
- [112] A. Fink and E. Brunner, “Optimization of continuous flow pump cells used for the production of hyperpolarized ^{129}Xe : A theoretical study,” *Applied Physics B*, vol. 89, no. 1, pp. 65–71, 2007.
- [113] G. M. Schrank, “A Novel, Finite-Element Model for Spin-Exchange Optical Pumping Using an Open-Source Code.” arXiv preprint arXiv:1911.01574, 2019.
- [114] G. M. Schrank, “Fluid and Thermal Dynamical Analysis of Three-Dimensional Spin-Exchange Optical Pumping Cells.” arXiv preprint arXiv:2005.08404, 2020.
- [115] M. Kelley, A. Burant, and R. T. Branca, “Resolving the discrepancy between theoretical and experimental polarization of hyperpolarized ^{129}Xe using numerical simulations and in situ optical spectroscopy,” *Journal of Applied Physics*, vol. 128, p. 144901, 10 2020.
- [116] C. Witte, M. Kunth, F. Rossella, and L. Schröder, “Observing and preventing rubidium runaway in a direct-infusion xenon-spin hyperpolarizer optimized for high-resolution hyper-CEST (chemical exchange saturation transfer using hyperpolarized nuclei) NMR,” *The Journal of Chemical Physics*, vol. 140, p. 84203, 2 2014.

-
- [117] I. C. Ruset, S. Ketel, and F. W. Hersman, “Optical Pumping System Design for Large Production of Hyperpolarized ^{129}Xe ,” *Physical Review Letters*, vol. 96, p. 53002, 2 2006.
- [118] S. T. G. S. GmbH, “BOROFLOAT® 33 – Technical Data.” <https://www.schott.com/en-ro/products/borofloat-p1000314/downloads>. Accessed on 24 July 2023.
- [119] VIN KAROLA INSTRUMENTS, “Corning Glass 7740 Properties.” <https://www.vinkarola.com/TechnicalInformation.htm>. Accessed on 24 July 2023.
- [120] C. Livermore and J. Voldman, “6.777J/2.751J Material Properties Database, Material: Pyrex Glass.” <http://web.mit.edu/6.777/www/matprops/pyrex.htm>, 2004. Accessed on 7 April 2020.
- [121] Engineering ToolBox, “Specific Heat of common Substances.” https://www.engineeringtoolbox.com/specific-heat-capacity-d_391.html, 2003. Accessed on 24 July 2023.
- [122] R. B. Bird, *Transport phenomena*. New York: John Wiley & Sons, Inc., revised 2nd ed., 2007.
- [123] S. Chapman, T. G. Cowling, D. Burnett, and C. Cercignani, *The Mathematical Theory of Non-uniform Gases: An Account of the Kinetic Theory of Viscosity, Thermal Conduction and Diffusion in Gases*. Cambridge Mathematical Library, Cambridge University Press, 1990.
- [124] M. Chase, *NIST-JANAF Thermochemical Tables*, pp. 1–1951. J. Phys. Chem. Ref. Data, Monograph 9, fourth ed., 1998.
- [125] B. E. Poling, J. M. Prausnitz, and J. P. O’Connell, *Properties of Gases and Liquids*. New York: McGraw-Hill Education, 5th ed., 2001.
- [126] P. D. Neufeld, A. R. Janzen, and R. A. Aziz, “Empirical Equations to Calculate 16 of the Transport Collision Integrals $\Omega^{(l,s)*}$ for the Lennard-Jones (12–6) Potential,” *The Journal of Chemical Physics*, vol. 57, pp. 1100–1102, 8 1972.
- [127] T. Pavlin, *Hyperpolarized gas polarimetry and imaging at low magnetic field*. PhD thesis, California Institute of Technology, Pasadena, 2003.
- [128] R. Chrapkiewicz, W. Wasilewski, and C. Radzewicz, “How to measure diffusional decoherence in multimode rubidium vapor memories?,” *Optics Communications*, vol. 317, pp. 1–6, 2014.
- [129] M. T. Repetto, *Improvements in production and storage of HP- ^{129}Xe* . PhD thesis, Johannes Gutenberg-Universität Mainz, Mainz, 2015.

- [130] Y.-Y. Fu and J. Yuan, “Intrinsic transverse relaxation mechanisms of polarized alkali atoms enclosed in radio-frequency magnetometer cell,” *Chinese Physics B*, vol. 28, no. 9, p. 98504, 2019.
- [131] G. Norquay, *Spin-Exchange Optical Pumping and Nuclear Magnetic Resonance of ^{129}Xe* . PhD thesis, University of Sheffield, Sheffield, 2014.
- [132] M. S. S. Freeman, *The Efficiency Limits of Spin Exchange Optical Pumping Methods of ^{129}Xe Hyperpolarization: Implications for in vivo MRI Applications*. PhD thesis, Duke University, Durham, 2015.
- [133] Z. Wu, M. Kitano, W. Happer, M. Hou, and J. Daniels, “Optical determination of alkali metal vapor number density using Faraday rotation,” *Applied Optics*, vol. 25, no. 23, pp. 4483–4492, 1986.
- [134] B. Chann, E. Babcock, L. W. Anderson, and T. G. Walker, “Measurements of ^3He spin-exchange rates,” *Physical Review A*, vol. 66, p. 32703, 9 2002.
- [135] E. Vliegen, S. Kadlecik, L. W. Anderson, T. G. Walker, C. J. Erickson, and W. Happer, “Faraday rotation density measurements of optically thick alkali metal vapors,” *Nuclear Instruments and Methods in Physics Research Section A: Accelerators, Spectrometers, Detectors and Associated Equipment*, vol. 460, no. 2, pp. 444–450, 2001.
- [136] M. Antonacci, A. Burant, W. Wagner, and R. Branca, “Depolarization of nuclear spin polarized ^{129}Xe gas by dark rubidium during spin-exchange optical pumping,” *Journal of Magnetic Resonance*, vol. 279, pp. 60–67, 2017.
- [137] R. Merritt, C. Purcell, and G. Stroink, “Uniform magnetic field produced by three, four, and five square coils,” *Review of Scientific Instruments*, vol. 54, pp. 879–882, 7 1983.
- [138] G. Collier, *Metastability Exchange Optical Pumping (MEOP) of ^3He in situ*. PhD thesis, Jagiellonian University, Kraków, 2011.
- [139] N. Tsopelas and N. J. Siakavellas, “Performance of circular and square coils in electromagnetic–thermal non-destructive inspection,” *NDT & E International*, vol. 40, no. 1, pp. 12–28, 2007.
- [140] S. R. Parnell, E. B. Woolley, S. Boag, and C. D. Frost, “Digital pulsed NMR spectrometer for nuclear spin-polarized ^3He and other hyperpolarized gases,” *Measurement Science and Technology*, vol. 19, no. 4, p. 45601, 2008.
- [141] A. H. Couture, T. B. Clegg, and B. Driehuys, “Pressure shifts and broadening of the Cs D_1 and D_2 lines by He, N_2 , and Xe at densities used for optical pumping

- and spin exchange polarization,” *Journal of Applied Physics*, vol. 104, p. 94912, 11 2008.
- [142] C. Glaser, F. Karlewski, J. Kluge, J. Grimmel, M. Kaiser, A. Günther, H. Hattermann, M. Krutzik, and J. Fortágh, “Absolute frequency measurement of rubidium $5S$ - $6P$ transitions,” *Physical Review A*, vol. 102, p. 12804, 7 2020.
- [143] I. Saha, P. Nikolaou, N. Whiting, and B. M. Goodson, “Characterization of violet emission from Rb optical pumping cells used in laser-polarized xenon NMR experiments,” *Chemical Physics Letters*, vol. 428, no. 4, pp. 268–276, 2006.
- [144] H. Shang, B. Zhou, W. Quan, H. Chi, J. Fang, and S. Zou, “Measurement of rubidium vapor number density based on Faraday modulator,” *Journal of Physics D: Applied Physics*, vol. 55, no. 33, p. 335106, 2022.
- [145] J. R. Birchall, M. R. H. Chowdhury, P. Nikolaou, Y. A. Chekmenev, A. Shcherbakov, M. J. Barlow, B. M. Goodson, and E. Y. Chekmenev, “Pilot Quality-Assurance Study of a Third-Generation Batch-Mode Clinical-Scale Automated Xenon-129 Hyperpolarizer,” *Molecules*, vol. 27, no. 4, 2022.
- [146] E. Babcock, I. Nelson, S. Kadlecsek, B. Driehuys, L. W. Anderson, F. W. Hersman, and T. G. Walker, “Hybrid Spin-Exchange Optical Pumping of ^3He ,” *Physical Review Letters*, vol. 91, p. 123003, 9 2003.
- [147] G. D. Cates, D. R. Benton, M. Gatzke, W. Happer, K. C. Hasson, and N. R. Newbury, “Laser production of large nuclear-spin polarization in frozen xenon,” *Physical Review Letters*, vol. 65, pp. 2591–2594, 11 1990.
- [148] M. He, S. H. Robertson, S. S. Kaushik, M. S. Freeman, R. S. Virgincar, J. Davies, J. Stiles, W. M. Foster, H. P. McAdams, and B. Driehuys, “Dose and pulse sequence considerations for hyperpolarized ^{129}Xe ventilation MRI,” *Magnetic Resonance Imaging*, vol. 33, no. 7, pp. 877–885, 2015.
- [149] E. R. Oteiza, *Search for a permanent electric dipole moment in xenon-129 using simultaneous helium-3 magnetometry*. PhD thesis, Harvard University, Cambridge, 1992.
- [150] M. A. Bouchiat and J. Brossel, “Relaxation of Optically Pumped Rb Atoms on Paraffin-Coated Walls,” *Physical Review*, vol. 147, pp. 41–54, 7 1966.
- [151] N. N. Kuzma, B. Patton, K. Raman, and W. Happer, “Fast Nuclear Spin Relaxation in Hyperpolarized Solid ^{129}Xe ,” *Physical Review Letters*, vol. 88, p. 147602, 3 2002.

- [152] A. R. Young, S. Appelt, A. Ben-Amar Baranga, C. Erickson, and W. Happer, “Three-dimensional imaging of spin polarization of alkali-metal vapor in optical pumping cells,” *Applied Physics Letters*, vol. 70, pp. 3081–3083, 6 1997.
- [153] S. R. Parnell, M. H. Deppe, S. Ajraoui, J. Parra-Robles, S. Boag, and J. M. Wild, “Measurement of laser heating in spin exchange optical pumping by NMR diffusion sensitization gradients,” *Journal of Applied Physics*, vol. 107, p. 94904, 5 2010.